THE SEARCH FOR HIGH ENERGY GAMMA-RAY EMISSION FROM TWO WHITE DWARF PULSAR CANDIDATES EUVE J0317-85.5 AND J1912-4410 USING FERMI-LAT DATA

by

LURGASHO HRISTO MINNIE

A thesis submitted to the
Department of Physics
in conformity with the requirements for
the degree of Magister Scientiae

University of the Free State
Faculty of Natural and Agricultural Sciences
South Africa
Supervisor: Prof. Petrus J. Meintjes
Co-Supervisor: Dr. Jacques Maritz

Dedication

This dissertation is dedicated to my mother and grandmother.

"...perhaps it will develop under my pen." - Fyodor Mikhailovich Dostoyevsky

Abstract

The discovery of the first fast spinning, highly magnetic neutron star or "pulsar" (Hewish, Bell, Pilkington, Scott, and Collins (1968)) opened the doors to the possibility that fast spinning, highly magnetic white dwarfs could mimic the same behavior seen in these pulsars. Indeed, the first discovery of a binary "white dwarf pulsar" AR Scorpii by Marsh et al. (2016) confirmed that possibility. EUVE J0317-85.5 (J0317) is an isolated magnetic white dwarf which showed optical (Barstow et al. (1995)) and far-ultraviolet (FUV, Ferrario, Vennes, Wickramasinghe, Bailey, and Christian (1997)) pulsations at a spin period of 725 seconds (12 minutes) and its first harmonic ∼362.9 seconds. This was also confirmed with new optical data from the BOOTES-6 and 7 robotic telescopes. Using archival X-ray data from ROSAT, possible soft X-ray pulsations were also found at the first harmonic. Observations from *Fermi*-LAT revealed low-level γ-ray pulsations in the 0.5-10 GeV energy range at both the spin period P=724.65±0.54s at $\sim 4.01\sigma$ ($\sim 3.72\sigma$ using the H-test Test Statistic) and its first harmonic P=362.65±0.29s at $\sim 3.77\sigma$ ($\sim 3.61\sigma$ using H-test Test Statistic). The γ-ray light curve phase-folded on the rotation period was phase-aligned with the new BOOTES-6 and BOOTES-7 optical folded light curves using the same spin ephemeris suggesting a similar origin of the optical and γ-ray photons in J0317. *Fermi*-LAT observations of the confirmed white dwarf pulsar J191213.72-441045.1 (J1912) revealed γ-ray pulsations in the 0.5-10 GeV energy range at a period P=319.99±0.35s at $\sim 5.74\sigma$ ($\sim 4.73\sigma$ with H-test Test Statistic) for which the phase-folded γ-ray light curve is also in phase with the optical folded light curves using the same spin ephemeris provided by Pelisoli, Marsh, et al. (2023). In both of these systems, the γ-rays could be produced by the curvature radiation mechanism in which electrons slide along the magnetic field line emitting γ-rays modulated at the white dwarf rotation period.

Acknowledgements

First and foremost, I would like to thank God, Jesus and the Holy Spirit for giving me the strength, energy and providing protection to me and my family throughout the course of this study. I would also like to thank my family and friends who motivated and inspired me to pursue my dreams. I also express my deeply felt gratitude and appreciation towards my supervisor Prof. Petrus J. Meintjes and co-supervisor Dr. Jacques Maritz for their guidance, advice, kindness, patience and wisdom during this study. Without their assistance, this dissertation would not be possible. I am also grateful for Spencer Tendai Madzime who helped me with Python scripts for data analyses. I am forever thankful to the members of Grid Related Research Group (GRRG) at the Engineering Science Department of the University of the Free State for interdisciplinary input in my research. My gratitude also extends towards everyone in the Astrophysics Group at the Physics Department at the University of the Free State for their inputs and helpful suggestions. Last but certainly not least, I would like to dearly thank the Interdisciplinary Centre for Digital Futures (ICDF) for financial assistance and the High Performance Computing (HPC) centre at the University of the Free State for providing computational resources to complete this research.

Contents

List of Tables

List of Figures

[1] "https://www.physics.mcgill.ca/~pulsar/magnetar/main.html"

[2] http://ds9.si.edu/doc/ref/how.html

Acronyms

AXPs: Anomolous X-ray Pulsars

BJD: Barycentric Julian Date

BOOTES: Burst Observer and Optical Transient Exploring System

DEC: Declination

EUVE: Extreme Ultraviolet Explorer

eV: electron Volt

FAP: False-Alarm Probability

FITS: Flexible Image Transport System

FOV: Field of View

FUV: Far Ultraviolet

FWHM: Full-width at Half Maximum

GLS: Generalized Lomb-Scargle

GTI: Good Time Intervals

HEASARC: High Energy Astrophysics Archive

HJD: Heliocentric Julian Date

HRI: High Resolution Imager

IFS: Independent Fourier Spacing

LAT: Large Area Telescope

LPTs: Long-period Transients

MG: Mega Gauss

NASA: National Aeronautics Space and Administration

PSF: Point Spread Function

RA: Right Ascension

ROI: Region of Interest

ROSAT: Roentgen Satellite

SGRs: Soft Gamma-ray Repeaters

SED: Spectral Energy Distribution

SSB: Solar System Barycenter

TS: Test Statistic

UT: Universal Time

WWZ: Weighted Wavelet Z-transform

Chapter 1

Introduction

The pulsar-like behaviour from AR Scorpii (Marsh et al. (2016), Buckley et al. (2018)) did open the astronomical doors for similar systems consisting of a fast spinning, highly magnetized white dwarf star that is either isolated or in a binary system to display similar pulsar-like behaviour across the electromagnetic spectrum.

EUVE J0317-85.5 (hereafter J0317) discovered by Barstow et al. (1995) displayed optical pulsations at a period of P=725.4±0.9s for which the light curve showed large amplitude ∼0.1 mag sinusoidal variations. Barstow et al. (1995) proposed this to be the period of rotation of the white dwarf in J0317. J0317 is accompanied by a white dwarf companion LB 9802 but Barstow et al. (1995) found no evidence of accretion occurring in this system (J0317 and LB 9802 are separated by ∼210 AU (Vennes et al. (2003))) making J0317 an isolated white dwarf. Far-ultraviolet (FUV) pulsations at the spin period P=725.5±0.8s and its first harmonic P∼362.9s were found by Ferrario et al. (1997) and they determined a magnetic field of B_d=450 MG for J0317. Radio (Barrett et al. (1999)) and X-ray (Harayama et al. (2013), Dessert et al. (2022)) observations did not reveal any significant emission in either waveband from J0317. Nevertheless, a search for possible γ-ray pulsed emission from J0317 is explored in this dissertation using the *Fermi*-LAT spacecraft because given its relatively fast spin period (∼12 min) and high magnetic field (∼450 MG), J0317 could emit γ-rays via the curvature radiation process (Usov (1988) and references therein). This process occurs because the synchrotron loss timescale scales as $\tau_{syn} \propto \gamma^{-1}B^{-2}$ seconds (Ghisellini (2013)) and

above the white dwarf polar cap $\tau_{syn} \leq 10^{-10}$ seconds implying that the synchrotron losses will be rapid and the charged particles will slide along the curved magnetic field lines producing curvature photons with energies $\leq$10 GeV. Both AR Scorpii and AE Aquarii (see Meintjes, Madzime, Kaplan, and van Heerden (2023) and references therein) showed low-level pulsed γ-ray emission that could be attributed to the curvature radiation mechanism.

J191213.72−441045.1 (hereafter J1912) discovered by Pelisoli, Marsh, et al. (2023) and Schwope, A. et al. (2023) is an interesting binary system with a white dwarf (primary) and an M-dwarf (secondary) in a 4.03 h orbit about a common centre of mass. This system exhibits pulsed emission modulated at the white dwarf rotation period of ∼5.3 min from radio up to the X-ray waveband. Pelisoli, Marsh, et al. (2023) detected flaring behaviour in the XMM-Newton data from J1912 which was suggested to be due to mass transfer from the M-dwarf to the white dwarf. Pelisoli, Sahu, et al. (2023) could only determine an upper limit on the magnetic field of $B \leq 50$ MG of the white dwarf. Since at the time of writing this dissertation, no γ-ray analysis was performed on J1912, we searched for possible pulsed γ-ray emission from J1912 using *Fermi*-LAT. If detected, the pulsed γ-rays could be due to curvature radiation or other radiation processes such as inverse Compton scattering (ICS) mechanism in which charged particles, especially electrons, from the M-dwarf are captured in the white dwarf magnetosphere and re-accelerated to higher energies which consequently upscatter seed photons of the M-dwarf.

Purpose of This Dissertation

The purpose of this dissertation is to search for non-thermal pulsed γ-ray pulsations from both J0317 and J1912 using ∼15 years of *Fermi*-LAT data. Pulsed γ-ray emission from either or both of these white dwarf systems could be further evidence of pulsar-like behaviour from fast rotating, highly magnetized white dwarfs either isolated or in binary systems.

Outline of This Dissertation

- Chapter 2 provides an overview of white dwarfs, magnetic white dwarfs, particle acceleration in white dwarf magnetospheres and a brief overview on pulsars.

- Chapter 3 gives a thorough background on J0317 and J1912.
- Chapter 4 contains new optical observations of J0317 with the BOOTES-6 and BOOTES-7 robotic telescopes, a periodic analysis of J0317 using soft X-ray data from the ROSAT telescope is given in section 4.2 and a γ-ray analysis of J0317 using $\sim$15 years of *Fermi*-LAT data is given in section 4.3.
- Chapter 5, a γ-ray analysis of the binary system J1912 is given using *Fermi*-LAT data.
- Chapter 6 gives the conclusions.
- Appendix A gives the periodic analysis of the ROSAT data using different time bin sizes.
- Appendices B, C, D and E contains periodogram control tests done for both J0317 and J1912 to test the validity of the analysis techniques.
- Appendix F gives a background to the radiation processes.
- Appendix G contains peer-reviewed conference proceedings papers from the High Energy Astrophysics in Southern Africa (HEASA) 2023 and 2025 conference.

Chapter 2

Overview

2.1 White Dwarf Stars

White dwarfs are very dense stars with a mass comparable to or higher than that of our own Sun (1 $M_{\odot}$~2×10^{33}g) and with a size approximately that of the Earth (R_{Earth}~6×10^{8}cm). These stars are the end-point of stellar evolution when stars similar to our Sun have used up all of their thermal nuclear fusion products in their cores. Most stars like our Sun burn hydrogen to helium in their core and they are known as main sequence stars and occupy the diagonal strip on the Hertzsprung-Russell (Hertzsprung (1905), Russell (1919), see Figure 2.1) diagram. The conversion of hydrogen into helium is a very slow process and can last a very long time ranging from millions to billions of years depending on the star's mass. This fusion of elements inside the core of stars is what powers most stars. However, there comes a point in the stellar evolution when helium (He) is converted to carbon (C) followed by the expansion of the star's outer layers. During this process the outer layers get expelled into space and what is left is a dense stellar core known as a white dwarf. White dwarfs are known as dead stars because they reached a point in their evolution where they ran out of thermonuclear fuel. And as a result, they do not possess the necessary thermal and radiation pressure to counteract their own gravity. And so, the electrons in the white dwarf core are pushed tightly together and occupy the lowest energy states. When this happens, the white dwarf core is known as degenerate. These degenerate electrons exert a pressure to balance the gravity and this pressure is well-known as the "electron degeneracy pressure". And this is the reason why white

dwarfs are such dense stars. They have a density of about 1×10^6g cm^{-3} which is approximately a million times more dense than Earth and they have radii of about 5×10^8 cm (Camenzind (2007)). There are different types or classes of white dwarfs and they are briefly highlighted in the next section.

2.1.1 Types of White Dwarfs

Like normal stars, white dwarfs are mainly classified by the features that exist in their spectra (Carroll and Ostlie (2017)). These features can be either absorption and/or emission lines created by elements that exist in the white dwarf atmospheres. A majority of white dwarfs show only "pressure-broadened hydrogen absorption lines" in their spectra and these are called DA white dwarfs. DB white dwarfs only show Helium (He) absorption lines and DC white dwarfs are devoid of lines in their spectra. DQ white dwarfs show traces of Carbon (C) in their spectra and DZ white dwarfs show traces of metal lines (Carroll and Ostlie (2017)). White dwarf atmospheres are complex and show a variety of elements in their spectra. The emission and absorption lines in the white dwarf's spectra are mainly dependent on their surface temperature which ranges from 4000 K to about 150 000 K (Fontaine, Brassard, and Bergeron (2001)). See Van Horn (2015) for a complete description of the properties and characteristics of white dwarfs. The magnetic field strength of a white dwarf is another interesting characteristic and white dwarfs with very high magnetic fields (10^6-10^9 G, (Ferrario, de Martino, and Gänsicke (2015)) are called magnetic white dwarfs (MWDs).

2.1.2 Magnetic White Dwarfs

The magnetic field origin in white dwarfs has been a topic of discussion for many years. It has been proposed by Ferrario and Wickramasinghe (2005) that the magnetic fields in isolated white dwarfs could likely be a result of remnants from a main-sequence phase where the initial magnetic flux of the main-sequence star has been conserved during the evolution to the white dwarf phase. Another scenario suggests that there is a common magnetic field origin between planets and white dwarfs (Isern, Garca-Berro, Klebi, and Lorn-Aguilar (2017)). In the latter scenario, a dynamo is generated by the phase separation (the non-degenerate envelope and the solid, degenerate core)

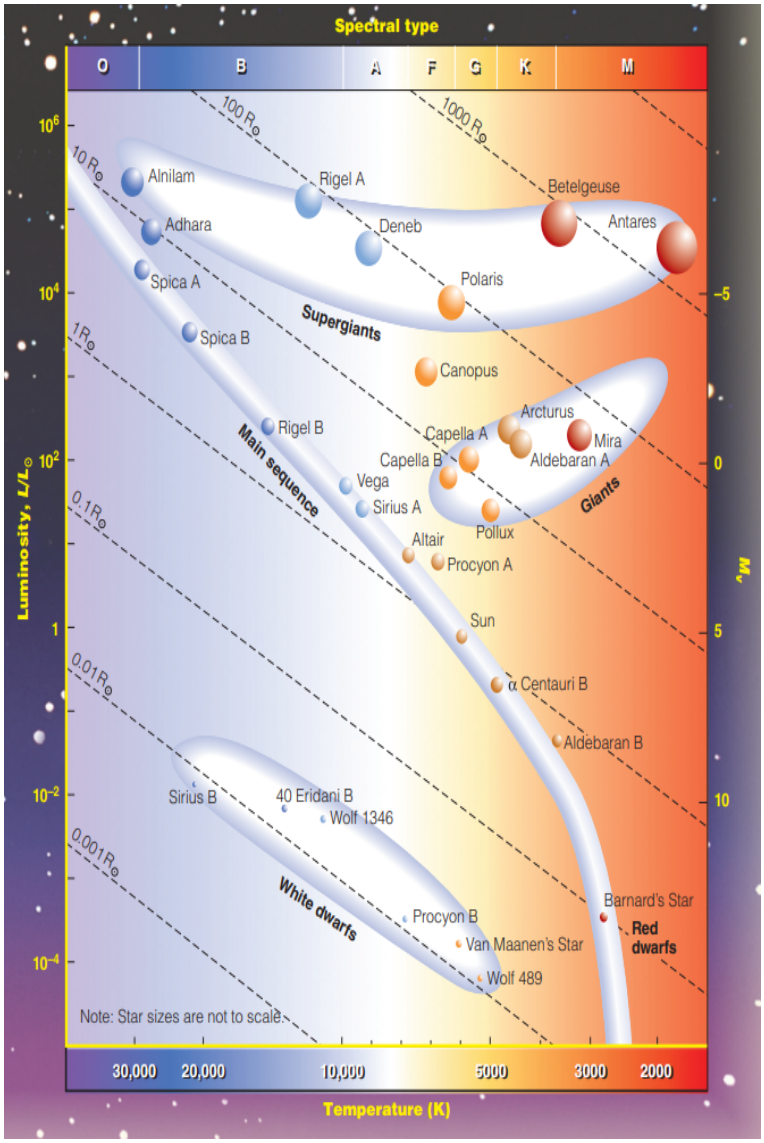

Figure 2.1: The H-R diagram showing the relation between the luminosity with respect to the solar luminosity (1 $L_{\odot}$~4×10^{26}Watt), effective temperature, spectral type and the absolute magnitude (M_V) of various stars and the Sun occupying the diagonal strip (main-sequence) and white dwarfs at the bottom left. Figure adopted from Seeds and Backman (2016).

upon the white dwarf crystallization. This is similar to Earth, where a solid core is surrounded by a liquid core which causes a dynamo to be produced and hence results in Earth's magnetic field.

Strong magnetic fields can also be produced by a differentially rotating, hot and convective corona caused by the merger of two degenerate cores (Wickramasinghe and Ferrario (2000), Garca-Berro et al. (2012)). During this process, the remnants of the two degenerate cores will consist entirely of a central, primary white dwarf and on top of this white dwarf will be a hot corona consisting of approximately half of the secondary's (the other degenerate core) mass. This hot corona is highly convective and differentially rotates and is affected by the "magnetorotational instability". This essentially leads to a dynamo and hence to the production of strong magnetic fields (see Garca-Berro et al. (2012) and references therein).

2.2 White Dwarfs in Binary Systems

There are two main branches of binary systems in which the primary star is the white dwarf, namely non-interacting and interacting binaries. In both these binary classes the primary star (more massive star) and secondary star (usually a late-type main-sequence star) orbit a common centre of mass that is usually close to the primary star. The magnetic field of the primary star in binary systems is believed to be generated by a crystallization- and rotation driven dynamo (Schreiber, Belloni, Gänsicke, Parsons, and Zorotovic (2021)). In this scenario, the primary is spun-up by accretion of angular momentum from its secondary. Then, as the primary cools, its carbon/oxygen core begin to freeze into a lattice structure. This causes the solid phase to become richer in oxygen and essentially sinks and the carbon excess mixes with the outer liquid envelope and gets redistributed by Rayleigh-Taylor instabilities. This very strong density stratification, rapid rotation and convection leads to a strong magnetic field in the primary (see Schreiber et al. (2021) for further details). In a non-interacting binary there is no interaction between the secondary and primary star because they are separated by large distances. In interacting binaries, something peculiar happens when the secondary star evolves to a stage where its outer layers expand which then fills its Roche lobe[1] (Roche-lobe overflow, Warner (2003)) from where random thermal motions causes the plasma to flow through the inner Lagrangian point L_1 (point of zero effective gravity). The L_1 point is orbiting perpendicular to this motion at more than $1{\times}10^7$cm s^{-1} (Hellier (2001))

[1]Gravitational equipotential surface around stars in binary systems

where the plasma stream swings into an orbit around the primary instead of flowing directly towards it (see Figure 2.2). An accretion disc can only form when the magnetic field of the primary is weak and the secondary is close enough to allow the plasma to form a ring at the "circularization radius" (radius where the angular momentum is equivalent to that of the plasma at L_1 point) where the plasma is spread into a disc due to viscosity and the conservation of angular momentum. These systems are referred to as Cataclysmic Variable stars (CVs) and can then be further subdivided into non-magnetic and magnetic CVs.

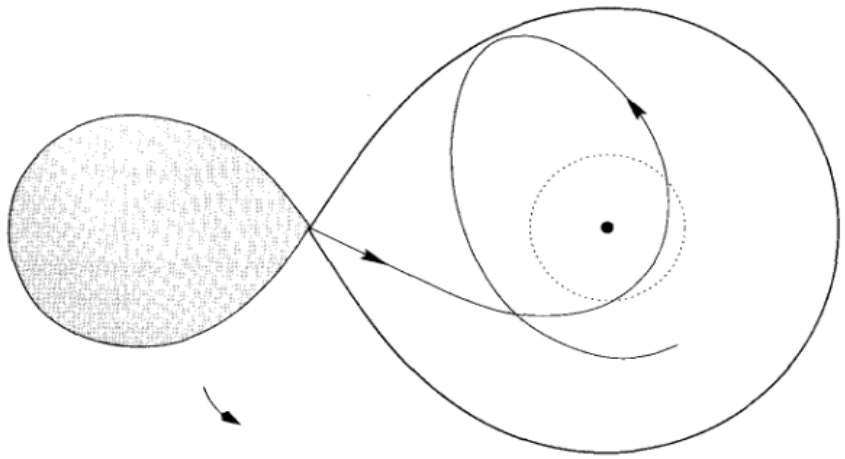

Figure 2.2: Top view of plasma stream from the secondary (left) to the Roche lobe of the primary (right) where the plasma stream collides with itself and forms a ring at the circularization radius (dotted circle). Figure adopted from Hellier (2001).

2.2.1 Non-Magnetic CVs

In non-magnetic CVs, the white dwarf has a magnetic field $B \leq 10^5$G (King and Shaviv (1984)) meaning that this weak magnetic field can not intercept the ballastic stream from the secondary before it reaches the circularization radius from where it can spread into a disc due to viscosity. These systems occasionally experience outbursts and/or super-outbursts that are caused by the increase in the rate of mass accretion onto the surface of the white dwarf. Non-magnetic CVs are subdivided into dwarf novae which experience outbursts and/or super-outbursts and novalikes

which generally do not experience outbursts or super-outbursts. The reader is referred to Smith (2006) and references therein for a thorough review of dwarf novae and novalikes.

2.2.2 Magnetic CVs

The white dwarfs in magnetic CVs have a strong magnetic field that ranges between 10^6-10^8 G (Wu, K. and Kiss, L. L. (2008)) and can be subdivided into polars and intermediate polars.

Polars

If the primary's magnetic field strength is sufficiently strong (∼10-200 MG, Wu (2000)), the mass-flow from the secondary star rams into the magnetic field from where the field lines guide the flow to the polar cap regions to accrete there. The gravitational potential energy released from this mass accretion is what drives the emission from these systems. This class of magnetic CVs are known as polars (AM Herculis types, after its prototype AM Her Wolf (1924), Berg and Duthie (1977), Tapia (1977)) and they are mainly characterized by their highly polarized cyclotron emission (V∼5%-30%, Stockman et al. (1992)). In polars, the primary's magnetic field is strong enough to cause it to rotate synchronously meaning that the spin period (P_{spin}) of the white dwarf becomes comparable to the orbital period (P_{orb}) of the binary system (Cropper (1990)). Gravitational tidal forces further synchronize the secondary star's rotation period with the binary's orbital period (e.g Warner (2003)). This synchronicity between P_{spin} and P_{orb} is believed to be due to the interaction between the primary and the secondary's dipole magnetic fields (Campbell (1985)). Warner (2003) estimated $P_{orb}\leq$4.6 hours for most polars. This is due to the accreting matter flowing along the primary's magnetic field lines and hitting the magnetic poles (see Figure 2.3). This accretion column above the primary's magnetic poles is where most of the observed flux from these systems originate. For a thorough review of polars the reader is kindly referred to Cropper (1990), Warner (2003) and references therein.

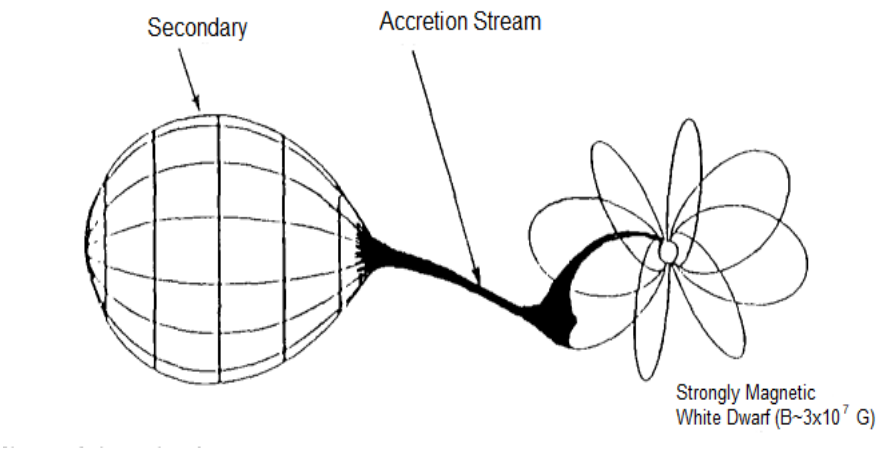

Figure 2.3: The magnetic white dwarf in AM Her types accretes matter from late-type main-sequence star via its magnetic field lines and directs the matter onto the magnetic poles. Figure adopted from Cropper (1990).

Intermediate Polars

When the white dwarf's magnetic field in magnetic CVs is less than ∼5 MG (Wickramasinghe, Wu, and Ferrario (1991)), the magnetic energy density is not high enough to disrupt the accretion disc formation around the primary. In some cases, the primary's magnetic field can truncate the accretion disc's inner edge and prevent stellar material from reaching its equatorial surface at which point the stellar material siphons (flow) along the primary's magnetic field to accrete near the poles (Warner (1996)). See Figure 2.4 for an illustration. Accretion disc formation is not the defining characteristic of these systems because discless accretion states have been proposed (see Warner and Wickramasinghe (1991) and Buckley (1997)). These systems are referred to as intermediate polars (also called DQ Herculis types after its prototype Nova DQ Herculis 1934, Walker (1954)) and are mainly characterized by the asynchronism between the primary's spin period (P_{spin}) and the orbital period (P_{orb}) of the binary system. The rotation period of the primary in these systems ranges between ∼33 seconds and ∼2 hours (Patterson (1994)). However, white dwarfs in these systems with spin periods less than 33 seconds have recently been discovered namely the P_{spin}∼25 second LAMOST J024048.51+195226.9 (Pelisoli et al. (2021)) and the P_{spin}∼29 second CTCV J2056−3014 (Lopes de Oliveira, Bruch, Rodrigues, Oliveira, and Mukai (2020)). A majority of these systems

share the relation where $P_{spin}\sim 0.1 P_{orb}$ (Hellier (1996)) in which the $P_{orb}\geq 4$ hours (King and Lasota (1991)). The weak magnetic fields of the primary star and the existence of an accretion disc in intermediate polars are the main reasons why circular polarized emission is so rarely observed and could be less than 0.1 per cent in circularly polarized emission (Wickramasinghe et al. (1991) and references therein). When the accretion disc's inner edge meets the primary's magnetic field lines, it forms arc-shaped accretion curtains above the primary's surface (Parker (2005)). As this stellar material settles onto the primary's surface, strong shocks are produced resulting in optical to X-ray emission. For an in-depth review of intermediate polars, the reader is referred to Patterson (1994), Warner (2003) and references therein.

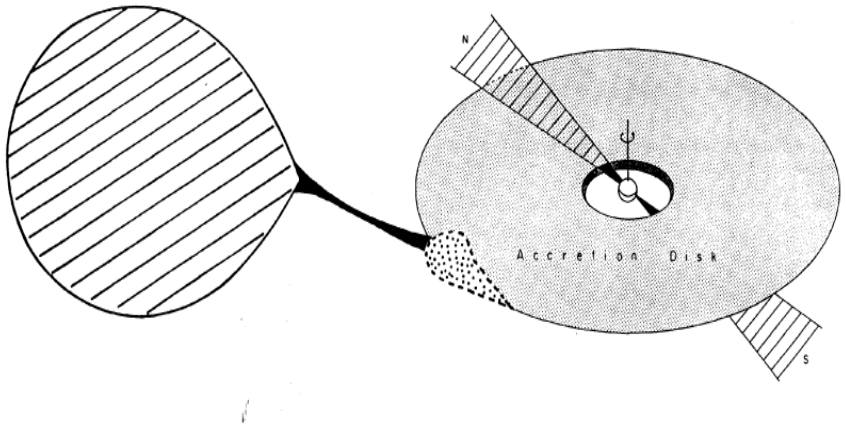

Figure 2.4: Illustration of an intermediate polar (DQ Her system) showing the formation of an accretion disc truncated at the magnetosphere of the primary. The point where the stream from the secondary hits the accretion disc is called the hot spot. Figure adopted from Patterson (1994).

2.3 Isolated Magnetic White Dwarfs

The magnetic field strength from isolated magnetic white dwarfs have been observed to range between 10^3-10^9 G (Wickramasinghe and Ferrario (2000), Ferrario et al. (2015)). As briefly discussed in Section 2.1.2, the origin of these high fields in these white dwarfs could be of fossil origin or could result from the merger of two white dwarf stars – so-called "double degenerate merger scenario" (García-Berro et al. (2012)) – with initial individual magnetic fields that ranges in the kilo Gauss regime. Brinkworth, Burleigh, Lawrie, Marsh, and Knigge (2013) found that 67% of isolated magnetic white dwarfs in their sample have rotation periods between 27 minutes and 6 days. SDSS J221141.80+113604.4 is an isolated magnetic white dwarf that was recently discovered by Kilic, Kosakowski, Moss, Bergeron, and Conly (2021) to have a spin period of 70 seconds and magnetic dipole field strength of $B_d \sim 15$ MG making it the fastest rotating isolated magnetic white dwarf to date. This combination of fast rotation periods and strong magnetic fields in these isolated white dwarfs could make them mimic the behavior in pulsars.

The same behavior is also observed from white dwarfs in binary systems (e.g. AR Scorpii and AE Aquarii). This suggests that the magnetospheres of white dwarfs could be sites for particle acceleration and hence the production of non-thermal high energy emission under certain conditions (Usov (1988), Lobato et al. (2017)). In the next section, a brief overview of particle acceleration in these systems will be given and is based on Section 2 of Meintjes et al. (2023) and references therein.

2.4 Particle Acceleration in White Dwarf Magnetospheres

The magnetic and electric fields in a co-moving reference frame with a highly conducting plasma can be given by the following expressions respectively (Jackson (1975))

$$\begin{aligned} \mathbf{B}' &= \Gamma \left[\mathbf{B} - \frac{1}{c}(\mathbf{v} \times \mathbf{E}) \right] \\ \mathbf{E}' &= \Gamma \left[\mathbf{E} + \frac{1}{c}(\mathbf{v} \times \mathbf{B}) \right] \end{aligned} \tag{2.1}$$

where $\boldsymbol{B'}$ and $\boldsymbol{E'}$ are the magnetic electric fields in the co-moving frame respectively, the unprimed $\boldsymbol{E}$ and $\boldsymbol{B}$ are the fields in the laboratory (stationary) reference frame respectively. The Lorentz factor is Γ and $\mathbf{v}$ gives the relative velocity between the co-moving and laboratory reference frames. For a fluid conductivity of $\sigma \to \infty$ the electric field $\boldsymbol{E'} \to \mathbf{0}$ in the co-moving reference frame and the fields in the laboratory frames reduces to

$$\begin{aligned} \mathbf{B} &= \Gamma \mathbf{B}' \\ \mathbf{E} &= -\Gamma(\bar{\beta} \times \mathbf{B}') \end{aligned} \tag{2.2}$$

where $\bar{\beta} = \mathbf{v}/c$. For a charged particle with charge Ze, the maximum energy that it attains is given by

$$\begin{aligned} \epsilon_{max} &= Ze \int \mathbf{E} \cdot \mathbf{ds} \\ &= q\beta\Gamma B' R_s \end{aligned} \tag{2.3}$$

where R_s is the size of the source. It is thus seen that for fast spinning compact objects i.e. $\beta\Gamma \gg 1$, the kinetic energy due to rotation can accelerate charged particles to high energies even if the compact object has a moderate magnetic field strength. The famous Hillas diagram (Hillas (1984), Lobato et al. (2017)) is shown in Figure 2.5 showcasing the magnetic field and size requirements of different objects to accelerate ions and protons to energies of $\epsilon_{max} \sim 10^{20}$ eV.

From Figure 2.5 it is evident that AE Aquarii, AR Scorpii and white dwarfs with similar parameters can indeed accelerate particles to energies of $\epsilon_{max} \sim 10^{20}$ eV (ignoring particle energy losses). Indeed, as was shown by Usov (1988), the magnetospheres of fast spinning, highly magnetic white dwarfs could possibly be sites for particle acceleration and hence the generation of γ-rays. The "scale height" of an isolated white dwarf atmosphere is given by (Usov (1988))

$$H_s \approx \frac{kT_s R^2}{m_p G M} \sim 10^4 \left(\frac{R}{10^9 cm}\right)^2 \left(\frac{M}{M_\odot}\right)^{-1} \left(\frac{T_s}{10^5 K}\right) cm \tag{2.4}$$

where $R \sim 10^9$cm, $M \sim 1 M_\odot$ and $T_s \leq 10^5$ K is the radius, mass and the surface temperature of the

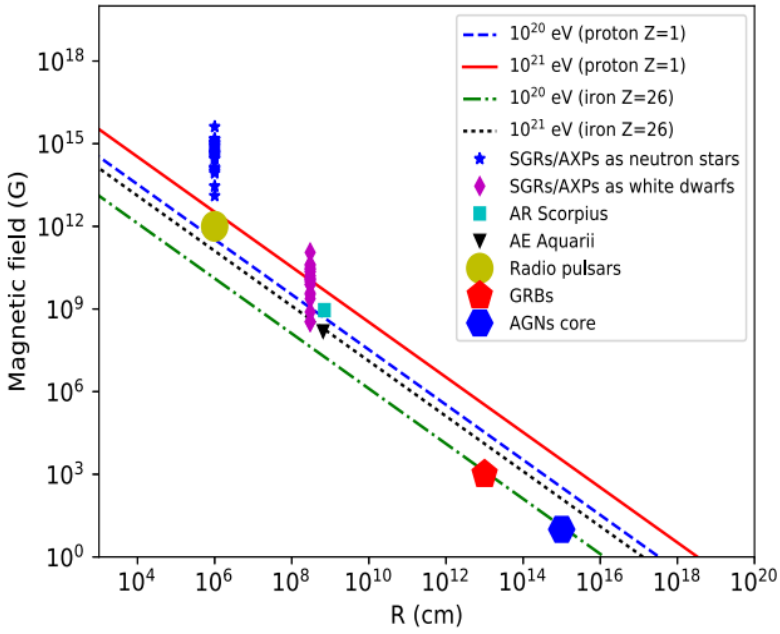

Figure 2.5: Hillas diagram showing the $\vec{B}$-field (in Gauss) vs the size of the object that is required to accelerate charged particles to high energies. The diagonal lines shows the requirements to accelerate heavy nuclei (iron) and protons to energies of 10^{20} eV and 10^{21} eV respectively. The positions of AE Aquarii and AR Scorpii is also shown. Figure adopted from Lobato et al. (2017).

white dwarf respectively. This scale height is smaller than the white dwarf radius and in the absence of accretion from the secondary, this scale height region essentially becomes a vacuum. The rotating magnetic white dwarf in vacuo will essentially induce a non-zero electric field component (Deutsch (1955), Goldreich and Julian (1969))

$$E_{\parallel} = \frac{\mathbf{E} \cdot \mathbf{B}}{|\mathbf{B}|} \neq 0 \tag{2.5}$$

along the **B**-field lines. The electric field component causes an electric force ($F = qE_{\parallel}$) which will extract charged particles from the white dwarf's surface to form a magnetosphere with particle

density (Goldreich and Julian (1969))

$$n_{GJ} = \frac{\mathbf{\Omega} \cdot \mathbf{B}}{2\pi ce} \approx 10^4 B_6 \Omega \quad cm^{-3} \tag{2.6}$$

where $\Omega = 2\pi/P$ is the spin frequency of the white dwarf and B_6=10^6 G is the magnetic field approximated by $B \approx B_p(R/r)^3$ (dipole configuration) a distance r from the white dwarf's centre. Equation 2.6 implies that electric potentials only exist where $n < n_{GJ}$ (where $n_{GJ} = \rho_{GJ}/e$). In the corotating frame, Gauss's law can be written as $\boldsymbol{\nabla \cdot E} = 4\pi(\rho - \rho_{GJ})$ and if we only consider a one-dimensional case, this expression would become $\partial E_{\parallel}/\partial s = 4\pi(\rho - \rho_{GJ})$ where s is a distance along the magnetic field lines. Then the potential drop along s can be written as $\Delta\Phi = -\int E_{\parallel} ds \approx 2\pi(\rho_{GJ} - \rho)h^2$ (Goldreich and Julian (1969), Ruderman and Sutherland (1975)) where h is the accelerating gap height. Hence for $n < n_{GJ}$, the $E_{\parallel}$ will be "unscreened" resulting in a potential drop to accelerate particles, the condition $n = n_{GJ}$ will "screen" $E_{\parallel}$ resulting in no particle acceleration and the condition $n > n_{GJ}$ will essentially quench the electric potential. Closer to the white dwarf the electrons will radiate away their energy on time scale (Ghisellini (2013))

$$t_{sync} \sim \frac{7.75 \times 10^8}{\gamma_e B^2} \quad s \tag{2.7}$$

due to synchrotron radiation. Ultimately, the electrons lose their perpendicular velocity component with respect to the **B**-field over t_{sync}. For typical values (e.g. AE Aquarii and AR Scorpii) $B \sim 10^6$ G and $\gamma_e \leq 10^6$, $t_{sync} \leq 10^{-10}$ s implying that the synchrotron channel rapidly shuts off close to the white dwarf's surface and electrons essentially move along the **B**-field lines emitting curvature radiation (Ruderman and Sutherland (1975))

$$\epsilon_{CR} = \frac{3\hbar c \gamma_e^3}{2R_c} \tag{2.8}$$

where the curvature radius is given by

$$R_c \approx \sqrt{\frac{Rc}{\Omega}} \tag{2.9}$$

If the **B**-field strength of the white dwarf is high enough, then these curvature photons can create electrons (e^-) and positrons (e^+) according to the process

$$\gamma + B \rightarrow e^- + e^+ + B \tag{2.10}$$

if the energy of the photons exceed twice the rest mass energy of an electron ($\epsilon_\gamma \geq 2m_e c^2$, Erber (1966)). These secondary particles (e^- and e^+) can then further be accelerated along the "open" **B**-field lines to produce radiation which consequently results in another electron-positron ($e^\pm$) pair ultimately resulting in a "pair cascade process". The condition for pair ($e^\pm$) production is given by (Chen and Ruderman (1993))

$$\left(\frac{e\Delta V_{max}}{m_e c^2}\right)^3 \frac{\hbar}{2m_e c R_c} \frac{h_{max}}{R_c} \frac{B_p}{B_q} \approx \frac{1}{15} \tag{2.11}$$

where $B_q = m_e^2 c^3/(e\hbar) = 4.4\times10^{13}$G is the "quantum electrodynamic field". The maximum potential difference of the accelerator gap is given by (Lobato, Coelho, and Malheiro (2015), Lobato et al. (2017), Ruderman and Sutherland (1975), Cáceres, deCarvalho, Coelho, deLima, and Rueda (2016))

$$\Delta V_{max} \approx \frac{B\Omega^2 R^3}{2c^2} \tag{2.12}$$

and the maximum height of this gap is $h_{max} = \frac{1}{\sqrt{2}} \left(\frac{R^3\Omega}{c}\right)^{1/2}$ (Kashiyama, Ioka, and Kawanaka (2011), Lobato et al. (2017), Cáceres et al. (2016)). Using the above expressions, the "threshold for magnetic pair production" is given by (Meintjes et al. (2023))

$$\alpha = 3log(\Delta V_{max}) + log(h_{max}) - 2log(R_c) + log(B_p) \approx 33 \tag{2.13}$$

This condition implies that curvature photons that are produced close to the surface of the white dwarf may either be transparent or opaque to the magnetosphere. If curvature radiation is the dominant energy loss mechanism, then $\tau_c \approx 180 R_c^2 \gamma^{-3}$ (Ochelkov and Usov (1980)) and if we assume that $\tau_c = \tau_{cross}$ (where $\tau_{cross} \sim h_{max}/c$ is the crossing time of the accelerator gap of width h_{max} which

we assume is proportional to the acceleration time) resulting in the maximum electron energy

$$\gamma_{max} \approx \left(\frac{180 R_c^2 c}{h_{max}} \right)^{1/3} \tag{2.14}$$

Using these expressions, Meintjes et al. (2023) showed that both AR Scorpii and AE Aquarii could emit γ-rays via the curvature radiation mechanism with energies $\leq$50 GeV. Therefore, it is possible that either or both EUVE J0317-85.5 and J191213.72−441045.1 might emit γ-rays via the same curvature radiation mechanism with energies $\leq$50 GeV for which the *Fermi*-LAT observatory is well equipped to detect photons in this energy range due to the long data baseline (more than a decade).

Since fast rotating, highly magnetic white dwarfs show similar characteristics to pulsars, a very brief overview of pulsars will now be given. The reader is kindly referred to the given references for an in-depth discussion on pulsars.

2.5 Pulsars

Neutron stars are extremely dense stars weighing more than the Sun with radii of $\sim$10 km. Neutron stars form when massive stars (M>8$M_\odot$, Lattimer and Prakash (2004)) undergo supernova explosions (Baade and Zwicky (1934)) at the end of their lives. There are two types of supernova explosions: Type Ia, where the mass of the white dwarf exceeds the Chandrasekhar limit ($\sim$1.44 $M_\odot$) as a result of accretion from a secondary star and consequently implodes resulting in a supernova explosion, Type Ib represents a core collapse of a massive star that lost their hydrogen outer layer before exploding, Type Ic results from the core collapse of a massive star that lost both its Hydrogen and Helium outer layers before exploding. Type II (contains strong hydrogen lines Carroll and Ostlie (2017)) is where a supergiant star runs out of nuclear fusion energy because of its iron core and implodes forming a neutron star (see Vink (2011) and references therein for a discussion on supernova explosions). When neutron stars spin very rapidly and have huge magnetic fields, they produce pulsed electromagnetic radiation and are known as pulsars (Hewish et al. (1968)). See Figure 2.6 for an illustration.

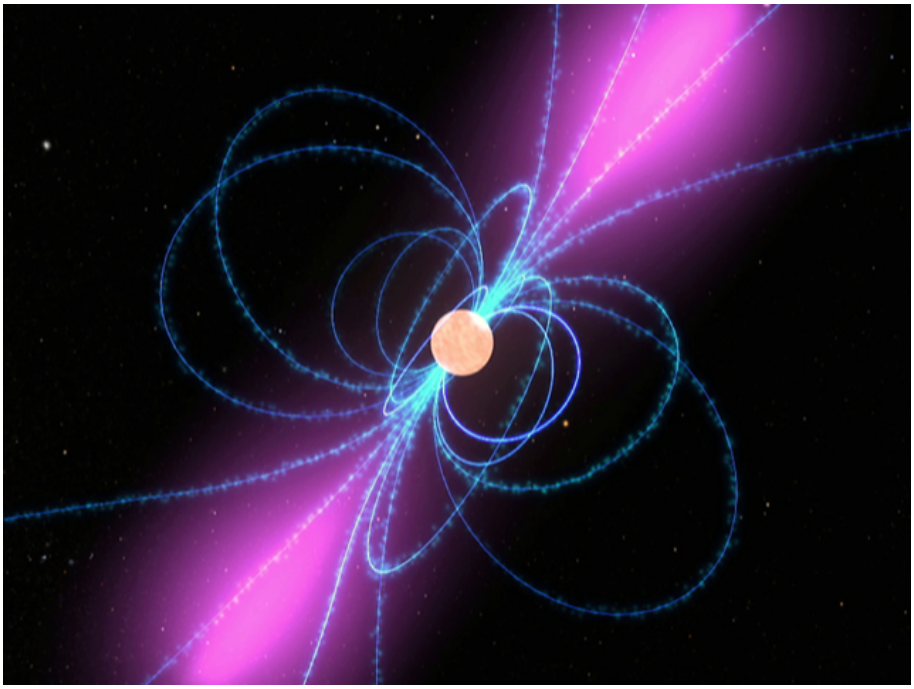

Figure 2.6: Illustration displaying the beamed emission from a pulsar. *Image credit:NASA*

A majority of isolated pulsars have rotation periods that range between 0.002 and 8.5s (Young, Manchester, and Johnston (1999)). This period distribution is not set in stone because pulsars with rotation periods in the millisecond range have been discovered and these are known as millisecond pulsars[2]. For example, the fastest rotating pulsar to date is PSR J1748-2446ad with a period of P_{spin}=0.00139595482s (Hessels et al. (2006)) and the pulsar with the longest rotation period is PSR J0901-4046 with P_{spin}=75.89s (Caleb et al. (2022)). Pulsars also have enormous magnetic fields ranging from 10^{11}-10^{13} G (Olausen and Kaspi (2014)) with some pulsars, known as magnetars, having magnetic fields exceeding $\geq 10^{14}$ G. This combination of rapid rotation and high magnetic fields give pulsars their famous characteristic: they produce pulsed/beamed radiation from their magnetic poles.

[2]Millisecond pulsars usually occur in binary systems where they have been spun-up as a result of mass accretion from their companions.

2.5.1 Emission from Pulsars

In electrodynamics, it is well-known that moving charged particles induce a $\boldsymbol{B}$-field. Additionally, a moving $\boldsymbol{B}$-field can also induce an electric potential that can accelerate charged particles[3]. This concept is the driving mechanism that explains the pulsed emission that is seen from pulsars. In a simplistic view, the magnetic field morphology in pulsars is assumed to be dipolar (Goldreich and Julian (1969), Sturrock (1971), Ostriker and Gunn (1969)) similar to what one might see if one throws iron filings near a bar magnet. If this magnetic dipole rotates and is misaligned with its rotation axis, then this magnetic dipole must radiate electromagnetic radiation at its rotation frequency and the power of this emission can be estimated by (see Goldreich and Julian (1969), Shapiro and Teukolsky (1983) and references therein)

$$\dot{E}_{dip} = \frac{dE_{dip}}{dt} = -\frac{2|\boldsymbol{m}|^2}{3c^3}\Omega^4 \sin^2\alpha \tag{2.15}$$

where $|\boldsymbol{m}|{=}B_p R^3/2$ is the magnetic moment with B_p the polar magnetic field of the pulsar and R its radius, $\Omega{=}2\pi/P$ the rotational angular frequency and α the angle between the magnetic and spin axis of the pulsar. The rotational kinetic energy of this magnetic dipole is

$$E = \frac{1}{2} I \Omega^2 \tag{2.16}$$

where $I{\approx}MR^2$ is the pulsar's "moment of inertia". Then the rate of loss of this rotational kinetic energy is

$$\dot{E} = -\frac{4\pi^2 I \dot{P}}{P^3} \tag{2.17}$$

where $\dot{P}$ is the rate of change of spin period of the pulsar. If we assume that "magnetic dipole radiation" (Ostriker and Gunn (1969)) is the dominant energy loss mechanism then the pulsar's surface magnetic field can be determined by equating equations 2.15 and 2.17 which results in

$$B_s = \sqrt{\frac{3c^3}{8\pi^2}\frac{I}{R^6 \sin^2\alpha} P\dot{P}} \tag{2.18}$$

[3]Faraday's Law was discovered by Micheal Faraday in 1831.

The strength of the magnetic field is the highest at the poles of the pulsar. In this dipole magnetic field morphology, there exist closed and "open" magnetic field lines (see Figure 2.7). The closed magnetic field lines extend to a distance known as the light cylinder radius (R_{LC}, Gold (1969)) given by

$$R_{LC} = \frac{c}{\Omega} = \frac{cP}{2\pi} \tag{2.19}$$

where c gives the speed of light and P is the rotational period of the pulsar. At the light cylinder radius, R_{LC}, the $\boldsymbol{B}$-field lines co-rotate with a velocity equal to c. Beyond R_{LC}, the $\boldsymbol{B}$-field lines can not close because all the co-rotating trapped particles effectively move with the speed of light and these particles become super-relativistic which increases their relativistic mass which consequently exerts a load on the magnetic fields and hence force these field lines "open" (Goldreich and Julian (1969)). On both magnetic poles, there exist circular regions with their circumferences defined by the foot point of the last "open" magnetic field line. These regions are called polar cap regions and they have radii (R_{PC}, Sturrock (1971)) on the order of

$$R_{PC} \approx R\theta_p \approx \sqrt{\frac{2\pi R^3}{cP}} \tag{2.20}$$

where R is the star's radius and θ_p is the angular radius of the polar cap (see Figure 2.7).

Above the polar caps of a rotating pulsar, an electric potential is induced which can be estimated according to Goldreich and Julian (1969) for an aligned rotator (rotation axis and magnetic axis are parallel) by

$$\Delta\phi = \frac{B_p \Omega^2 R^3}{2c^2} \tag{2.21}$$

where B_p is the polar magnetic field and $\Omega = 2\pi/P$ is the rotation angular frequency of the pulsar. This electric potential difference will result in a Lorentz force $e[(\boldsymbol{v}/\mathrm{c})\times\boldsymbol{B}]$ (where bold symbols indicate vectors) on the charged particles (electrons, ions and protons) that greatly exceeds the gravitational force of the pulsar by 10 orders of magnitude (Lorimer and Kramer (2005)) and as a result, the charged particles get extracted from the pulsar's surface. This effectively means that regions above the polar caps of pulsars can not be devoid of particles and so an approximation of

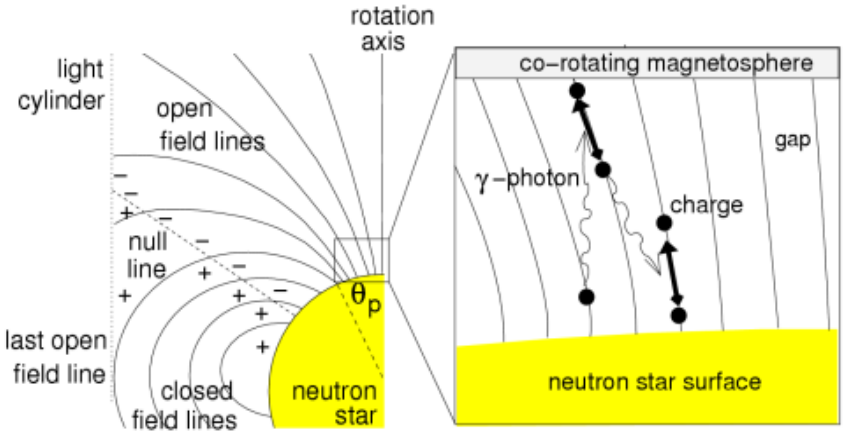

Figure 2.7: Magnetosphere of a pulsar where the rotation axis and magnetic axis are aligned. Inset shows particle extraction and acceleration above the polar cap. Figure adopted from Lorimer and Kramer (2005).

the density of these charged particles is given by (Goldreich and Julian (1969), Becker et al. (2009))

$$\rho_c = \frac{\boldsymbol{\nabla}\cdot\mathbf{E}}{4\pi} = -\frac{\boldsymbol{\Omega}\cdot\mathbf{B}}{2\pi c}\frac{1}{1-|\boldsymbol{\Omega}\times\mathbf{r}/c|^2} \tag{2.22}$$

This equation then reduces to the particle number density provided by equation 2.6 where $n_{GJ}=\rho_c/e$ is called the "Goldreich-Julian density" (Goldreich and Julian (1969)) and fills the regions bound by closed $\boldsymbol{B}$-field lines to make up the magnetosphere. Equations 2.22 and 2.6 only apply if the currents (charged particles) in the magnetosphere are negligible i.e. in the co-rotation frame $\boldsymbol{E'}=0$, which implies that

$$\boldsymbol{E} = -\frac{1}{c}(\boldsymbol{\Omega}\times\mathbf{r})\times\boldsymbol{B} \tag{2.23}$$

where $\boldsymbol{B}$ and $\boldsymbol{E}$ are the magnetic and electric fields in a stationary frame respectively, and $\boldsymbol{\Omega}\times\mathbf{r}$ is the co-rotating velocity. If the electric field component (equation 2.5) along the $\boldsymbol{B}$-field direction is non-zero then this $E_{\parallel}$ can accelerate charged particles to ultra-relativistic velocities (Michel (1991)). This non-zero $E_{\parallel}$ can accelerate the electrons/positrons along the $\boldsymbol{B}$-field lines consequently emitting radiation. The electromagnetic radiation appears as pulses when it intercepts the line of sight

of a stationary observer as the pulsar rotates. It should be noted that these equations apply only to the aligned rotator where the spin and the magnetic axis of the pulsar are parallel. But these equations do not differ significantly for counter-aligned (oblique) configurations (Becker et al. (2009)) where the magnetic axis is inclined at some angle with respect to the rotation axis. Over the years, various theoretical models have been constructed to try and explain the exact nature of pulsar emission regions and mechanisms. These models are only briefly discussed in the following sections and the reader is referred to given references for a thorough discussion on these pulsar models.

2.5.2 Polar Gap Model

In this pulsar model, a majority of the electromagnetic radiation is created above the polar caps of the pulsar (Sturrock (1971)). There exists a potential difference $\Delta\phi$ between the edge and the center of the polar cap which Sturrock (1971) showed to be

$$\Delta\phi \sim \left(\frac{B_s\Omega}{2c}\right) h_s^2 \tag{2.24}$$

where h_s is the height above the polar cap where charged particles are accelerated. Sturrock (1971) assumed this height to be of the same order as polar cap radius (R_{PC}, Equation 2.20). This potential difference extracts charged (primary) particles from the pulsar surface which are accelerated by an electric field component (Equation 2.5) along the "open" $\boldsymbol{B}$-field lines and emit radiation (photons) via the curvature radiation (equation 2.8) mechanism because the synchrotron radiation losses (see equation 2.7) are rapid near the pulsar surface. The production of γ-rays and hence pair production above the pulsar's polar caps can also occur due to inverse Compton scattering (ICS) mechanism where thermal photons from the pulsar surface are upscattered to very high energies by relativistic electrons (see A. K. Harding and Muslimov (2002) for a discussion of the ICS mechanism above pulsar polar caps). In some cases, the positrons (e^+) can flow back towards the polar cap where they heat up those regions to produce pulsed thermal radiation that can be detected from the optical up to the soft X-ray regimes (Ruderman and Sutherland (1975), Arons (1981), Cáceres et al. (2016)). It is in these gaps (where $E_\parallel$ is unscreened) above the polar cap

(also called inner or polar gaps) where non-thermal emission emanates (Sturrock (1971), Ruderman and Sutherland (1975), Arons and Scharlemann (1979), Chen and Ruderman (1993)). A majority of this non-thermal emission from pulsars occurs in the radio band (Usov and Melrose (1995)). The mechanism that produces pulsed radio emission must be a coherent process because of the high brightness temperatures ($\sim 10^{29}$K, Manchester and Taylor (1977)) of the radio emission that is measured from pulsars. Some plausible mechanisms for radio emission include coherent curvature emission (Sturrock (1971), Ruderman and Sutherland (1975), Melikidze, Gil, and Pataraya (2000), Mitra, Gil, and Melikidze (2009)), "beam-driven relativistic plasma emission" (Weatherall (1994) and references therein) and anomalous Doppler emission (Lyutikov, Blandford, and Machabeli (1999) and references therein). These mechanisms suffer certain short-comings as criticized by Melrose, Rafat, and Mastrano (2020).

2.5.3 Outer Gap Model

Pulsed emission could also occur at regions close to the pulsar's light cylinder between the boundary of the closed $\boldsymbol{B}$-field and the last "open" $\boldsymbol{B}$-field lines (see Figure 2.8) . In these regions, there exist gaps where the electric field is unscreened ($E_{\parallel} \neq 0$) and the charged particles can be accelerated and hence emit γ-rays and/or X-rays in a fan beam as the pulsar rotates. These regions are known as outer gap regions and begin between the "null surface" line where $\boldsymbol{\Omega} \cdot \boldsymbol{B} \equiv 0$ and the closed magnetic field line extending towards the light cylinder (Cheng, Ho, and Ruderman (1986)).

The γ-rays and/or X-rays could be produced by the curvature, synchrotron or the inverse Compton scattering (ICS) mechanism inside the gap but ICS mechanism can be less effective if the density of thermal photons provided by the pulsar surface is low (Lorimer and Kramer (2005)). This model was proposed by Cheng et al. (1986) because the very high-energy pulsed γ-ray emission from young pulsars (Vela and Crab, see paper 2 of Cheng et al. (1986)) could not be sufficiently explained by the polar cap model. It also became apparent that predicted beam sizes of the radiation produced near the polar caps were too small to explain the wide pulse profiles observed in pulsars which emit very high energy γ-rays (Hirotani (2006)). This outer gap model sufficiently explained the double-peaked γ-ray pulse phase profile observed from young pulsars because fan beam γ-ray emission could

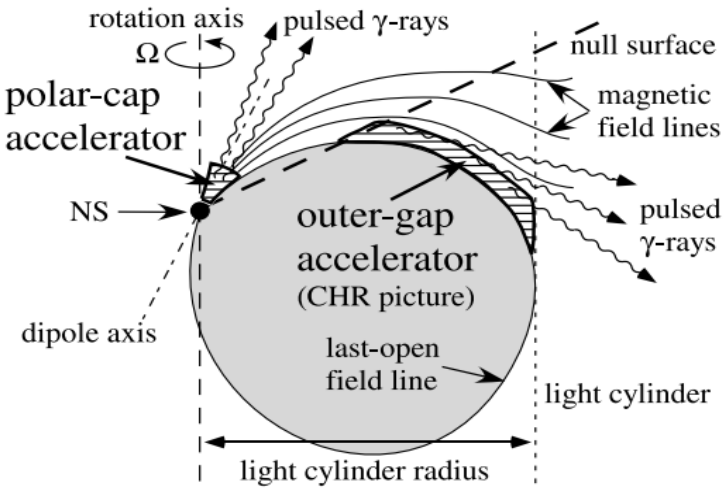

Figure 2.8: A side-view of an inclined pulsar showing both outer gap regions and polar cap regions where particle acceleration and hence emission occurs. Only one wing is shown but there could be four outer gap regions (two at each magnetic pole). Figure adopted from Hirotani (2006).

be emitted from outer gaps from both magnetic poles of the pulsar (Cheng et al. (1986)). However, considering only outgoing current and only one outer gap, Romani and Yadigaroglu (1995) and Romani (1996) showed that an emission beam that is dense near the edge could produce a double-peak γ-ray pulse phase when the line of sight of the observer intercepts these γ-ray beam regions. Single-peaked γ-ray phase-folded light curves from PSR B1055-52 (Thompson et al. (1999)) and PSR B1509-58 (Kuiper et al. (1998)) could also be explained by this model where only one of the fan beams are perceived by the observer. Radio emission is generally not associated with this pulsar model but there are some exceptions, for example, the Crab pulsar for which γ-ray emission is sufficiently explained by the outer gap model, shows radio emission which is phase-aligned with its γ-ray emission implying similar emission regions (Moffett and Hankins (1996)). In this scenario, incoming and outgoing γ-rays could produce e^+ and e^- pairs that move toward the pulsar and the light cylinder, respectively. This motion could produce a "two-stream instability" in the pulsar's outer magnetosphere generating "non-homogeneous and separated plasma clouds" for which the emission or scattering process of the cloud produce the radio emission that is phase-aligned with

the γ-ray pulses (see Ng, Takata, Leung, Cheng, and Philippopoulos (2014) and references therein).

2.5.4 Slot Gap Model

Another model for pulsar emission that is worth mentioning is the so-called slot gap (Arons and Scharlemann (1979), Arons (1983)). This model can be thought of as an intermediary of the polar and outer gaps. In this model, emission takes place at a higher altitude along the last open magnetic field lines. It is assumed that at last "open" $\boldsymbol{B}$-field line, $E_{\parallel}$ and the electric potential responsible for particle acceleration vanishes (Arons (1983), Muslimov and Harding (2003), A. Harding and Muslimov (2005)). The slot gap (see Figure 2.9) forms because the electric field near this boundary is lower and the electrons need a higher altitude to be accelerated and hence emit photons to produce pairs. Thus, the pair formation front (PFF) occurs at an increasingly higher altitude and eventually curves upward becoming asymptotically tangent to the last "open" $\boldsymbol{B}$-field line leaving a narrow region known as the slot gap region (Muslimov and Harding (2003), A. Harding and Muslimov (2005)).

Inside the slot gap region, $E_{\parallel}$ is unscreened and can gradually accelerate particles to higher altitudes to initiate pair formation at the slot gap's inner edge and the radiation from these pairs results in a "wide, hollow cone of high energy emission" due to the flaring of the magnetic field lines (Muslimov and Harding (2003)). This model predicts the wide, double-peaked pulse profiles of young pulsars quite well (see A. K. Harding, Stern, Dyks, and Frackowiak (2008)). This slot gap model suggested by Muslimov and Harding (2003) is also an update on the original model by Arons and Scharlemann (1979) in that it includes the effects of inertial frame dragging and slot gap geometry on the electric field, $E_{\parallel}$, within the slot gap region. It also explains the the high energy pulsed emission from millisecond pulsars well (A. K. Harding, Usov, and Muslimov (2005)). In young pulsars, the slot gap could sustain high energy primary beams that could interact with the propagation of low energy pairs to produce plasma instabilities resulting in pulsed radio emission (A. K. Harding et al. (2008)).

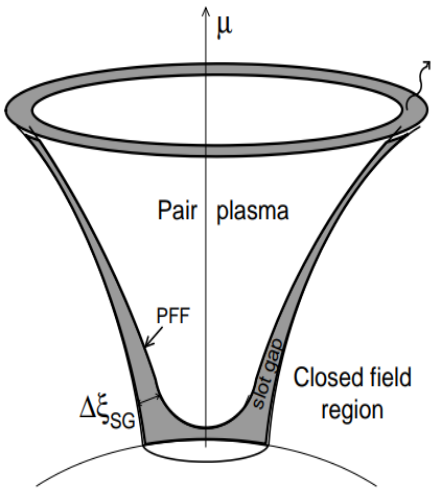

Figure 2.9: An illustration showing the slot gap region between the pair formation front (PFF) and the last open field line. Here $\boldsymbol{\mu}$ is the magnetic moment of the pulsar and $\Delta\xi_{SG}$ is the slot gap thickness (see Muslimov and Harding (2003) for details). Figure adopted from A. Harding and Muslimov (2005).

2.6 White Dwarf Pulsars

Highly magnetic white dwarfs (MWDs) with a fast rotation period might also mimic the behavior that is seen in pulsars. These MWDs could emit pulsed radiation across the entire electromagnetic spectrum and has been theorized to even emit pulsed γ-ray emission (Usov (1988)). As mentioned in section 2.4, Meintjes et al. (2023) showed that these MWDs could emit pulsed γ-rays with energy $\leq$50 GeV via the curvature radiation mechanism. Today, these fast rotating, highly MWDs are called white dwarf pulsars. The term "white dwarf pulsar" has recently been redefined by Segura et al. (2025) as non-accreting binary systems containing a fast rotating white dwarf star as the primary and a late-type main sequence star nearly filling its Roche lobe as the companion. These binary systems typically emit multi-wavelength pulsed emission modulated at the white dwarf's spin. The radio emission in these systems are likely caused by the interaction between the white dwarf's

magnetic field and the companion's photosphere especially in tight binary orbits (see Marsh et al. (2016), Pelisoli, Marsh, et al. (2023)). However, long-period transients (LPTs) has been discovered to emit strongly coherent polarized radio pulses on the minute timescale (see e.g. GLEAM-X J162759.5-523504 Hurley-Walker et al. (2022) and GPM J183910 Hurley-Walker et al. (2023)). Rea et al. (2024) explored the possible compact object in both GLEAM-X J162759.5-523504 (∼18-minute period) and GPM J183910 (∼21-minute period) as being either a neutron star or a highly magnetic white dwarf in the rotating dipole scenario but both scenarios fail to explain the coherent transient radio emission from these systems. These two sources might also lack a companion but further observations are needed to confidently confirm this statement (see Rea et al. (2024) and references therein). Some candidate/confirmed white dwarf pulsars have been discovered over the years including the transient radio white dwarf pulsar GCRT J1745-3009 with rotation period of ∼77 minutes (Hyman et al. (2005)) with magnetic field $\sim 10^9$G (Zhang and Gil (2005)), the radio-pulsing white dwarf binary AR Scorpii with spin period of ∼1.97 minutes (Marsh et al. (2016)) with magnetic field up to ∼500 MG (Buckley et al. (2018), although recently Barrett and Gurwell (2025) refined the white dwarf's magnetic field in AR Sco to ∼15 MG using submillimeter observations), the ∼33 second white dwarf AE Aquarii (Patterson, Branch, Chincarini, and Robinson (1980)) which has been shown to propel stellar material from its companion away from the binary system (Wynn, King, and Horne (1997), Meintjes and Venter (2005)) and has shown possible TeV (10^{12} eV) emission (Meintjes (1993)) and the fastest rotating isolated white dwarf SDSS J221141.80+113604.4 with a spin period of ∼70 seconds (Kilic et al. (2021)). The recently discovered white dwarf binary system J191213.72−441045.1[4] and the isolated white dwarf EUVE J0317-855 will be the main focus of this dissertation. The next chapter gives the reader a thorough background on both EUVE J0317-855 and the confirmed white dwarf pulsar J191213.72−441045.1.

[4]Only a γ-ray analysis will be performed on this source as it has only been recently detected from radio through X-rays by Pelisoli, Marsh, et al. (2023), Pelisoli, Sahu, et al. (2023) and Schwope, A. et al. (2023)

Chapter 3

Background on Target Sources

3.1 Isolated White Dwarf EUVE J0317-855 (RE J0317-853)

3.1.1 Discovery of EUVE J0317-855

EUVE J0317-855 (RE J0317-853, hereafter J0317) was discovered by the ROSAT (Roentegen Satallite, Trmper (1982a)) Wide Field Camera (WFC) and the Extreme Ultraviolet Explorer (EUVE, Bowyer and Malina (1991)) surveys at a right ascension (RA) of 03h 17m 15.85s and a declination (DEC) of -85°32'25.45" (J2000). Barstow et al. (1995) first identified this source as a highly magnetic white dwarf with a magnetic field strength of $B{\approx}340$ MG which showed optical modulations at a period of 12 minutes which they assumed to be the spin period of the white dwarf. The latter mentioned authors derived a radius of $R{\sim}0.0035$ $R_{\odot}$, a mass of M$\sim$1.35 $M_{\odot}$, a distance of $d{\sim}36$ pc (1 pc=$3.09{\times}10^{16}$ m) and an effective temperature of T_e=49 000 K making it the most massive, hottest and fastest spinning isolated white dwarf upon its discovery. Barstow et al. (1995) assumed the magnetic field structure to be a dipole that is offset from the centre by 0.2 of the white dwarf radius in the direction of the southern magnetic pole. Barstow et al. (1995) also discovered a nearby non-magnetic white dwarf LB 9802 which appeared to be associated with J0317 but they did not find any evidence of mass accretion because of the large binary separation of 600 AU (1 AU=$1.50{\times}10^{11}$ m). This large binary separation meant that J0317 is essentially an isolated highly magnetic white dwarf.

3.1.2 Optical Observations of J0317

Optical observations of J0317 were made by Barstow et al. (1995) in 1994 July and November using the University of Cape Town high-speed CCD (charged-coupled device) photometer onboard the 1.0m SAAO ("South African Astronomical Observatory"[1]) telescope. The observations were made at a wavelength of ∼5000 $\mathring{A}$ (1 $\mathring{A}$=1×10^{-10} m) at 10 second exposure time in unfiltered light. Optical light curves of duration 3000, 7990 and 14 300 seconds were obtained and analyzed by Barstow et al. (1995). The 14 300 second optical light curve is shown in Figure 3.1. This light curve shows 20 oscillation cycles of J0317 for which Barstow et al. (1995) determined a mean magnitude of 14.82 and a variation in the oscillation semi-amplitude of 0.084 mag. They performed a Fourier transform on the optical data which resulted in the power spectrum shown in Figure 3.2. Barstow et al. (1995) determined this strong peak to correspond to P=725.4±0.9s with some fainter harmonics at 1/2 and 1/3 of the main period also visible in the power spectrum. They further folded their optical data on this spin period to produce a folded light curve shown in Figure 3.2.

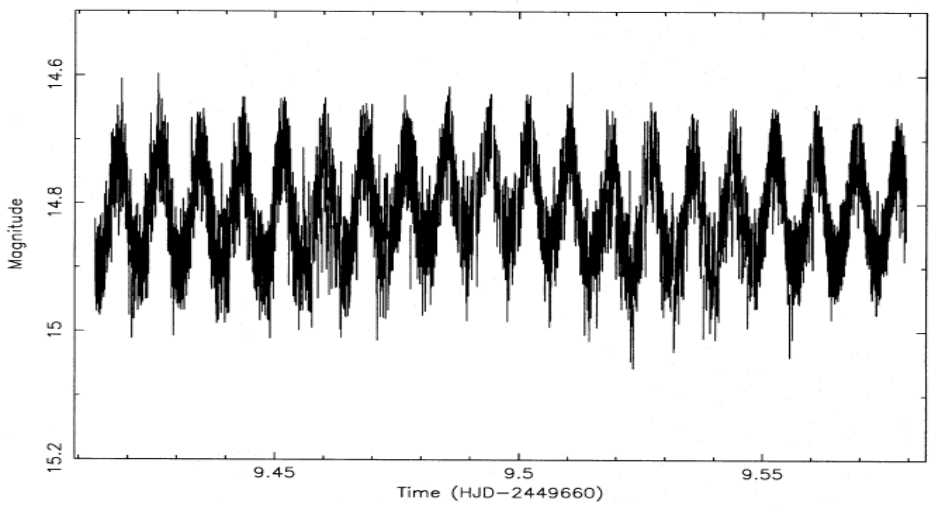

Figure 3.1: Optical (λ∼5000$\mathring{A}$) light curve of J0317 taken on 13/14 November 1994 with the University of Cape Town CCD high-speed photometer onboard the 1.0m SAAO telescope. Figure adopted from Barstow et al. (1995).

[1] http://www.saao.ac.za/

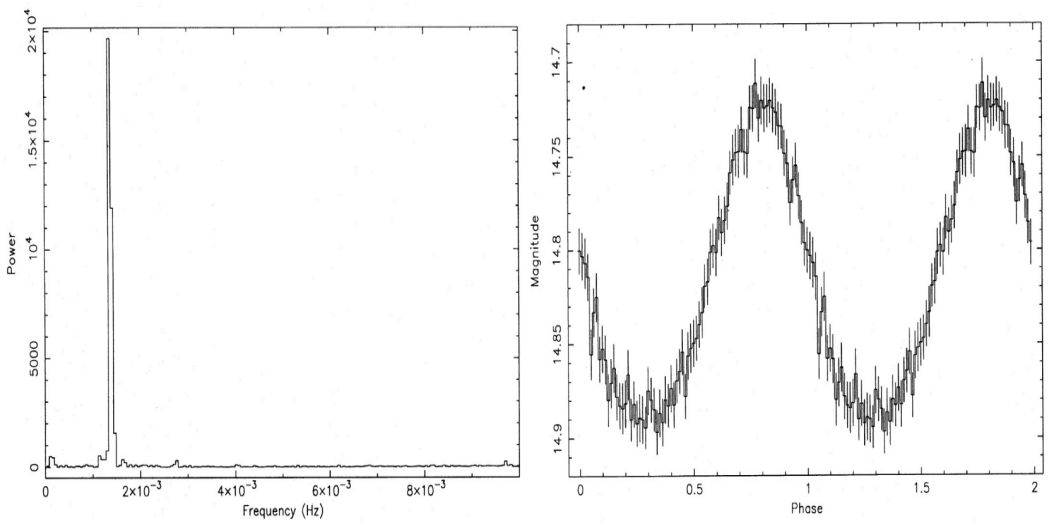

Figure 3.2: Fourier Transform (left) of Figure 3.1 showing strong peak at period $P\sim$725.4 s with some fainter harmonics also visible along with folded light curve (right) on the determined 725.4 s period. Phase zero corresponds to an epoch of HJD (Heliocentric Julian Date) 2449669. Adopted from Barstow et al. (1995).

It is evident that this folded light curve is single-peaked per rotation cycle of the white dwarf which could be interpreted as observing only one of the white dwarf's magnetic poles.

3.1.3 Ultraviolet Observations of J0317

J0317 was observed with the Extreme Ultraviolet Explorer (EUVE, Bowyer and Malina (1991)) Deep Survey (DS) imager at a wavelength $\lambda\sim100\mathring{A}$ from 3 June 1996 05:03:04 to 5 June 1996 09:51:35 (Universal Time, UT) for an exposure of 42 000 seconds by Ferrario et al. (1997). A periodic analysis of the Extreme Ultraviolet (EUV) data by Ferrario et al. (1997) revealed photometric variations at a period of P=725.5±0.8s and an additional periodicity at P=362.9s which is the first harmonic of the rotation period of J0317. Figure 3.3 shows a periodogram of the EUVE DS data showing the rotation period (P=725.5s) and its first harmonic (P=362.9s). Figure 3.4 shows the EUVE DS phase-folded light curves on the rotation period and its first harmonic of J0317.

It is clear that the EUVE DS phase-folded light curve on the spin period is double-peaked per rotation phase contrary to the optical phase-folded light curve (see Figure 3.2) obtained by Barstow

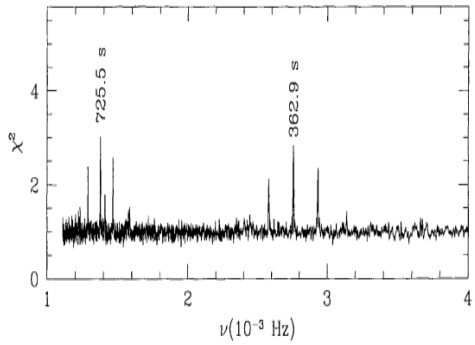

Figure 3.3: Periodogram of the EUVE DS data reveals pulsations at the spin period P=725.5s and first harmonic P=362.9s of the spin period. Figure adopted from Ferrario et al. (1997).

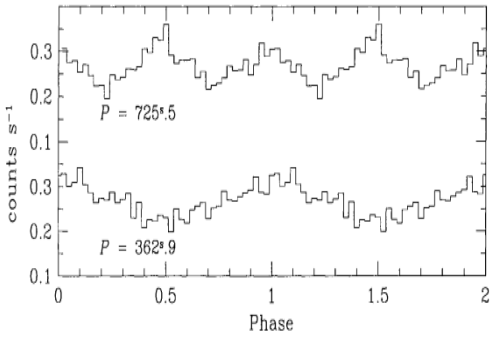

Figure 3.4: Folded EUVE DS light curve on the spin period(top) and its first harmonic(bottom). The first minimum is at an epoch HJD=2450237.72019. Figure adopted from Ferrario et al. (1997)

.

et al. (1995) which is single-peaked on the same spin period. Ferrario et al. (1997) suggested that this additional periodicity at half the rotation period of J0317 in their EUV data could be explained by the presence of "surface abundance inhomogeneities" which are caused by helium or other heavier elements at both magnetic poles. From spectropolarimetric observations in the wavelength λ=4200-7200$\mathring{A}$, Ferrario et al. (1997) found 8% peak level circularly polarized emission. Ferrario et al. (1997) also found that this circular polarization varies with period of 725±10 s which further confirmed that the photometric period of 725s is indeed as a result of the white dwarf rotation initially found by Barstow et al. (1995). Both the centered and off-centered magnetic field structure were considered by Ferrario et al. (1997), and they found that an off-centered dipole field with strength B_d=450 MG that is offset by 35% with respect to the stellar radius best describes their results. Ferrario et al. (1997) also determined $i = 60°$ viewing angle to the dipole axis and the angle between the spin and magnetic axes $\beta = 40°$ making J0317 an oblique rotator. The magnetic field morphology of J0317 is rather intricate and using phase-resolved, far ultraviolet Hubble Space Telescope[2] spectra obtained from the Faint Object Spectrograph (FOS), Burleigh, Jordan, and Schweizer (1998) revealed that the magnetic fields present on J0317 range between 180-800 MG over the white dwarf surface.

[2] https://science.nasa.gov/mission/hubble/overview/about-hubble/

Burleigh et al. (1998) achieved this by expanding the magnetic field into its spherical harmonics. Burleigh et al. (1998) also found the viewing angle to the magnetic axis of J0317 to be $i = 34°$ and the angle between the rotation and magnetic axes to be $\beta = 29°$. New ultraviolet observations were done by Vennes et al. (2003) using the EUVE and the Hubble Space Telescopes. Vennes et al. (2003) refined the rotation period of J0317 to be P=725.7277±0.0001s and folded the EUVE DS light curve on this period which also resulted in a double-peaked structure, as shown in Figure 3.5 below.

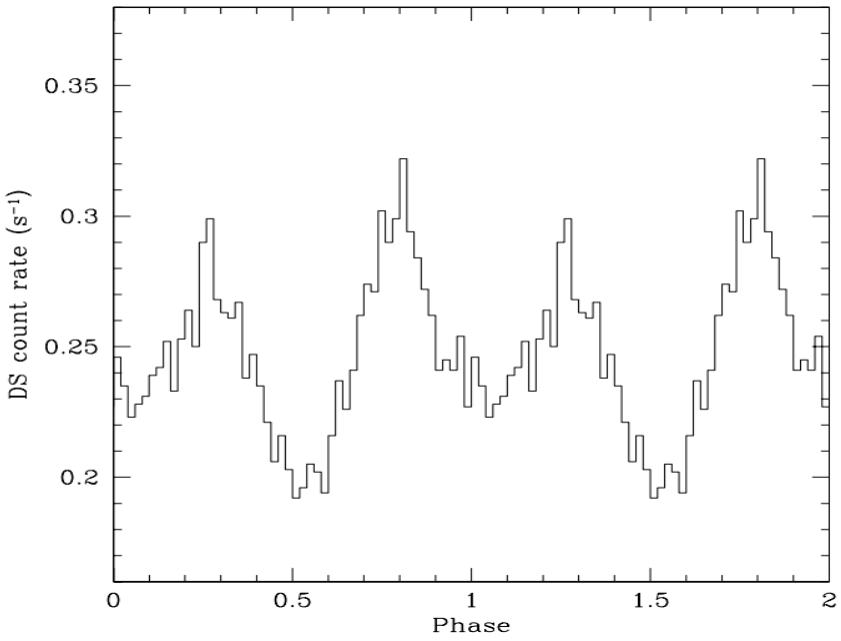

Figure 3.5: Folded EUVE DS light curve on spin period 725.7277s using spectropolarimetric ephemeris. Phase zero corresponds to the maximum optical polarization. Figure adopted from Vennes et al. (2003).

A spectropolarimetric ephemeris of HJD=2451845.16014(6)+0.00839962(1)E was used to create Figure 3.5 where the figures in brackets are the uncertainty in the last digit and E is an integer. They also determined the angular separation between J0317 and LB 9802 (non-magnetic white dwarf companion) to be 7.2″ away which corresponds to a projected separation of 200 AU. By using spectropolatimetry, Vennes et al. (2003) determined that J0317 has an overall magnetic field

of B≤185 MG and a magnetic spot of B≥425 MG. These authors also constructed a phase-averaged optical to ultraviolet spectral energy distribution of J0317 shown in Figure 3.6 below.

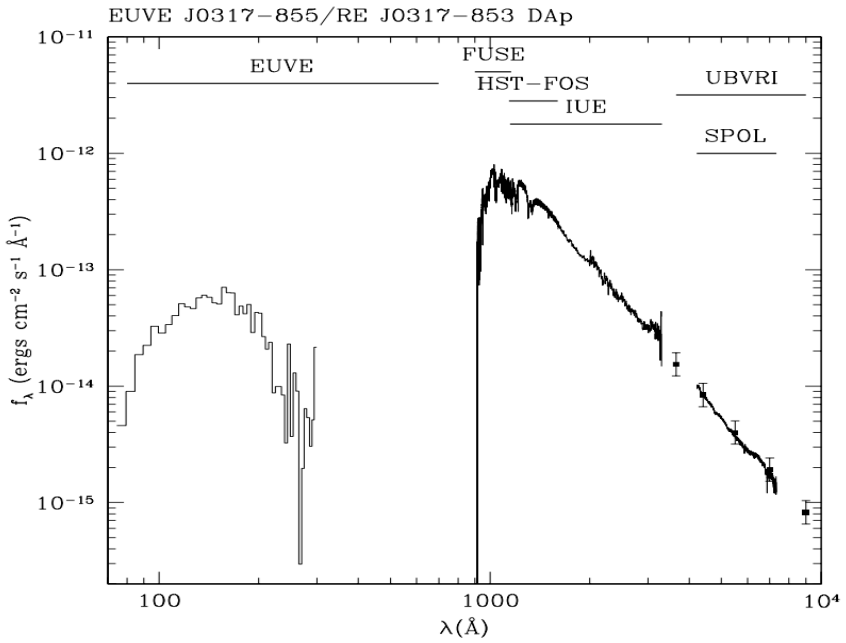

Figure 3.6: Phase-resolved optical to ultraviolet spectral energy distribution (SED) using data from different telescopes. The SED was constructed using an effective temperature of T_e=33 800 K. Figure adopted from Vennes et al. (2003).

This SED was constructed using spectropolarimetric data from EUVE, Hubble Space Telescope's Faint Object Spectrograph (FOS), the European Space Agency's International Ultraviolet Explorer[3] (IUE), Far Ultraviolet Spectroscopic Explorer (FUSE, Moos et al. (2000)) and the Steward Observatory CCD spectropolarimeter (SPOL, Schmidt, Stockman, and Smith (1992)). Both Ferrario et al. (1997) and Vennes et al. (2003) classified J0317 as a DAp (see section 2.1.1 for a short description of the types of white dwarfs) white dwarf with the "p" denoting that J0317 emits polarized light due to its high magnetic field. Given J0317's relative fast spin period, high mass, high effective temperature and large magnetic field, Ferrario et al. (1997) concluded that J0317 could be a result of a double degenerate merger scenario.

[3] "https://www.esa.int/Science_Exploration/Space_Science/IUE_overview"

3.1.4 X-ray Observations of J0317

A search for non-thermal X-ray emission from J0317 was done by Harayama et al. (2013) using the Suzaku X-ray satellite (Mitsuda et al. (2007). J0317 was observed from 16 July 2009 14:13 (UT) to 17 July 2009 03:30 (UT) for about 60 000 seconds. These authors mainly used Suzaku's "X-ray Imaging Spectrometer" (XIS, Koyama et al. (2007)) which covers the 0.5-10 keV energy range. The XIS consists of a single back-illuminated charge-coupled device (CCD) camera called XIS1 and three front-illuminated cameras XIS0, XIS2 and XIS3. The XIS2 camera was not used since it was damaged on 9 November 2006. The "Hard X-ray Detector" (HXD, Takahashi et al. (2007)) which covers the 10-600 keV bandpass was also not used because of its sensitivity limitations. No significant X-ray radiation were detected from J0317 as shown in Figure 3.7 below.

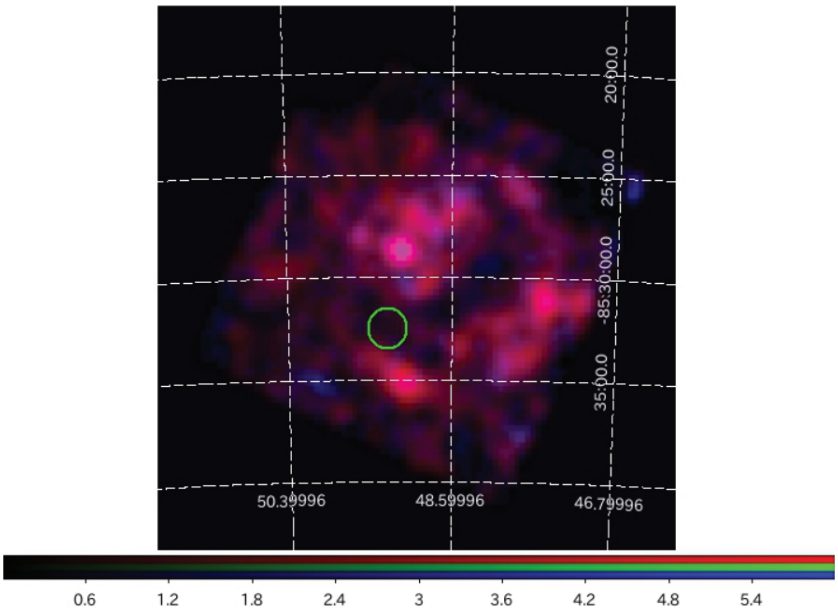

Figure 3.7: Suzaku XIS image showing the energy-resolved 2-10 keV (blue) and 0.5-2 keV (red) regions. The green 1' circle shows the position of J0317 (RA=49.147°, DEC=-85.481°, J2000) Figure adopted from Harayama et al. (2013).

Harayama et al. (2013) derived a 1σ upper limit of 1.7×10^{-13} erg cm^{-2}s^{-1} on the X-ray flux in the 2-10 keV energy band. Harayama et al. (2013) determined this X-ray flux of J0317 by combining the systematic errors of the non-X-ray and cosmic X-ray background in the "field of view" (FOV) of the XIS. Harayama et al. (2013) also assumed a conversion efficiency from the magnetic dipole radiation (see equation 2.15) into X-ray flux which can be calculated using $\eta = L_X/L_{sd}$ where L_X is the 2-10 keV band X-ray luminosity and L_{sd} is the spin-down luminosity (equation 2.17). The conversion efficiency for most pulsars are in the range ∼0.001-1% (Possenti, A. et al. (2002)). Harayama et al. (2013) determined an upper limit on the conversion efficiency of η <0.05% for J0317 as shown in Figure 3.8 below.

Harayama et al. (2013) determined J0317's spin-down luminosity using the equations described in Ikhsanov, N. R. and Biermann, P. L. (2006) and the upper limit of η <0.05% for J0317 does, as mentioned by Harayama et al. (2013), exclude white dwarf pulsars as possible anomoloys X-ray pulsars (AXPs, pulsars having spin periods of several seconds with no accompanied massive companion Mereghetti (2001)) and soft gamma-ray repeaters (SGRs, <1s transient events with soft (∼20-30 keV photon energy, see Mereghetti (2001)) bursts) as previously mentioned by Malheiro, Rueda, and Ruffini (2012) but this value of the conversion efficiency could hint that the magnetosphere environments of white dwarfs could not be so different from those in pulsars.

J0317 was observed by Dessert et al. (2022) with the "Chandra X-ray Observatory" using the ACIS-I ("Advanced CCD Imaging Spectrometer", Weisskopf et al. (2003)) instrument with no grating with a total exposure time of 37.42 ks (Observation ID No.22326, Principal Investigator Benjamin Safdi). The goal of this observation was to search for axions[4] which could produce X-ray emission through axion-photon conversion in highly magnetized white dwarfs as proposed by Dessert, Long, and Safdi (2019). Dessert et al. (2022) produced pixelated count maps in 4 energy bins within energy range 1-9 keV with width of 2 keV each. The pixel in right ascension (RA) and declination (DEC) was ∼0.492″ (physical length) for which the RA direction is the width in "RA×cos(Dec)". See Figure 3.9 below.

The image is centered at J0317's position which is at RA_0=49°18′37.77″ and DEC_0≈-85°32′25.81″

[4]These are hypothetical elementary particles that could explain dark matter.

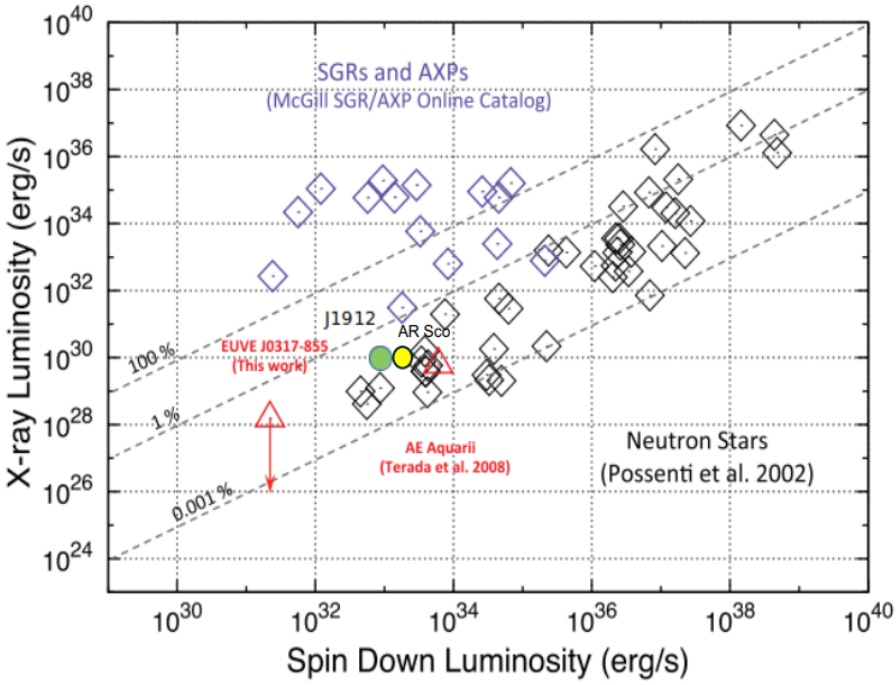

Figure 3.8: 2-10 keV X-ray luminosity vs the spin-down luminosity of neutron star pulsars (Possenti, A. et al. (2002)), EUVE J0317-855, AE Aquarii (red triangle next to yellow circle, Terada et al. (2008)) and soft-gamma ray repeaters (SGRs) and Anomolous X-ray Pulsars (AXPs) from the McGill Online Magnetar Catalog[a]. Figure adopted from Harayama et al. (2013). J1912 is shown as a green circle and was manually added based on parameters from Pelisoli, Marsh, et al. (2023), Pelisoli, Sahu, et al. (2023) and Schwope, A. et al. (2023).AR Sco is also shown as a yellow circle based on parameters from Marsh et al. (2016), Buckley et al. (2018) and references therein.

[a] "https://www.physics.mcgill.ca/~pulsar/magnetar/main.html"

(Dec. 2020 epoch) and shows that no counts are observed at the position of J0317. The non-detection of X-rays from both Suzaku and Chandra observatories might suggest that either J0317 does not emit X-rays, or that more sensitive X-ray telescopes such as the proposed Lynx X-ray Observatory (Team (2018)), which would increase the sensitivity by ∼2 orders of magnitude compared to the Chandra X-ray telescope, are needed to gauge the X-ray emission from J0317 and other highly magnetized white dwarfs. This non-detection of X-rays could on the other hand hint at low electron-positron cascade process which might imply a higher transparency to possible γ-rays in

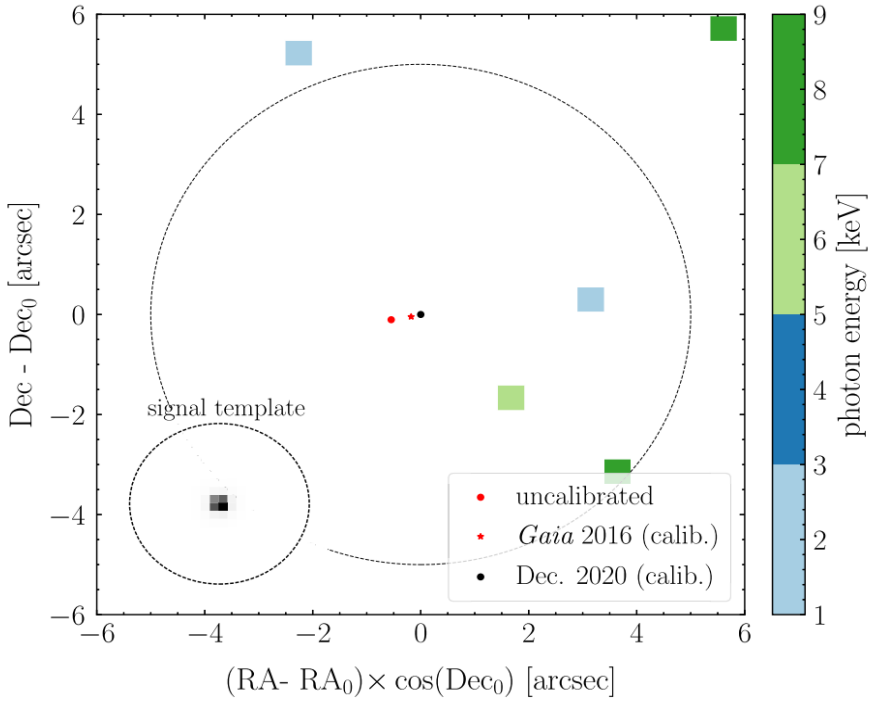

Figure 3.9: Binned counts in 1-9 keV energy range of J0317. The intermediary location of J0317 at different calibrations using the Gaia epoch (J2016.0, Gaia Collaboration et al. (2021)) and Dec. 2020 refers to the position of J0317 as of December 2020 using proper motion measurements from Gaia. The 5″ radius dashed circle shows the extent of the region of interest (ROI) and the inset shows the signal template for the first energy bin in grey scale. Figure adopted from Dessert et al. (2022).

the magnetosphere (see earlier discussion on γ-ray opacity in white dwarf magnetospheres based on values calculated for AE Aquarii and AR Scorpii (Meintjes et al. (2023))

3.1.5 Radio Observations of J0317

In 1996, a short ∼64 min radio observation with the Australian Telescope Compact Array (ATCA, Stevens, Wark, Edwards, Breen, and Lee-Waddell (2014)) detected a strong, highly circularly polarized radio flare from J0317 with no quiescent emission. Barrett et al. (1999) carried out ∼20 hours of radio observations using ATCA but found no flaring activity from J0317 and these authors set a radio flux upper limit of ∼0.3 mJy (1 Jy=10^{-26}Wm^{-2}Hz^{-1}). Barrett et al. (1999) also did

extensive optical spectroscopy which also showed no such flaring activity from J0317 but these authors did not rule out flaring activity from J0317 on longer time scales. Given a ∼0.3 mJy upper limit on the radio flux, the MeerKAT (Jonas and MeerKAT Team (2016)) radio telescope with its 64 antennas will be much more sensitive than ATCA to search for radio emission from J0317.

The following section will give the reader an overview of the radio to X-ray studies done on the binary system J191213.72−441045.1.

3.2 Binary White Dwarf J191213.72−441045.1

3.2.1 Discovery of J191213.72−441045.1

J191213.72−441045.1 (hereafter J1912) is a white dwarf binary system (the second white dwarf pulsar alongside AR Sco) that was discovered by Pelisoli, Marsh, et al. (2023) with a spin period P_{spin}=319.34903(8)s that is in a tight binary orbit of ∼4.03 hours with a secondary companion of spectral type M4.5±0.5. This binary system is at a distance of $d = 237\pm5$ pc. The white dwarf has a mass of M=1.2±0.2 $M_\odot$ and the secondary companion (M-dwarf) has a mass of M=0.25±0.5 $M_\odot$. The M-dwarf fills approximately 90% of its Roche lobe. Pelisoli, Marsh, et al. (2023) did detect a flare in the optical and X-ray light curves for which they propose that it is an "accretion-induced flare" which could be interpreted as early onset mass transfer from the M-dwarf to the primary in J1912. They also determined an orbital inclination of $i = 37°$. Pelisoli, Sahu, et al. (2023) refined the white dwarf mass of J1912 to M=0.59±0.02 $M_\odot$, with radius R=0.0131±0.004 $R_\odot$, temperature of T_{eff}=11 485±90 K and they also determined an orbital inclination of $i = 59 \pm 6°$. Since there is no evidence of "Zeeman splitting" of the spectral lines in the spectra of J1912, Pelisoli, Sahu, et al. (2023) determined a $\boldsymbol{B}$-field strength with upper limit of ≤50 MG by calculating the "theoretical wavelength for Zeeman split components" of Lyman alpha (Ly α) emission line. They achieved this by using the energy levels calculated by Schimeczek and Wunner (2014) for hydrogen (H) in a $\boldsymbol{B}$-field.

3.2.2 Radio Observations of J1912

Pelisoli, Marsh, et al. (2023) observed J1912 for one hour on 22 June 2022 (block ID 1655920939) using the 856-1712 MHz L-band receivers on the MeerKAT (Jonas and MeerKAT Team (2016)) radio telescope. A longer observation of 7.55h on-target time was made following the detection of pulses in the one hour observation. The integration time was set to 2s and the primary calibrator PKS B1934-638 was used for delay corrections and instrumental bandpass. A secondary calibrator J1830-3602 was used to derive time-dependent complex gains. By using WSClean (Offringa et al. (2014)) and CASA (CASA Team et al. (2022)), 2 second images were produced of J1912 which resulted in a total of 13 552 snapshot images. A radio light curve with respect to the orbital phase and spin phase were created by these authors. They also created an accompanying Fourier transform of the radio data. The Fourier transform for the MeerKAT data was created by only using data around an orbital phase of 0.5 where the pulses from J1912 were visible. See Figure 3.10(**a**, **f** and **k**). From **f** it can be seen how incredibly narrow the radio peaks are at spin phase 0 and 1.0. This radio folded light curve closely resembles that seen from radio pulsars. From **k** the Fourier transform shows power at the spin period of ∼5.3 minutes and also reveals power at various orbital sideband frequencies. To explain the narrow radio pulse per spin period seen in **f**, Pelisoli, Sahu, et al. (2023) attributed this pulsed radio emission from J1912 to "electron-cyclotron maser emission" (Melrose (2017)) which originates from J1912's white dwarf magnetic polar region and produces radio emission along J1912's $\boldsymbol{B}$-field. They suggested that the radio emission is only produced when particles from the M-dwarf reaches J1912's polar region and that this radio emission is only seen at "superior conjunction" of the M-dwarf companion (at orbital phase 0.5) which also sufficiently explains why this "auroral" emission is only observed once per orbit (Pelisoli, Sahu, et al. (2023)).

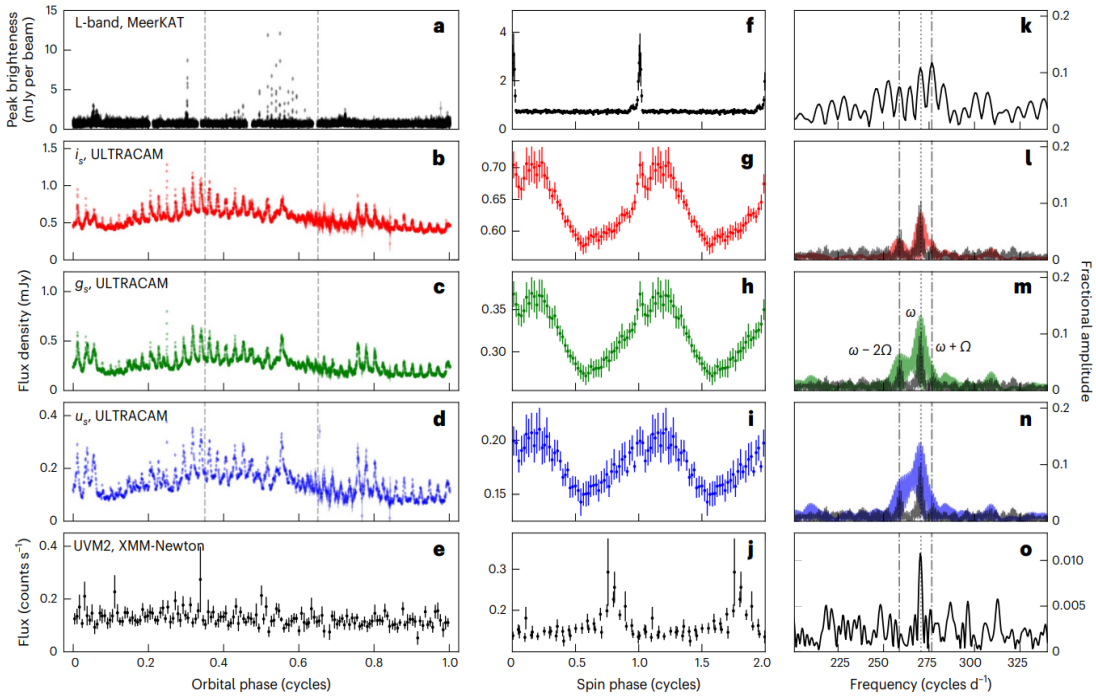

Figure 3.10: Multi-wavelength (radio to X-rays) data of J1912. MeerKAT light curve with respect to the orbital phase is shown in **a**. For the MeerKAT data, two orbits were folded without averaging. ULTRACAM light curves (unfolded for one orbit) shown in $\mathbf{b}-\mathbf{d}$ for filters i_s, g_s and u_s respectively. The uncertainties are sometimes smaller than the data points themselves but are shown in $\mathbf{a}-\mathbf{d}$. In **e**, X-ray light curve is shown from the XMM-Newton telescope where the uncertainties show the average in each phase bin. Regions marked by vertical dashed lines in $\mathbf{a}-\mathbf{d}$ were used to create the rotation phase average pulses shown in $\mathbf{f}-\mathbf{i}$. The error bars in $\mathbf{f}-\mathbf{j}$ show the average in the 50 phase bins. Figures $\mathbf{k}-\mathbf{o}$ show the Fourier transform for each of the respective wavelengths. The prominent peak corresponds to the spin frequency(ω) with some sideband frequencies also visible. For comparison, HIPPO Fourier transform data is also included in $\mathbf{l}-\mathbf{n}$ (in black). Figure adopted from Pelisoli, Marsh, et al. (2023)

3.2.3 Ultraviolet Observations of J1912

Pelisoli, Sahu, et al. (2023) observed J1912 for 12 orbits (see Table 1 of Pelisoli, Sahu, et al. (2023), split into three visits of four orbits) using the "Cosmic Origins Spectrograph" (COS, Green et al. (2011)) instrument that is part of the "Hubble Space Telescope" (HST). The G140L grating that is part of the COS instrument was centered at a wavelength of 1105$\mathring{A}$ which provided flux-calibrated

coverage between the wavelengths ≈1110-2150$\mathring{A}$ which spans the far ultraviolet (FUV) range. Light curves in the wavelength range 1110-2000$\mathring{A}$ were produced by these authors and data above 2000$\mathring{A}$ were discarded as a result of reduced signal-to-noise. The FUV light curve is displayed in Figure 3.11.

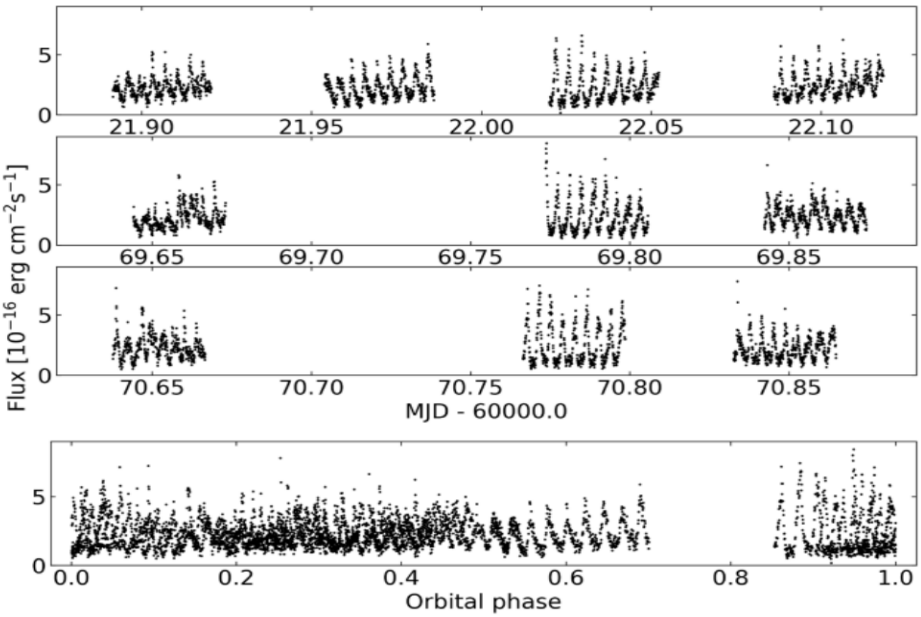

Figure 3.11: FUV (1100-2000$\mathring{A}$) light curve of J1912 with the top three panels showing the three HST visits and the gaps correspond to the different orbits. The larger gap in the 2nd and 3rd panel is due a data acquisition failure during orbits 8 and 10. The folded light curve (using orbital ephemeris by Pelisoli, Marsh, et al. (2023)) is shown in the bottom panel. Figure adopted from Pelisoli, Sahu, et al. (2023)

The FUV light curve's Fourier transform is displayed in Figure 3.12 and shows that the dominant frequency is the rotation frequency (ω) of the white dwarf but also show the beat frequency (ω-Ω) which was not detected by Pelisoli, Marsh, et al. (2023). The beat period's first harmonic (2ω-2Ω) and 2ω+Ω is also visible in the Fourier transform.

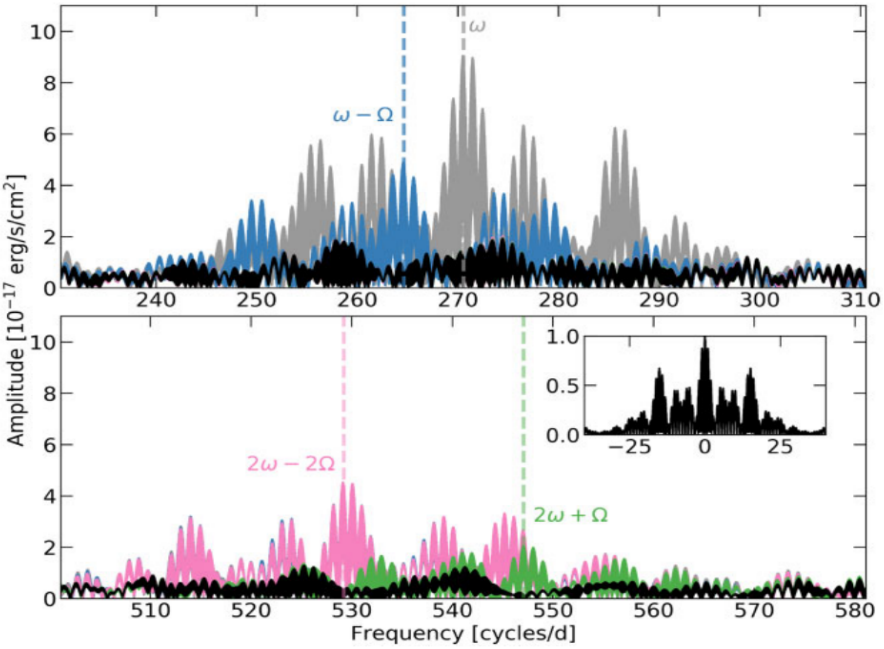

Figure 3.12: Top panel shows the Fourier transform of the FUV light curve around J1912's rotation frequency and its first harmonic in bottom panel where the inset displays the window function at the HST cadence. Strong aliasing in the power spectrum is due to the orbital visibility of J1912. Different pre-whitening stages is displayed by the different colors. The dotted lines shows the spin(ω), beat(ω-Ω), the beat's first harmonic(2ω-2Ω) and 2ω+Ω (possibly hinting at two-pole accretion with orbital reprocessing or modulation). Figure adopted from Pelisoli, Sahu, et al. (2023)

Pelisoli, Sahu, et al. (2023) then proceeded to fold the FUV data on to the spin ephemeris provided by Pelisoli, Marsh, et al. (2023)

$$BJD(TDB) = 2459772.142522(24) + 0.0036961693(10)E \tag{3.1}$$

with E giving the integer cycle number which resulted in Figure 3.13. Both Pelisoli, Sahu, et al.

(2023) and Pelisoli, Marsh, et al. (2023) only used data corresponding to orbital phase 0.35-0.65 because the shape of the pulses displays some orbital dependence.

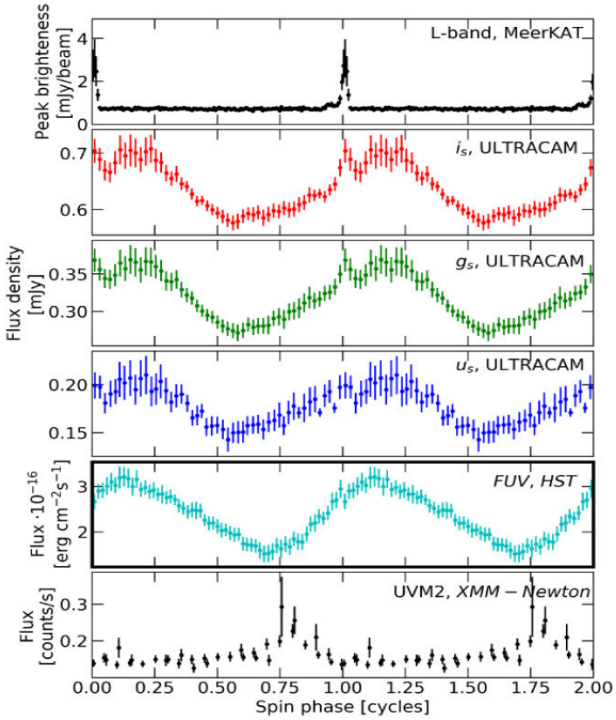

Figure 3.13: Folded FUV light curve is shown in the cyan color (thick border around it) along with ULTRACAM, MeerKAT and XMM-Newton data folded using the same ephemeris provided by Pelisoli, Marsh, et al. (2023). Figure adopted from Pelisoli, Sahu, et al. (2023)

From Figure 3.13, it can be seen that the radio feature from the the MeerKAT folded light curve is also present in the optical (ULTRACAM) phase-folded light curves and that the optical pulses are broad and appear to be a phase of ≈0.25 ahead of the narrow radio pulse. The X-rays (XMM-Newton) are a phase of ≈0.25 behind. Pelisoli, Sahu, et al. (2023) noted that the FUV pulse shape seems to be "somewhat transitional" between the optical (ULTRACAM) and X-rays (XMM-Newton) but Pelisoli, Marsh, et al. (2023) did caution that this pulse behaviour could be stochastic or not fully understood. Pelisoli, Marsh, et al. (2023) did note, however, that their optical and X-ray observations taken simultaneously revealed that the broad X-ray and optical pulses were

phase-aligned which was also noted by Schwope, A. et al. (2023) but became offset when compared to their spin ephemeris. Pelisoli, Sahu, et al. (2023) concluded that this offset could be dependent on systematic parameters and might not be J1912's persistent behaviour.

3.2.4 Optical Observations of J1912

Pelisoli, Marsh, et al. (2023) observed J1912 with the ULTRACAM instrument onboard the 3.58 m "European Southern Observatory (ESO) New Technology Telescope"[5] on five nights. Simultaneous observations were performed using three different filters. During the first 3 nights, filters u_s, g_s and i_s were used and the last two nights u_s, g_s and r_s were installed. Pelisoli, Marsh, et al. (2023) used the same exposures for filters g_s, r_s and i_s but increased it by a factor of 3 or 4 for u_s (see supplementary Table 1 of Pelisoli, Marsh, et al. (2023)). The optical light curves are shown in Figure 3.10 ($\mathbf{b}-\mathbf{d}$) phased using the orbital ephemeris (equation 3.2). The optical light curve phase-folded on the spin ephemeris is shown in Figure 3.10 ($\mathbf{g}-\mathbf{i}$) with accompanying Fourier transforms in $\mathbf{l}-\mathbf{n}$ which shows the dominant frequency occurring at the rotation frequency (ω) of the white dwarf with some orbital sideband frequencies also visible. The Fourier transform of the "High Speed Photo-Polarimeter" (HIPPO, Potter et al. (2008)) data that is part of the 1.9 meter telescope at the "South African Astronomical Observatory" (SAAO) is also shown in black in $\mathbf{l}-\mathbf{n}$. An orbital ephemeris was established by Pelisoli, Marsh, et al. (2023) using photometric archival data from the "Transiting Exoplanet Survey Satellite" (TESS, Ricker et al. (2014)) during sector 13 with cadence of 30 minutes and sector 27 with cadence of 10 minutes. Pelisoli, Marsh, et al. (2023) derived an orbital ephemeris of

$$BJD(TDB) = 2459784.98308(19) + 0.16811989(36)E \tag{3.2}$$

with E being the integer cycle number and BJD indicating the "barycentric Julian date" in "Barycentric Dynamical Time(TDB)" scale. The Fourier transform of the TESS optical data is shown in Figure 3.14 which revealed a predominant frequency at 5.948136(13) cycles d^{-1} ($\sim$4.03

[5] "https://www.eso.org/public/teles-instr/lasilla/ntt/"

hours) with the first harmonic also visible and the error in parenthesis shows the uncertainty on the last two digits and was obtained via bootstrapping. The phase-folded light curve on the orbital period using the orbital ephemeris (equation 3.2) is also shown on the right in Figure 3.14. From Figure 3.14, Pelisoli, Marsh, et al. (2023) explained that this large amplitude might be a result of the magnetic field of the primary interacting with the M-dwarf and producing non-thermal emission. The light curve asymmetry might be due to the possibility that the power released caused by the interaction of the primary's and M-dwarf's magnetic field might be larger on the M-dwarf's leading face (where shocks usually occurs) than on its trailing face. Misalignment of the primary's rotation axis with the orbital plane could also result in a variation in the dissipation rate with orbital phase which could also cause the observed asymmetry.

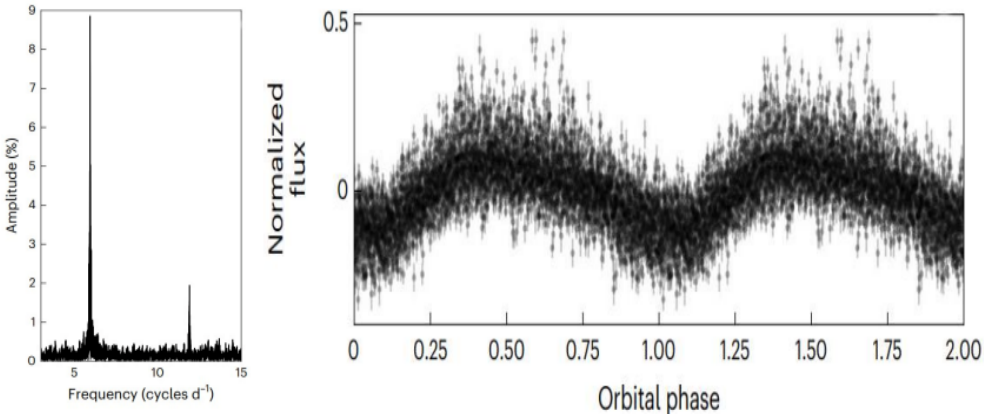

Figure 3.14: Left figure showing the Fourier transform of TESS optical data showing the orbital frequency ∼5.95 cycles d^{-1} and its first harmonic, with right figure showing the normalized and median subtracted TESS light curve folded on the orbital ephemeris (equation 3.2). Error bars show 1σ uncertainties. Figure adopted from Pelisoli, Marsh, et al. (2023)

3.2.5 X-ray Observations of J1912

The field of view of J1912 was observed by the eROSITA (Predehl, P. et al. (2021)) instrument onboard the "Spectrum-Roentgen-Gamma" (SRG, Sunyaev, R. et al. (2021)) observatory 4 times during the eRASS1 through eRASS4 all-sky surveys in 2020 and 2021. J1912 was discovered as

an X-ray source during these surveys. Schwope, A. et al. (2023) reduced the X-ray data of J1912 to obtain a total of 57 photons and found fluxes in the 0.2-2.3 keV energy range of 3.2, 0.9, 1.1, 1.0×10^{-13}erg cm^{-2}s^{-1} for eRASS1, 2, 3 and 4 surveys respectively. Further X-ray observations using the XMM-Newton (Lumb, Jansen, and Schartel (2012)) observatory were made on 17/18 September 2022 for a total exposure time of 43 000s. Schwope, A. et al. (2023) used the EPIC X-ray camera in full-frame mode with the fast-imaging mode optical monitor with time resolution of 0.5 seconds together with the UVM2 filter for which the effective wavelength is 231 nm (1nm = 1×10^{-9}m). Schwope, A. et al. (2023) obtained a total of 3430 photons using the EPIC-pn instrument which resulted in a average rate of 0.0825 s^{-1} (0.2-10 keV). A simultaneous 50 min observation with XMM-Newton and the ULTRACAM New Technology Telescope (NTT) of J1912 were obtained by Schwope, A. et al. (2023) and they produced a cutout of ∼50 min of sky-subtracted X-ray light curve shown in Figure 3.15. This EPIC-pn light curve shows clear evidence of quasi-periodic variability with a ∼5 min pulse separation. This light curve also shows an increase in the count rate to about 1.07 s^{-1} in the 32 s time bin and 1.69 s^{-1} in a 16 s time bin. A search for periodicity was done by Schwope, A. et al. (2023) using the Z_n^2 (Buccheri et al. (1983)) statistic and the analysis of variance (AOV) method in the period range 100-450s shown in Figure 3.16.

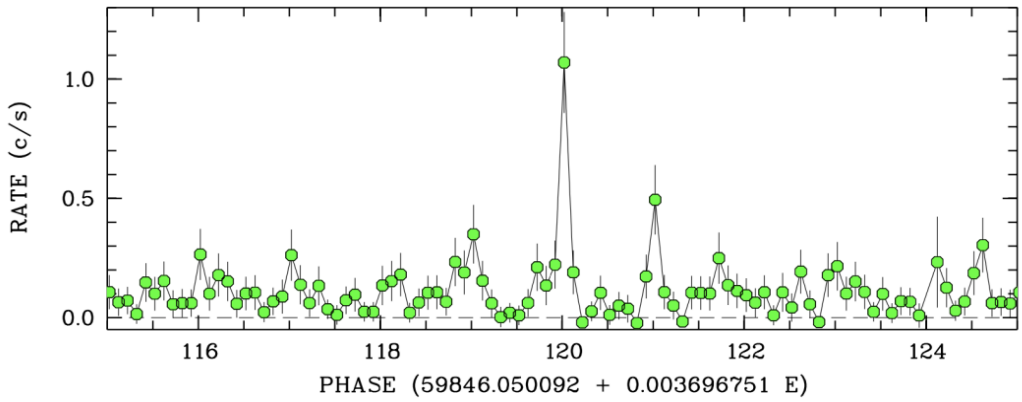

Figure 3.15: 50 min cutout XMM-Newton EPIC-pn ligth curve for orbital phase 333.226-33.444 using a 32 s time bin. Figure adopted from Schwope, A. et al. (2023)

.

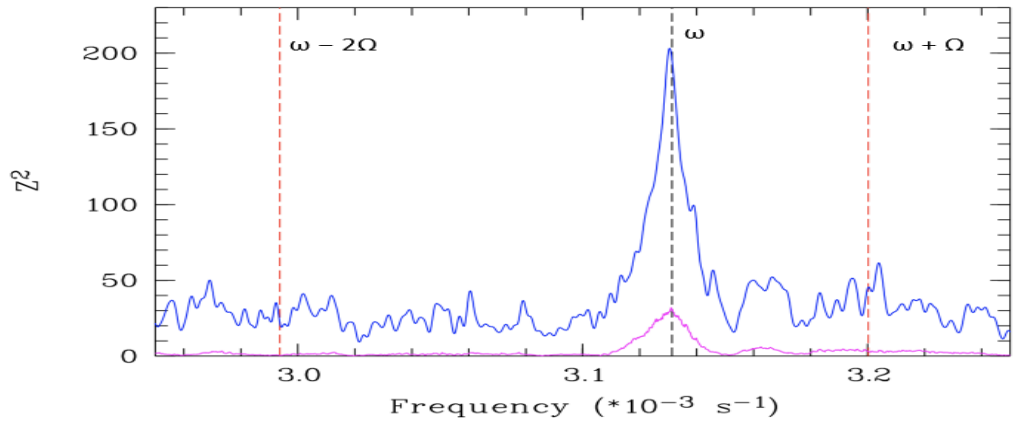

Figure 3.16: Z_n^2 statistic (blue) together with the AOV (magenta) method showing pulsations at the rotation frequency(ω, black dashed line) and expected beat frequency (ω+Ω, right line) and the sideband frequency (ω-2Ω, left line) are also shown. Figure adopted from Schwope, A. et al. (2023)

.

The prominent peak in Figure 3.16 is at a frequency of 0.0031505 d^{-1} or a period of 319.43 s for the Z_n^2 statistic and 319.35 s for the AOV method. Schwope, A. et al. (2023) then proceeded to produce rotation phase-folded X-ray, UV and optical light curves with 20 bins per spin cycle shown in Figure 3.17 below.

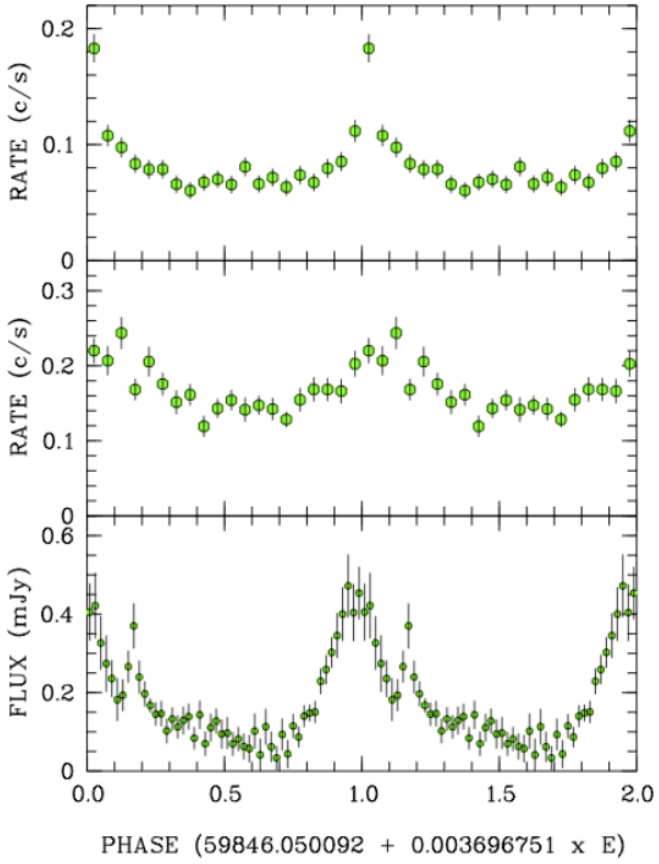

Figure 3.17: Spin phase-folded light curves showing EPIC-pn X-rays (top), OM/UVM2 (middle) and g-band ULTRACAM (bottom). Figure adopted from Schwope, A. et al. (2023)

The XMM-Newton EPIC-pn folded light curve peaks at a different phase compared to the Pelisoli, Marsh, et al. (2023) XMM-Newton folded light curve (see Figure 3.13(bottom)) because Schwope, A. et al. (2023) used a different spin ephemeris compared to equation 3.1 derived by Pelisoli, Marsh, et al. (2023). The spin ephemeris that Schwope, A. et al. (2023) used was BMJD(TDB)= 59846.050092 + 0.003696715E which corresponds to a phase of 0.715 of the Pelisoli, Marsh, et al. (2023) spin ephemeris. Interesting to note is the narrow feature in Pelisoli, Marsh, et al. (2023) ULTRACAM folded light curves (see Figure 3.10($\mathbf{g-i}$)) is also present in Figure 3.17

(bottom) albeit at a different phase. Simultaneous XMM-Newton and ULTRACAM observations of J1912 revealed a feature that does not agree with the broad or narrow pulses (see Figure 3.18) and Pelisoli, Sahu, et al. (2023) proposed that this might be an "accretion-induced flare" as a result of mass transfer from the secondary to the primary in J1912.

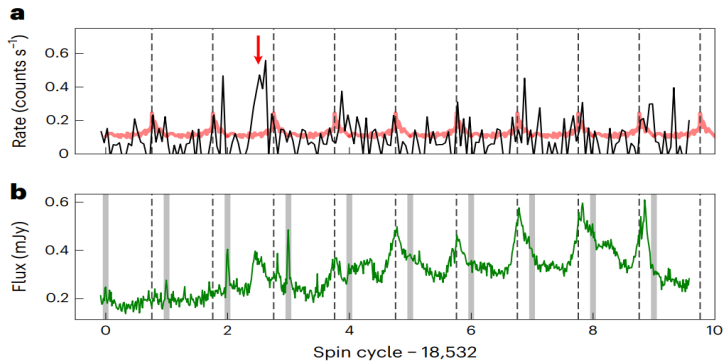

Figure 3.18: Simultaneous X-ray XMM-Newton data (**a**) and optical ULTRACAM g_s band data where the red curve in (**a**) presents the rotation-phase averaged X-ray data over the entire observation and the vertical dashed lines in both (**a**) and (**b**) represents the X-ray pulses. The grey shaded vertical lines in (**b**) represents integer rotation cycles coinciding with the narrow radio pulses. Possible flare is represented by red arrow. Figure adopted from Pelisoli, Marsh, et al. (2023)

Pelisoli, Marsh, et al. (2023) further produced a spectral energy distribution (SED) from the multi-wavelength observations made of J1912 which is shown in Figure 3.19. Pelisoli, Sahu, et al. (2023) supplied a geometric "seeding" model of J1912 to explain the broadband pulsed emission observed from this system (see Figure 3.20). This model sufficiently explains pulsed multi-wavelength emission from J1912 with the requirement that there is some residual accretion from the secondary to the primary.

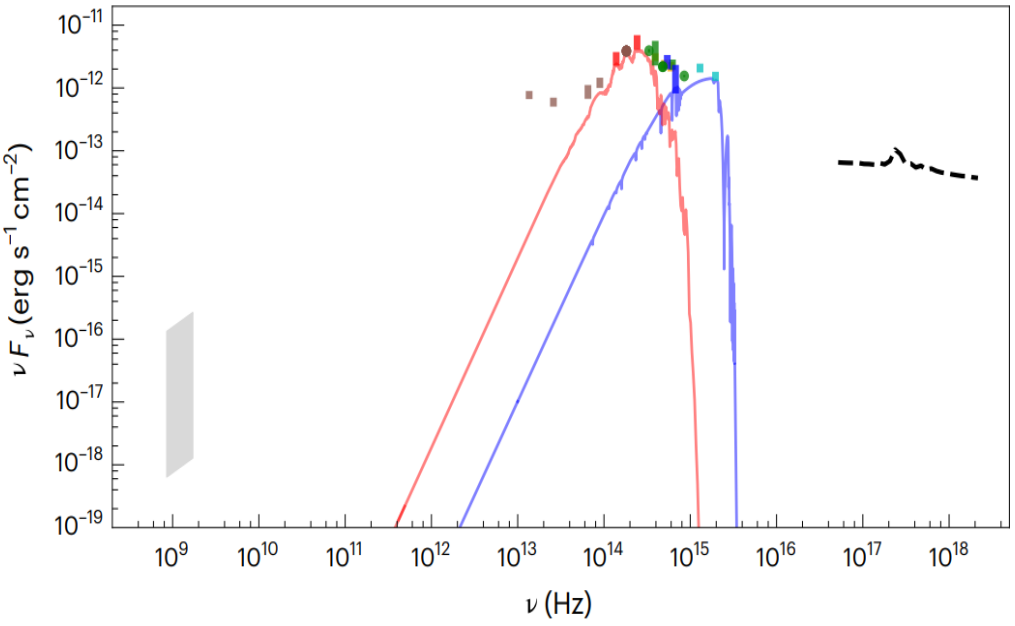

Figure 3.19: SED of J1912 with red and blue graphs showing the model atmospheres with of R_2=0.3$R_\odot$, T_2=3100 K for the M-dwarf and log g=9.0 and T_2=13000 K for the white dwarf at distance d=237 pc. The black dashed line shows the X-ray spectrum from XMM-Newton created by Schwope, A. et al. (2023) where they used a power law (power law index = 2.14±0.11) combined with absorption caused by the interstellar matter to obtain a good fit to their spectrum. The grey polygon shows the radio flux from MeerKAT and the coloured symbols displaying other flux measurements where the vertical bars representing the minimum to maximum value when multiple measurements are present. Figure adopted from Pelisoli, Marsh, et al. (2023)

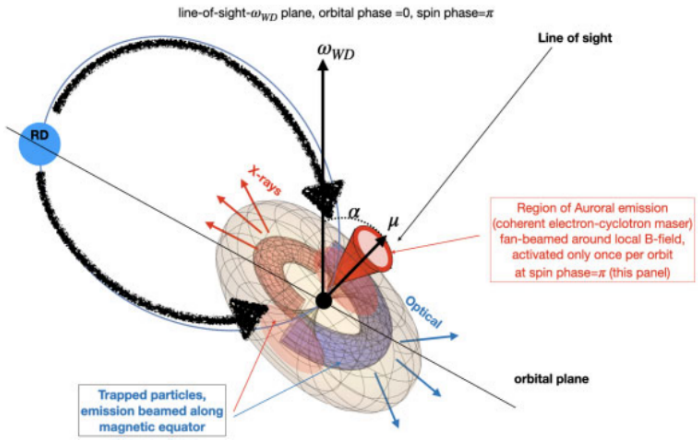

Figure 3.20: Geometric "seeding" model of J1912 when the primary (white dwarf) is at superior conjunction (orbital phase 0) from the vantage point of the observer (with the observer's line of sight at orbital inclination i above the binary plane at orbital phase 0.5). The magnetic moment (μ) of the primary is in the same plane as the rotation (ω_{WD}) axis and the line of sight (orbital phase 0.5) of the observer. Stellar material from secondary (M-dwarf) approaches the magnetic poles of the primary and produces "auroral" emission caused by "coherent electron-cyclotron maser emission". Particles trapped in equatorial regions of the magnetic field ("Van Allen radiation belts") of the white dwarf produces additional emission. Figure adopted from Pelisoli, Sahu, et al. (2023)

One question would now be, how would this system behave in the gamma-ray waveband? Would pulsed gamma-ray emission also be observed? And if detected, what would the emission mechanism be that produces the pulsed gamma-ray emission and what would that reveal about this system? The gamma-ray analysis using the *Fermi*-LAT observatory of J1912 forms part of this dissertation and will attempt to answer those questions in a systematic manner. The reader is referred to Chapter 5 for the gamma-ray analysis of J1912 using ∼15 years of *Fermi*-LAT data. Note: Only a gamma-ray data analysis using data from *Fermi*-LAT will be performed on J1912.

The next chapter discusses the data reductions and analyses of latest optical data using the BOOTES robotic telescope, archival soft X-ray data from the ROSAT telescope and gamma-ray data from *Fermi*-LAT of J0317. The optical and soft X-ray data of J0317 were added to support and possibly make a comparison to the behavior seen in the gamma-ray waveband of J0317.

Chapter 4

Data Reductions and Analyses of J0317

4.1 Latest 2024 BOOTES Optical Observations of J0317

The main purpose of this latest optical data of J0317 was to observe the most recent optical period behavior of J0317 and to possibly compare the phase-folded light curves in optical and γ-ray waveband.

4.1.1 Burst Observer and Optical Transient Exploring System (BOOTES)

Recent observations in the optical waveband of the isolated magnetic white dwarf J0317 were made using the "Burst Observer and Optical Transient Exploring System" (BOOTES, Castro-Tirado, A. J. et al. (1999)) network of robotic telescopes. This network began in 1998 as a Spanish-Czech collaboration project and the main goal of this project was to study optical emissions from very high energy events that occur in the Universe known as gamma-ray bursts (GRBs). These bursts usually occur when stars with mass $\sim$20 $M_{\odot}$ exhaust their thermonuclear fuel and collapse under their own gravity releasing gamma-rays and forming what is known a black hole[1]. GRBs can also be produced by colliding neutron stars in a binary system and these GRBs last for a very short time scale (less than a minute, Seeds and Backman (2016)) and also sometimes display a simultaneous optical counterpart that can be seen from Earth. As a result of its short time scale, robotic telescopes are excellent at observing these GRBs given alerts from other telescopes (see Gehrels and Mszros

[1]The final stage of stellar evolution and is known as a compact object (together with white dwarfs and neutron stars) with gravity so immense that not even light can escape its gravitational pull.

(2012) and references therein for a discussion on GRBs). BOOTES-1 was the first robotic telescope in Spain and was situated in the "Estacion de Sondeos Atmosfericos" (ESAt) at the "Centro de Experimentacion de el Arenosillo in Mazagon" and the second observatory, BOOTES-2, was placed at Estacion Experimental de La Mayora in Algarrobo Costa (Malaga)(Castro-Tirado (2011)). Soon additional robotic telescopes were placed all around the globe and to date, there are seven BOOTES robotic telescopes (see Figure 4.1).

Figure 4.1: The first world wide robotic telescopes network showing the locations of the seven robotic telescopes. Image credit:https://bootesnetwork.com/

Figure 4.2: Closer view of the Bootes-6 robotic telescope at the UFS-Boyden Observatory in Bloemfontein. The red glow in the atmosphere is a result of recent auroral activity in 2024.

Follow-up optical observations of J0317 were made mainly with BOOTES-6 and BOOTES-7 during times when these telescopes were not actively observing the sky for GRBs. BOOTES-6 (see Figure 4.2) is located at the Boyden Observatory, Maselspoort in Bloemfontein, South Africa (Longitude:26°24′13″E and Latitude:29°02′20″S) and BOOTES-7 is located in San Pedro de Atacama in Chile (Longitude:68°10′48.7″W and Latitude:22°57′09.8″S). Both BOOTES-6 and BOOTES-7 have more or less the same technical configurations as the other robotic telescopes (BOOTES-2, BOOTES-3, BOOTES-4 and BOOTES-5). See Table 2 of Hu et al. (2023) for complete comparison between the robotic telescope in the BOOTES network. BOOTES-6 is a 0.6 meter aperture Dolores Prez-Ramrez robotic telescope equipped with a mount slew speed >100 degrees per second with the Andor iXon[2] high quantum efficiency[3] electron multiplying charged-coupled device (CCD) camera that has a 95% peak quantum efficiency (van Heerden et al. (2024)) and contains the "Sloan Digital Sky Survey" (SSDS, Fukugita et al. (1996)) u', g', r', i' and United Kingdom of Infrared Telescope's ZY (Hewett, Warren, Leggett, and Hodgkin (2006)) filters. BOOTES-6

[2] https://andor.oxinst.com/downloads/uploads/iXon3_Hardware_Guide.pdf
[3] The quantum efficiency is just the imaging device's ability to convert collected photons to electrons.

includes a small dome constructed in collaboration with the University of the Free State's (UFS) Physics Department and UFS mechanical and electronic instrumentation division which contains two all-sky cameras, equipped with MORAVIAN C4 CMOS sensors with 16 millimeter f/2.8 lenses that enables the telescope to take pictures of the sky every second (see e.g. van Heerden et al. (2024) for a discussion).

J0317 was observed with BOOTES-6 from 12/02/2024 19:32:35 (UT) to 12/02/2024 23:07:22.983 (UT) for ∼3h 40 min. J0317 is located at a RA=03h 17m 15.8468594712s and DEC=-85° 32′ 25.558244556″ (J2000). It also has a visual white dwarf companion LB 9802 which is non-magnetic and located at a RA=03h 17m 19.1282833488s and DEC=-85°32′31.288377552″ (J2000). J0317 has a visual magnitude of 14.90±0.02 and LB 9802 a visual magnitude of 14.11±0.02 which is 7″ away from J0317 (Klebi, B., Jordan, S., Nelan, E., Bastian, U., and Altmann, M. (2010)). J0317 was observed by BOOTES-6 using a clear filter and an exposure time of 3 seconds. One of the images produced by BOOTES-6 is shown in Figure 4.3 below.

To extract the light curves from the BOOTES optical images, a pipeline developed by Ignacio Pérez García (publication in preparation) was used to automate the reduction and processing of astronomical images by downloading them from the BOOTES-8 servers. The optical frames were first handled by the registration script (bootes_register.py), which continuously monitors the incoming directory for new FITS (Flexible Image Transport System[4]) files and, for each one, reads and normalizes the header, moves the file to the archive tree, and applies the basic charged-coupled device (CCD) calibration (master bias + filter-dependent master flat). Before calibration it builds and stores saturation and near-saturation masks, then subtracts a 2-D sky background (sigma-clipped, windowed) and re-centers the image on the median sky level. The Vizier[5] service was used to load a catalog of stars within a 0.5° radius around the coordinates of J0317. After calibration it solves the astrometry[6]; if the solution is successful it downloads/attaches a local reference catalogue (the Gaia DR3 catalogue (Gaia Collaboration et al. (2021)) was used for unfiltered images) for that field, runs SExtractor (Source Extractor Bertin, E. and Arnouts, S. (1996)) and PSFEx (Point

[4] https://fits.gsfc.nasa.gov/fits_primer.html
[5] https://vizier.unistra.fr/
[6] https://astrometry.net/

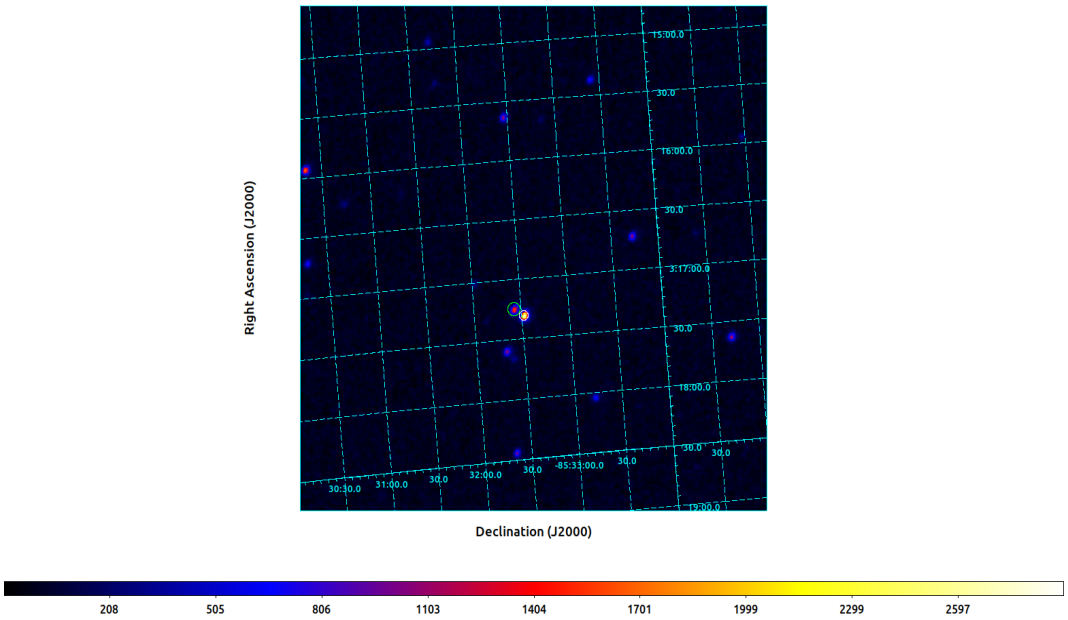

Figure 4.3: BOOTES-6 5'×5' image showing J0317 (green circle) and LB 9802 (white circle). Color bar shows the pixel values of image smoothed with a Gaussian kernel[a] with radius 3 and sigma value of 1.5.

[a] http://ds9.si.edu/doc/ref/how.html

Spread Function Extractor, Bertin (2013)) to obtain a PSF and image-quality metrics (Full-width at half maximum (FWHM), background, PSF entropy), and finally inserts all image-level metadata in MongoDB[7] database so that later stages can pick it up. Failed images are also inserted but flagged, keeping the processing trace.

In a second stage, the image-processing script is called on those registered images: it re-runs source extraction with the final PSF, performs an absolute photometric calibration by matching the detections to the attached catalogue and deriving a zero point and scatter, estimates the limiting magnitude, flux, error in flux, signal-to-noise ratio and applies a field-dependent astrometric/photometric fine-tuning across the image. The circular aperture had a 5 pixel radius and the annulus radius was between 7 and 9 pixels. BOOTES-6 has a pixel scale of $\sim 0.59''$/pixel. Each detection is

[7] https://www.mongodb.com/

then cross-matched against the BOOTES database (recent and archival images) with spatial and temporal constraints, and classified/flagged accordingly; the results are written back both to the image document and to the detections collection. Table 4.1 displays a short observation log of the BOOTES-6 observations. The extracted optical light curve of J0317 is shown in Figure 4.4.

Table 4.1: Short observation log for target field J0317 on 2024 February 12.

Date (UTC)	Start Time	Target	RA (°)	DEC (°)	Exp (s)	Filter	CCD	Elev (°)	Az (°)	Moon Dist (°)
2024-02-12	18:27:25	J0317	49.316	−85.540	15	–	0	32.6	183.3	86.9
2024-02-12	18:28:56	J0317	49.316	−85.540	1	–	0	32.6	183.3	86.9
2024-02-12	18:29:04	J0317	49.316	−85.540	2	–	0	32.6	183.3	86.9
2024-02-12	18:29:09	J0317	49.316	−85.540	3	–	0	32.6	183.3	86.9
2024-02-12	18:29:14	J0317	49.316	−85.540	4	–	0	32.6	183.3	86.9
2024-02-12	18:29:52	J0317	49.316	−85.540	5	–	0	33.0	183.5	86.9
2024-02-12	18:30:37	J0317	49.316	−85.540	7	–	0	32.8	183.4	86.9
2024-02-12	18:31:00	J0317	49.316	−85.540	10	–	0	32.8	183.4	86.9
2024-02-12	18:31:25	J0317	49.316	−85.540	15	–	0	32.8	183.4	86.9
2024-02-12	18:36:55	J0317	49.316	−85.540	15	–	0	32.6	183.3	86.9

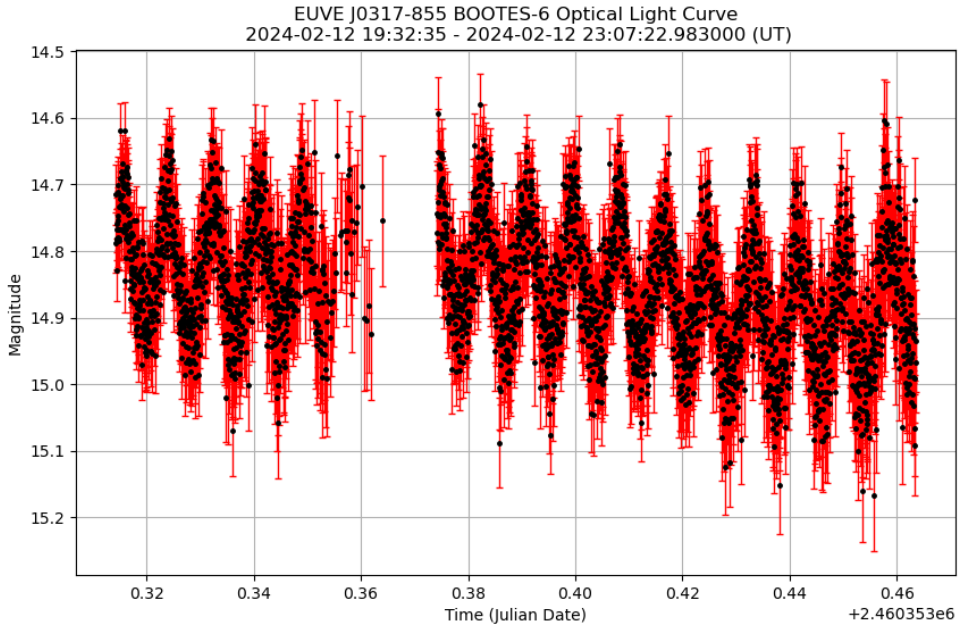

Figure 4.4: BOOTES-6 ∼3h 40min optical clear filter light curve of J0317 displaying highly variable, pulse-like behaviour. The gap was caused by a re-pointing of BOOTES-6 to a possible gamma-ray burst.

From Figure 4.4, it can be seen how highly variable J0317 is and the periodic behavior is also evident. The average difference in magnitude reaches a value of ∼0.4. Longer additional optical observations of J0317 were taken with both the Bootes-6 and Bootes-7 robotic telescopes (see Table 4.2 for a short observation log) to further gauge this periodic behavior of J0317 over a longer baseline for which the light curve is shown in Figure 4.5.

Table 4.2: Short observation log for target field J0317 from BOOTES-6 and 7 on 2024 June 13.

Date (UTC)	Start Time	Target	RA (°)	DEC (°)	Exp (s)	Filter	CCD	Elev (°)	Az (°)	Moon Dist (°)
2024-06-13	23:59:40	J0317	49.304	−85.541	30	Clear	0	25.2	190.3	92.3
2024-06-14	00:00:30	J0317	49.304	−85.541	30	Clear	0	25.2	190.3	92.3
2024-06-14	00:01:20	J0317	49.304	−85.541	30	Clear	0	25.2	190.3	92.3
2024-06-14	00:02:10	J0317	49.304	−85.541	30	Clear	0	25.1	190.2	92.3
2024-06-14	00:03:00	J0317	49.304	−85.541	30	Clear	0	25.1	190.2	92.3
2024-06-14	00:03:50	J0317	49.304	−85.541	30	Clear	0	25.1	190.2	92.3
2024-06-14	00:04:41	J0317	49.304	−85.541	30	Clear	0	25.1	190.2	92.3
2024-06-14	00:05:30	J0317	49.304	−85.541	30	Clear	0	25.1	190.1	92.3
2024-06-14	00:06:20	J0317	49.304	−85.541	30	Clear	0	25.1	190.1	92.3
2024-06-14	00:07:09	J0317	49.304	−85.541	30	Clear	0	25.0	190.1	92.3
2024-06-14	00:07:58	J0317	49.304	−85.541	30	Clear	0	25.0	190.1	92.3
2024-06-14	00:08:48	J0317	49.304	−85.541	30	Clear	0	25.0	190.1	92.3
2024-06-14	00:09:37	J0317	49.304	−85.541	30	Clear	0	25.0	190.1	92.3

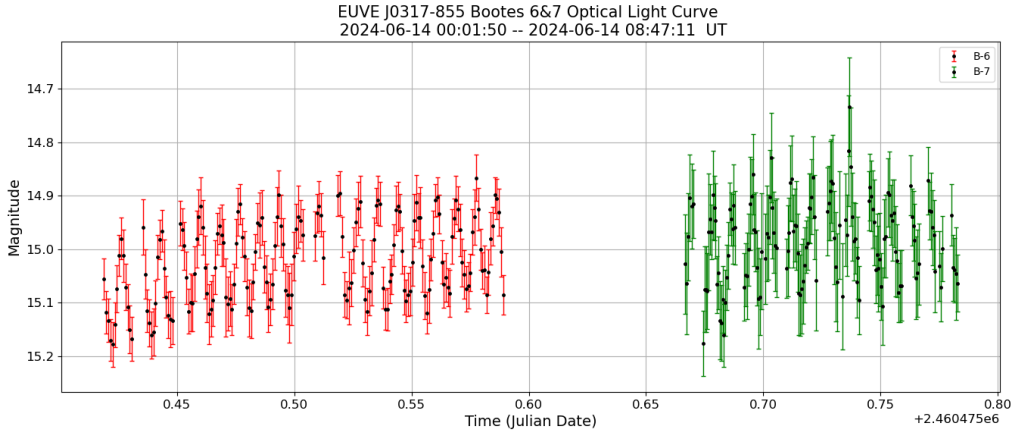

Figure 4.5: Bootes 6 (red) and 7 (green) optical light curve with clear filter showing the long-term periodic variability of J0317. The gap in the light curve is the time it took to switch between the two robotic telescopes.

This increase and decrease in brightness is believed to be due to the rotation of J0317. As was found by Barstow et al. (1995), the rotation period of J0317 is about ∼12 minutes. This new optical

data was then used to confirm this as the rotation period of J0317 and to see if there are any changes in the spin period. Lawrie et al. (2013) did detect a change in the period of $\dot{P}$=(-5.6±1.9)×10^{-14}ss^{-1} by looking whether a phase-folded light curve showed a shift in the position of the rotation period compared to earlier phase-folded light curves. They achieved this by observing J0317 for 17 years between 1994 and 2011 with the use of three different telescopes namely the 1.0 meter telescope at the "South African Astronomical Observatory" (SAAO), the "Panchromatic Robotic Optical Monitoring and Polarimetry Telescopes" (PROMPT) and ULTRACAM on the "New Technology Telescope" (NTT) in Chile. These authors determined the change in the period ($\dot{P} = dP/dt$) by using the O-C method (see Kepler et al. (1991) for further details). The observed times of maximum (O) were calculated by fitting a sine wave to the light curves taken at a given epoch and the calculated times of maximum (C) were calculated by using a linear ephemeris $C = T_0 + PE$ where T_0 is the reference time of maximum, E is the cycle number as measured from T_0 and P is the period. The C-values were subtracted from the O-values to obtain O-C values to which a parabola was fit to the O-C values using expression $O - C = \Delta T_0 + \Delta PE + 0.5P\dot{P}E^2$. Figure 4.6 below shows the resulting O-C diagram of J0317 adopted from Lawrie et al. (2013). Lawrie et al. (2013) did not provide the T_0 value they used to construct the O-C diagram in Figure 4.6.

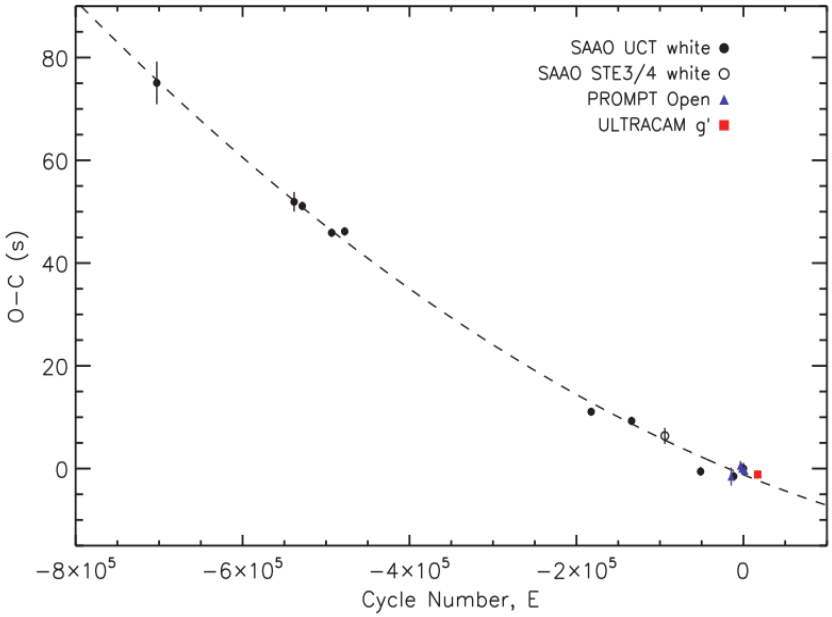

Figure 4.6: J0317's O-C diagram showing the best-fit parabola with the dashed line fitted to data taken from different telescopes. Figure adopted from Lawrie et al. (2013).

To perform an updated periodic analysis of the extracted light curve, the Lomb-Scargle technique (Lomb (1976), Scargle (1982)) was used, which was further generalized by Zechmeister, M. and Kürster, M. (2009). The goal with this new optical data was NOT to search for $\dot{P}$ because the baseline was too short but rather to compare the new phase-folded optical light curves with the γ-ray phase-folded light curves using the same spin ephemeris.

4.1.2 Barycentric Corrections

Before undertaking any periodogram analysis of any source, it is crucial to correct the photon arrival time recorded by the telescope, ground- or space-based, to a relatively stationary reference frame. This is because Earth cannot be regarded as a stationary reference frame because of its rotation about its spin axis and its orbital motion around the Sun. When the photon arrival times are not barycentric corrected, the path that the photons travel will constantly be changing with respect to

Earth and this will cause some photons to arrive later or earlier than others resulting in incorrect periodicities if a periodic signal is detected. The "solar system barycentre" (SSB) is taken as a relatively stationary reference frame situated just outside the Sun's surface (see Figure 4.7 below).

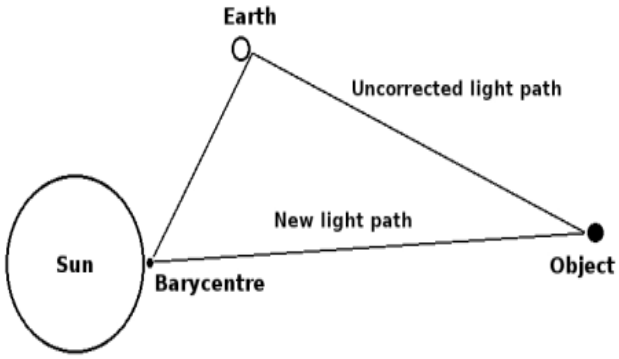

Figure 4.7: Correcting the photon path and arrival time from an astronomical object to the solar system barycentre (SSB). Figure adopted from Van Heerden (2015)

In general, the arrival time of each photon are corrected to the SSB by using the following equation (Lorimer and Kramer (2005))

$$t_{SSB} = t_{topo} + t_{corr} - \Delta D/f^2 + \Delta_{R_\odot} + \Delta_{S_\odot} + \Delta_{E_\odot} \tag{4.1}$$

where t_{topo} is the topocentric or observatory arrival time, t_{corr} describes the clock corrections to the observatory (topocentric) times, $\Delta D/f^2$ is a term that takes into account the electron density from the source along the line of sight of the observer (dispersion measure, DM), $\Delta_{R_\odot}$ is called the Roemer delay and corrects the time that light travels between observatory and the SSB, $\Delta_{S_\odot}$ is the Shapiro delay (Shapiro (1964)) that corrects for time delays caused by the space-time curvature due to the existence of other bodies in the solar system and $\Delta_{E_\odot}$ is the Einstein delay (Damour and Deruelle (1986)) that describes the time dilation of the photon arrival times at the observatory and the SSB as a result of the change in Earth's gravitational field and motion. Both Bootes-6 and

Bootes-7 telescopes recorded the time in Julian Date (JD) and Universal Time (UT). The JD is just the number of days and fraction of days from Juilian Day 0 which began on 1 January 4713 B.C. at noon and UT is the time standard based on Earth's rotation. The Julian Date was then converted to the Heliocentric Julian Date[8] (HJD) using the AstroPy (Astropy Collaboration et al. (2013)) ASTROPY.TIME time conversion package. Then these HJDs were then transformed to Barycentric Julian Date (BJD) using the online time conversion tool[9] provided by Eastman, Siverd, and Gaudi (2010). Only after this correction of the photon time stamps to the SSB can a periodic analysis finally be performed.

4.1.3 Lomb-Scargle Technique

When observing stars with ground-based telescopes, the obtained light curves will often have gaps either as a result of irregular data acquisition because the source is either only visible for a certain time of the night or technical difficulties may cause the telescope not to observe the target/source for a certain time. When this occurs, one has a light curve with data points (photons) that are irregularly spaced, and the normal approach like the Fourier Transform will fail as a result of the irregular sampling of the light curve. The Lomb-Scargle technique developed by Lomb (1976) and Scargle (1982) is best suited for searching for periodicities in unevenly spaced light curves. This technique works by fitting a range of sine waves with different frequencies to the light curve by using the method of least-squares (Barning (1963)) and then "plotting the reduction in the sum of the residuals against frequency". This method of least-squares gives an accurate measure of the power at various frequencies with respect to the overall variance of the dataset and can be thought of as a Fourier transform of irregularly spaced data (Lomb (1976)). The normalized Lomb-Scargle power (Scargle (1982), Horne and Baliunas (1986)) at a frequency $\omega = 2\pi f$ is given by

$$P_{LS}(\omega) = \frac{1}{2\sigma^2}\left\{\frac{\left(\sum_i (x_i - \bar{x})\cos\omega(t_i - \tau)\right)^2}{\sum_i \cos^2\omega(t_i - \tau)} + \frac{\left(\sum_i (x_i - \bar{x})\sin\omega(t_i - \tau)\right)^2}{\sum_i \sin^2\omega(t_i - \tau)}\right\} \tag{4.2}$$

[8] This is just the JD corrected for the differences in Earth's position relative to the Sun's center
[9] https://astroutils.astronomy.osu.edu/time/utc2bjd.html

where $\bar{x}$ is the average of the dataset, the variance is σ^2 and τ is the time lag between the data points and is defined as

$$\tau = \frac{1}{2\omega} \tan^{-1} \left\{ \frac{\sum_i \sin(2\omega t_i)}{\sum_i \cos(2\omega t_i)} \right\} \tag{4.3}$$

When the period of the source is unknown, caution must be taken in the periodogram analysis because the highest periodogram peak might not necessarily be the correct period. This arises because if one were to do a periodic analysis of pure noise, the maximum expected value of this pure noise spectrum over a given set of N frequencies with independent power scales as (Scargle (1982))

$$\langle Z(max) \rangle = \sum_{k=1}^{N} \frac{1}{k} \tag{4.4}$$

which logarithmically diverges with N. This effectively means that as the number of inspected frequencies increase in search for a peak in the periodogram, a large peak will likely emerge even if there is no signal present in the data. Given this statement, an important question typically in periodogram analysis must now be asked, and that is, what is the probability that this feature could have been caused by chance (noise) fluctuations? This is addressed by what is known as the "False-Alarm Probability" (FAP) and is given by (Scargle (1982), Horne and Baliunas (1986))

$$FAP(z) = 1 - [1 - e^{-z}]^N \tag{4.5}$$

with number of independent frequencies given by N. Under the assumption that the data is pure noise, the FAP provides the probability that a resulting peak of height z or higher will occur. The normal Lomb-Scargle periodogram has a few problems in that it does not take into consideration the errors on the measurements and it also assumes that the average of the fitted sinusoids and the mean of the data are equivalent which is generally not the case. Cumming, Marcy, and Butler (1999) introduced their "floating-mean periodogram" which includes an offset parameter c when fitting the range of sinusoids

$$y(t) = asin(\omega t) + bcos(\omega t) + c \tag{4.6}$$

to the data. This offset accounts for the statistical fluctuation of the mean of the sinusoids when

performing the fitting. Zechmeister, M. and Kürster, M. (2009) further generalized the Lomb-Scargle periodogram by weighing each observation by its errors and subtracting the weighted mean from the data. The Generalized Lomb-Scargle (GLS) periodogram then becomes

$$P(\omega) = \frac{1}{\sum w_i(y_i - \bar{y})^2}\left[\frac{\sum w_i y_i[\sum w_i cos\omega(t_i - \tau)]^2}{\sum w_i cos\omega t_i \sum w_i cos\omega(t_i - \tau)} + \frac{\sum w_i y_i[\sum w_i sin\omega(t_i - \tau)]^2}{\sum w_i sin\omega t_i \sum w_i sin\omega(t_i - \tau)}\right] \tag{4.7}$$

where $\bar{y} = \sum w_i y_i$ is the weighted mean, the sums are from $i = 1, 2, ..., N$ and τ is given by

$$tan(2\omega\tau) = \frac{\sum w_i sin2\omega t_i - 2\sum w_i cos\omega t_i \sum w_i sin\omega t_i}{\sum w_i cos2\omega t_i - [(\sum w_i cos\omega t_i)^2 - (\sum w_i sin\omega t_i)^2]} \tag{4.8}$$

in which

$$w_i = \frac{1}{W}\frac{1}{\sigma_i^2} \tag{4.9}$$

where $W = \sum \frac{1}{\sigma_i^2}$ with σ_i as the measurement errors. See Zechmeister, M. and Kürster, M. (2009) for a full derivation of these equations. This GLS periodogram is then normalized to unity and the FAP of a peak can be calculated using

$$FAP = 1 - [1 - Prob(z > z_0)]^M \tag{4.10}$$

where the number of independent frequencies is given by M and can be approximated as the number of periodogram peaks. The term $Prob(z > z_0)$ in equation 4.10 is different for different normalizations as pointed out by Cumming et al. (1999) and for the Zechmeister, M. and Kürster, M. (2009) normalization this term can be estimated by

$$Prob(z > z_0) = (1 - z_0)^{\frac{N-3}{2}} \tag{4.11}$$

See Table 1 in Zechmeister, M. and Kürster, M. (2009) for the different normalizations and their respective probabilities.

The GLS periodogram for the Bootes-6 light curve (see Figure 4.4) was then produced with the

help of a Python script[10] written by Zechmeister, M. and Kürster, M. (2009) and is shown in Figure 4.8 below.

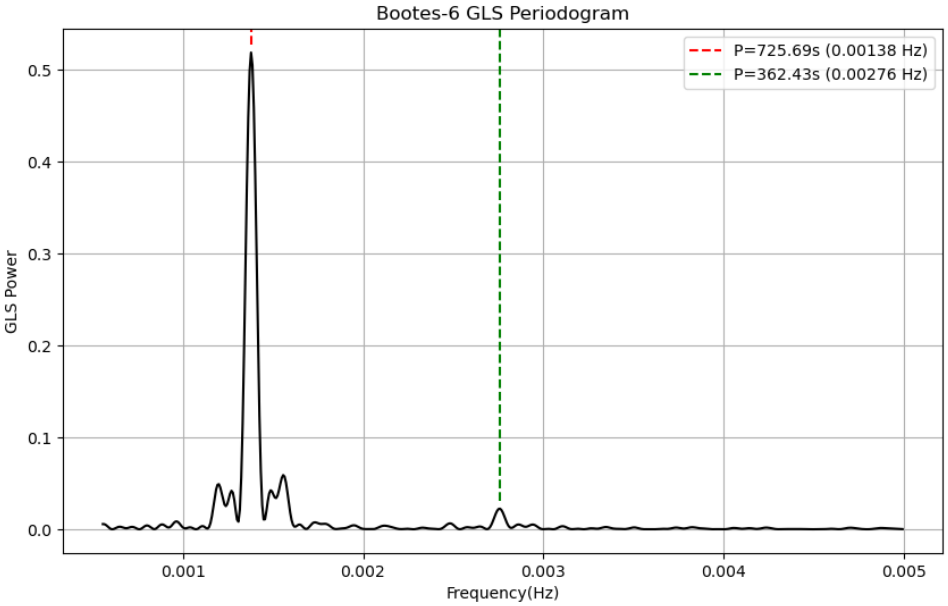

Figure 4.8: GLS Periodogram of the Bootes-6 February 2024 ligth curve in Figure 4.4 showing pulsations at the rotation period P∼725.69s and at half the rotation period (first harmonic) P∼362.43s

The predominant peak in the GLS periodogram corresponds to a period of P=725.69±0.16s which is the spin period of J0317. The sidelobes around the main peak in the periodogram result from the irregular sampling of the light curve and the finite observation duration resulting in a "spectral leakage" to nearby frequencies. There is another peak (shown with the green dotted vertical line in Figure 4.8) at a period of P=362.43±0.74s which corresponds to half the spin period of J0317. The uncertainties in the periods were calculated using the bootstrap method (Efron and Tibshirani (1994)). The basic idea of the bootstrap method for error calculation in periodgram analysis is to create "additional" observations of the source of interest. The bootstrap method works by randomly selecting data points with replacement from the light curve and create a number of

[10] "https://github.com/mzechmeister/GLS/blob/master/python/gls.py"

bootstrap samples ("additional" observations). The term "with replacement" is important because it means that in each of these bootstrap samples, some data points will be repeated and others might be omitted in order to simulate "additional" observations. From these bootstrap samples, the desired statistics (mean, standard deviation, etc) can be calculated. See Efron and Tibshirani (1994) for a comprehensive explanation of this method. 1000 light curves were created and for each of these light curves, the GLS periodogram was calculated. The error on both the spin period and first harmonic corresponds to the standard deviation of the peaks in the GLS periodograms of the bootstrap resampled light curves. The FAP (equation 4.10) on the spin period P=725.69±0.16s is FAP=0.0 and on the first harmonic P=362.43±0.74s is FAP=4.62×10^{-14}.

The Bootes-6 light curve was then folded on this dominant peak in the GLS periodogram using the ephemeris HJD=2450237.72019 provided by Ferrario et al. (1997) and is shown in Figure 4.9 below.

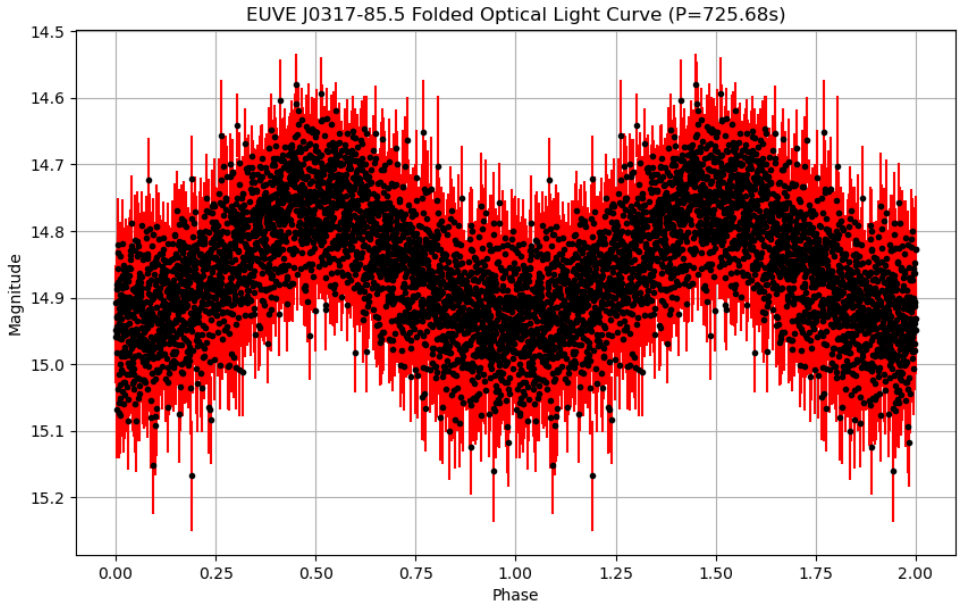

Figure 4.9: Folded Bootes-6 light curve (February 2024 light curve) on spin period P∼725.68s using ephemeris HJD=2450237.72019 by Ferrario et al. (1997).

This folded light curve on the spin period P∼725.69s appears to be single-peaked per rotation

and peaks at a spin phase ∼0.5. The FUV light curve (Figure 3.13) of Ferrario et al. (1997) was double-peaked per rotation and they assigned this additional periodicity at the first harmonic of the rotation period (P=362.9s of their FUV data) to surface inhomogeneities due to Helium or other heavier elements on the surface of J0317 at both magnetic poles. Further inspection of Figure 4.9 reveals a very faint second component at a spin phase of ∼1.0. It is barely visible because most of the optical emission is pulsed at J0317's rotation period.

The GLS periodogram for the light curve from both Bootes 6 and 7 observations of J0317 shown in Figure 4.5 were also computed and the periodogram is shown in Figure 4.10 below.

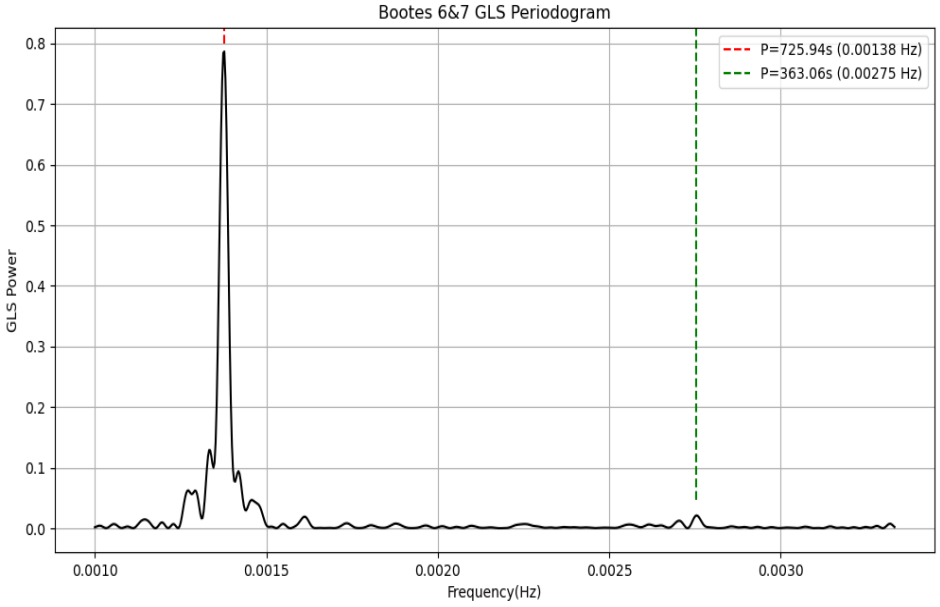

Figure 4.10: GLS periodogram of Bootes 6 and 7 optical light curve (June 2024 light curve, see Figure 4.5). Dominant pulsations is at the spin period P∼725.94s and the faint first harmonic at period P∼363.06s is also visible.

The dominant peak is at a period of P=725.94±0.69s and a very faint peak at a period of P=363.06±14.84s is also visible in Figure 4.10 shown by the green dotted line. The FAP of the spin period is FAP=1.75×10^{-102} and on the first harmonic is FAP=0.94. This high FAP on the first harmonic makes sense because of how faint the peak is in the GLS periodogram. The Bootes

6 and 7 light curve were then folded onto the dominant period of P∼725.94s using the Ferrario et al. (1997) ephemeris and is shown in Figure 4.11 below.

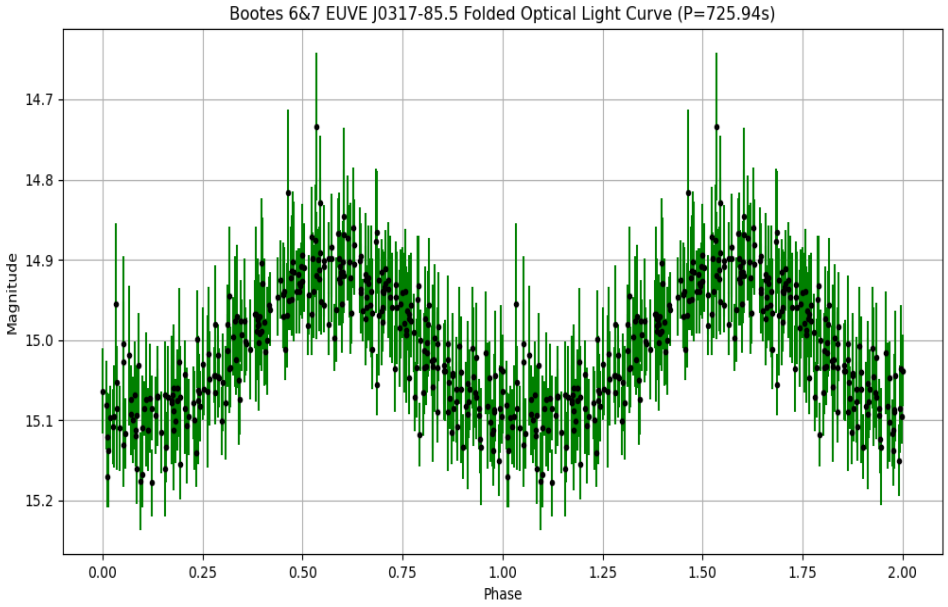

Figure 4.11: Folded Bootes 6 and 7 light curve (June 2024 light curve, see Figure 4.5) on spin period P∼725.94s using Ferrario et al. (1997) ephemeris.

The folded light curve in Figure 4.11 peaks at a spin phase of ∼0.5-0.6 and a second faint component at a spin phase ∼1.0 is also visible. We interpret these two components as optical pulsations emanating from both magnetic poles of J0317 as it rotates at it's spin period. The two Bootes light curves (Figure 4.4 and 4.5) were then combined and a GLS periodogram was created for the complete light curve which is ∼11 hours and is shown in Figure 4.12 below

The dominant peak is at a period of P=725.36±0.73s with FAP=0.0 and the faint peak (shown by vertical green dotted line) is at a period P=362.73±1.04s with FAP=9.22×10^{-10}. These periods will be taken as the spin period (P=725.36±0.73s) and the first harmonic (P=362.73±1.04s) of the spin period of this new optical data of J0317.

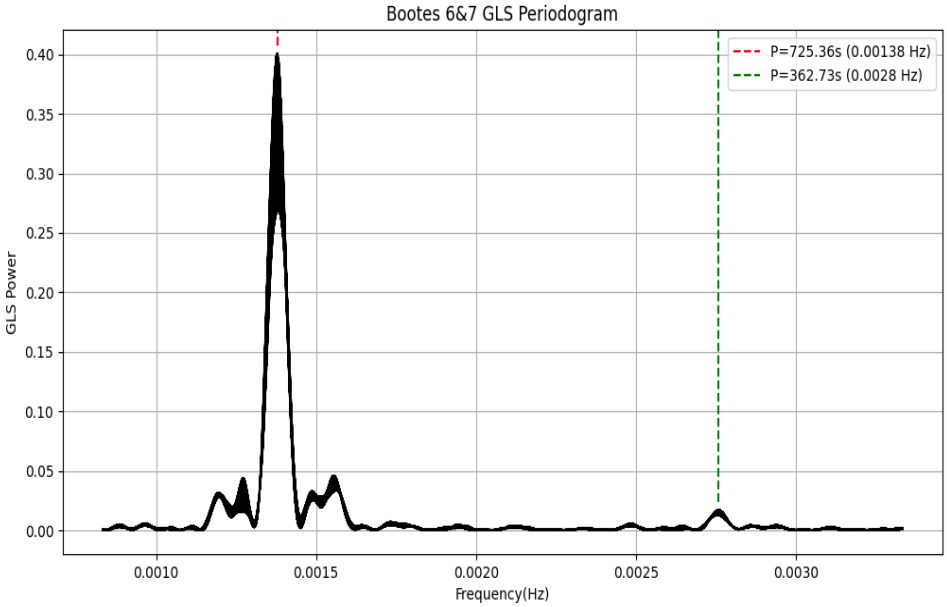

Figure 4.12: GLS periodogram of the combined light curves (February 2024 light curve Figure 4.4 and June 2024 light curve 4.5) showing pulsations at the spin period $P\sim$725.36s and its first harmonic $P\sim$362.73s.

4.1.4 Weighted Wavelet Z-transform (WWZ)

The common periodicity analysis techniques like the Fourier transform and Lomb-Scargle periodograms performs satisfactorily in detecting periodicities in light curves if the source does indeed show periodic behavior. But these methods can not capture the time evolution of the periodic signal. When a source shows periodic behavior it is also worthwhile to see if this periodic signal is variable or non-stationary over time. Since J0317 is essentially an isolated white dwarf, its rotation period is stable and hence we do not expect to detect a change in the rotation period from J0317 from this short observational baseline. The wavelet transform technique was explored to gather familiarity with the wavelet analysis technique so that it can be applied to sources in the future that do indeed show changes in their periodic signals, for example in accreting binary systems in which the primary either spins up (rotation period decreases with time) due to the accretion of

angular momentum from the companion (e.g. RX J2133.7+5107 Breus et al. (2025) with ∼17 year baseline) or spin down (rotation period increases with time) due to the interaction of the primary's magnetic field with the companion's magnetic field (e.g. AR Sco Stiller et al. (2018) with ∼15 year baseline). In wavelet analysis, a wavelet function is fitted to the light curve and it is simultaneously decomposed in both its time and frequency components. A wavelet function is localized in both frequency and time in order to assess the signal's time evolution contrary to the Lomb-Scargle technique that fits sinusoids (which are continuous functions) to the data. The reader is referred to Chapter 6 of Debnath and Debnath (2002) and references therein for an in-depth discussion on wavelet transforms and its applications.

As with Fourier transform techniques, the wavelet transform also suffers from uneven spacing of light curves. Foster (1996) addresses this issue by treating the wavelet transform as a weighted projection onto the "three trial functions"

$$\phi_1(t) = 1(t) = 1 \tag{4.12}$$

$$\phi_3(t) = sin(\omega(t-\tau)) \tag{4.13}$$

$$\phi_2(t) = cos(\omega(t-\tau)) \tag{4.14}$$

with model function

$$y(t) = \sum_i y_i \phi_i(t) \tag{4.15}$$

where y_i are the best fit coefficients in which the model function in equation 4.15 best fit the data (i.e.minimizing the sum of the squared residuals). Foster (1996) uses the abbreviated Morlet function

$$f(z) = e^{iz-cz^2} = e^{i\omega(t-\tau)-c\omega^2(t-\tau)^2} \tag{4.16}$$

as a wavelet function or a mother wavelet in the wavelet transform where c is known as the decay constant and describes how fast the Morlet wavelet decays. A typical value for c is $1/8\pi^2$. The weighted projection onto the trial functions are performed by using the statistical weights

$$w_i = e^{-c\omega(t_i-\tau)^2} \tag{4.17}$$

The power of the WWZ is then given by

$$WWZ = \frac{(N_{eff}-3)V_y}{2(V_x - V_y)} \tag{4.18}$$

where the effective number of data points is N_{eff}, V_x is the weighted variation of the data and V_y is the weighted variation of the model function. This WWZ power uses the Z-statistic (Foster (1996)) which is less sensitive to N_{eff}. See Foster (1996) for further details.

A wavelet analysis was then performed on the optical light curve (Figure 4.4) to see if there are any changes or transient behavior in the periodic signal of J0317. This was done with the help of a Python script[11] written by Sebastian Kiehlmann. The WWZ scalogram is shown in the middle of Figure 4.13 and it is a two-dimensional representation of the periodic signal i.e., time evolution of the period signal or how/if the periodic signal of J0317 changes with observation time. If J0317's periodic signal was changing with time, we would see the bright yellow horizontal feature in the WWZ scalogram change i.e., vary from being purely horizontal at a fixed frequency with respect to the observation time. The right panel in Figure 4.13 just shows the respective WWZ power spectrum and the bottom panel in Figure 4.13 shows the optical light curve. In order to find a balance between the time and frequency, the decay constant was chosen to be c=0.001. A frequency range of ∼0.0008-0.003 Hz with period step of 50 seconds was used. The WWZ scalogram is shown in Figure 4.13 below.

[11] "https://github.com/skiehl/wwz"

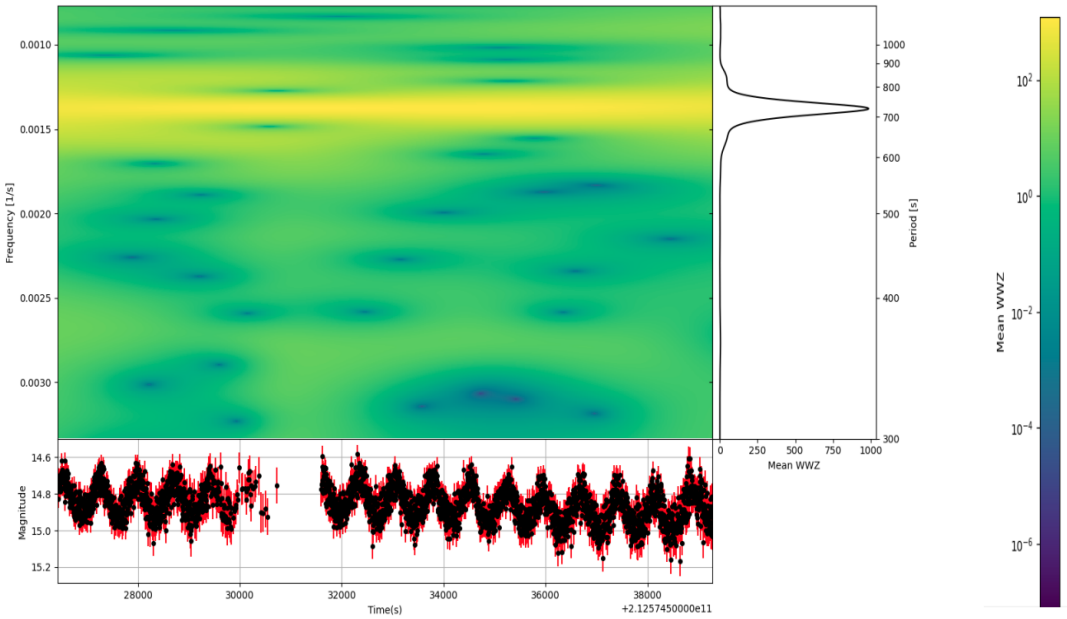

Figure 4.13: Middle panel showing the weighted wavelet Z-transform scalogram of February 2024 light curve in Figure 4.4, right panel showing the mean WWZ periodogram, and the bottom panel showing the light curve.

The peak in the mean WWZ periodogram corresponds to P=725.93±0.41s where the uncertainties were calculated by fitting the predominant peak with a Gaussian function utilizing the Python package SCIPY.OPTIMIZE[12] and then estimating the "full-width at half maximum" (FWHM) of the peak. From the WWZ scalogram, the bright yellow horizontal line shows the periodic signal with respect to time. There are no apparent changes in this horizontal line which suggest that the periodic signal is stable with respect to time. Interestingly, the wavelet analysis does not seem to sufficiently detect the first harmonic of the rotation period (P∼362s) but this could be that most of the optical photons are pulsed at the rotation period of J0317. The same analysis was done on the longer optical light curve in Figure 4.5. The frequency range of ∼0.0006-0.005 Hz with period step of 50 seconds with c=0.0001. The WWZ scalogram is shown in Figure 4.14 below.

The peak in the WWZ periodogram is at a period of P=725.37±0.12s and also appears to be

[12] https://docs.scipy.org/doc/scipy/reference/generated/scipy.optimize.curve_fit.html

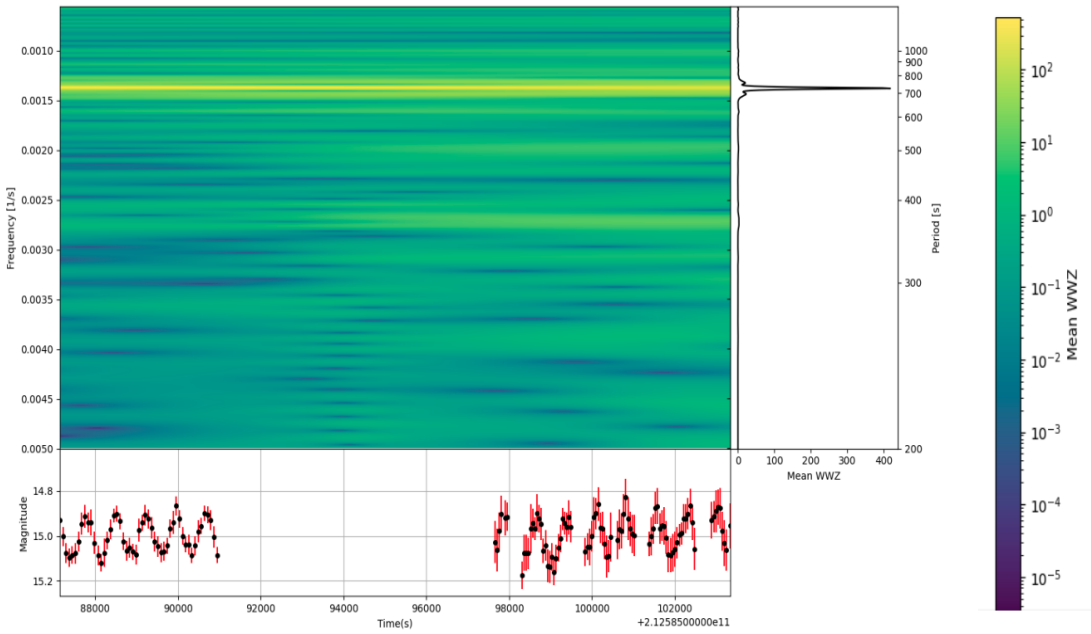

Figure 4.14: Middle panel showing the weighted wavelet Z-transform scalogram of June 2024 light curve in Figure 4.5, right panel showing the mean WWZ periodgram, and the bottom panel showing the light curve.

stable with respect to time. From these two WWZ scalograms, we can conclude that the periodic signal from J0317 is not transient and shows stability over the course of the optical observations. Although no change in the optical period of J0317 is detected over this short observation, the WWZ method can be applied to sources that do indeed show transient behavior over shorter time scales, especially quasi-periodic oscillations or dwarf nova oscillations in the disc of accreting systems.

4.2 X-ray Periodic Analysis of J0317

As was already mentioned in section 3.1.4, recent X-ray observations of J0317 by the Suzaku X-ray telescope carried out by Harayama et al. (2013) did not reveal any significant detections from J0317 and these authors provided a 1σ X-ray flux upper limit of 1.7×10^{-13} erg cm^{-2}s^{-1} in the 2-10 keV energy range. Dessert et al. (2022) also did not detect any significant X-ray emission from J0317 using the "Chandra X-ray Observatory". This might suggest that J0317 is not a strong

thermal/non-thermal X-ray emitter or that more sensitive X-ray telescopes are necessary to detect possible non-thermal X-rays from J0317. But X-rays can also be produced by thermal processes in these systems where charged particles can flow back towards and heat the white dwarf polar caps (see Cáceres et al. (2016) and references therein). See Appendix F for a discussion of the radiation processes. Archival X-ray data from the ROSAT X-ray Satellite were obtained and analyzed to investigate possible transient nature of X-rays from J0317.

4.2.1 ROSAT X-ray Satellite

The "ROentgen SATellite" (ROSAT) was an X-ray observatory developed by an international collaboration between Germany, the United States of America (USA) and the United Kingdom (UK). ROSAT was originally constructed and operated by the "Max-Planck-Institut fur Extraterrestrische Physik" (MPE) in Germany and was launched on 1 June 1990 by the USA. The main instrument of the ROSAT satellite is a four-fold "nested Wolter type I X-ray mirror system" with focal length of 240 cm and an aperture of 83 cm. The ROSAT observatory had a collecting area of 1141 cm^2 which is almost 3 times larger than the "Einstein observatory" (Giacconi and Tananbaum (1980)). ROSAT mainly detects X-rays in the 0.1-2 keV band and the mirror system has an "on-axis angular resolution" at half power width of about $5''$ (Trmper (1982b)). ROSAT carries three imaging X-ray detectors two of which are the "Position Sensitive Proportional Counters" (PSPC) with angular resolution of $\sim 30''$ (FWHM) at the center of the "field-of-view" (FoV) with width of 2°. The PSPC also has energy resolution of $\sim$45% FWHM at 1 keV. The third imaging detector onboard ROSAT was provided by NASA and is the "High Resolution Imager" (HRI) which has a FoV of $36'$ and an on-axis angular resolution at half energy with of $7''$ (Trmper (1982b)) together with a time resolution of about 61 microseconds[13]. Each incoming soft X-ray photon is individually counted and mapped onto a 4096×4096 grid by determining the center of the electron burst generated by the X-ray photon in the microchannel plate (MCP, Morse (1994)). ROSAT was launched into orbit at an altitude $\sim$575 km and its objectives was a "first X-ray all-sky survey" (Trmper (1982b)) using an imaging telescope. ROSAT was decommissioned on 12 February 1999 after successful completion

[13] "https://heasarc.gsfc.nasa.gov/docs/rosat/hri.html"

of its mission. Figure 4.15 below shows the ROSAT observatory.

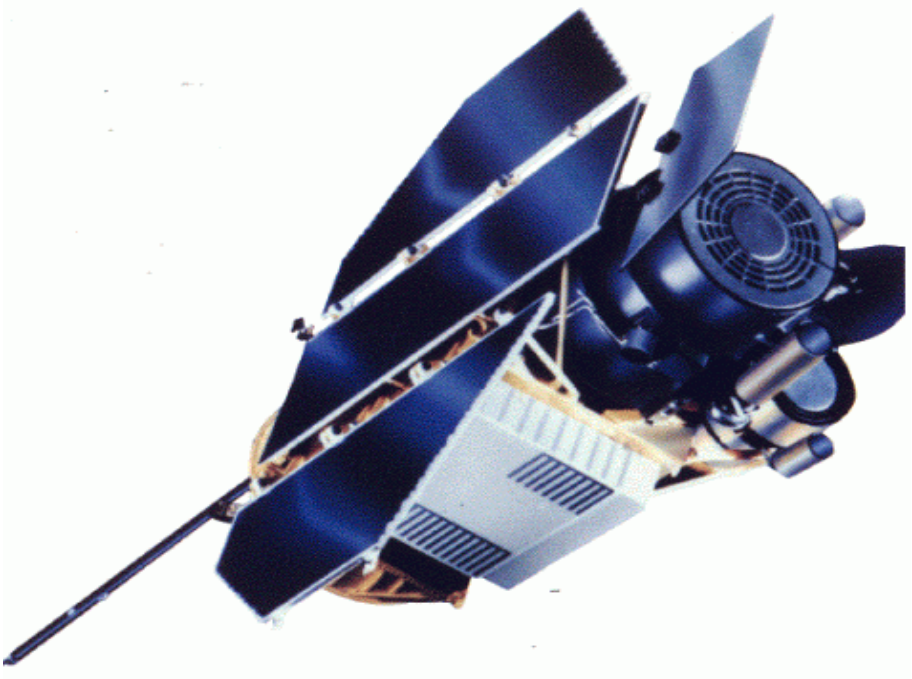

Figure 4.15: Artist's concept for the ROSAT observatory. *Image Credit: Max Planck Institut for Extraterrestrial Physics*

4.2.2 ROSAT Data Reduction and Analysis

High Resolution Imager (HRI) Observations

Archival ROSAT X-ray data of J0317 was obtained from NASA's "High Energy Astrophysics Science Archive Research Center" (HEASARC[14]). J0317 was observed with ROSAT's High Resolution Imager (HRI) from 01 April 1996, 11:54:28.000 (Universal Time, UT) to 14 April 1996, 23:40:52.00 (UT). Additional observations were made from 29 August 1996, 17:49:13.00 (UT) to 21 October 1996, 11:27:42.00 (UT). The principal investigator was Matthew Roger Burleigh. The observation was in pointing mode and instrument set up was in nominal mode meaning that the instrument was collecting good quality data. The nominal right ascension was RA=49.32000° (J2000) and nominal

[14] "https://heasarc.gsfc.nasa.gov/cgi-bin/W3Browse/w3browse.pl"

declination DEC=-85.54000° (J2000).

4.2.3 Barycentric Corrections

After retrieving the data from the HEASARC website, the first important step was to correct the photon arrival times to the "Solar System Barycenter" (SSB). This was performed on both the event files from the first and second set of observations. The event files are in FITS[15] format and contain data such as the recorded time of the X-ray events, the standard "Good Time Intervals" (GTIs) which are the times when good science data were taken which exclude times of high background counts and Earth occultations. The command "ROSBARY"[16] that is part of the HEASoft[17] data analysis software provided by NASA was used to correct the photon arrival times to SSB. This tool first corrects the times in the orbit file to the barycenter. The orbit file contains information about the telescope's position as it orbits the Earth. Secondly, "ROSBARY" applies the correction to the photon arrival time by interpolating on the correction computed for the times in the orbit file. After this correction, the light curve can then be extracted from the event file.

4.2.4 Light Curve Extraction

Extracting a light curve from the barycentric corrected event files, the two sets of observations were first combined and analyzed with XSELECT[18] (version 2.5b) which is a command line interface used for X-ray astrophysical data analysis and is part of the HEASoft (version 6.33.2) software provided by NASA. The event file showing J0317 is shown in Figure 4.16 below and was plotted with DS9[19] software.

[15] "https://fits.gsfc.nasa.gov/fits_primer.html"
[16] "https://heasarc.gsfc.nasa.gov/docs/software/lheasoft/help/rosbary.html"
[17] "https://heasarc.gsfc.nasa.gov/docs/software/heasoft/"
[18] "https://heasarc.gsfc.nasa.gov/ftools/xselect/"
[19] "https://sites.google.com/cfa.harvard.edu/saoimageds9"

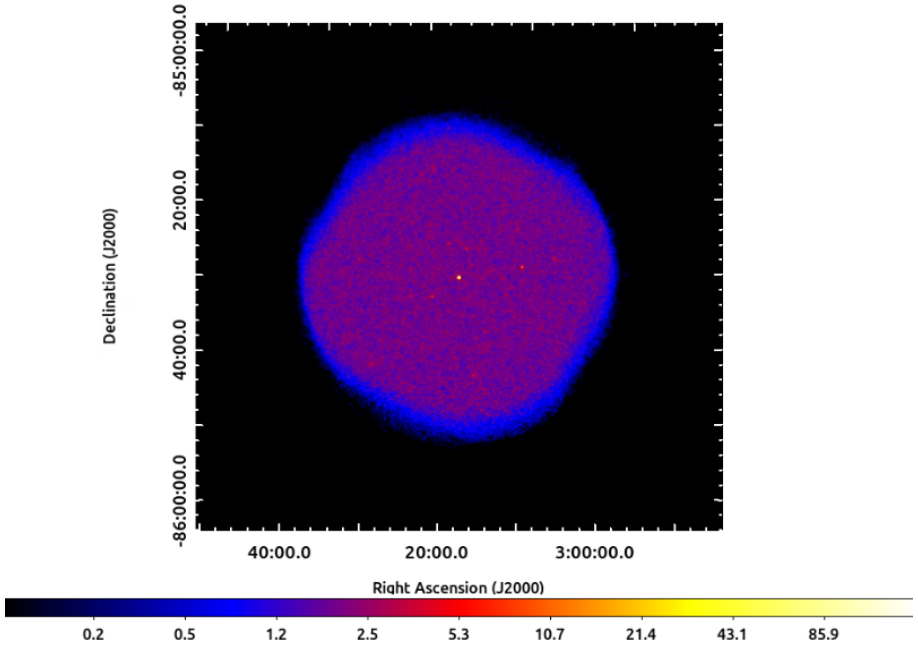

Figure 4.16: ROSAT HRI event file showing J0317 in the center. The image scale is set to logarithmic to make J0317 more visible against the background and smoothed with a Gaussian kernel with radius 3 and sigma value of 1.5.

In X-ray light curve extractions, one should have a source region and a background region. The source region encapsulates the source of interest. This region is usually a circle with specific radius. The background region is a region that is devoid of any sources having similar dimensions as the source region. This background region will be used to create background subtracted light curves. A circular source region with a radius of $17^{''}$ centered at J0317's position (RA=$03^h17^m16.1750^s$, DEC=-85°$32^{'}25.45^{''}$, Klebi, B. et al. (2010)) was chosen and the background and source regions are shown in Figure 4.17 below.

The background was subtracted from the source region by using the BACKSCAL[20] parameter, which is a scaling factor. BACKSCAL is given by the area of the region divided by the total detector pixel area. The scaling factor for the background region was BACKSCAL$\sim 5.4\times10^{-5}$. This scaling factor can be calculated and looked up in the FITS file's header. The corrected count

[20] "https://www.swift.ac.uk/analysis/xrt/backscal.php"

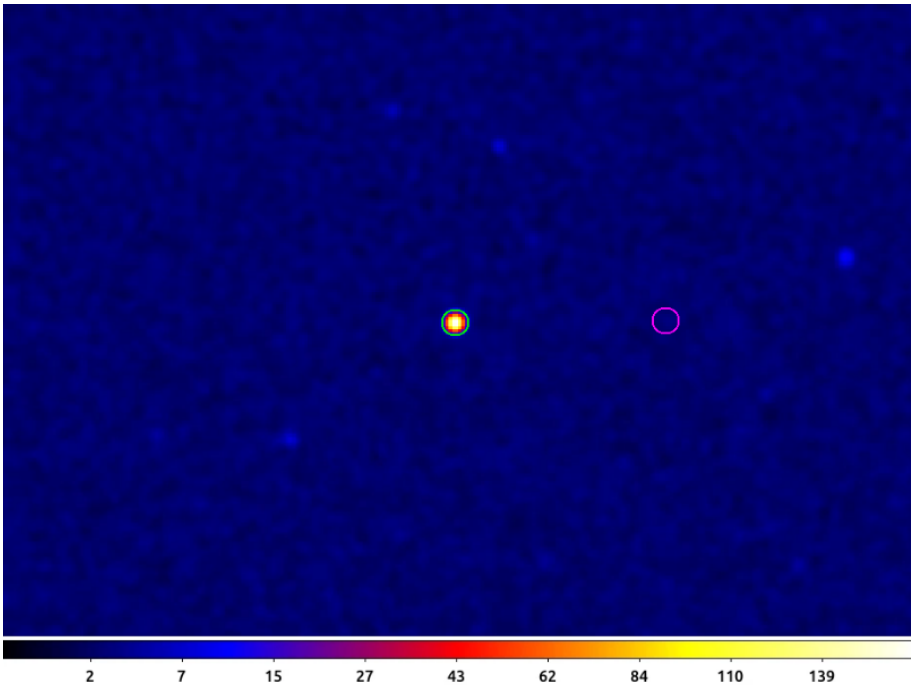

Figure 4.17: Source region (green circle) with radius of 17″ and the 17″ background region (magenta). The color bar displays the counts per pixel where 1 pixel = 4.0000003″

rate was calculated using RATE_COR = RATE-RATE_BG×BACKSCAL and the corrected error in the count rate was calculated using

$$ERROR\_CORR = \frac{ERROR + ERROR\_BG}{2\sqrt{2}} \tag{4.19}$$

The background subtracted ROSAT X-ray light curve binned at 100 seconds is shown in Figure 4.18 below

4.2.5 Periodic Analysis of ROSAT X-ray Light Curve

A periodic analysis was performed on the light curve in Figure 4.18 using the generalized Lomb-Scargle (GLS, see section 4.1.3) technique. The frequency range was chosen to be 0.000125 to 0.0033 Hz to include both the rotation period (P=725.5s) and its first harmonic (P=362.9s). An oversampling factor of 10 was used to distinguish closely spaced frequencies. The GLS periodgram

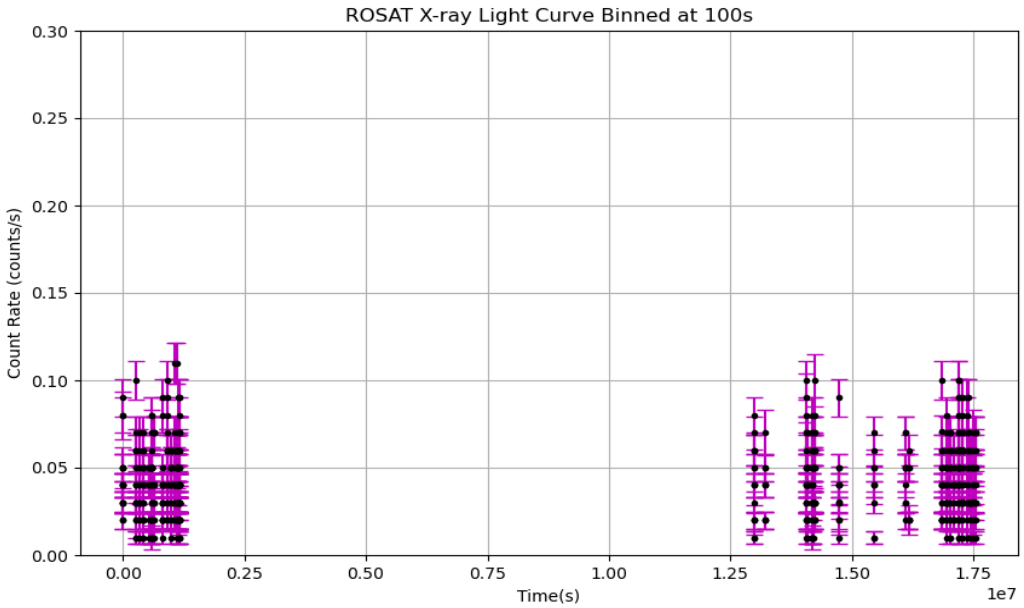

Figure 4.18: ROSAT HRI light curve (0.1-2.4 keV) of J0317 binned at 100s. The light curve spans ∼2 months and 14 days

is shown in Figure 4.19 below

The maximum peak in the GLS periodogram occurs at a period of P=362.82±0.33s (Minnie, Meintjes, and Maritz (2024)) with a FAP=3.28×10^{-5} (yellow horizontal line in Figure 4.19) where errors were calculated using the bootstrap method (Efron and Tibshirani (1994)). This FAP means that there is a ∼99.99997% probability that this peak is real and not caused by random chance fluctuations in the periodogram. This corresponds to a ∼4σ detection. The magenta horizontal line is at FAP=0.01 (99% or ∼2.33σ) and the blue horizontal line at FAP=0.60 (40% or ∼0.25σ). As shown in Figure 4.19, the rotation period P=725.5s is not significant above the background noise and this is rather puzzling. But this could likely be explained by the fact that the ROSAT satellite **could not resolve both J0317 and LB 9802**(J0317's non-magnetic white dwarf companion)[21]. And so, some soft X-ray (0.1-2.4 keV) photons might emanate from LB 9802 and this could nullify

[21]Likely because the ROSAT's angular resolution and the separation between J0317 and LB 9802 are the same with ∼7″ (Vennes et al. (2003))

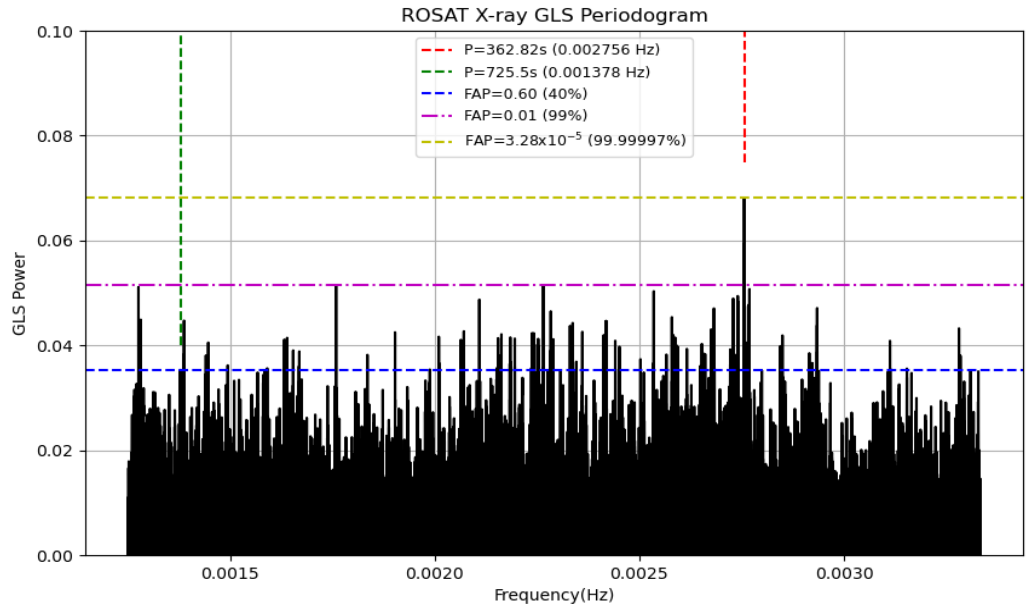

Figure 4.19: GLS periodogram for light curve in Figure 4.18 showing pulsations at period P=362.82s (red dashed vertical line) and the position of the spin period (P=725.5s, green dashed line). The FAP levels are also shown as horizontal lines.

the periodicity at P=725.5s. To investigate this further, the ROSAT HRI light curve was phase-folded on the spin period P=725.5s using the ephemeris HJD=2450237.72019 provided by Ferrario et al. (1997). The folded X-ray light curve on spin period P=725.5s is shown in Figure 4.20 below. This folded light curve on the spin period appears to be double-peak at spin phase 0.0 and 0.5 and is in phase with the far ultra-violet (FUV) folded light curve of Ferrario et al. (1997) (see Figure 3.4). This might suggest that the FUV photons and the soft X-ray photons are being produced at the same regions on J0317. The ROSAT X-ray light curve was then phase-folded on the period of the maximum peak in the GLS periodogram which corresponds to P=362.82±0.33s using the the same ephemeris and the light curve is shown in Figure 4.21. This phase-folded light curve on P∼362.82s appears to be single-peaked at a spin phase of 0.5. This phase-folded light curve appears to be out of phase with Ferrario et al. (1997) phase-folded light curve on the same period (see Figure 3.4). A possible explanation could be ROSAT's inability to resolve both J0317 and LB 9802. From

spectropolarimetric ultraviolet studies, Vennes et al. (2003) did suggest that J0317 could contain a "$B \geq 425$ MG magnetic spot with an underlying $B \leq 185$ MG field" which could contribute to this dominant first harmonic and its out-of-phase phase-folded soft X-ray light curve compared to the ultraviolet phase-folded light curve of Ferrario et al. (1997) (see Figure 3.4). We interpret these **possible pulsations** at the rotation period (P=725.5s) and its first harmonic ($P \sim$362.82s) in the soft (0.1-2.4 keV) X-ray range as charged particles flowing back towards and heating the white dwarf polar caps (Cáceres et al. (2016)) producing the pulsed soft X-ray radiation as J0317 rotates.

In order to strengthen this claim, a longer high resolution uninterrupted soft X-ray observation of J0317 is needed. A spectral analysis of J0317 would also be beneficial in order to further constrain the exact origin of pulsed thermal soft X-ray emission that is being observed from J0317 and unfortunately ROSAT's HRI instrument has a very crude spectral response[22] and a spectral analysis could not be performed.

The process of creating light curves (especially X-ray light curves) involves binning photons together in time bins and this can result in a loss of information and so the effect of different time bins was also investigated and the reader is referred to Appendix A to see its effect on the periodic analysis on the ROSAT HRI data. Nevertheless, J0317 does appear to show some pulsed soft X-ray emission marginally at the spin period ($P \sim$725.5s) and its first harmonic ($P \sim$362.82s). The following section performs a Rayleigh Test (Mardia (1972)) on the ROSAT X-ray data to look for and confirm the periodic signal that was found using the GLS periodogram.

4.2.6 Rayleigh Test of ROSAT X-ray Data

The process of binning data in time bins to create light curves and hence perform a periodic analysis on the resulting light curve results in a loss of information. The Lomb-Scargle techniques are sufficiently suited to detect periodic signals in binned X-ray light curves but there does exist another method that is more robust than the Lomb-Scargle techniques and does not require one to bin data into time bins. This technique searches for periodicities by directly using the barycentric corrected time of arrival of photons (i.e. unbinned data) and is called the Rayleigh Test (Mardia

[22] "https://hea-www.harvard.edu/rosat/rsdc_www/HRI_CAL_REPORT/node24.html"

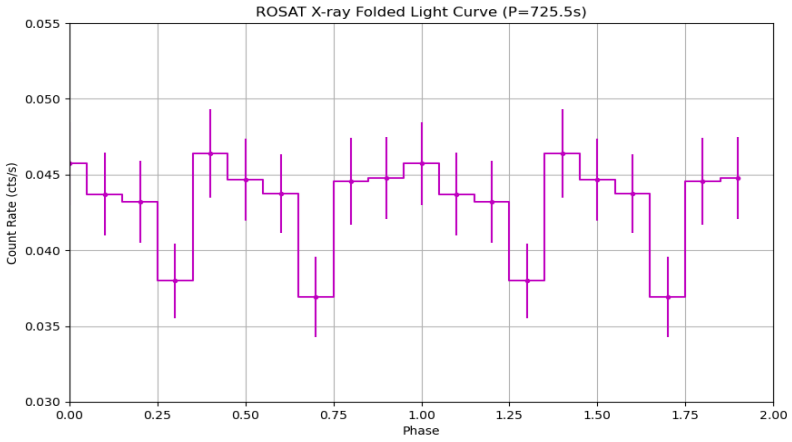

Figure 4.20: ROSAT X-ray light curve (0.1-2.4 keV) folded on the rotation period P=725.5s using ephemeris HJD=2450237.72019 provided by Ferrario et al. (1997). Two rotation cycles are shown.

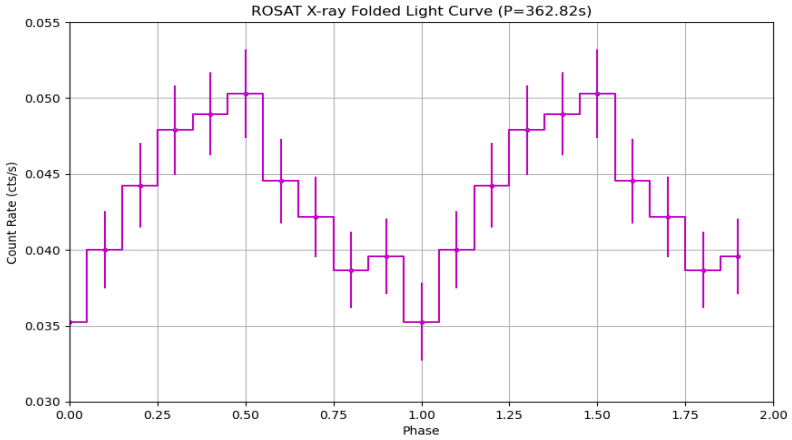

Figure 4.21: ROSAT X-ray light curve (0.1-2.4 keV) folded on the first harmonic of spin period $P\sim$362.82s using the same ephemeris. Two rotation cycles are shown for clarity.

(1972)). See section 4.4.5 for a discussion on the Rayleigh Test. X-ray photons were extracted from a "region of interest" (ROI) of $17''$ centered on J0317's position (RA=$03^h17^m16.1750^s$, DEC=-$85°32'25.45''$, Klebi, B. et al. (2010)). These X-ray photons were then used to perform the Rayleigh

Test using a Python script[23]. The Rayleigh power spectrum is given in Figure 4.22 below.

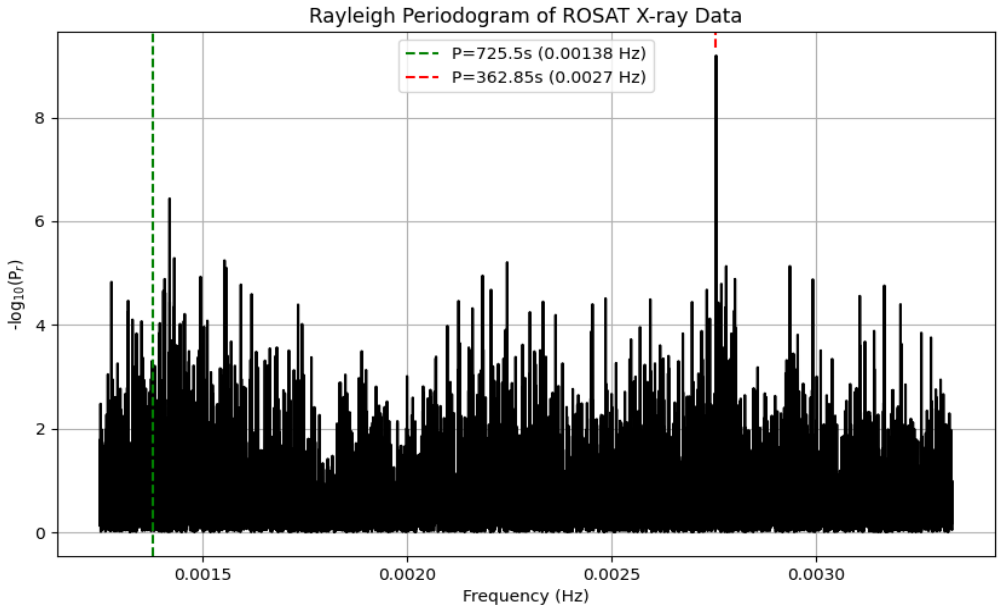

Figure 4.22: Rayleigh Periodgram showing pulsations at a period of P=362.85±0.18s. The vertical green dashed line show the position of the spin period of J0317.

The dominant peak in the Rayleigh periodogram is at a period P=362.85±0.18s with the error calculated using the bootstrap method. This peak is at a $-log_{10}(P_r)$=9.19 which corresponds to a $\sim 7.48\sigma$ detection with respect to the background noise of the periodogram. As with the GLS periodogram (see Figure 4.19), the spin period (P=725.5s) of J0317 is not significant compared to the background noise in the Rayleigh periodogram. These X-ray photons were then phase-folded on both the spin period (P=725.5s, see Figure 4.23) and the first harmonic of the rotation period ($P\sim$362.85s, see Figure 4.24) using the ephemeris provided by Ferrario et al. (1997). The phase-folded light curve on the spin period also appears to be in phase with that of Ferrario et al. (1997) (see Figure 3.4) similar to Figure 4.20 found using the GLS technique. Conversely, the phase-folded light curve on the first harmonic is single-peaked at a spin phase of ∼0.6 and is out-

[23] https://github.com/jradavenport/rayleigh/blob/master/rayleigh.py

of-phase compared to Figure 3.4 of Ferrario et al. (1997) which was also evident in Figure 4.21. As mentioned in section 4.2.5, this misalignment of the light curves phase-folded on the first harmonic of the rotation period between the X-rays and far-ultraviolet (see Figure 3.4) could be due to the fact that the ROSAT spacecraft **could not resolve both J0317 and LB 9802** or that J0317 could possess multi-polar magnetic fields that could contribute to this misalignment of phase-folded light curves.

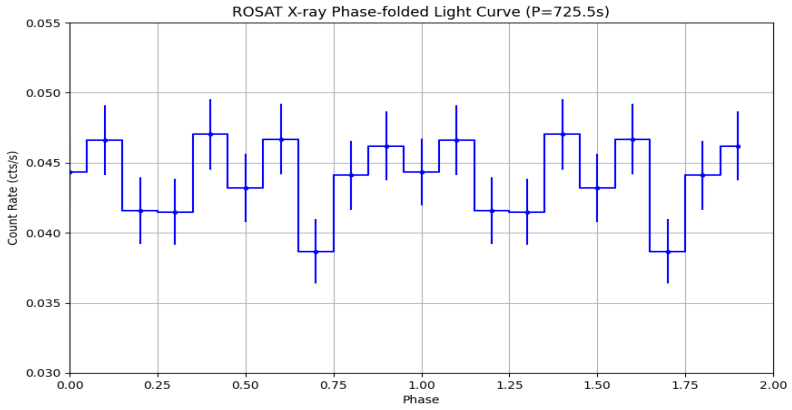

Figure 4.23: ROSAT X-ray (0.1-2.4 keV) photons phase-folded on the spin period P=725.5s using ephemeris HJD=2450237.72019 provided by Ferrario et al. (1997). Two rotation cycles are shown.

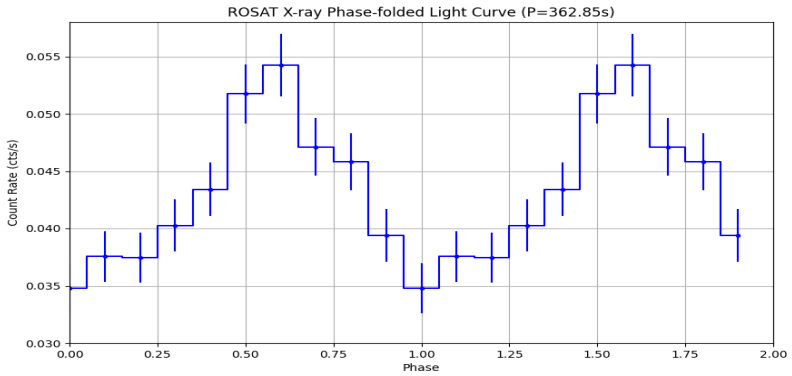

Figure 4.24: ROSAT X-ray (0.1-2.4 keV) photons phase-folded on the first harmonic of spin period P∼362.85s using the same ephemeris. Two rotation cycles are shown.

The following section describes the analysis of γ-ray data of J0317 using the *Fermi*-LAT observatory.

4.3 *Fermi*-LAT γ-ray Analysis of J0317

This section is outlined as follows:

- Section 4.3.1 gives a brief overview is given on the *Fermi*-LAT observatory.
- Section 4.3.2 describes the data acquisition process.
- Section 4.4.1 describes the data analysis of the retrieved *Fermi*-LAT data using aperture photometry.
- Section 4.4.2 gives a brief discussion of the maximum likelihood analysis process used to reduce and analyze *Fermi*-LAT data and gives the reader a sense of why it is more accurate than aperture photometry.
- Section 4.4.3 gives the process followed (data cuts and selections) for a binned likelihood analysis.
- Section 4.4.4 gives the unbinned analysis of the *Fermi*-LAT data.
- Section 4.4.5 describes the periodic analysis performed on the *Fermi*-LAT data using the Rayleigh Test.
- Section 4.4.6, a new method called TS gating (Madzime and Meintjes (2023), Madzime (2021)) is introduced in an **attempt to increase the visibility** of J0317 building on the standard binned and unbinned likelihood analyses.
- The validity of TS gating method is tested by performing control tests on sourceless regions away from J0317's position and are given in Appendices B and C.

4.3.1 *Fermi*-LAT Observatory

The "Large Area Telescope" (LAT) onboard the "Fermi Gamma-ray Space Telescope" (*Fermi*), previously known as *GLAST* ("Gamma-ray Large Area Space Telescope") was launched by NASA on 11 June 2008 on a Delta II Heavy launch vehicle in a 565 km altitude orbit at a 25.6° inclination relative to Earth's equator and with a ∼96 minute orbital period (Atwood et al. (2009), Ackermann et al. (2012)). The LAT is a "pair-conversion" observatory where the individual γ-ray photons convert into e^- and e^+ pairs and are then recorded by the instrument. A method of reconstruction of the e^- and e^+ pairs is used to estimate the incident γ-ray photon's direction and energy. In order to achieve this, the *Fermi*-LAT observatory consists of several instruments including a converter-tracker which has 16 high-Z material planes necessary for the incident γ-rays to convert to $e^{\pm}$ pairs, a calorimeter that measures the energy deposition due to the $e^{\pm}$ pairs, and an "anti-coincidence detector (ACD)". The ACD's purpose is to efficiently reject charged-particle background caused by the cosmic-ray background radiation. See Figure 4.25 below for a schematic diagram of the LAT.

Fermi-LAT has a large effective area that is a function of energy >8000 cm^2 at normal incidence[24]. *Fermi*-LAT can detect γ-ray photons having energies from below "20 MeV to more than 300 GeV". It also has a "field of view" (FoV) of ∼2.4 steradian (sr) at 1 GeV which enables it to observe the whole sky every 3 hours with a time resolution of <10 μs. The reader is referred to Atwood et al. (2009), Ackermann et al. (2012) and references therein for a full technical description of *Fermi*-LAT's instrumentation and performance.

4.3.2 *Fermi*-LAT Data Products

Once the γ-ray events have passed filtering and reconstruction algorithms (see Section 3.1 of Ackermann et al. (2012)), the reconstructed γ-ray photons are then made accessible to the scientific community and can be retrieved from the "*Fermi* Science Support Centre" (FSSC[25]). About 15 years of γ-ray data of J0317 was retrieved from FSSC using time range 2009-01-01 00:00:00, 2024-11-05 00:00:00 (Gregorian format). A search radius of 15° centered on J0317's coordinates

[24] https://fermi.gsfc.nasa.gov/ssc/data/analysis/documentation/Cicerone/Cicerone_Introduction/LAT_overview.html

[25] "https://fermi.gsfc.nasa.gov/cgi-bin/ssc/LAT/LATDataQuery.cgi"

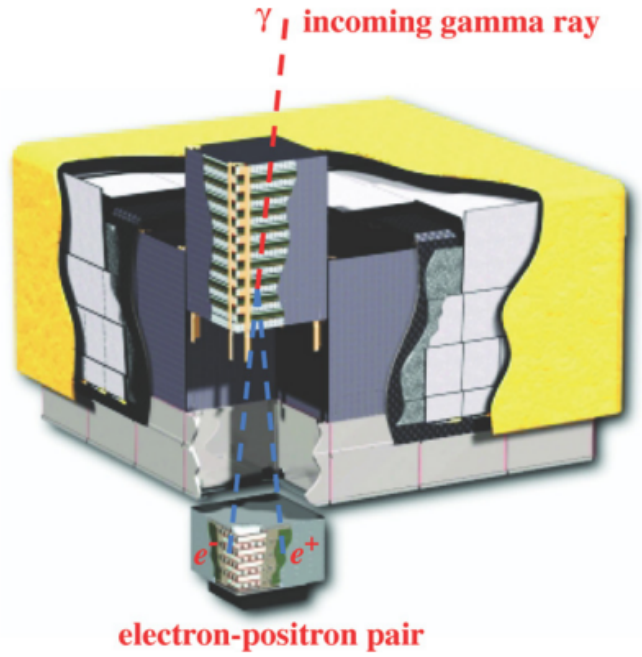

Figure 4.25: Illustration of the LAT showing incident γ-ray photon to $e^{\pm}$conversion. LAT's dimensions are 1.8m×1.8m×0.72m. Figure adopted from Atwood et al. (2009).

(RA=49.31602858°, DEC=-85.54043285°, J2000) was used. This search radius was specifically chosen to cover *Fermi*-LAT "point-spread function" (PSF). The PSF is the probability distribution function between the true and reconstructed direction of the detected γ-ray photons from a point source (Ackermann et al. (2013)). *Fermi*-LAT's PSF is energy-dependent (broader at lower energies and becomes narrower at higher energies) and containment radius of 68% at the normal incidence for 100 MeV photons is ∼4° meaning that 68% of the detected 100 MeV photons will fall within a 4° radius of the true source position (Atwood et al. (2009)). Similarly, at an energy of ∼500 MeV 68% of the detected 500 MeV photons will fall within a ∼1° radius of the true source position (with the PSF decreasing at higher energies, see Ackermann et al. (2013)). Gamma-ray data sets of J0317 in the energy range spanning 0.1-500 GeV and 0.5-10 GeV were retrieved and analyzed. The lower energy region selected between 0.5-10 GeV was due to the fact that theoretical estimates (see Meintjes et al. (2023)) seem to suggest that γ-rays that were produced via curvature radiation

would have energies below 50 GeV (upper limit).

4.4 Data Reductions and Analysis

4.4.1 Aperture Photometry

The technique of aperture photometry[26] was used to extract a γ-ray light curve of J0317 using the $\sim$15 years of γ-ray data in both the 0.1-500 GeV and 0.5-10 GeV energy ranges (the 0.5-10 GeV energy range was included because these fast rotating, highly magnetic white dwarfs could emit γ-rays in this range via the curvature radiation mechanism, see Meintjes et al. (2023) and references therein). This was achieved using the *Fermi*-LAT analysis software called *Fermitools*[27] (version 2.2.11). First, the photon event files were combined into one file using the command `gtselect` and only events from a "Region Of Interest" (ROI) of 0.6° were selected to exclude spurious background γ-ray emission from other sources especially when the source lies in a crowded field (Madzime and Meintjes (2023)). Next, good time intervals (GTIs) were created using `gtmktime`. The GTIs include the times where the data can be considered valid which exclude times when J0317 was too close to the limb of the Earth and when it was within 5° of the Sun. After this, a 30 second light curve of J0317 was then created using `gtbin` command and the exposure for each time bin was determined using the `gtexposure` command. The exposure just refers to the amount of time the instrument has spent on a specific region of the sky. As this technique is a model independent approach, `gtexposure` still requires an estimate of the spectral index[28] of the source which was chosen to be -2.1 for J0317. This allowed for a reasonably accurate estimation of the flux estimates of J0317. The resulting light curve file was then barycentric corrected using `gtbary` and the rate (counts/exposure) and the error (error/exposure) in the rate was then calculated. The final aperture photometry γ-ray light curves of J0317 for both 0.1-500 GeV and 0.5-10 GeV is shown in Figures 4.26 and 4.28 respectively.

From these light curves and their respective GLS periodogram, it is clear that there seem to be no significant pulsations at both the spin period P=725.5s and it's first harmonic P=362.9s in

[26] "https://fermi.gsfc.nasa.gov/ssc/data/analysis/scitools/aperture_photometry.html"
[27] "https://github.com/fermi-lat/Fermitools-conda/wiki"
[28] Photon spectral index

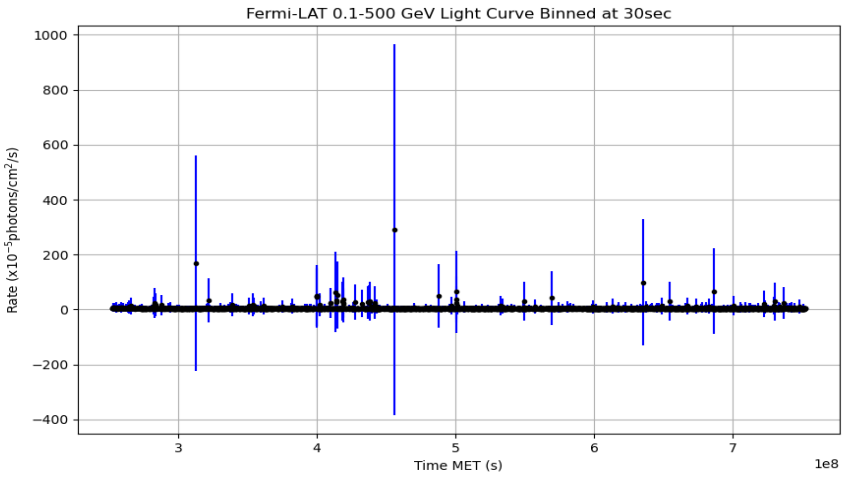

Figure 4.26: J0317 *Fermi*-LAT 0.1-500GeV γ-ray aperture photometry light curve binned at 30 seconds.

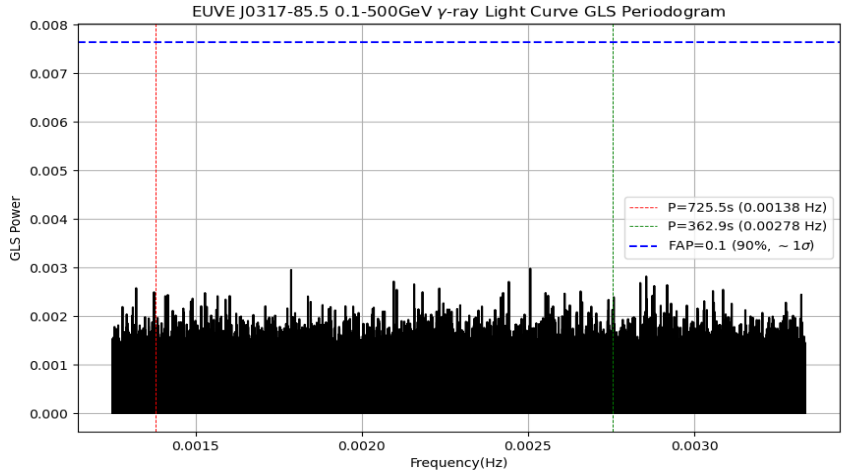

Figure 4.27: GLS periodogram of 0.1-500 GeVγ-ray light curve in Figure 4.26 showing no significant pulsation at the spin period P=725.5s and its first harmonic P=362.9s

both energy bands. But this technique of aperture photometry does not take the background into consideration and is a very crude way to look for periodicities, especially if the source is a very faint γ-ray emitter which we expect J0317 (evident from the large error bars) to be. A more robust

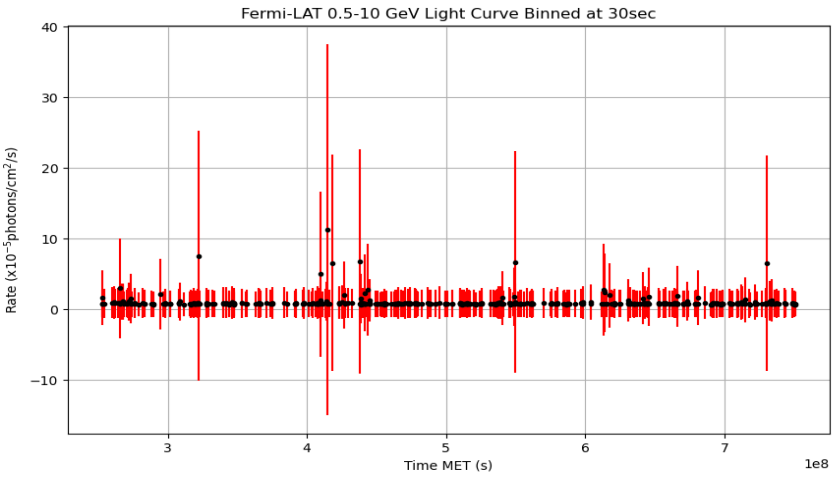

Figure 4.28: J0317 *Fermi*-LAT 0.5-10GeV γ-ray aperture photometry light curve binned at 30 seconds.

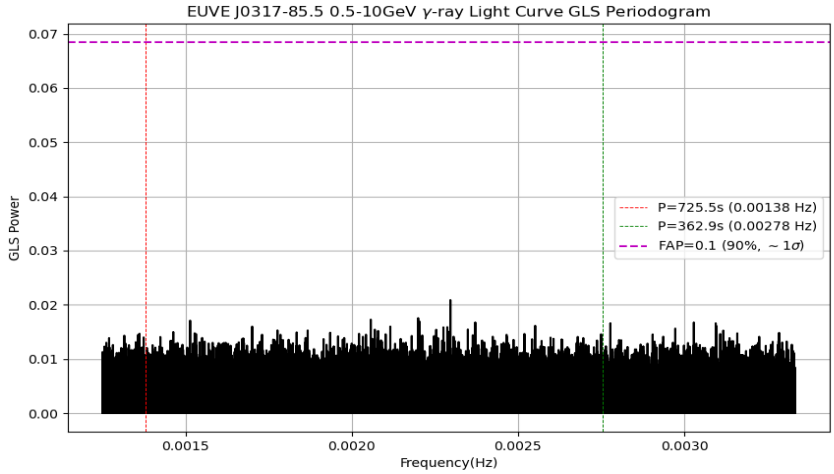

Figure 4.29: GLS periodogram of 0.5-10 GeV γ-ray light curve in Figure 4.28 showing no significant pulsation at the spin period P=725.5s and its first harmonic P=362.9s

method is needed to sufficiently model and take into consideration nearby γ-ray sources in the ROI that might interfere with the possible γ-ray emission from J0317. This method is widely used in the γ-ray astrophysics community and is called Maximum Likelihood Analysis.

4.4.2 Maximum Likelihood Analysis

The method of likelihood analysis was first used by Mattox et al. (1996) to analyze data from the "Energetic Gamma Ray Experiment Telescope" (EGRET). First introduced by Fisher (1925), the technique of likelihood can be used for parameter estimation and refers to the degree to which the data supports a statistical hypothesis or can be thought of as the "joint probability of the observed data given the hypothesis". The maximum likelihood estimator is the estimate that maximizes the likelihood or produces the maximum probability that a hypothesis can be tested for a certain data set.

In *Fermi*-LAT analysis, the likelihood L is estimated by the multiplication of the probabilities of observing detected events in each bin. If the expected number of γ-ray events in the i-th bin is m_i being a function of the source model, then the probability of detecting n_i events in this bin is given by the "Poisson distribution"

$$p_i = m_i^{n_i} \frac{e^{-m_i}}{n_i!} \tag{4.20}$$

The likelihood L will then be the multiplication of p_i for all i. Since the sum of the expected number of γ-ray events in the i-th bin m_i is practically just the total number of expected events N_{exp} predicted by the source model, the likelihood L can then be written as

$$L = e^{-N_{exp}} \prod_i \frac{m_i^{n_i}}{n_i!} \tag{4.21}$$

and for finite-sized bins where n_i may be greater than 1 this likelihood is referred to as "binned likelihood analysis". As previously mentioned, the idea of binning results in a loss of information. Making the size of the bins infinitely small so that n_i is 0 or 1, then equation 4.21 reduces to

$$L = e^{-N_{exp}} \prod_i m_i \tag{4.22}$$

which is a more accurate likelihood and is known as the "unbinnned likelihood analysis[29]". A

[29] "https://fermi.gsfc.nasa.gov/ssc/data/analysis/documentation/Cicerone/Cicerone_Likelihood/Likelihood_formula.html"

method of hypothesis testing was then introduced by Neyman and Pearson (1967) which they called the "likelihood ratio test" and is basically the ratio of the likelihood that no source is present ("null hypothesis") for the data and the likelihood of the source present ("alternative hypothesis") of the same data. Wilks (1938) further provided an analytical expression for the likelihood ratio that a χ^2 distribution which defines the so-called Test Statistic[30] given by

$$TS = -2ln\left[\frac{L_{max,0}}{L_{max,1}}\right] \tag{4.23}$$

where $L_{max,0}$ is the maximum likelihood for null hypothesis (model without the source) and $L_{max,1}$ is the likelihood for a model with a point source present at the location. Equation 4.23 essentially gives the "detection significance of a source" which can be estimated by $\sigma \sim \sqrt{TS}$ (Mattox et al. (1996)).

4.4.3 Binned Likelihood Analysis

A binned likelihood analysis[31] was then performed on J0317 using ∼15 years of *Fermi*-LAT γ-ray data spanning 2009-01-01 00:00:00 to 2024-11-05 00:00:00 (Gregorian format) and using a ROI=10°. This ROI size was chosen to account for *Fermi*-LAT's broad "point-spread function" (PSF) at lower energies. The energy range for binned likelihood analysis was 0.1-500 GeV. The event files were combined into one file using `gtselect` for which only "SOURCE class" events "`evclass=128`" together with event type "`evtype=3`" (for photons converting at both the FRONT and BACK of the telescope tracker). These data selection cuts are the recommended cuts for *Fermi*-LAT data analysis[32]. A zenith angle value of `zmax`=90° was chosen to limit γ-ray emission from Earth's limb. Then, good time intervals (GTIs) were then obtained using `gtmktime` together with filter expression "`(DATA_QUAL>0)&&(LAT_CONFIG==1)`". A 2D counts map (Figure 4.30) was then created for J0317 using `gtbin` to see the contribution of other sources in the ROI.

Then, the photons were binned into a 14.14°×14.14° region with 0.1° per pixel resolution using

[30] https://fermi.gsfc.nasa.gov/ssc/data/analysis/documentation/Cicerone/Cicerone_Likelihood/Likelihood_overview.html
[31] https://fermi.gsfc.nasa.gov/ssc/data/analysis/scitools/binned_likelihood_tutorial.html
[32] "https://fermi.gsfc.nasa.gov/ssc/data/analysis/scitools/"

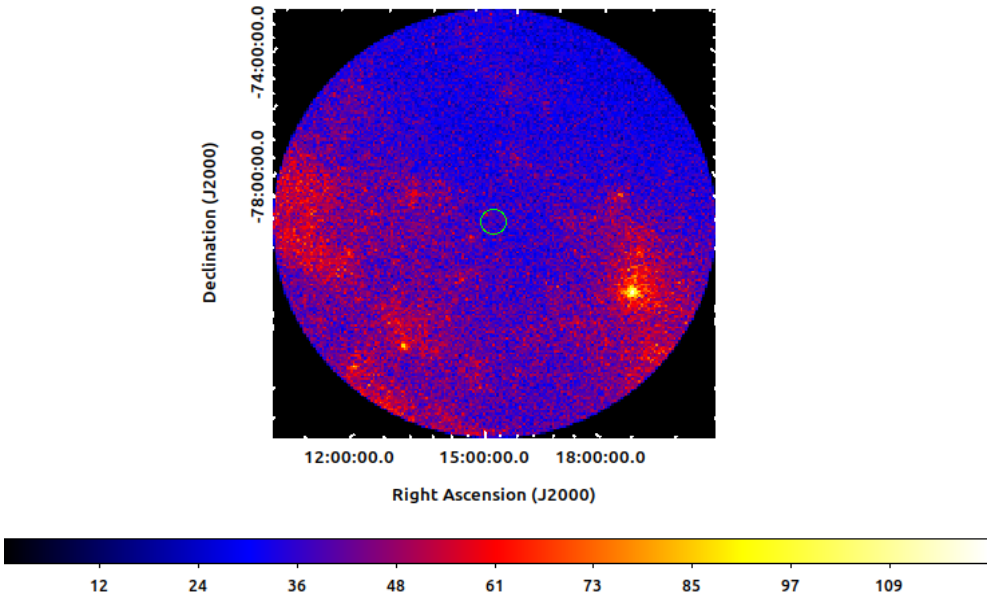

Figure 4.30: 0.1-500 GeV 200×200 pixel counts map with 0.1° per pixel resolution of J0317 (0.6° radius green circle). The color bar displaying the counts per pixel value.

37 logarithmically uniform energy bins (∼10 logarithmically spaced bins per decade) to create a 3D counts cube utilizing the `CCUBE` option in `gtbin`. From Figure 4.30, the need to model the background γ-ray emission from other sources in the ROI is evident. To achieve this, two background model templates were used. The Galactic diffuse background "`gll_iem_v07.fits`" and isotropic background emission "`iso_P8R3_SOURCE_V3_v1.txt`"[33]. A spatial and spectral model for all the sources in the ROI were created using the "4FGL catalog Data Release 4" (4FGL-DR4, Ballet, Bruel, Burnett, Lott, and collaboration (2024)) and since J0317 is not part of 4FGL-DR4 catalog it was manually added to the model using a simple power law model described as

$$\frac{dN}{dE} = N_0 \left[\frac{E}{E_0}\right]^{-\Gamma} \tag{4.24}$$

which describes the point sources' differential photon flux where N_0 is the flux normalization

[33] "https://fermi.gsfc.nasa.gov/ssc/data/access/lat/BackgroundModels.html"

(photons/cm^2/s/MeV), E_0 is the reference energy usually kept at 1 GeV and Γ is the spectral index which describes the slope of the spectrum. For the purpose of this study, only power-law models were explored for both J0317 and J1912 (see Chapter 5) to determine the flux values and to avoid possible overfitting by introducing more complex spectral models because of limited photon statistics. This source model was created with the `LATSourceModel`[34] Python module. The "`Prefactor`" and "`Index`" of J0317 were free parameters during the binned maximum likelihood fitting. A radius of 5° was chosen to free the normalization parameter of sources with a 5σ detection significance. Beyond the radius of 5°, the source parameters in the model were fixed to their 4FGL-DR4 catalog values. The optimization algorithm was set to "`NewMinuit`"[35] and a fit tolerance of `tol=0.0001`. The fit tolerance determines when the fitting is considered to have converged (best-fit parameters were found that maximizes the likelihood) and effectively means that the optimizer will continue until changes in the fit parameters or likelihood is smaller than the specified threshold. The count spectrum and the residuals for the binned likelihood analysis of J0317 in the 0.1-500 GeV energy range is shown in Figures 4.31 and 4.32 respectively.

[34] "https://github.com/physicsranger/make4FGLxml"

[35] "https://fermi.gsfc.nasa.gov/ssc/data/analysis/documentation/Cicerone/Cicerone_Likelihood/Fitting_Models.html"

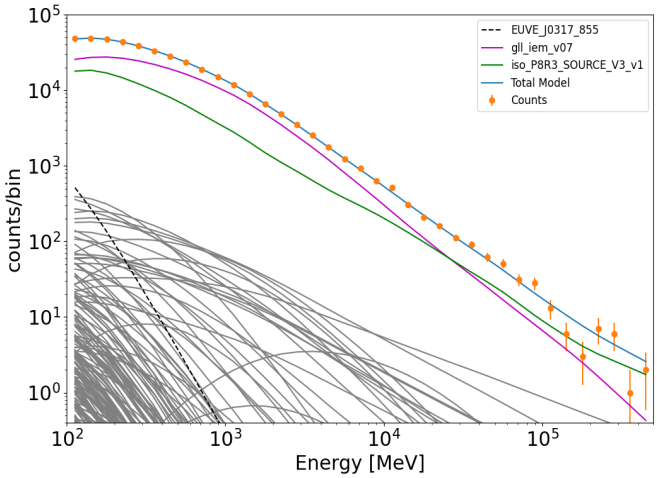

Figure 4.31: Binned likelihood analysis counts spectrum of J0317 (black dashed line) in the energy range 0.1-500 GeV modeled as a simple power law. Galactic diffuse (magenta) and isotropic (green) background models are also shown along with background sources (grey lines) in the ROI.

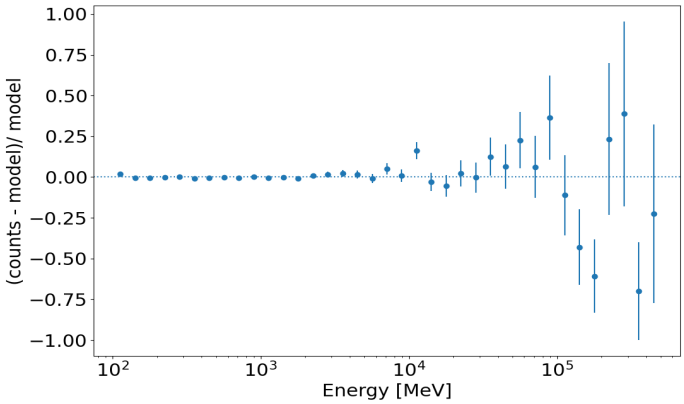

Figure 4.32: Residual fit of the binned likelihood analysis of J0317 in the 0.1-500 GeV range modeled as a simple power law.

Table 4.3 provides the summarized results from the binned likelihood analysis of J0317 in 0.1-500 GeV energy range where N_{pred} is the predicted counts the model predicted and TS is the test statistic (equation 4.23). From these results, it is evident that J0317 is marginally detected with

Spectral Model	Flux (photons/cm^2/s)	N_{pred}	TS	Significance
Power-Law	$(5.02\pm1.48)\times10^{-9}$	1032.33	14.39	3.79σ

Table 4.3: J0317 binned likelihood analysis results in the 0.1-500 GeV energy range.

significance of $\sim3.79\sigma$ which is below *Fermi*-LAT detection threshold of 5σ. To further gauge this marginal significance in the 0.1-500 GeV energy range, binned test statistic (TS) and residual maps were created using `gttsmap`. The best-fit output model was used as the source model. In this source model, all the parameters were fixed except for the isotropic and galactic diffuse sources. The tool `gttsmap` computes a significance map based on the maximum likelihood TS and functions by "moving a putative point source through a grid of locations on the ROI while maximizing the likelihood at each grid point"[36]. New, fainter sources not present in the source model appear at local maxima of the TS map hence J0317 was intentionally removed from the model to see if it is marginally significant above the background. The binned TS and residual map of J0317 is shown in Figure 4.33 below.

From the TS map in Figure 4.33, J0317 (green circle) is only marginally significant above the background in the 0.1-500 GeV energy range. Despite the low significance in the 0.1-500 GeV band, an attempt has been made to construct a "Spectral Energy Distribution" (SED) of J0317. This was achieved using the Python package "FermiPy" (Wood et al. (2017)). The same simple power-law model for J0317 was used to produce the SED in Figure 4.34 below.

The SED in Figure 4.34 shows that most of the flux points are 95% upper limits calculated by FermiPy due to J0317 $\sim3.79\sigma$ detection significance which is below the 5σ. The slope of the butterfly plot corresponds to spectral index $\Gamma= 3.39\pm1.12$. The accompanying histogram shows the Test Statistic (TS) vs Energy in MeV and shows most photons would be detected at lower energies (below $\sim$10 GeV) and so an unbinned likelihood analysis on this energy range was then performed.

[36] "https://fermi.gsfc.nasa.gov/ssc/data/analysis/scitools/likelihood_tutorial.html"

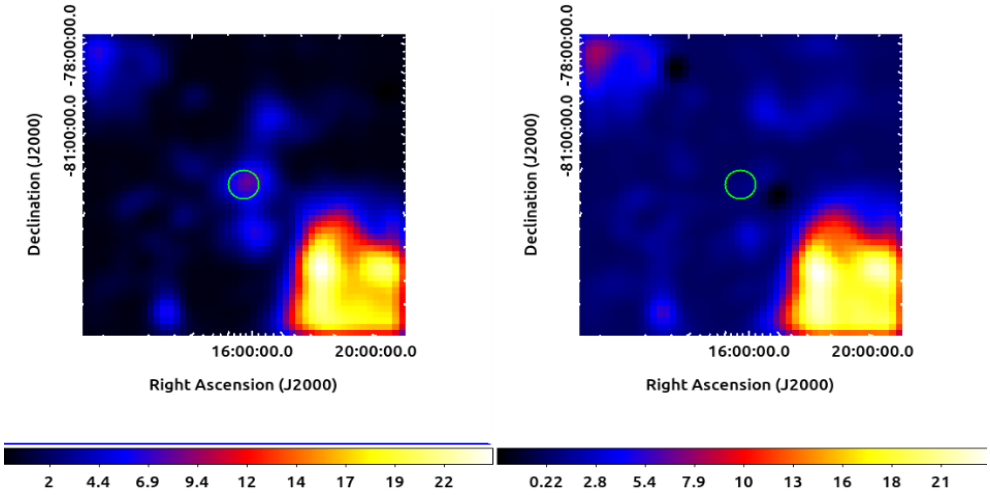

Figure 4.33: 50×50 pixel with 0.25°pixel^{-1} resolution TS Map (left) and residuals map (right) of J0317 (0.6° radius green circle) in the 0.1-500 GeV range. The color bar show the TS value and both images underwent Guassian smoothing with radius 3 and sigma value of 1.

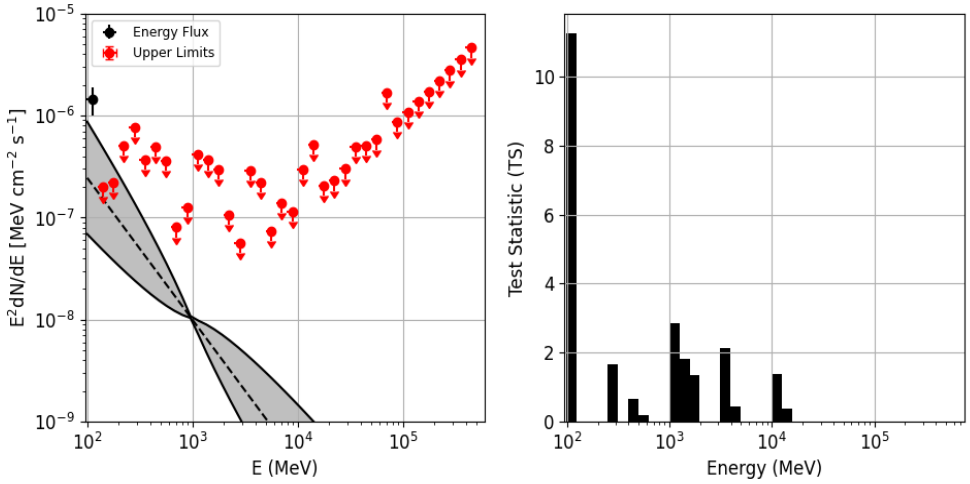

Figure 4.34: Spectral Energy Distribution (SED) of J0317 in 0.1-500 GeV range. Accompanying histrogram shows the Test Statistic (TS) distribution with energy.

Spectral Model	Flux (photons/cm^2/s)	N_{pred}	TS	Significance
Power-Law	$(1.18\pm0.89)\times10^{-10}$	39.71	1.26	1.12σ

Table 4.4: J0317 unbinned likelihood analysis results in 0.5-10 GeV range. The flux represents the integral photon flux.

4.4.4 Unbinned Likelihood Analysis

An unbinned likelihood analysis[37] was conducted on J0317 using 0.5-10 GeV γ-ray data spanning $\sim$15 years (2009-01-01 00:00:00 to 2024-11-05 00:00:00). This likelihood analysis approach is more accurate than the binned analysis because it computes the log-likelihood for each individual γ-ray event and avoids the process of binning events together which results in information loss. This accuracy in the "unbinned" approach comes at the expense of being computationally demanding depending on the number of detected photons. Hence, a smaller "Region Of Interest" ROI=1° (this ROI was kept the same for unbinned analysis for **uniformity** for both J0317 and J1912 (see Chapter 5)) centered on J0317 position (RA=49.31602858°, DEC=-85.54043285°, J2000) was chosen and much of the data selection cuts were held the same as in the binned analysis i.e. "`(DATA_QUAL>0)&&(LAT_CONFIG==1)`" filter for the GTIs, `zmax`=90° to limit γ-rays from Earth's limb etc. The source model included J0317 modeled as a power-law (Equation 4.24) together with background sources in the 4FGL-DR4 catalog including the galactic isotropic diffuse components. The results from the unbinned likelihood analysis is summarized in Table 4.4 below

The unbinned likelihood analysis of J0317 in 0.5-10 GeV revealed a detection significance of $\sim1.12\sigma$ which is beneath the *Fermi*-LAT detection threshold (5σ). Both binned and unbinned likelihood analysis suggest that J0317 might be a very weak γ-ray emitter using the standard analysis techniques. Albeit the low significance of γ-rays in the 0.5-10 GeV band from J0317, a search for **possible low-level γ-ray pulsations from J0317** was carried out.

4.4.5 Periodic Analysis

Searching for periodic signals in sparse γ-ray data can be quite challenging using the traditional method such as the Fourier transforms or Lomb-Scargle techniques. Fortunately, a new method

[37] "https://fermi.gsfc.nasa.gov/ssc/data/analysis/scitools/python_tutorial.html"

has been developed that is especially accustomed to search for pulsations in sparse γ-ray data and this technique is known as the "Rayleigh Test" introduced by Mardia (1972). The Rayleigh test statistic is given by

$$2n\bar{R_l^2} = 2n(\bar{C_l^2} + \bar{S_l^2}) \tag{4.25}$$

where $\bar{C}$ and $\bar{S}$ are the cosine and sine components respectively expressed as

$$\bar{S} = \frac{1}{n}\sum_{i=1}^{n} sin(2\pi l\theta_i) \tag{4.26}$$

$$\bar{C} = \frac{1}{n}\sum_{i=1}^{n} cos(2\pi l\theta_i) \tag{4.27}$$

where n is the number of γ-ray events, l is the harmonic number and θ_i corresponds to the pulse phase of each photon arrival time given by

$$\theta_i = 2\pi frac\left[\phi_0 + \frac{1}{P}(t_i - T_0) + \frac{1}{2}\frac{\dot{P}}{P^2}(t_i - T_0)^2\right] \tag{4.28}$$

where $\dot{P}$ is the period derivative, T_0 gives the reference time, ϕ_0 is the phase offset, P is the rotation period and $frac$ just refers to the fractional part of the term in brackets. From the Rayleigh test statistic, the Rayleigh power ($n\bar{R_l^2}$) can be computed which is half the Rayleigh test statistic and is analogous to the Fourier power in the "Fast Fourier Transform" (FFT) analysis. de Jager, Raubenheimer, and Swanepoel (1989) estimated that the Rayleigh power can be expressed as a function of the signal strength (p) expressed as

$$n\bar{R_l^2} = \frac{np^2}{4} + 1 \tag{4.29}$$

with n the number of data points. In the absence of a periodic signal (uniform distribution), the Rayleigh test statistic ($2n\bar{R_l^2}$) follows the χ^2 probability distribution with two "degrees of freedom" (dof) and the probability that the pulse phase θ_i follows a "uniform distribution" can be expressed

by

$$Pr(> n\bar{R}_l^2) = e^{-n\bar{R}_l^2} \tag{4.30}$$

The peak significance in a Rayleigh power spectrum can then be estimated by taking the logarithm of the probability

$$-Log_{10}(Pr) = 0.434n\bar{R}_l{}^2 \tag{4.31}$$

The Rayleigh test is a powerful method to search for periodicities in sparse and irregularly spaced data because this test works directly on the barycentric corrected photon arrival times. Given the sparsity and low significance of J0317 in the γ-ray regime, the Rayleigh test was performed on the unbinned likelihood analysis data in the 0.5-10 GeV band. A periodic search in this specific energy range was especially chosen because a recent study conducted by Meintjes et al. (2023) revealed that these fast rotating and highly magnetic white dwarfs (AR Scorpii Kaplan (2021), AE Aquarii Madzime (2021)) could emit pulsed γ-ray emission at $\leq$50 GeV.

The unbinned likelihood analysis event file was then used to search for periodic pulsations in γ-rays using the Rayleigh test. First, the ROI was further reduced to ROI=0.6° centered on J0317's position to limit background contamination then the probability that a γ-ray photon from this ROI belongs to J0317 was then calculated using `gtsrcprob`[38] for which only γ-ray photons that have a probability of greater 80% were used to run the Rayleigh test. The *Fermi* Science Tools (version v11r5p3[39]) software package which contains the command `gtpsearch` was used to run the Rayleigh test on the event file. This tool corrects the arrival time of photons to the "solar system barycenter" (SSB) and produces a Rayleigh power spectrum for this high probability photon event file. This tool samples the Rayleigh power around a spin frequency with independently-spaced Fourier frequencies. This concept of "Independent Fourier Spacing" (IFS) is just the value by which independent frequencies are spaced and ensures that significant peaks are not missed. The IFS$\approx 1/T$ where T is the observation baseline. The resultant Rayleigh periodogram of the spin

[38] "https://fermi.gsfc.nasa.gov/ssc/data/p7rep/analysis/scitools/help/gtsrcprob.txt"
[39] "https://fermi.gsfc.nasa.gov/ssc/data/analysis/software/v11r5p3.html"

period of J0317 is shown in Figure 4.35 below.

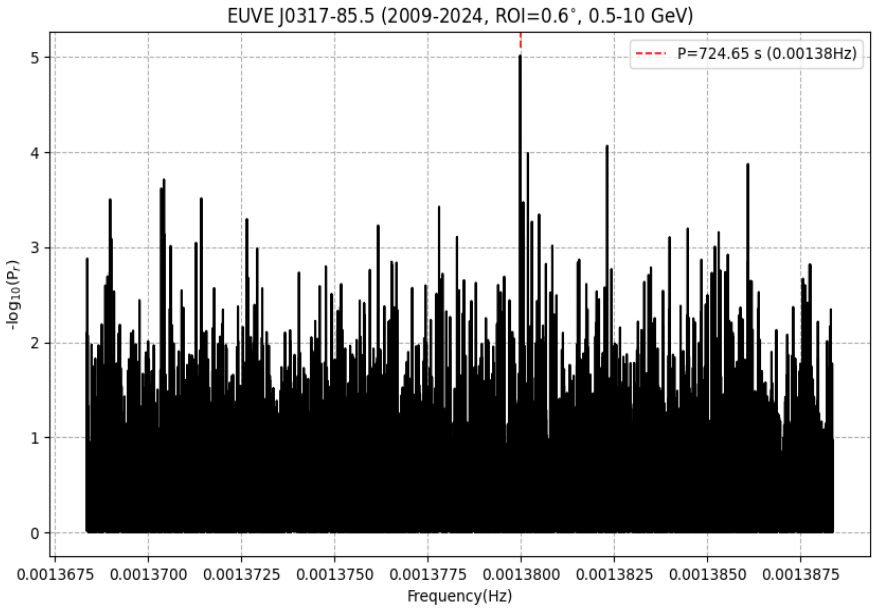

Figure 4.35: Rayleigh Periodogram of J0317 in 0.5-10GeV showing γ-ray pulsations at period P=724.65±0.54s.

This Rayleigh periodogram was produced using a sampling frequency of 2.00×10^{-11} Hz (1% of the Fourier resolution 2.00×10^{-9} Hz) using 1×10^{6} trial frequencies which resulted in a period search range from 720s to 730s. The predominant peak in the Rayleigh periodogram corresponds to a period of P=724.65±0.54s with a -$\log_{10}(P_r)$=5.02 ($\sim4.01\sigma$[40]). This spin period agrees well with what Madzime and Meintjes (2023) found in their initial γ-ray analysis of J0317 (also see Minnie et al. (2024)). The γ-ray events were then folded on this spin period using the spin ephemeris provided by Ferrario et al. (1997) and pulsar timing software package "`TEMPO2`" (version 6.3, Hobbs, Edwards, and Manchester (2006)) with the *Fermi* plug-in. The phase-folded γ-ray light curve of J0317 is shown in Figure 4.36 below.

The phase-folded γ-ray light curve (top left) in Figure 4.36 appears to peak at a spin phase of

[40]Significances are estimated as the standard deviation of the maximum peak compared to the noise level of the periodogram and error on peak are obtained using the bootstrap method

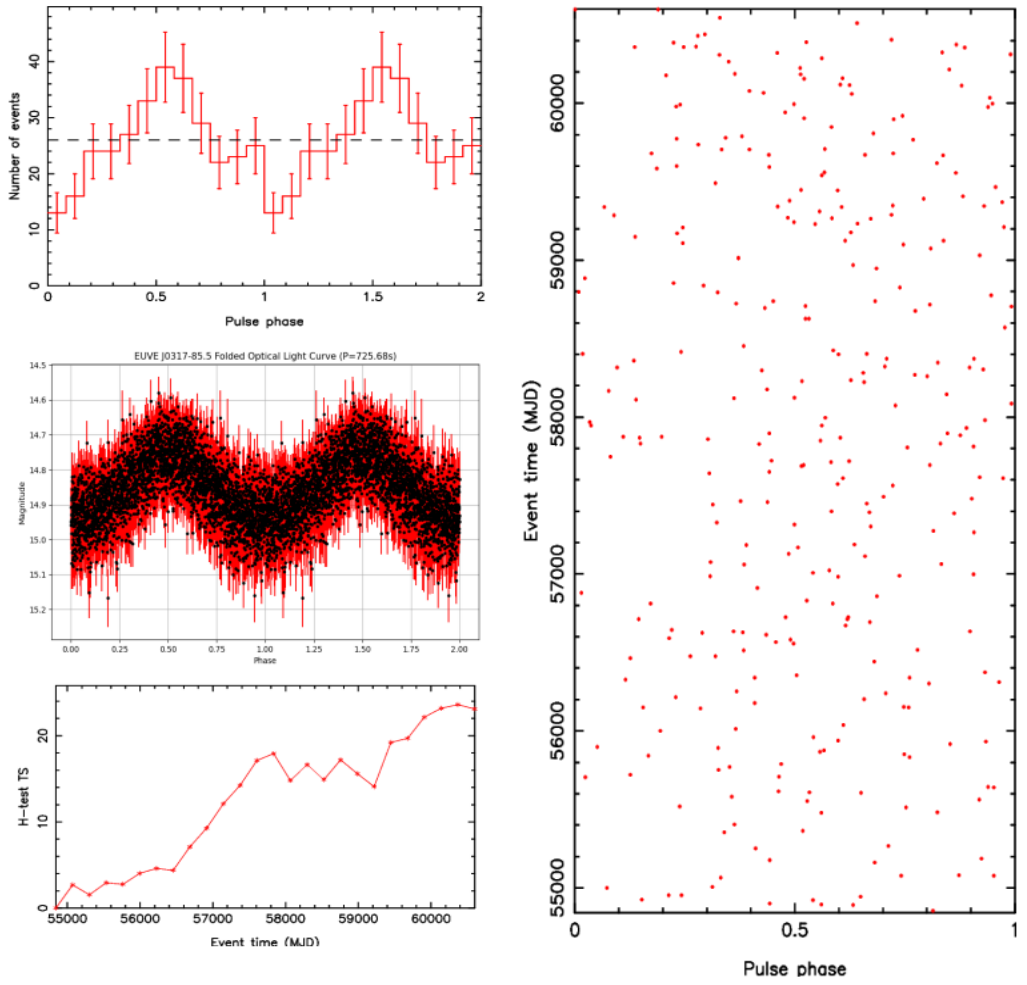

Figure 4.36: J0317 0.5-10GeV folded γ-ray light curve (top left) on spin period P=724.65±0.54s, BOOTES optical phase-folded light curve on the spin period using the same ephemeris (middle), H-test TS diagram (bottom left) and the γ-ray phasogram (right).

∼0.5-0.6 using the ephemeris by Ferrario et al. (1997). The "H-test Test Statistic" (de Jager et al. (1989), de Jager, O. C. and Bsching, I. (2010)) shows an increase in power at the spin period as more data are acquired and reaches a maximum of TS∼23. Using the "H-test Test Statistic", the probability of uniformity scale as Prob(>H)=e$^{-0.4H}$ (see de Jager, O. C. and Bsching, I. (2010)) where H is the maximum "H-test Test Statistic". This TS∼23 has a probability of uniformity of

1.01×10^{-4} which corresponds to a Gaussian significance of $\sim3.72\sigma$. The phasogram just shows the distribution of γ-ray photons with spin phase. There appears to be a second faint peak at spin phase of $\sim$0.9-1.0. We interpret this second faint peak perhaps as the first harmonic of J0317's rotation period. This phase-folded γ-ray light curve is phase-aligned with the optical phase-folded light curve (see Figure 4.36) suggesting possibly that the optical and γ-ray photons are emanating from the same region of J0317. To further confirm this second faint peak in the γ-rays, a Rayleigh periodogram was produced to search for pulsations at the first harmonic of the rotation period and is shown in Figure 4.37 below.

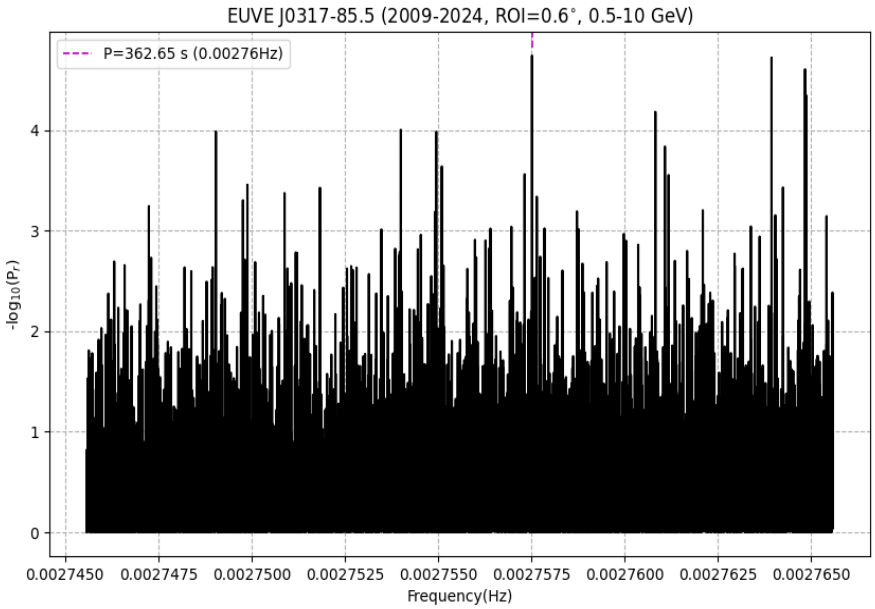

Figure 4.37: Rayleigh Periodogram of J0317 in 0.5-10GeV showing γ-ray pulsations at the first harmonic of the J0317's spin period P=362.65$\pm$0.29s.

The dominant peak in the Rayleigh periodogram is at a period P=362.65$\pm$0.29s with a $-log_{10}(P_r)$ =4.74 ($\sim3.77\sigma$). This peak is not very significant compared to the noise as was evident from its faint visibility in the folded light curve in Figure 4.36. The γ-ray events were then folded on this first harmonic of the J0317's spin period using the same spin ephemeris by Ferrario et al. (1997)

and is shown in Figure 4.38 below.

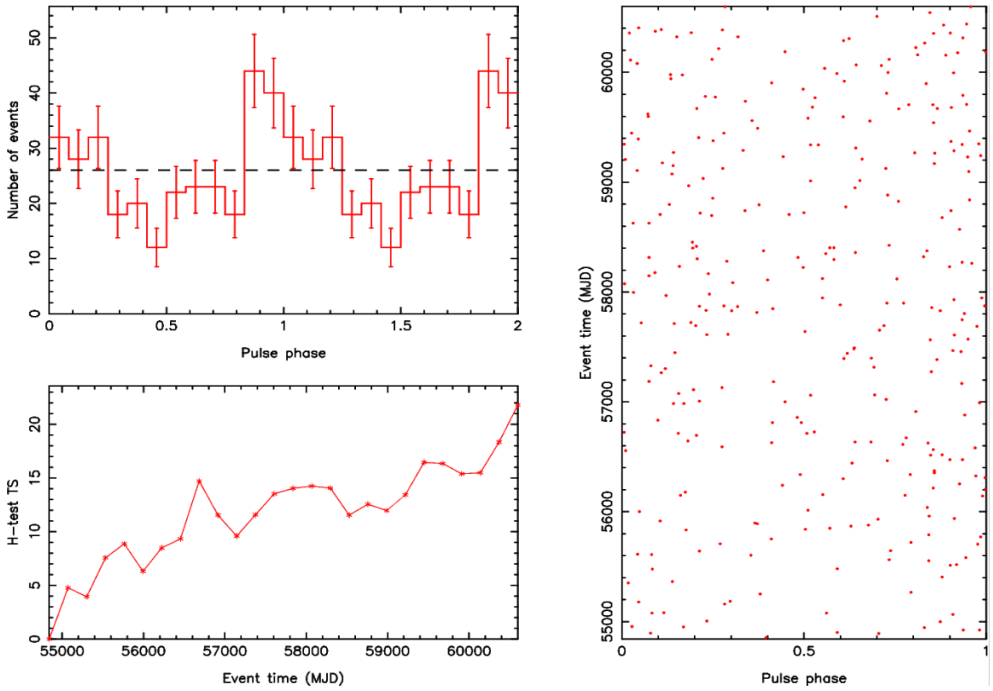

Figure 4.38: J0317 0.5-10GeV folded γ-ray light curve (top left) on first harmonic of the rotation period P=362.65±0.29s using Ferrario et al. (1997) ephemeris along with the H-test TS (bottom left) graph and the phasogram (right).

The phase-folded γ-ray light curve on the first harmonic (see Figure 4.38) of the rotation period is again very noisy but it does peak at a spin phase of ∼0.9-1.0 where it peaked in Figure 4.36 and the H-test test statistic reaches a value of TS∼22 (probability of uniformity ∼1.517×10^{-4} which corresponds to a Gaussian significance of ∼3.61σ). We quote the "H-test Test Statistic" significance as a more robust estimation of significance because it avoids the application of statistical penalties to the periodogram.

Although the standard binned and unbinned likelihood analyses did not reveal significant γ-ray emission from J0317, there does appear to be some low-level pulsed γ-ray emission emanating from J0317. RA and DEC restrictions (see section 5.4.1) were explored for J0317 but resulted in insufficient photons for a reliable periodic analysis. The binned and unbinned analysis were repeated for the respective energy ranges but this time using a more refined technique compared

to the standard analysis.

4.4.6 Test Statistic (TS) Gating

The concept of TS gating was developed by Madzime (2021), Madzime and Meintjes (2023) and references therein in their search for pulsed γ-ray emission from fast spinning, highly magnetized white dwarfs. TS gating is analogous to pulsar gating[41]. In the pulsar gating technique, you only focus on the off-pulse region of the pulsar's phase-folded light curve to enhance the contribution of fainter background sources. In much the same way, after running a likelihood analysis we can only focus on time bins having a positive test statistic (TS>0) and ignore negative TS time bins. By doing this, we can only focus on time bins where *Fermi*-LAT registered significant time tagged γ-ray photons from the ROI in an attempt to enhance the visibility of a weak periodic γ-ray signal compared to the standard binned and unbinned likelihood analysis.

TS Gated Binned Analysis

The same ∼15 years of *Fermi*-LAT data in the 0.1-500 GeV band of J0317 was used for this TS gated binned likelihood analysis. The entire data set was divided into 5-day time bins and then an unbinned analysis was performed on the 5-day time bins. The unbinned analysis was used to assess the TS of each of those 5-day time bins and only the resultant time bins that showed a TS>0 were used for a binned likelihood analysis. The same data selection cuts for each 5-day time bin were used as in the standard binned likelihood analysis (see section 4.4.3). A binned 2D TS gated counts map is shown in Figure below

Compared to the counts map in Figure 4.30, there appears to be more counts coming from J0317 region (green circle) in Figure 4.39. J0317 was again modeled by power-law model (equation 4.24) with sources from the 4FGL-DR4 catalog included in the source model along with the isotropic and galactic diffuse components. The normalization parameters of source within a 5° radius from J0317 having a TS>25 were treated as free parameters while fixing the parameters of sources beyond 5° to their 4FGL-DR4 catalog values. The counts spectrum (Figure 4.40) and the residuals (Figure

[41] "https://fermi.gsfc.nasa.gov/ssc/data/analysis/scitools/pulsar_gating_tutorial.html"

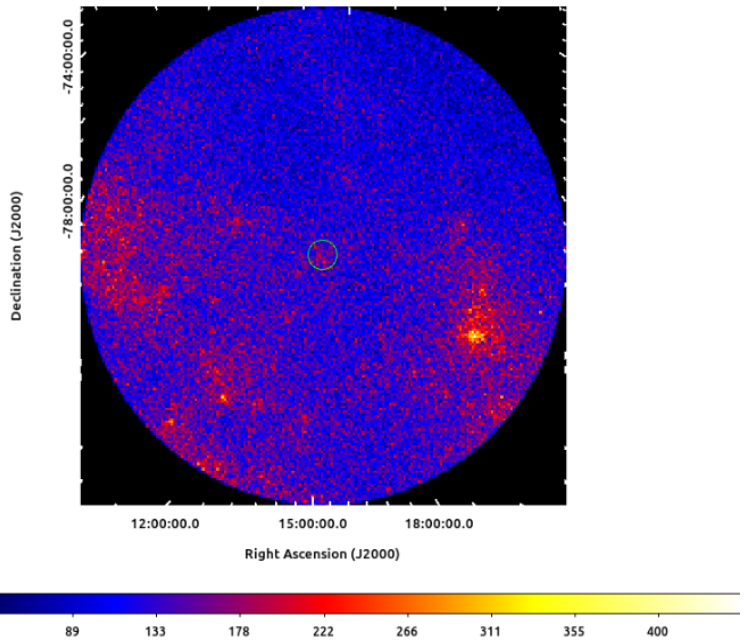

Figure 4.39: 0.1-500 GeV 200×200 pixel TS gated counts map with 0.1° per pixel resolution of J0317 (0.6° radius green circle). The color bar displays the counts per pixel value.

4.41) of the TS gated binned likelihood analysis is shown below.

From Figure 4.41, it is evident that the power-law model satisfactorily describes the emission from J0317 and becomes less efficient above ∼10 GeV evident from the scatter in the residuals. Table 4.5 below provides the results from the TS gated binned likelihood analysis.

This is an increase in the significance compared to the normal binned likelihood analysis as shown in Table 4.3. To further confirm this attempt at improving the visibility of J0317, binned

Spectral Model	**Flux (photons/cm^2/s)**	N_{pred}	**TS**	**Significance**[1]
Power-Law	$(2.95\pm0.22)\times10^{-8}$	3961.81	293.17	17.12σ

Table 4.5: J0317 TS gated binned likelihood analysis results in the 0.1-500 GeV band.The flux represents is the integral photon flux.

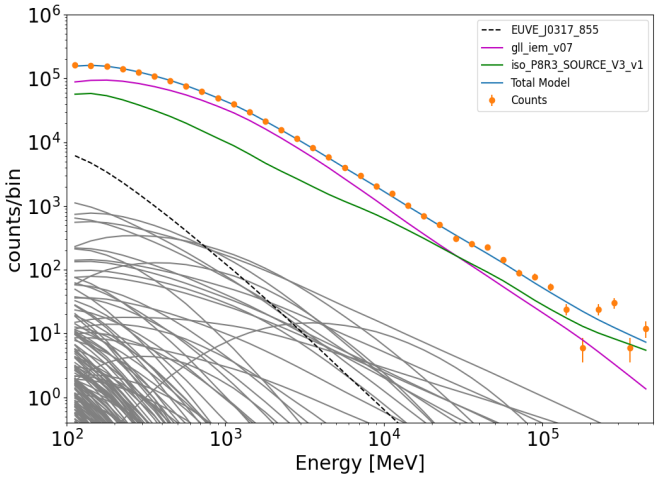

Figure 4.40: TS gated binned likelihood analysis counts spectrum of J0317 (black dashed line) in the 0.1-500 GeV energy range modeled as a simple power law. Isotropic (green) and galactic diffuse (magenta) background models are also shown along with background sources (grey lines) in the ROI.

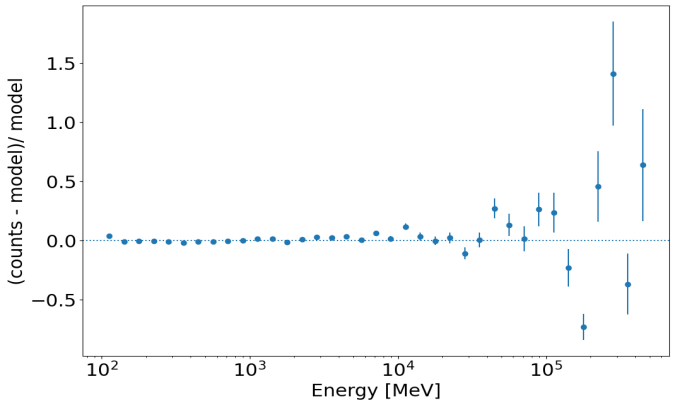

Figure 4.41: TS gated residual fit of the binned likelihood analysis of J0317 in the 0.1-500 GeV range modeled as a simple power law.

TS and residual maps were created and is shown in Figure 4.42 below.

From the TS map, it can be seen that the TS gating method improves the visibility of J0317

[1]NOT the TRUE significance but an attempt to improve the visibility of J0317 with TS gating method.

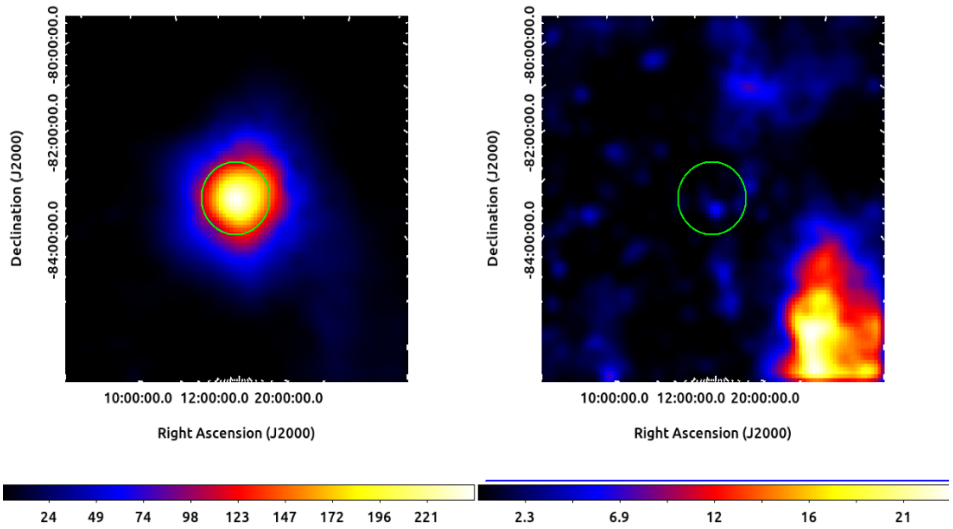

Figure 4.42: 0.1-500 GeV 100×100 pixel binned TS gated TS (left) and residual (right) map with 0.1° per pixel resolution of J0317 (1° radius green circle). TS value is shown by the color bar and smoothing of the maps were done with a σ=1.5 Gaussian kernel.

in the γ-rays. The residual map is generally flat in TS space but some bright sources may appear in the residual map and these are sources that are not in the source model and hence not in the 4FGL-DR4 catalog. A spectral energy distribution (SED) for the TS gated data was then produced using FermiPy with 9 energy bins per decade to take into consideration the sparseness of the γ-ray data. J0317's SED is shown in Figure 4.43 along with the TS distribution with energy. The upper limits in the SED corresponds to 95% confidence interval when data points have a TS<4.

From the SED in Figure 4.43, it is clear that the power-law model describe J0317's emission well below ∼10 GeV and the slope of the fitted line i.e. the spectral index is Γ=3.26±0.20. The histogram also shows that the emission is mostly produced below ∼10 GeV.

This TS gated method clearly increases the visibility of these faint sources that would otherwise be missed using the standard analysis techniques. The same procedure was performed by using the unbinned likelihood analysis on the TS gated data of J0317 in the 0.5-10 GeV band.

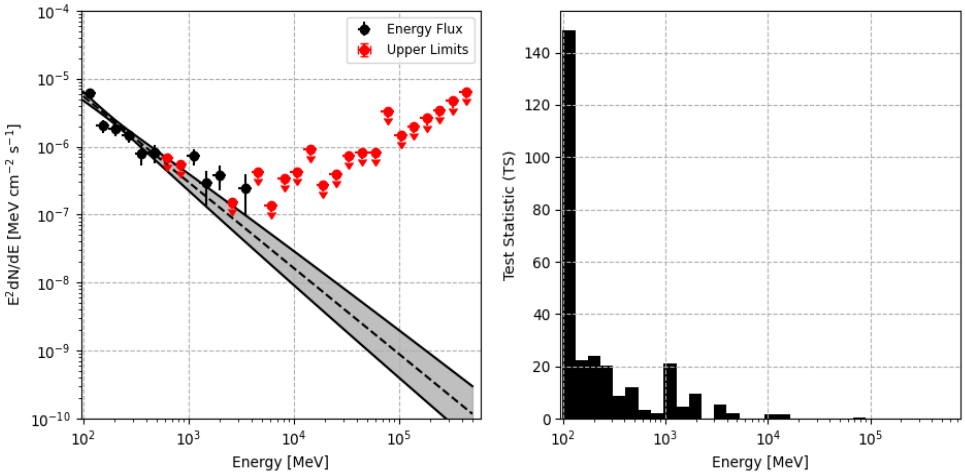

Figure 4.43: Spectral Energy Distribution (SED) of J0317's TS gated data in the 0.1-500 GeV range. Accompanying histogram shows the Test Statistic (TS) distribution with energy.

Spectral Model	**Flux (photons/cm^2/s)**	N_{pred}	**TS**	**Significance^2**
Power-Law	$(4.27\pm0.35)\times10^{-9}$	448.03	257.49	16.05σ

Table 4.6: J0317 TS gated unbinned likelihood analysis results in energy range 0.5-10 GeV. The flux represents the integral photon flux.

4.4.7 TS Gated Unbinned Analysis

TS gating analysis was then performed on the 0.5-10 GeV energy band using a ROI=1° centered around J0317's position and again only the 5-day time bins that showed positive TS (TS>0) were used to perform an unbinned likelihood analysis while keeping the standard data selection cuts recommended by *Fermi*-LAT the same. The TS gated unbinned analysis results are shown in Table 4.6.

The improved visibility is also observed in the unbinned likelihood analysis using the TS gated data in the 0.5-10 GeV band compared to the standard unbinned likelihood analysis (see Table 4.4). This high visibility was then confirmed by producing unbinned TS and residual maps using `gttsmap` along with the best-fit source model. The best-fit source model contains the optimized parameters of J0317 and the other sources' optimized parameters that were left as free parameters

during the fitting. J0317 was intentionally omitted from the model to produce the unbinned TS map. The unbinned TS and residual map is shown in Figure 4.44 below.

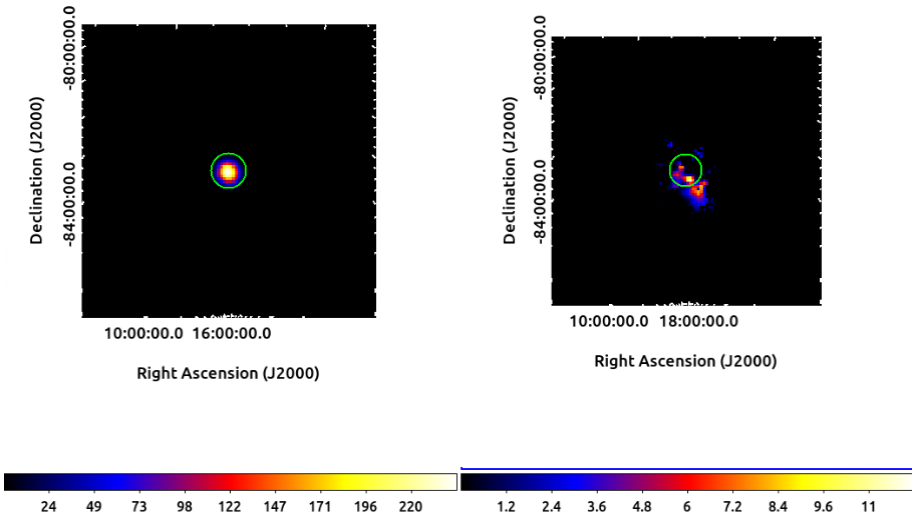

Figure 4.44: 0.5-10 GeV 100×100 pixel unbinned TS gated TS (left) and residual (right) map with 0.1° per pixel resolution of J0317 (0.6° radius green circle). TS Value is shown by the color bar.

The TS map of the TS gated data clearly shows the visibilty of J0317 in the γ-ray band. The residual map does show some background emission near the vicinity of J0317 but at a low significance. Because of the visibility of J0317 using the TS gated method, an unbinned likelihood analysis SED was created for the 0.5-10 GeV energy range using the `pyLikelihood`[42] Python script. This is shown in Figure 4.45 where Γ=3.23±0.21 is the spectral index which signifies emission at lower energies. The TS distribution with energy is also shown to confirm this emission at lower energies (<10 GeV).

[2]NOT the TRUE significance but an attempt to improve the visibility of J0317 with TS gating method.

[42]"https://github.com/fermi-lat/pyLikelihood"

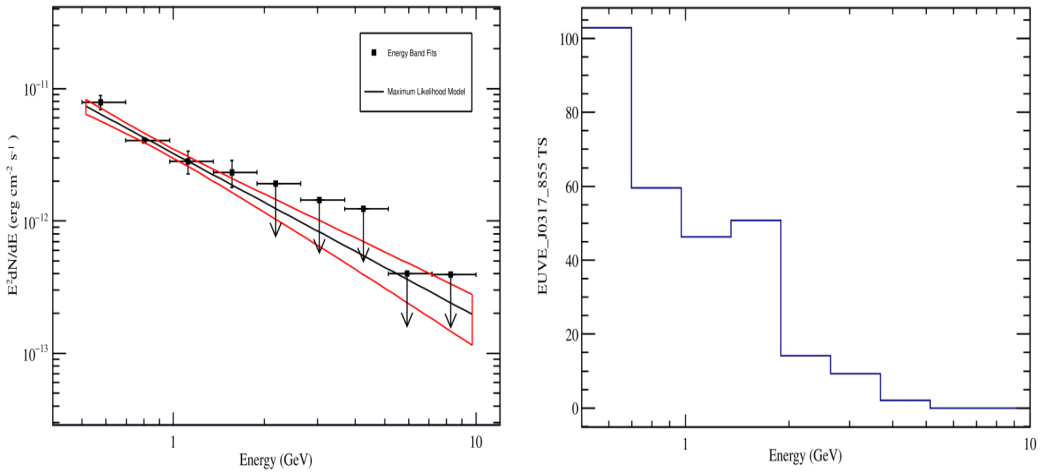

Figure 4.45: Spectral Energy Distribution (SED) of J0317's TS gated data in the 0.5-10 GeV range. Accompanying histogram shows the Test Statistic (TS) distribution with energy.

4.4.8 Periodic Analysis

The Rayleigh test was utilized to search for pulsations using this TS gated event file. The probability that each photon originates from J0317's position was calculated using `gtsrcprob` for which only γ-ray photons having a probability of greater than 80% were kept to search for γ-ray pulsations. The Rayleigh periodogram is shown in Figure 4.46 below.

The predominant peak in the periodogram is at a period of P=724.65$\pm$0.56s with a -$\log_{10}$(P$_r$)=4.60 ($\sim$3.60σ). This periodogram looks much noisier compared to the one produced for the normal unbinned analysis in Figure 4.35 and that can be explained if one looks at the residual map (Figure 4.44) of J0317's region where there are still background emission emanating from it. The γ-ray events were then folded on this spin period using the spin ephemeris provided by Ferrario et al. (1997) which is shown in Figure 4.47 below. H-test TS$\sim$21 which gives $\sim$3.50σ in the Gaussian distribution.

The phase-folded light curve of the TS gated data on the highest peak in the Rayleigh periodogram reveals that it is still phase-aligned with the BOOTES optical light curve (see Figure

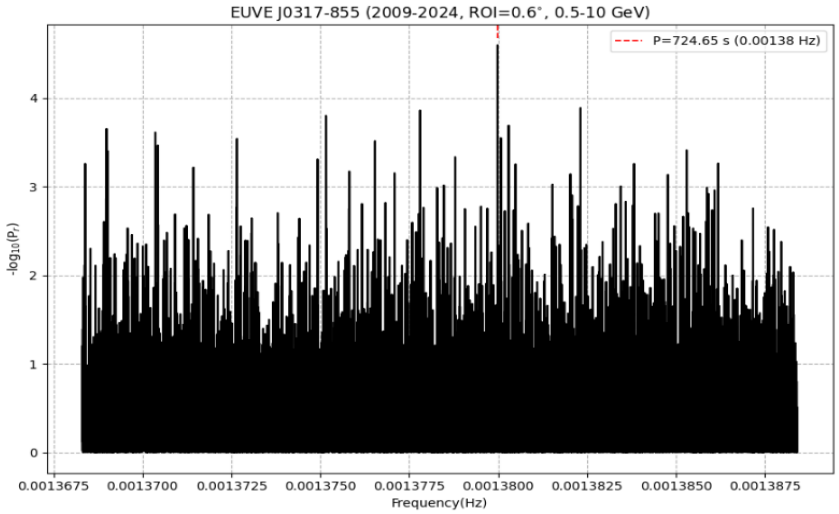

Figure 4.46: Rayleigh Periodogram of the TS gated data of J0317 in 0.5-10 GeV showing γ-ray pulsations at period P=724.65±0.56s.

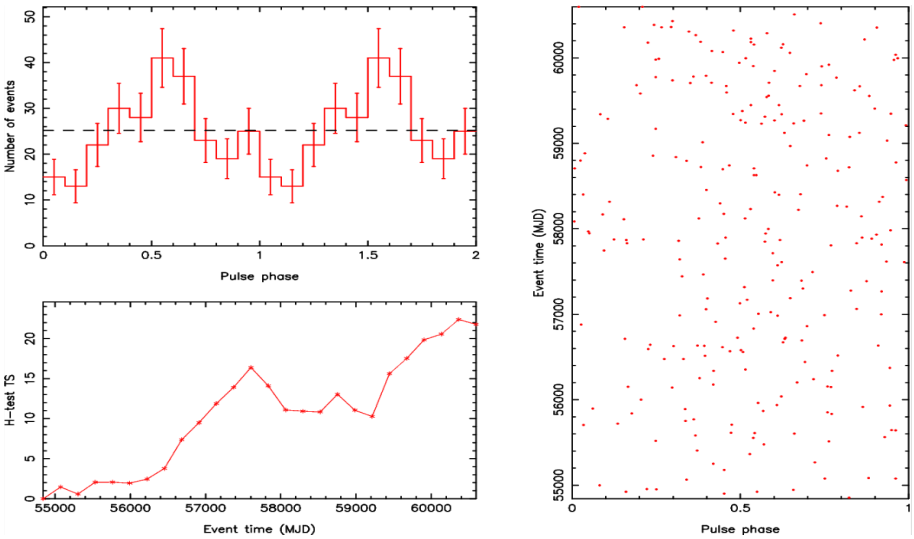

Figure 4.47: J0317 TS gated 0.5-10 GeV folded γ-ray light curve (top left) on first harmonic of the spin period P=725.65±0.56s using Ferrario et al. (1997) ephemeris along with the H-test TS (bottom left) graph and the phasogram (right).

4.9) and there is still a sliver of a peak at a spin phase of ∼0.9-1.0 which we interpret as the first harmonic of the J0317's rotation period. We attribute this low-level γ-ray pulsation at energy <10

GeV to the curvature radiation process (see Appendix F.4 for a discussion on the curvature radiation mechanism) where electrons get extracted from J0317's surface due to the relatively high spin period (∼12 min) and very high $\boldsymbol{B}$-field (∼450 MG). The electrons quickly lose their perpendicular velocity component with respect to the $\boldsymbol{B}$-field in a time interval of τ_{sync}∼10^{-10} s (Meintjes et al. (2023)) and cease to spiral along the $\boldsymbol{B}$-fields. These electrons then glide along the $\boldsymbol{B}$-field lines emitting γ-rays modulated at the spin period of J0317. The reader is referred to Appendix B and C for control tests done on sourceless regions away from J0317 to test the validity of the methods used in this section.

The following chapter deals with the *Fermi*-LAT γ-ray analysis of the binary system J1912.

Chapter 5

Fermi-LAT γ-ray Analysis of J1912

Since J1912 was discovered quite recently, there has been no analysis done on J1912 in the γ-ray energy band. J1912 is a white dwarf binary system containing an M4.5$\pm$0.5 secondary star in a $\sim$4.03 hour orbit. The white dwarf in this binary system rotates at period of P_{spin}=319.34903(8)s (Pelisoli, Marsh, et al. (2023)) and has a magnetic ($\boldsymbol{B}$) field strength of $\leq$50 MG (Pelisoli, Sahu, et al. (2023)). See section 3.2 for a thorough background of J1912.

The chapter is outlined as follows:

- In section 5.1, aperture photometry is performed on the retrieved *Fermi*-LAT data and light curves (0.1-500 GeV and 0.5-10 GeV) are extracted on which a periodic analysis is performed using the generalized Lomb-Scargle technique.
- Section 5.2 describes the binned maximum likelihood analysis on the 0.1-500 GeV energy band to get a sense of where in this energy range possible γ-rays from J1912 might emanate from.
- In section 5.3, an unbinned maximum likelihood analysis is conducted on the 0.5-10 GeV range since the binned likelihood analysis revealed that most of the γ-ray emission comes from energies $\leq$10 GeV. As mentioned in section 4.4.2, an unbinned analysis is more accurate than the binned approach because it treats each photon individually without binning them which might result in a loss in information. The accuracy of the unbinned likelihood analysis

does come at an expense of being more computationally intensive as the number of photons increase.

- In section 5.4, a periodic analysis is conducted on the unbinned likelihood analysis *Fermi*-LAT data in the 0.5-10 GeV since most of the γ-ray emission might come from this range and a recent study conducted by Meintjes et al. (2023), revealed that these fast spinning, highly magnetic white dwarfs might emit pulsed γ-ray emission in this energy range.

- A new method is introduced in section 5.4.1 called RA and DEC restriction to gauge the periodic behaviour of J1912 in the γ-ray waveband. RA and DEC restrictions were explored for the isolated white dwarf J0317 but the restrictions resulted in insufficient γ-ray photons for a reliable periodic analysis.

- Sections 5.5 and 5.6 describe respectively, the binned and unbinned likelihood analysis of J1912 using the TS gating method in an attempt to increase the visibility of J1912.

- A periodic analysis using the Rayleigh test in 5.7 is performed on the TS gated unbinned data and the RA and DEC restrictions are applied to this TS gated unbinned on which a periodic analysis is performed.

- The validity of the TS gating method on J1912 is also tested on sourceless regions away from J1912's coordinates and is given in Appendices D and E.

5.1 Aperture Photometry

Aperture photometry was performed using ∼15 years (2009-01-01 00:00:00 to 2024-11-05 00:00:00) of *Fermi*-LAT data in the 0.1-500 GeV and 0.5-10 GeV energy range on J1912's position with RA=288.057166° and DEC=-44.17919007° (J2000). Using `gtselect`, only photons from a "Region Of Interest" ROI=0.6° centered on J1912's position was considered to limit background γ-ray emission. The GTIs were calculated using `gtmktime` and these events were binned at 10 seconds using `gtbin`. To calculate the exposure of each time bin, a spectral index of -2.1 was used since the spectral index of J1912 in γ-rays is not known and this value provides a good estimate for most

faint γ-ray sources. And the photon arrival times were barycentric corrected using `gtbary`. The 0.1-500 GeV 10 second bin light curve of J1912 is shown in Figure 5.1 below

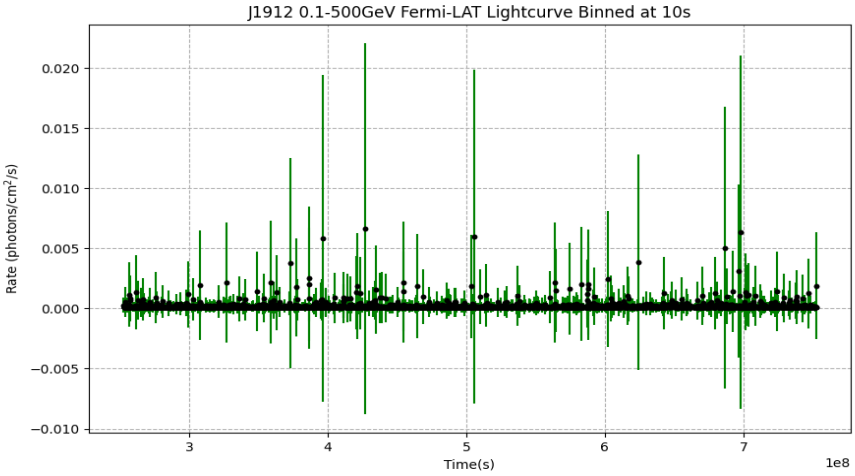

Figure 5.1: J1912 *Fermi*-LAT 0.1-500GeV γ-ray aperture photometry light curve binned at 10 seconds.

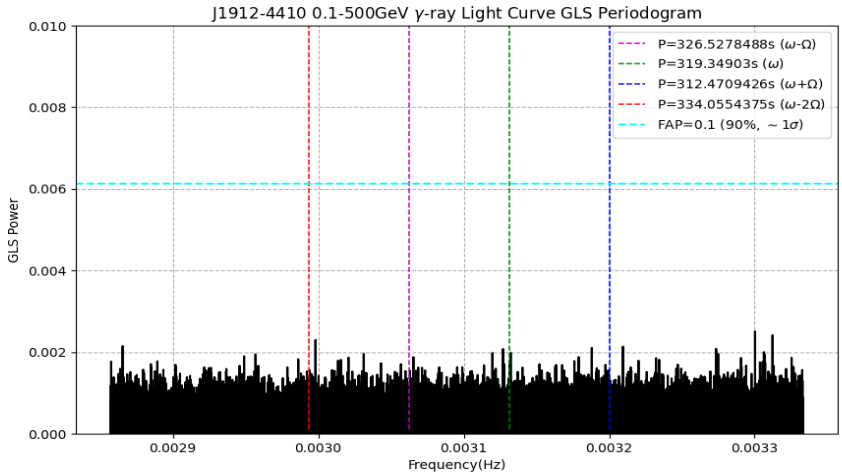

Figure 5.2: GLS periodogram of 0.1-500 GeV γ-ray light curve in Figure 5.1 showing no significant pulsation at the spin period $P\sim$319.34s or at the other orbital side-band frequencies.

A GLS periodogram of Figure 5.2 was then performed using a frequency range of ∼0.00333-0.00286 Hz to include the spin frequency of J1912 as well as the orbital side-band frequency because J1912 is known to emit pulsed emission at those orbital side-band frequencies (see Pelisoli, Marsh, et al. (2023), Pelisoli, Sahu, et al. (2023) and Schwope, A. et al. (2023)). The GLS periodogram of J1912 is shown in Figure 5.4.

A 10 second binned light curve of the 0.5-10 GeV energy band and respective GLS periodogram was also created and is shown in Figures below

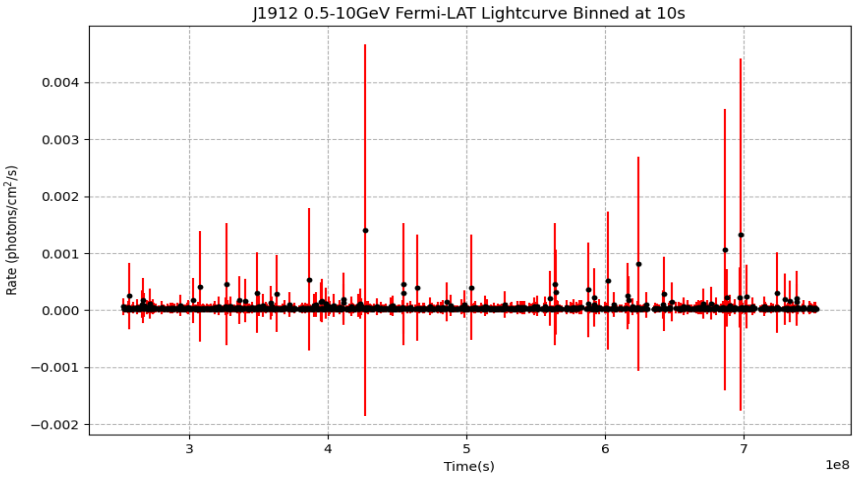

Figure 5.3: J1912 *Fermi*-LAT 0.5-10GeV γ-ray aperture photometry light curve binned at 10 seconds.

From both GLS periodograms, it is evident that there are no significant (not a single peak crosses the $\sim 1\sigma$ line) pulsations at the spin period or at the other orbital side-band frequencies of J1912 but as mentioned in Chapter 5, aperture photometry does not take the background into account and for this a likelihood analysis is needed.

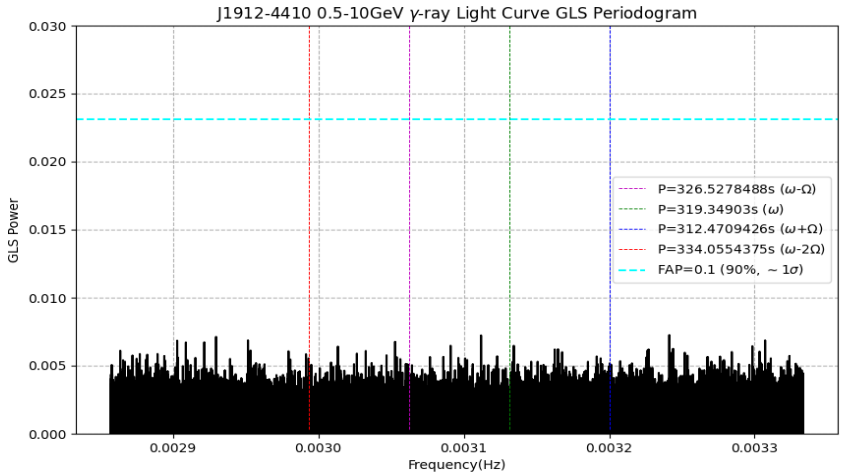

Figure 5.4: GLS periodogram of 0.5-10 GeVγ-ray light curve in Figure 5.3 showing no significant pulsation at the spin period $P\sim$319.34s or at the other orbital side-band frequencies.

5.2 Binned Likelihood Analysis

A binned maximum likelihood analysis[1] was then performed on J1912 using $\sim$15 years of *Fermi*-LAT γ-ray data spanning 2009-01-01 00:00:00 to 2024-11-05 00:00:00 and using a ROI=10° to account for *Fermi*-LAT's broader "Point-Spread Function" (PSF) at lower energies (the PSF becomes narrower at higher energies). The energy range for binned likelihood analysis was 0.1-500 GeV. The event files were combined into one file using `gtselect` for which only "SOURCE class" events "`evclass=128`" together with event type "`evtype=3`" (for events converting at both the BACK and FRONT of the telescope tracker). A zenith angle value of "`zmax`=90°" was chosen to limit γ-ray emission from Earth's limb. Then, good time intervals (GTIs) were then obtained using `gtmktime` along with filter expression "`(DATA_QUAL>0)&&(LAT_CONFIG==1)`". A 2D counts map (Figure 5.5) was then created for J1912 using `gtbin` to see the contribution of other sources in the ROI.

The photons were binned into a 14.14°×14.14° region with 0.1° per pixel resolution using 37 logarithmically uniform energy bins ($\sim$10 logarithmically spaced bins per decade) to create a 3D counts

[1] https://fermi.gsfc.nasa.gov/ssc/data/analysis/scitools/binned_likelihood_tutorial.html

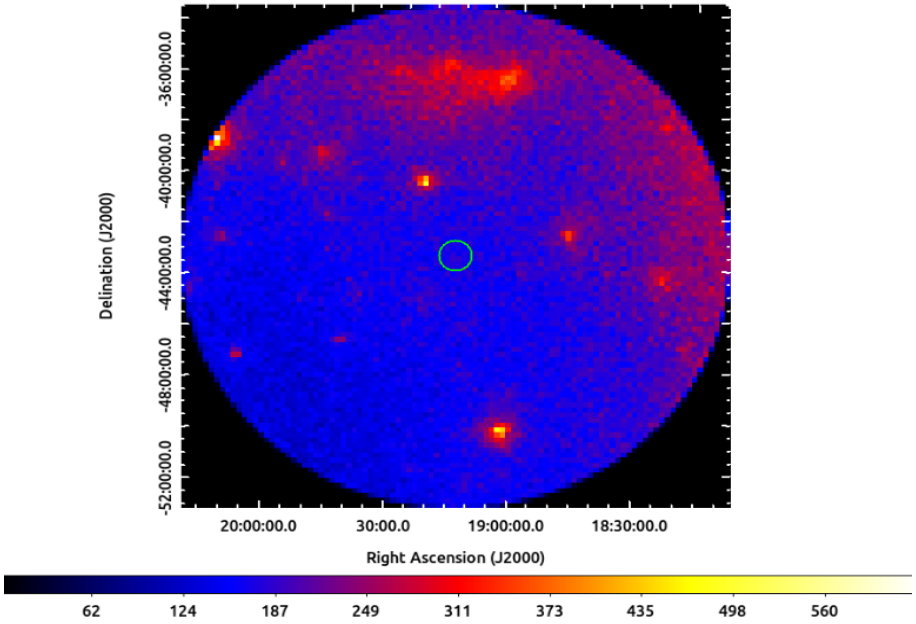

Figure 5.5: 0.1-500 GeV 200×200 pixel counts map with 0.1° per pixel resolution of J1912 (0.6° radius green circle). The color bar displays the counts per pixel value.

cube utilizing the `CCUBE` option in `gtbin`. The "Galactic diffuse background `gll_iem_v07.fits`" and isotropic background emission "`iso_P8R3_SOURCE_V3_v1.txt`" [2] was used and the spatial and spectral model for all the γ-ray sources in the ROI was created using the "4FGL Data Release 4 catalog" (4FGL-DR4, Ballet et al. (2024)) and J1912 was manually added to the source model and was modeled as a simple power law (equation 4.24). The "`Prefactor`" and "`Index`" of J1912 were treated as free parameters during the binned maximum likelihood fitting. A radius of 5° was chosen to free the normalization parameter of sources with a 5σ detection significance. Beyond the radius of 5°, the parameters of γ-ray sources were fixed to their catalog values. The optimization algorithm was set to `NewMinuit`[3] and a fit tolerance of `tol=0.0001`. The count spectrum and the residuals for the binned likelihood analysis of J1912 in the 0.1-500 GeV energy range is shown in Figure 5.5 and 5.7 respectively.

[2] "https://fermi.gsfc.nasa.gov/ssc/data/access/lat/BackgroundModels.html"

[3] "https://fermi.gsfc.nasa.gov/ssc/data/analysis/documentation/Cicerone/Cicerone_Likelihood/Fitting_Models.html"

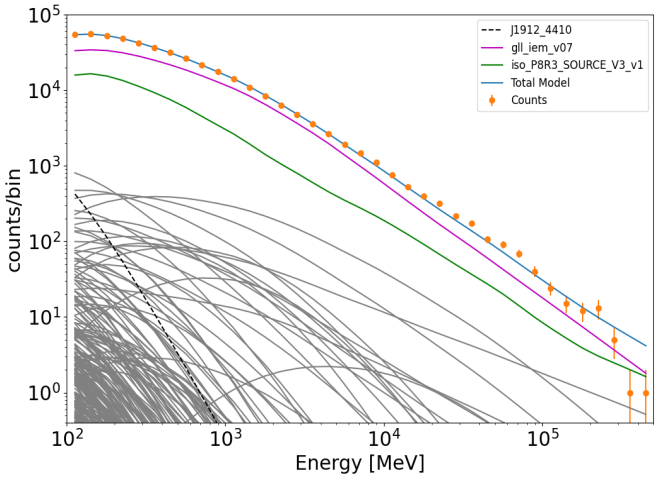

Figure 5.6: Binned likelihood analysis counts spectrum of J1912 (black dashed line) in the 0.1-500 GeV energy band modeled as a simple power law. Galactic diffuse (magenta) and isotropic (green) background models are also shown along with background sources (grey lines) in the ROI.

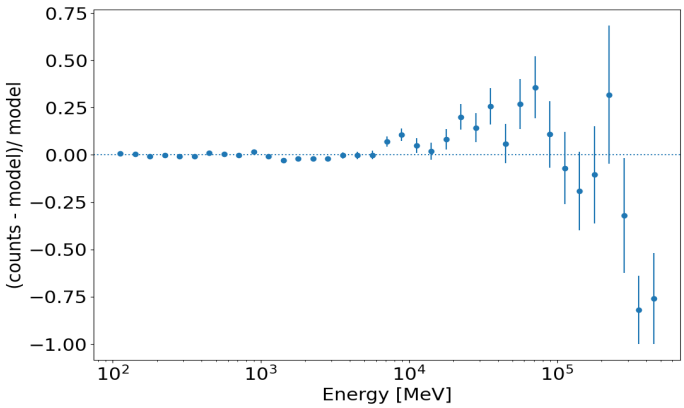

Figure 5.7: Residual fit of the binned likelihood analysis of J1912 in the 0.1-500 GeV energy band modeled as a simple power law.

The residuals (Figure 5.7) shows that the power law model adequately describes the emission from J1912 at energies <10 GeV. The results from the binned analysis is shown in Table 5.1.

Using the binned likelihood analysis reveals that J1912 is marginally detected at a significance

Spectral Model	Flux (photons/cm^2/s)	N_{pred}	TS	Significance
Power-Law	$(4.40\pm1.80)\times10^{-9}$	831.83	7.89	2.81σ

Table 5.1: J1912 binned likelihood analysis results in 0.1-500 GeV energy band. The flux represents the integral photon flux.

of $\sim2.81\sigma$ which is below the 5σ detection threshold set by *Fermi*-LAT. Binned TS and residual maps of J1912 were then created using `gttsmap` which is shown in Figure 5.8 below.

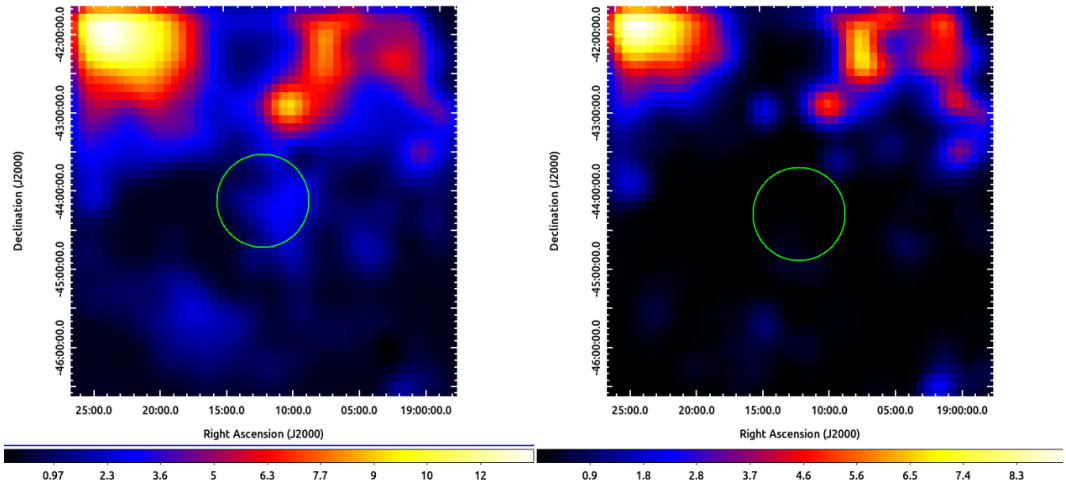

Figure 5.8: 50×50 pixel with 0.1°pixel^{-1} resolution binned TS Map (left) and residuals map (right) of J1912 (0.6° radius green circle) in the 0.1-500 GeV energy band. The color bar displays the TS value with the images smoothed with Gaussian kernel of radius 3 and sigma value of 1.

The binned TS map shows that J1912 is not really significant above the background which is clear based on its overall detection significance. A spectral energy distribution (SED) of J1912 in the 0.1-500 GeV range was created with FermiPy (Wood et al. (2017)) despite the low detection significance and is shown in Figure 5.9 below along with the TS distribution with energy.

The SED of J1912 is littered with 95% upper limits as was expected from its low detection significance ($\sim2.81\sigma$). FermiPy was unable to plot a butterfly plot due to this low significance. The TS distribution also show that J1912 might be emitting γ-ray at lower energies and so an unbinned analysis was performed on the 0.5-10 GeV range.

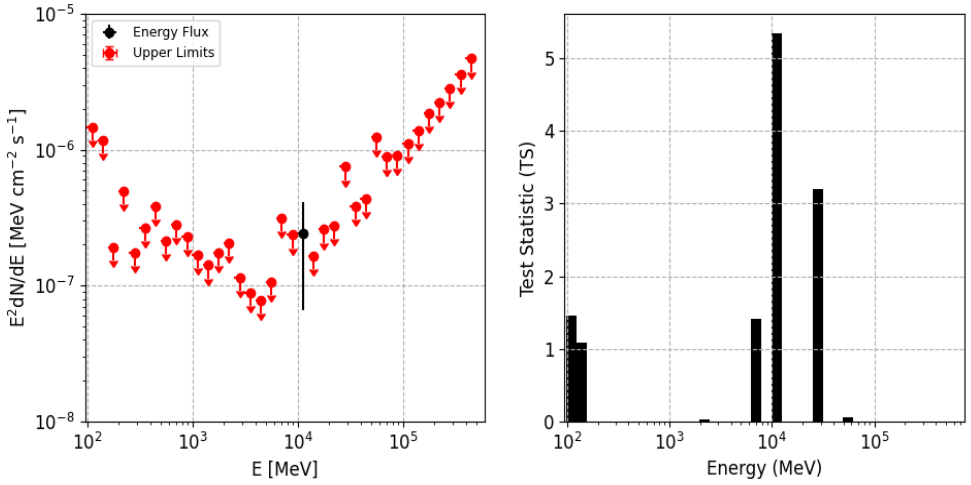

Figure 5.9: SED of J1912 in 0.1-500 GeV band. Accompanying histrogram shows the Test Statistic (TS) distribution with energy.

Spectral Model	**Flux (photons/cm^2/s)**	N_{pred}	**TS**	**Significance**
Power-Law	$(2.98\pm1.44)\times10^{-10}$	102.00	5.43	2.33σ

Table 5.2: J1912 unbinned likelihood analysis results in the 0.5-10 GeV energy band. The flux represents the integral photon flux.

5.3 Unbinned Likelihood Analysis

An unbinned likelihood analysis was conducted on J1912 using 0.5-10 GeV γ-ray data spanning $\sim$15 years (2009-01-01 00:00:00 to 2024-11-05 00:00:00). A small ROI=1° (to limit the background γ-ray emission and because *Fermi*-LAT PSF becomes narrower at higher energies (Atwood et al. (2009))) centered on J1912 position (RA=288.057166°, DEC=-44.17919007°, J2000) was chosen and much of the data selection cuts were held the same as in the binned analysis i.e. "`(DATA_QUAL>0)&&(LAT_CONFIG==1)`" filter for the GTIs, "`zmax`=90°" to limit γ-rays from Earth's limb etc. The source model included J1912 modeled as a power-law (Equation 4.24) together with background sources from the 4FGL-DR4 catalog including the isotropic and galactic diffuse components. The results from the unbinned likelihood analysis are summarized in Table 5.2.

The unbinned likelihood analysis of J1912 in the 0.5-10 GeV band also reveals no significant

γ-ray emission above the 5σ detection threshold. This low significance of $\sim 2.33\sigma$ might suggest low level γ-ray emission coming from J1912. A search for periodicities were conducted in the 0.5-10 GeV band of J1912 using the Rayleigh test (see section 4.4.5).

5.4 Periodic Analysis

The unbinned likelihood analysis event file was used perform a Rayleigh test on the photon arrival times. The probability that the photons originate from J1912 was calculated using `gtsrcprob` and only photons having a probability >80% were kept for periodic analysis. The region of interest were further reduced to ROI=0.6° to further limit spurious background emission. The tool `gtpsearch` was used to perform the Rayleigh test. This tool performs on-the-fly barycentric corrections of the photon arrival times. A sample frequency of 2.00×10^{-11} Hz (1% of the Fourier resolution of 2.00×10^{-11} Hz) which resulted in search range between ∼316-322 seconds. The spin ephemeris "BJD(TDB) = 2459772.142522(24) + 0.0036961693(10)E" provided by Pelisoli, Marsh, et al. (2023) was used as reference time to compute the phases of the photon arrival times. The Rayleigh periodogram of J1912 in the 0.5-10 GeV energy band is shown in Figure 5.10 below along with a zoomed-in version around the spin period shown in Figure 5.11. The γ-ray photons were then folded onto the spin period P=319.34903s of J1912 using the Pelisoli, Marsh, et al. (2023) and "`TEMPO2`" (Hobbs et al. (2006)). The phase-folded γ-ray light curve of J0317 is shown in Figure 5.12 along with the "H-test Test Statistic" (TS) and the phasogram. Although the folded γ-ray light curve on the spin period P=319.34903s show some signatures of pulsed behavior, the "H-test TS" (de Jager et al. (1989), de Jager, O. C. and Bsching, I. (2010)) reveals that it is insignificant and the TS reaches a value of TS∼5 (see Figure 5.12).

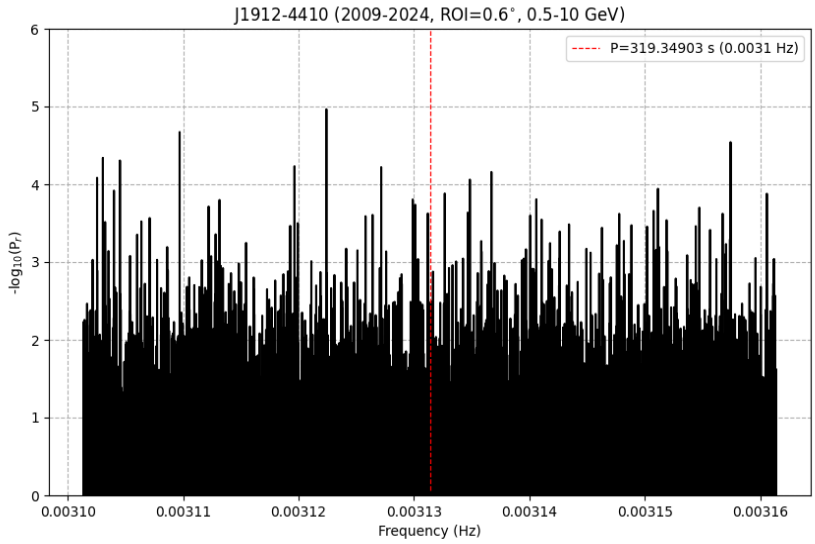

Figure 5.10: Rayleigh Periodogram of J1912 in 0.5-10GeV with vertical dashed line showing the position of spin period of J1912.

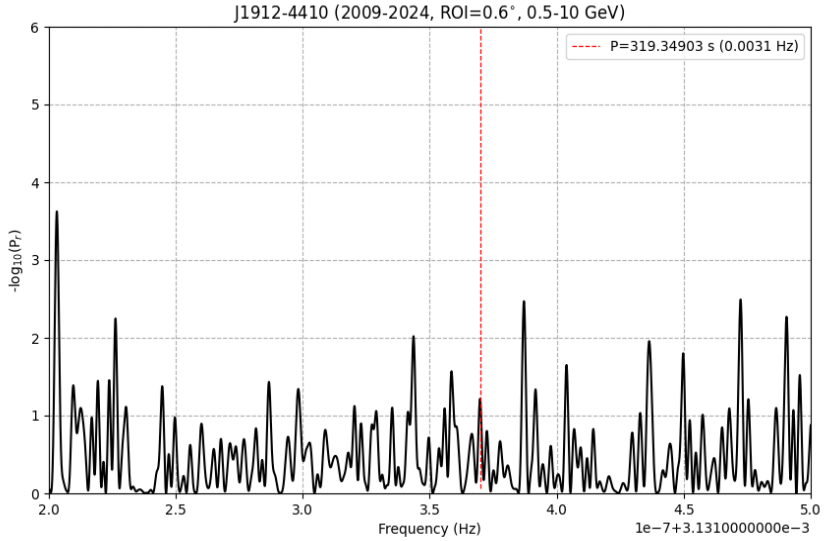

Figure 5.11: Zoomed in Rayleigh periodogram of J1912 in 0.5-10GeV with vertical dashed line showing the position of spin period of J1912

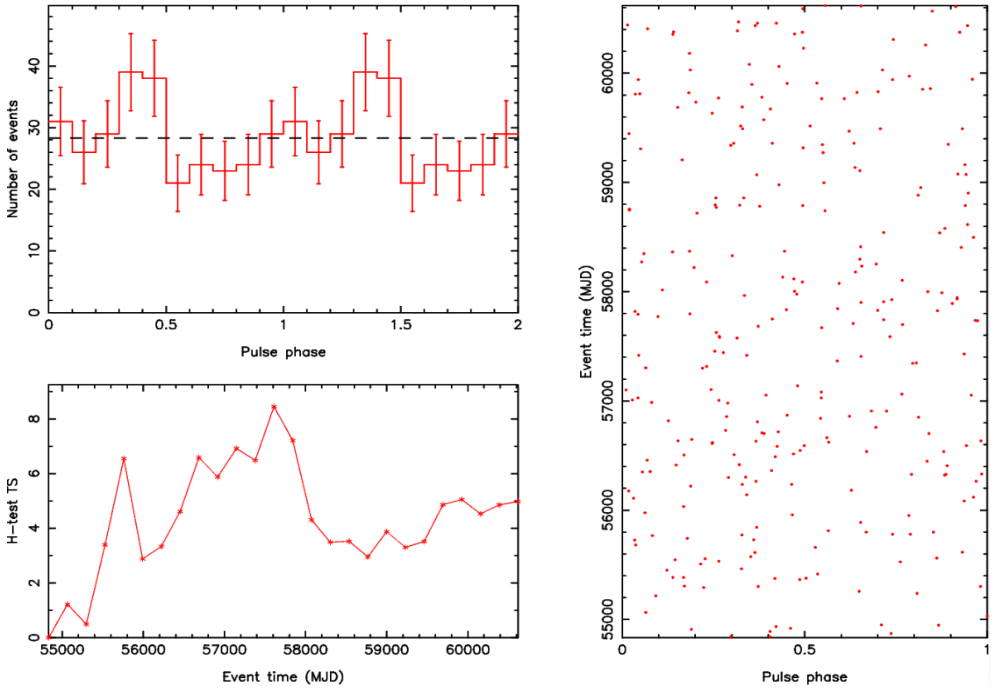

Figure 5.12: J1912 0.5-10GeV folded γ-ray light curve (top left) on spin period P∼319.34903 s using Pelisoli, Marsh, et al. (2023) ephemeris along with the H-test TS (bottom left) graph and the phasogram (right).

5.4.1 RA and Dec Restriction

Although the H-test TS revealed a low significance of the spin period in the γ-rays, the folded γ-ray light curve (Figure 5.12) did show some pulsed behavior. To further explore this, the event file with the high probability (>80%) photons were further subjected to an event selection by using the fact that *Fermi*-LAT records the declination (DEC) and right ascension (RA) of the detected γ-ray photons. J1912's coordinates are RA=288.057166° and DEC=-44.17919007° (J2000) and by selecting only high probability γ-ray photons that contains a declination lying between -45°≤DEC≤-44° and from this range selecting further only high probability γ-ray photons with right ascension lying between 288°≤RA≤289°, a final event file was created using these criteria. Although the source's coordinates appear to be at the edge of this range, photons from J1912 and the background are still randomly spread in the ROI. Applying these restrictions removes most of

those randomly spread photons (i.e., photons still having recorded RA and DEC coordinates outside these restrictions) in the ROI. Decreasing these RA and DEC restriction ranges even further results in insufficient γ-ray photons for a reliable periodic analysis. The Rayleigh test was performed on this final event file and is shown in Figure 5.13.

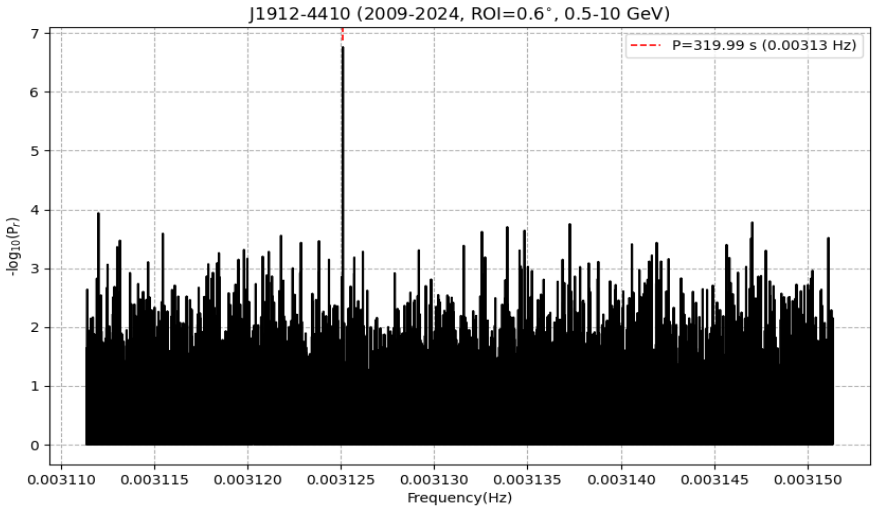

Figure 5.13: Rayleigh Periodogram of RA and DEC restricted event file of J1912 in 0.5-10GeV showing pulsations at period P=319.99±0.35s .

The Rayleigh test on the RA and Dec restricted event file revealed a very strong peak at a period of P=319.99±0.35s with a -$\log_{10}$(P$_r$)=6.76 which corresponds to a $\sim$5.74σ detection compared to the noise. The γ-ray events were then folded on this period using the spin ephemeris provided by Pelisoli, Marsh, et al. (2023) and the phase-folded light curve is shown in Figure 5.14 below.

The phase-folded γ-ray light curve on the predominant period $P\sim$319.99s (see Figure 5.13) is single-peaked per rotation and peaks at a spin phase of $\sim$0.2 and the H-test TS reaches a very high value of TS$\sim$30 (probability of uniformity of $\sim 6.14\times10^{-6}$ with a Gaussian significance of $\sim$4.37σ) suggesting a significant detection. This phase-folded γ-ray light curve in the 0.5-10 GeV range is phase-aligned with the optical and UV folded light curves (see Figure 3.13) obtained by Pelisoli, Marsh, et al. (2023) and Pelisoli, Sahu, et al. (2023) respectively using the same spin ephemeris.

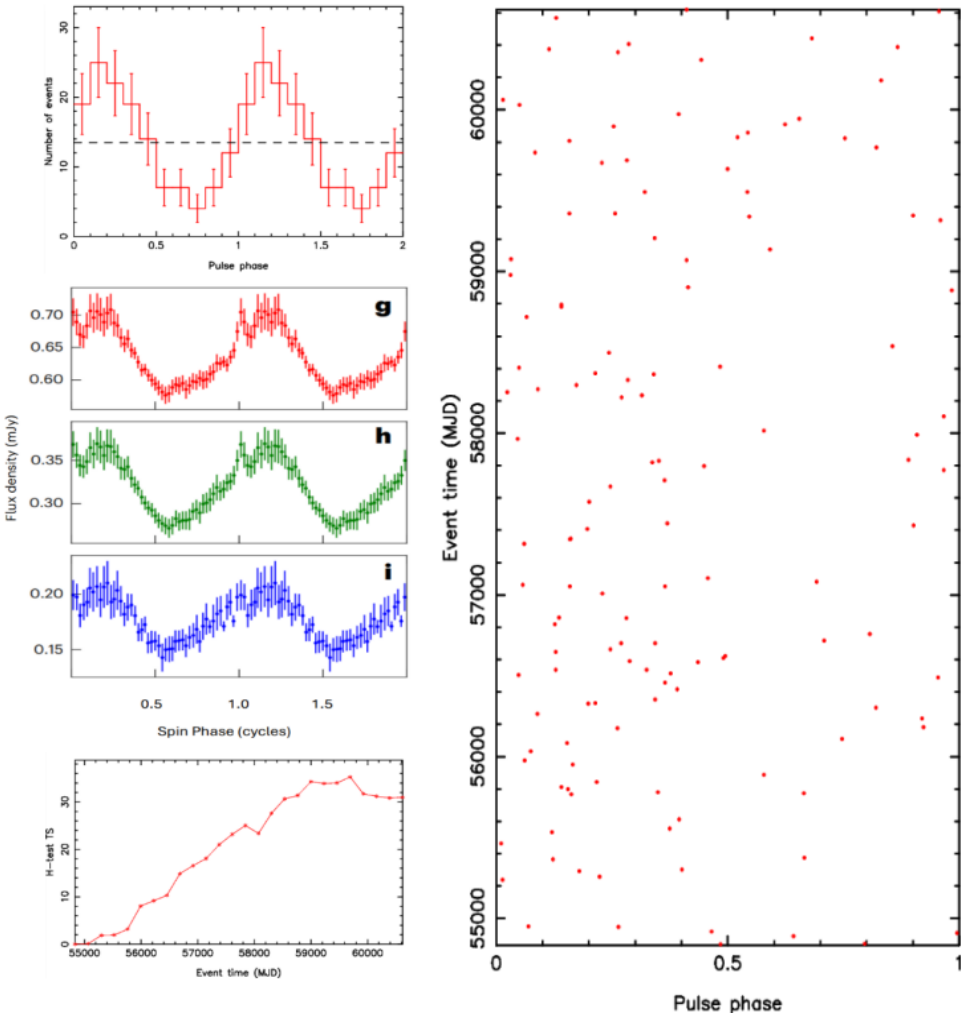

Figure 5.14: J1912 0.5-10GeV folded γ-ray light curve (top left) on period P=319.99±0.35s using Pelisoli, Marsh, et al. (2023) ephemeris along with the H-test TS (bottom left) graph and the phasogram (right). Figures **g**, **h** and **i** in the left middle give respectively, the i_s, g_s and u_s filter ULTRACAM folded light curves (from Pelisoli, Marsh, et al. (2023)) using the same spin ephemeris.

This might possibly suggest that the optical, UV and γ-ray photons might be originating from the same location on the white dwarf in J1912 as it rotates at a period of ∼319s (5.3 minutes). Thus, we interpret this peak in the Rayleigh periodogram as the period at which the γ-ray photons are being pulsed towards the observer.

Both the binned analysis in the 0.1-500 GeV range and unbinned analysis in the 0.5-10 GeV range reveals that low level γ-ray emission from J1912. We find a $\sim 2.81\sigma$ (see Table 4.3) for the binned likelihood analysis and a $\sim 2.33\sigma$ (see Table 5.2) detection significance for the unbinned likelihood analysis which is below the 5σ detection threshold. The Rayleigh test also revealed no significant pulsations in the 0.5-10 GeV energy at the spin period of J1912 but after applying the RA and DEC restriction revealed a strong peak at close to the rotation period of J1912. The TS gating method (Madzime (2021), Madzime and Meintjes (2023)) was then performed on both the two $\sim$15 year data sets (0.1-500 GeV and 0.5-10 GeV) of J1912.

5.5 TS Gated Binned Likelihood Analysis

A TS gated analysis (see section 4.4.6 for explanation on the TS gating method) was performed on the $\sim$15 years of *Fermi*-LAT data of J1912 in the 0.1-500 GeV energy band using a ROI=10° centered on J1912 position (RA=288.057166°, DEC=-44.17919007°, J2000). The TS gating analysis involves dividing the whole $\sim$15 years of data into 5-day time bins and conducting an unbinned analysis on each of those 5-day time bins while keep the usual data selection cuts i.e. the filter for the GTIs "`(DATA_QUAL>0)&&(LAT_CONFIG==1)`", "`zmax`=90°" to exclude γ-rays from the limb of the Earth etc) the same for each 5-day time bin. Then, only time bins with TS>0 are considered and are then used to do a binned likelihood analysis. A TS gated counts map of the J1912's region is displayed in Figure 5.15 below.

Compared to the normal binned likelihood analysis counts map in Figure 5.5 the TS gated counts map in Figure 5.8 seems to show more photons originating from J1912 (ROI=0.6° circle). J1912 was modeled by power-law model (equation 4.24) with sources from the 4FGL-DR4 catalog included in the source model together with the isotropic and galactic diffuse components. The sources' normalization parameters within a 5° radius from J1912 having a TS>25 were treated as free parameters while beyond the 5°, the parameters of the sources were fixed to their 4FGL-DR4 catalog values. The counts spectrum and the residuals of the TS gated binned likelihood analysis is shown in Figures 5.16 and 5.17 respectively.

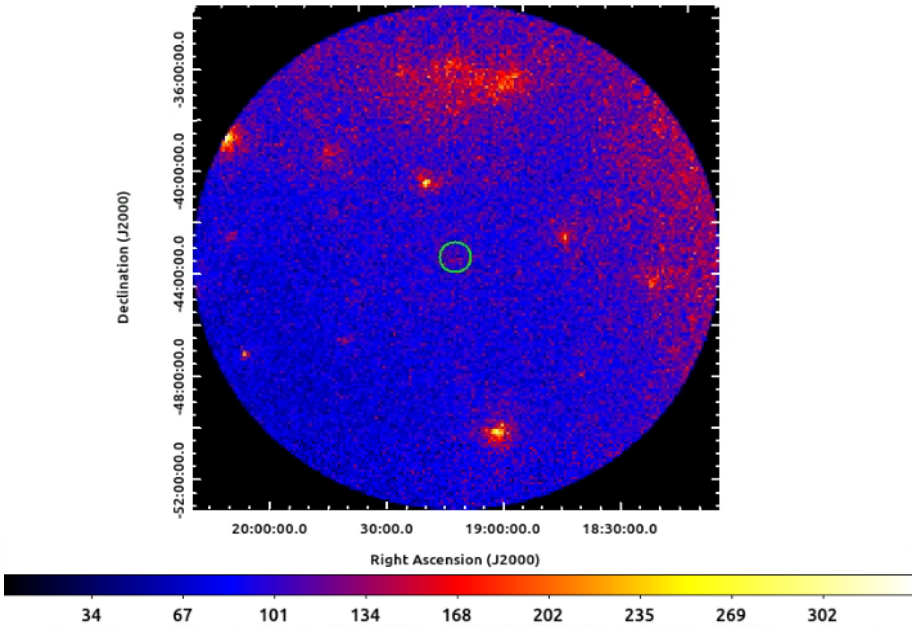

Figure 5.15: 0.1-500 GeV 200×200 pixel TS gated counts map with 0.1° per pixel resolution of J1912 (0.6° radius green circle). The color bar displays the counts per pixel value.

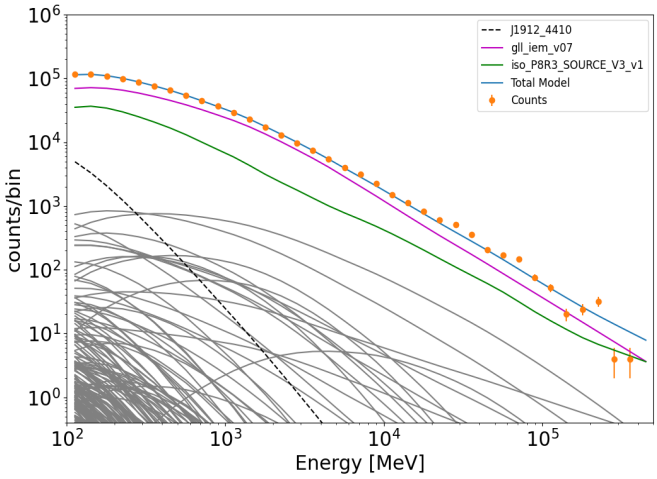

Figure 5.16: TS gated binned likelihood analysis counts spectrum of J1912 (black dashed line) in the 0.1-500 GeV band modeled as a simple power law. Isotropic (green) and galactic diffuse (magenta) background models are also shown along with background sources (grey lines) in the ROI.

Spectral Model	Flux (photons/cm^2/s)	N_{pred}	TS	Significance[3]
Power-Law	$(3.08\pm0.30)\times10^{-8}$	3627.74	208.71	14.45σ

Table 5.3: J1912's TS gated binned likelihood analysis results in e 0.1-500 GeV range. The flux represents the integral photon flux.

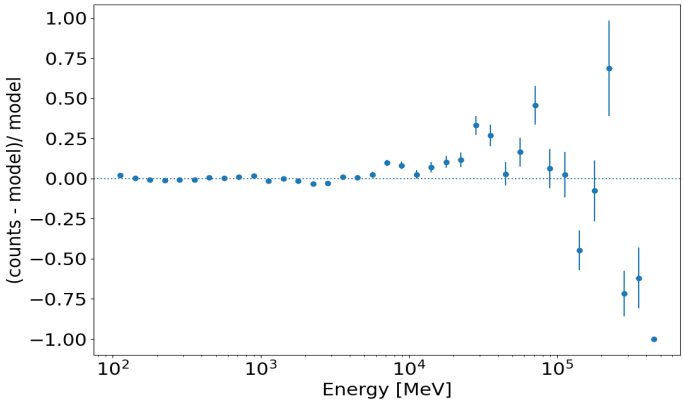

Figure 5.17: TS gated residual fit of the binned analysis of J1912 in the 0.1-500 GeV band modeled as a simple power law.

The counts spectrum (Figure 5.16) and residual fit (Figure 5.17) shows that J1912 is sufficiently modeled as a power law below the ∼10 GeV energy range. Above ∼10 GeV, the residuals becomes scattered signifying less γ-ray photons above this threshold of ∼10 GeV. A summary of the TS gated binned likelihood analysis of J1912 in the 0.1-500 Gev range is displayed in Table 5.3.

Using the TS gated greatly increases the significance from $\sim2.81\sigma$ (normal binned likelihood analysis, see Table 5.1) to $\sim14.45\sigma$ which is far above the *Fermi*-LAT detection threshold of 5σ. To further justify this attempt to improve the visibility of J1912, TS and residual maps of J1912's region were produced and is shown in Figure 5.18 below.

From the TS map after applying the TS gating, it is clear that J1912 is visible in the γ-rays. This TS gated data was then used to create a "Spectral Energy Distribution" (SED) of J1912 in the 0.1-500 GeV band. This was achieved with "FermiPy" (Wood et al. (2017)) and the SED along with the TS distribution with energy is shown in Figure 5.19 below.

[3]NOT the TRUE significance but an attempt to improve the visibility of J1912 with TS gating method.

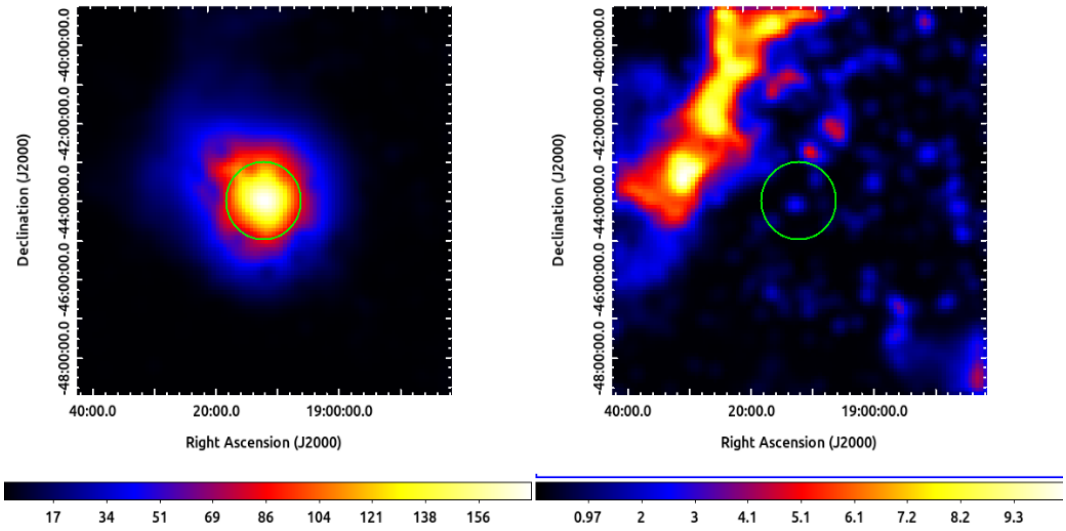

Figure 5.18: 100×100 pixel with 0.1°pixel^{-1} resolution TS gated binned TS Map (left) and residuals map (right) of J1912 (1° radius green circle) in the 0.1-500 GeV band. The color bar show the TS value and both images were smoothed with a σ=1.5. Gaussian kernel.

The spectral index of J1912 in the 0.1-500 GeV band is Γ=3.40±0.50 which is a steep spectrum where the upper limits shows the 95% confidence interval for flux values with TS<4. This suggest that J1912 is emitting most of its γ-rays at lower energies i.e., a low-level γ-ray emitter. The TS distribution with energy also shows that most of J1912 γ-ray emission occurs at energies below ∼10 GeV. Taking this into consideration, an unbinned analysis in the 0.5-10 GeV band was performed.

5.6 TS Gated Unbinned Likelihood Analysis

TS gating analysis was then conducted on the 0.5-10 GeV band using a ROI=1° centered around J1912's position to limit the emission from background γ-ray sources and again only the 5-day time bins that showed TS>0 were used to perform an unbinned likelihood analysis while keeping the standard data selection cuts recommended by *Fermi*-LAT the same. The results from the TS gated unbinned analysis of J1912 is shown in Table 5.4.

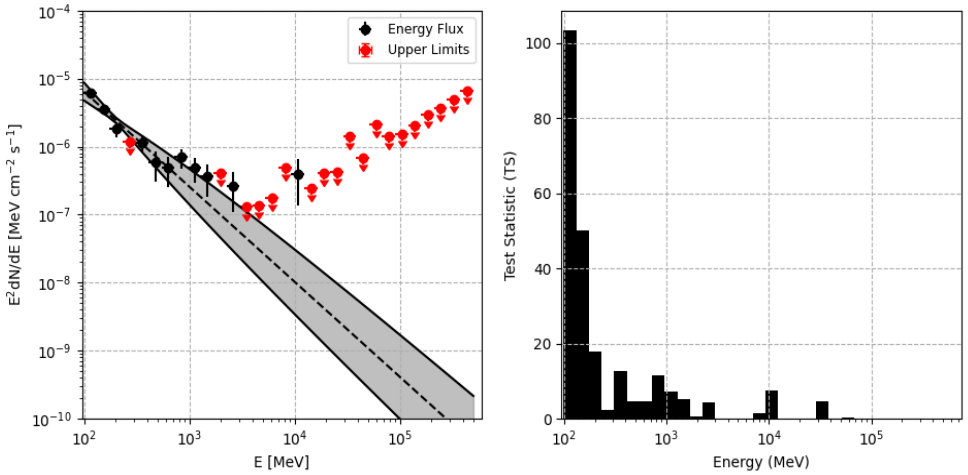

Figure 5.19: Spectral Energy Distribution (SED) of J1912's TS gated data in the 0.1-500 GeV range. Accompanying histrogram shows the Test Statistic (TS) distribution with energy.

Spectral Model	**Flux (photons/cm^2/s)**	N_{pred}	**TS**	**Significance**[4]
Power-Law	$(4.62\pm0.38)\times10^{-9}$	395.73	221.46	14.88σ

Table 5.4: J1912's TS gated unbinned likelihood analysis results in 0.5-10 GeV band. The flux represents the integral photon flux.

The improved visibility is also observed in the unbinned likelihood analysis using the TS gated data in the 0.5-10 GeV band compared to the standard unbinned likelihood analysis (see Table 5.2). This clear visibility of J1912 was then confirmed by producing unbinned TS and residual maps using `gttsmap` together with the best-fit source model. J1912 was intentionally removed from the source model and all sources' parameters were fixed to their 4FGL-DR4 catalog values except the isotropic and galactic diffuse components that were treated as free parameters to produce the unbinned TS map. The TS gated unbinned TS and residual map is shown in Figure 5.20 below.

A SED of J1912 in the 0.5-10 GeV band was then produced using the `pyLikelihood` Python script which also produces the TS distribution with energy. These are shown in Figure 5.21 below

The spectral index of J1912 in the 0.5-10 GeV range is Γ=3.34±0.18 which signifies γ-ray

[4]NOT the TRUE significance but an attempt to improve the visibility of J1912 with TS gating method.

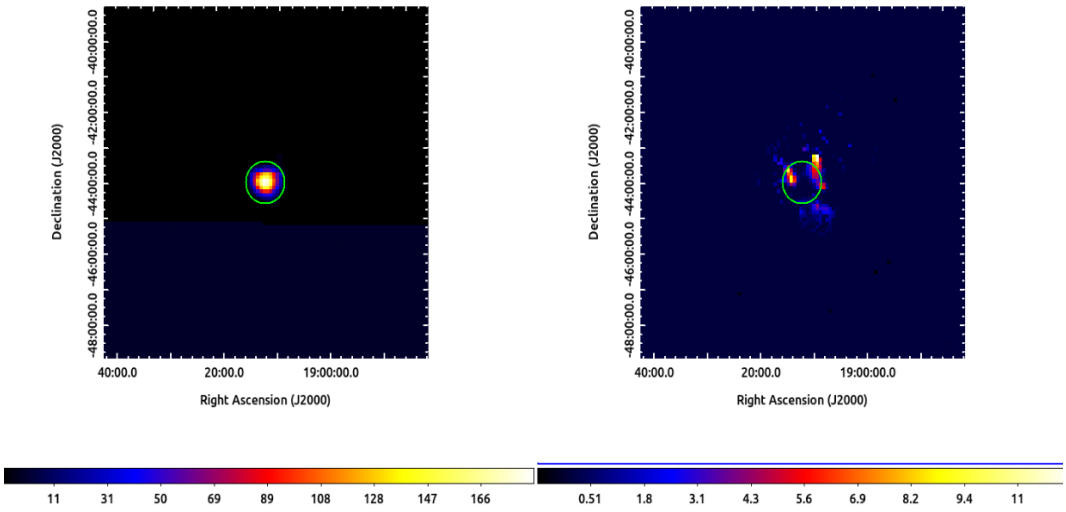

Figure 5.20: 100×100 pixel with 0.1°pixel^{-1} resolution TS gated unbinned TS Map (left) and residuals map (right) of J1912 (0.6° radius green circle) in the 0.5-10 GeV band. The color bar show the TS value.

emission from J1912 emanating from lower energies. This is further confirmed by the high TS values at lower energies in the TS distribution with energy in Figure 5.21.

5.7 Periodic Analysis

The Rayleigh test was utilized to search for pulsations using this TS gated event file. The probability that each photon originates from J1912's position was calculated using `gtsrcprob` for which only γ-ray photons having a probability of greater than 80% were kept to search for γ-ray pulsations. The ROI was further reduced to ROI=0.6° limit the background emission. The Rayleigh periodogram is shown in Figure 5.22 together with a zoomed-in version in Figure 5.23. A sampling frequency of 2.01×10^{-11} Hz (1% of the Fourier resolution 2.01×10^{-9} Hz) with 2×10^{6} trial frequencies which resulted in a search range of ∼317-321s.

There appears to be a peak close to the position of the spin period in the Rayleigh periodogram but it is part of the noise. The γ-ray photons in the TS gated event file were then folded on this

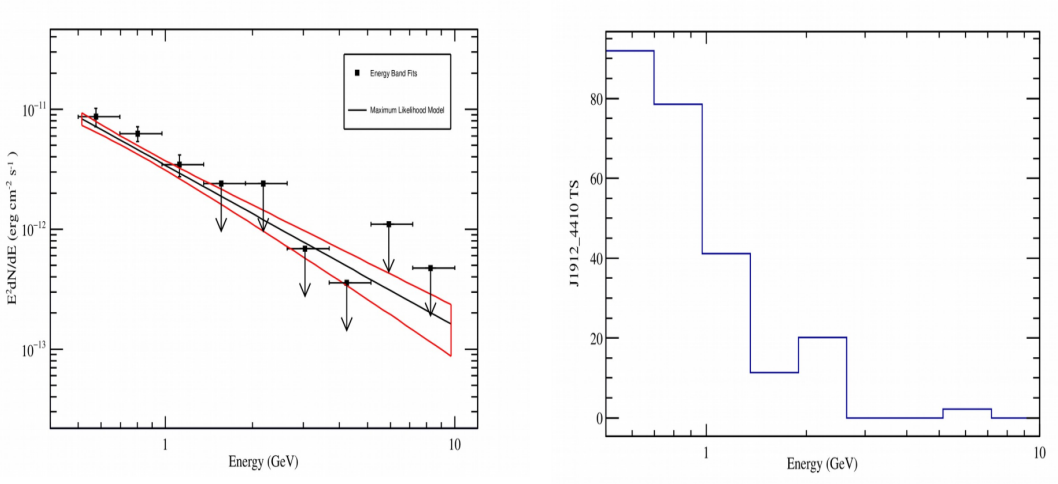

Figure 5.21: Spectral Energy Distribution (SED) of J1912's TS gated data in the 0.5-10 GeV range. Accompanying histogram shows the Test Statistic (TS) distribution with energy.

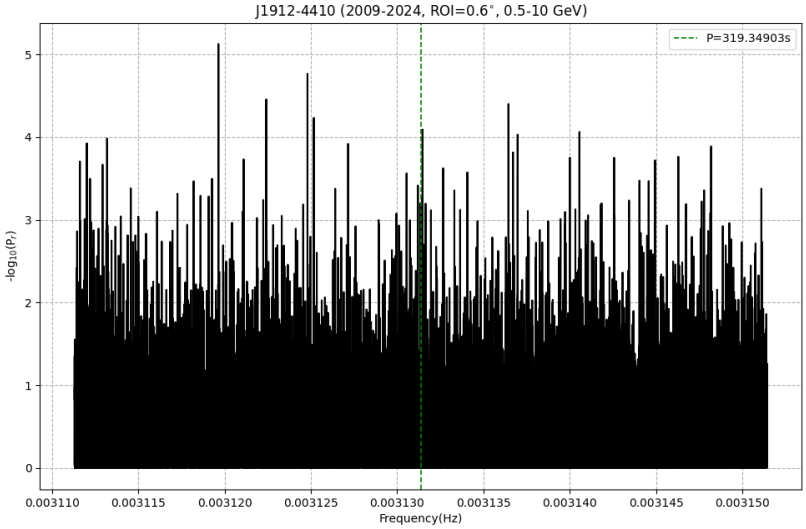

Figure 5.22: Rayleigh Periodogram of TS gated event file of J1912 in 0.5-10GeV with vertical dashed line showing the position of spin period of J1912.

spin period using the spin ephemeris provided by Pelisoli, Marsh, et al. (2023) and is shown Figure 5.24.

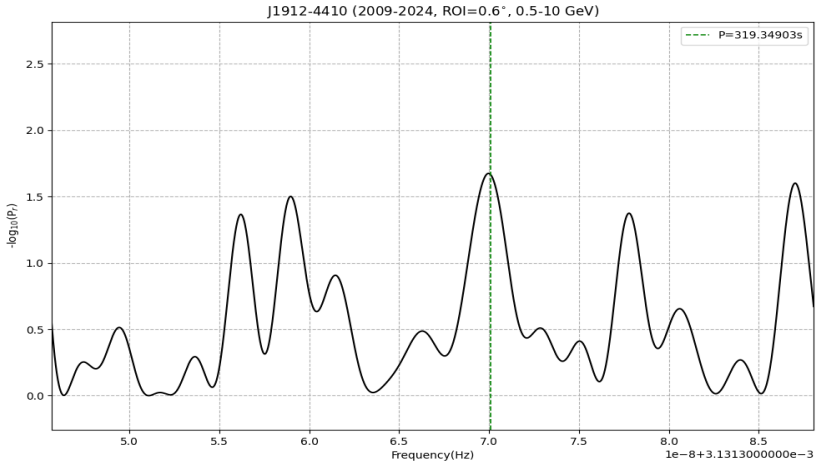

Figure 5.23: Zoomed in Rayleigh periodogram of J1912 in 0.5-10GeV with vertical dashed line showing the position of spin period of J1912

The phase-folded γ-ray light curve in Figure 5.24 does show some pulsed behavior but the H-test TS reveals that it is not significant at a TS$\sim$8.

5.7.1 TS gated RA and Dec Restriction

The high probability TS gated event file was then further subjected to RA and DEC restrictions (see section 5.4.1). From these high probability γ-ray photons, only those that have a declination in the range -45°$\leq$DEC$\leq$-44° and from this range only γ-ray photons that have a right ascension lying in the range 288°$\leq$RA$\leq$289° was used for a for the Rayleigh test which is shown in Figure 5.25 below.

The dominant peak in the Rayleigh periodogram is at a period of P=319.99$\pm$0.34s at significance of $\sim 3.55\sigma$ which is similar to the one found in the normal unbinned likelikhood analysis using the RA and DEC restriction method (see Figure 5.13) although the periodogram is a much noisier. Phase-folding the γ-ray events on this period using the Pelisoli, Marsh, et al. (2023) spin ephemeris results in Figure 5.26

The phase-folded γ-ray light curve in Figure 5.26 does appear to show some pulsed emis-

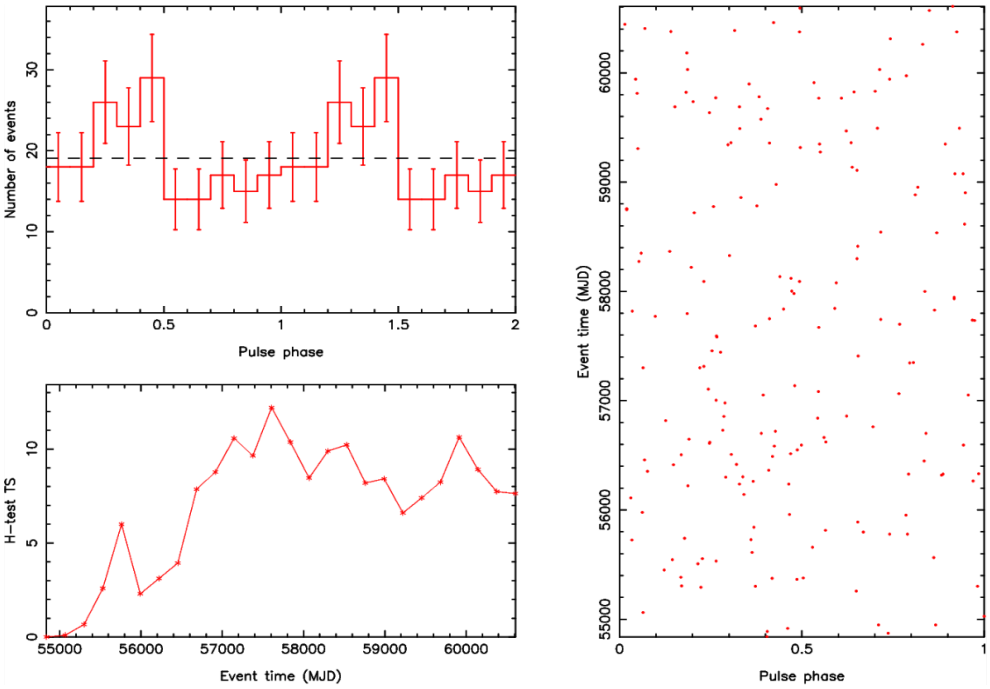

Figure 5.24: TS gated J1912 0.5-10GeV folded γ-ray light curve (top left) on spin period $P\sim$319.34903 s using Pelisoli, Marsh, et al. (2023) ephemeris along with the H-test TS (bottom left) graph and the phasogram (right).

sion and is also in phase with the optical and UV folded light curves (see Figure 3.13). The H-test TS also shows significant pulsations at this period with TS$\sim$20 (probability of uniformity $\sim 3.355\times10^{-4}\approx 3.40\sigma$). We interpret this low-level pulsation at the period $P\sim$319.99s especially in Figures 5.13 and 5.14 as γ-rays in the 0.5-10 GeV being modulated at the spin period of J1912 due to curvature radiation. Pelisoli, Marsh, et al. (2023) did detect flaring behavior from J1912 which points to mass transfer from the secondary (M-dwarf) to the primary (white dwarf) in J1912. Pelisoli, Sahu, et al. (2023) also developed a geometric seeding model (see Figure 3.20) that explains most of J1912's behavior with the requirement that there should be significant mass transfer. Charged particles from the photosphere of the M-dwarf can get trapped in the primary's magnetosphere in J1912 and get re-accelerated along the magnetic poles of the primary emitting γ-rays via the curvature radiation process modulated at the white dwarf's rotation period in J1912. See Appendix D and E for control tests done on sourceless regions away from J1912.

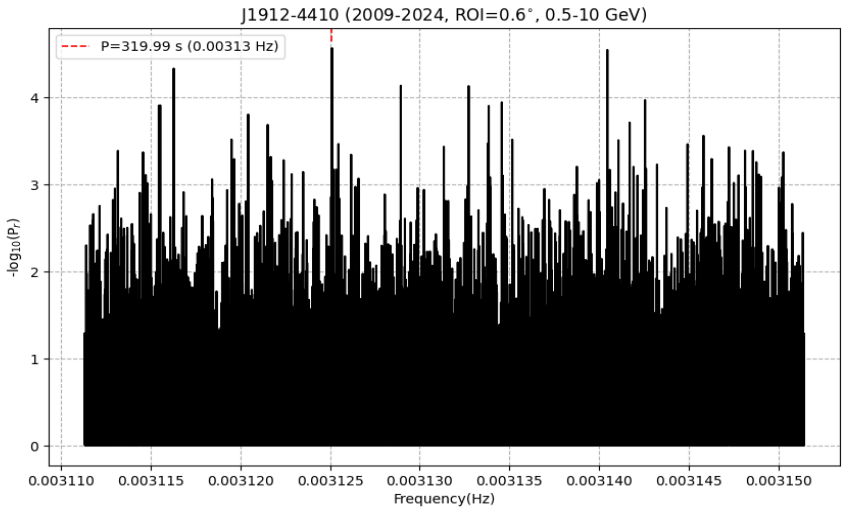

Figure 5.25: Rayleigh Periodogram of RA and DEC restricted event file of J1912 in 0.5-10GeV showing pulsations at period P=319.99±0.34s.

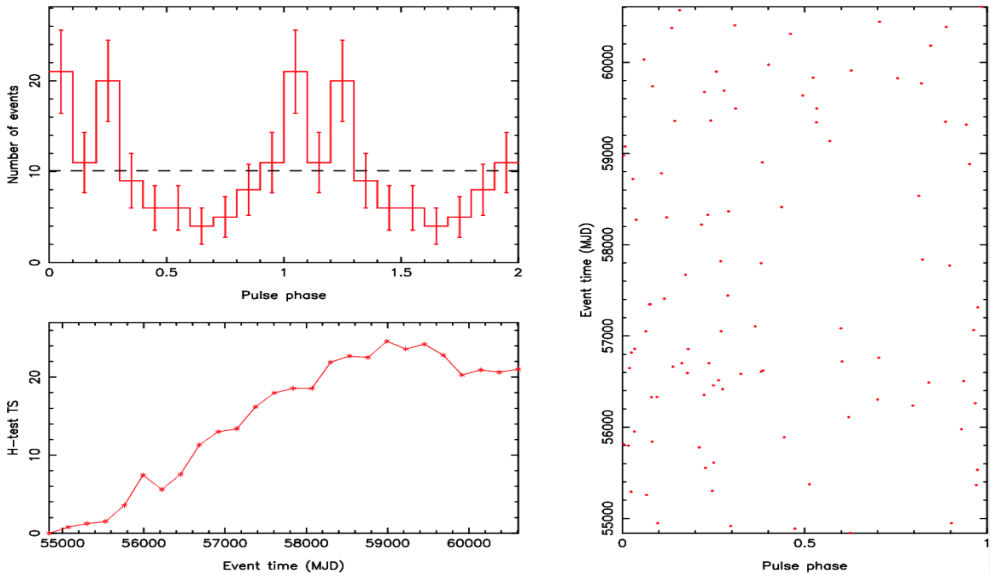

Figure 5.26: J1912 0.5-10GeV folded γ-ray light curve (top left) on spin period P=319.99±0.34s using Pelisoli, Marsh, et al. (2023) ephemeris along with the H-test TS (bottom left) graph and the phasogram (right).

Chapter 6

Conclusions

The goal of this study was to search for periodic pulsed γ-ray emission from both the isolated highly magnetic white dwarf EUVE J0317-85.5 (J0317, Barstow et al. (1995)) and the recently discovered white dwarf binary system J191213.72−441045.1 (J1912, Pelisoli, Marsh, et al. (2023)).Theories suggests that highly magnetic and fast spinning white dwarfs might mimic the pulsed behavior seen from pulsars. Multi-wavelength pulsed emission from both of these systems has been detected suggesting that "white dwarf pulsars" might become a new class of gamma-ray source.

For J0317, new optical data using the BOOTES-6 and BOOTES-7 robotic telescopes confirmed that J0317 still emits pulsed optical emission at its spin period of P_{spin}=725.36±0.73s and we also detect faint optical pulsation at period P=362.73±1.04s and interpret this as the first harmonic period possibly resulting from emission emanating from the second magnetic pole of J0317 given that the angle between rotation and magnetic axis is $\beta \sim 40°$ (Ferrario et al. (1997)). Ferrario et al. (1997) also found pulsations at both the rotation period and its first harmonic in their far-ultraviolet (FUV) data of J0317. The phase-folded optical light curve on the rotation period of J0317 using the Ferrario et al. (1997) spin ephemeris reveals that it is double-peaked per rotation contrary to Barstow et al. (1995) single-peaked optical light curve. A wavelet analysis of the optical data revealed no changes in the spin period of J0317 suggesting that J0317 is spinning at a fairly stable rate as expected. Longer continuous optical data of J0317 would be useful to confirm this

because Lawrie et al. (2013) did detect a period change of $\dot{P}$=(-5.6±1.9)×10^{-14}ss^{-1}.

A periodic analysis of soft X-rays (0.1-2.4 keV) using the archived data from ROSAT's HRI instrument revealed dominant pulsations at a period of P=362.82±0.33s for which the phase-folded light curve on this period is single-peaked per rotation using the Ferrario et al. (1997) ephemeris. The generalized Lomb-Scargle (GLS, Zechmeister, M. and Kürster, M. (2009)) periodogram of this soft X-ray light curve did not reveal pulsations at the rotation period P∼725.5s which was puzzling. The soft X-ray light curve phase-folded on the spin period did show a double peak feature which was phase aligned with the FUV folded light curve from Ferrario et al. (1997). This was also seen when performing a Rayleigh Test (Mardia (1972)) on the unbinned X-ray photons from a region of interest (ROI) of 17$''$ centered on J0317's coordinates. The Rayleigh periodogram revealed dominant pulsations at a period of P=362.85±0.18s and no significant pulsations were found at the spin period P=725.5s. The phase-folded light curve on the rotation period (P=725.5s) were also aligned with far-ultraviolet (FUV) phase-folded light curves of Ferrario et al. (1997) but the phase-folded light curve on the first harmonic of the rotation period (P∼362.85s) were single-peaked at phase ∼0.6 but out-of-phase with the FUV phase-folded light curves of Ferrario et al. (1997). The non-detection of the spin period in both the GLS and the Rayleigh periodogram could be due to the fact that the ROSAT telescope could not resolve J0317 and white dwarf (non-magnetic) companion LB 9802 which is about 7$''$ away from J0317. The possible presence of a magnetic hot spot with magnetic field strength B≤450 MG (Vennes et al. (2003)) could also explain the dominant pulsations at the first harmonic of the spin period and also the misalignment of the folded soft X-ray light curve on the first harmonic compared to the FUV (Ferrario et al. (1997)) light curve phase-folded on the same period using the same spin ephemeris. These **possible soft X-ray pulsations** could be due to the backward flow of charged particles towards the polar cap of the white dwarf and therefore heating the polar caps producing soft X-ray photons through thermal bremsstrahlung (Cáceres et al. (2016)) which is modulated at the spin period's first harmonic. Future high resolution soft X-ray observations of J0317 are needed to confirm this possible detection.

A high energy γ-ray analysis was performed on J0317 using ∼15 years of *Fermi*-LAT data. A

binned maximum likelihood analysis was performed on the 0.1-500 GeV energy range to get a sense of where in this energy range most of the emission might occur if there are any γ-ray emission emanating from J0317. The standard binned likelihood analysis did not reveal any significant γ-rays from J0317 revealing a detection significance of $\sim 3.79\sigma$ which is below *Fermi*-LAT's detection threshold of 5σ. The results from the binned likelihood analysis did give an indication that most of the emission might be $\leq$10 GeV and so an unbinned likelihood analysis was performed on the energy range 0.5-10 GeV. This unbinned likelihood also revealed a low significance of $\sim 1.12\sigma$. Nevertheless, a search for periodicty in the 0.5-10 GeV energy was conducted using the Rayleigh test which revealed possible γ-ray pulsations at a period P=724.65$\pm$0.54s with a significance of $\sim 4.01\sigma$ ($\sim 3.72\sigma$ using the H-test Test Statistic) which agreed with the γ-ray period found by Madzime and Meintjes (2023). The folded γ-ray light curve on this period using the Ferrario et al. (1997) ephemeris was consistent with a single-peaked light curve within the noise errors (see Figure 4.36). This second peak corresponded to a period of P=362.65$\pm$0.29s at $\sim 3.77\sigma$ ($\sim 3.61\sigma$ using the H-test Test Statistic) in the Rayleigh periodogram. This folded γ-ray light curve was found to be remarkably in phase with the recent BOOTES-6 and BOOTES-7 optical light curves which suggest that the optical and the γ-ray photons might be coming from the same regions on J0317. We suggest that this possible γ-ray pulsations from J0317 might be due to the curvature radiation mechanism where charged particles slide along the curved magnetic field lines emitting γ-rays modulated at the rotation period of J0317. Using the same γ-ray data, a new analysis technique called TS gating (Madzime (2021), Madzime and Meintjes (2023)) was employed to see if one could possibly increase the visibility by only focusing on time bins where the Test Statistic (TS) is greater than zero. The TS gated binned and unbinned analysis revealed a detection significance of $\sim 17.12\sigma$ and $\sim 16.05\sigma$ respectively which was further confirmed with test statistic and residual maps. It is stressed that these are not the new detection significances of J0317 but rather an attempt to increase the visibility of the source utilizing the TS gating method. The Rayleigh test on the TS gated event file also revealed pulsations at a period of P=724.65$\pm$0.56s with a significance of $\sim 3.60\sigma$ ($\sim 3.50\sigma$ with the H-test TS). This slight decrease in significance could be due to the fact that most of the time bins were removed during the TS gating procedure. The folded γ-ray light curve on this period

still revealed a double-peaked structure with the second faint peak being attributed to the first harmonic of the rotation period with faint γ-ray emission possibly due to the curvature radiation mechanism emanating from the second magnetic pole of J0317. We performed control tests on sourceless regions away from the region of J0317 and confirmed that the pulsations from J0317 are inherent to J0317.

For J1912, a standard binned likelihood analysis in the 0.1-500 GeV energy range revealed a significance of $\sim$2.81σ and the binned likelihood analysis also suggested possible emission at lower energies i.e. $\leq$10 GeV. The unbinned likelihood analysis also revealed a low significance of $\sim$2.33σ. A periodic analysis of the 0.5-10 GeV γ-ray data revealed no significant pulsations at the spin period of J1912 but the phase-folded light curve on the spin period using the Pelisoli, Marsh, et al. (2023) spin ephemeris did reveal pulsed behavior. A declination (DEC) restriction right ascension (RA) technique was employed on the region of interest of J1912 to only allow γ-ray photons with DEC between -45°$\leq$DEC$\leq$-44° and from this range only photons with RA between 288°$\leq$RA$\leq$289° was used in the Rayleigh test. This revealed a very high peak in the Rayleigh periodogram at a period of P_{spin}=319.99$\pm$0.35s at $\sim$5.74σ ($\sim$4.73σ using the H-test Test Statistic)significance. The folded γ-ray light curve on this period using the Pelisoli, Marsh, et al. (2023) spin ephemeris revealed a single-peaked structure that is remarkably in phase with optical folded light curves of Pelisoli, Marsh, et al. (2023). This γ-ray pulsations at this period could be due to the curvature radiation mechanism where particles get extracted from the white dwarf's surface, moving along the magnetic field lines and hence emit curvature photons. Pelisoli, Marsh, et al. (2023) did detect flaring behavior from J1912 which could suggest residual mass transfer from the M-dwarf to the primary (white dwarf) in J1912. Since Pelisoli, Sahu, et al. (2023) could only propose an upper limit $\approx$50 MG on the magnetic field strength of the primary, charged particles from the M-dwarf can get trapped in the primary's magnetosphere and get re-accelerated along the magnetic poles and emitting γ-rays modulated at the spin period. TS gated binned and unbinned likelihood analyses of the same data revealed a significance of $\sim$14.45σ and $\sim$14.88σ respectively which was also confirmed with TS and residual maps of J1912's region. Again, not the new significance of J1912 but an attempt to

increase the visibility of J1912. RA and DEC restricted periodic analysis of the TS gated event file revealed a very noisy periodogram but still giving a maximum period at P=319.99±0.34s with a significance of $\sim 3.55\sigma$ ($\sim 3.40\sigma$ using H-test Test Statistic). This noisy periodogram is explained by the removal of the time bins with TS<0 during the TS gating analysis. For both J0317 and J1912, we quote the H-test Test Statistics as a more robust representation of the peak significances because it avoids the application of statistical penalties to the periodograms. Control tests on sourceless regions away from J1912 were also performed to confirm that the γ-ray pulsations are inherent to J1912 and not an artifact of the analysis techniques.

The detection of possible γ-ray pulsations at the spin period of both the isolated highly magnetic, fast rotating white dwarf J0137 and the fast spinning white dwarf binary system J1912 suggest that these systems do behave as pulsars albeit emitting γ-ray pulsations at a **low-level** due to their longer periods and lower magnetic fields.

6.1 Future Work

Future research will include delving deeper into the new class of gamma-ray sources called white dwarf pulsars and doing extensive γ-ray analysis on a candidate or confirmed white dwarf pulsar using *Fermi*-LAT. A search for γ-ray pulsations from the target white dwarf pulsar will be carried out in order to strengthen the motivation for curvature radiation as a plausible mechanism for the pulsed γ-ray emission from these systems. Radio observations of the target white dwarf pulsar could also be carried out using the MeerKAT telescope to study the possible pulsar behaviour of the white dwarf in the radio band and make comparisons to the γ-rays in terms of pulse profiles.

Bibliography

Ackermann, M., Ajello, M., Albert, A., Allafort, A., Atwood, W. B., Axelsson, M., ... Zimmer, S. (2012, oct). The fermi large area telescope on orbit: Event classification, instrument response functions, and calibration. *The Astrophysical Journal Supplement Series*, *203*(1), 4. Retrieved from https://dx.doi.org/10.1088/0067-0049/203/1/4 doi: 10.1088/0067-0049/203/1/4

Ackermann, M., Ajello, M., Allafort, A., Asano, K., Atwood, W. B., Baldini, L., ... Zimmer, S. (2013, feb). Determination of the point-spread function for the fermi large area telescope from on-orbit data and limits on pair halos of active galactic nuclei. *The Astrophysical Journal*, *765*(1), 54. Retrieved from https://dx.doi.org/10.1088/0004-637X/765/1/54 doi: 10.1088/0004-637X/765/1/54

Arons, J. (1981, September). Pair creation above pulsar polar caps - Steady flow in the surface acceleration zone and polar CAP X-ray emission. *ApJ*, *248*, 1099-1116. doi: 10.1086/159239

Arons, J. (1983, March). Pair creation above pulsar polar caps : geometrical structure and energetics of slot gaps. *ApJ*, *266*, 215-241. doi: 10.1086/160771

Arons, J., & Scharlemann, E. T. (1979, August). Pair formation above pulsar polar caps: structure of the low altitude acceleration zone. *ApJ*, *231*, 854-879. doi: 10.1086/157250

Astropy Collaboration, Robitaille, T. P., Tollerud, E. J., Greenfield, P., Droettboom, M., Bray, E., ... Streicher, O. (2013, October). Astropy: A community Python package for astronomy. *AAP*, *558*, A33. doi: 10.1051/0004-6361/201322068

Atwood, W. B., Abdo, A. A., Ackermann, M., Althouse, W., Anderson, B., Axelsson, M., ... Ziegler, M. (2009, may). The large area telescope on the fermi gamma-ray space telescope mission. *The Astrophysical Journal*, *697*(2), 1071. Retrieved from https://dx.doi.org/

10.1088/0004-637X/697/2/1071 doi: 10.1088/0004-637X/697/2/1071

Baade, W., & Zwicky, F. (1934, Jul). Remarks on super-novae and cosmic rays. *Phys. Rev.*, *46*, 76–77. Retrieved from https://link.aps.org/doi/10.1103/PhysRev.46.76.2 doi: 10.1103/PhysRev.46.76.2

Ballet, J., Bruel, P., Burnett, T. H., Lott, B., & collaboration, T. F.-L. (2024). *Fermi large area telescope fourth source catalog data release 4 (4fgl-dr4).* Retrieved from https://arxiv.org/abs/2307.12546

Barning, F. J. M. (1963, August). The numerical analysis of the light-curve of 12 Lacertae. *BAIN*, *17*, 22.

Barrett, P., McConnell, M., Drake, S., Lim, J., Ferrario, L., & Vennes, S. (1999, April). Radio and Optical Observations of RE J0317−853: a Suspected 2.2 MeV Gamma-Ray Source. In *Aas/high energy astrophysics division #4* (Vol. 4, p. 33.10).

Barrett, P. E., & Gurwell, M. A. (2025, jun). Submillimeter observations of the white dwarf pulsar ar sco. *The Astrophysical Journal*, *986*(1), 78. Retrieved from https://doi.org/10.3847/1538-4357/add725 doi: 10.3847/1538-4357/add725

Barstow, M., Jordan, S., ODonoghue, D., Burleigh, M., Napiwotzki, R., & Harrop-Allin, M. (1995). Re j0317–853: the hottest known highly magnetic da white dwarf. *Monthly Notices of the Royal Astronomical Society*, *277*(3), 971–985.

Becker, W., et al. (2009). *Neutron stars and pulsars* (Vol. 357). Springer.

Berg, R. A., & Duthie, J. G. (1977). The nature of am herculis. *Astrophysical Journal, Vol. 211, p. 859-865*, *211*, 859–865.

Bertin, E. (2013, January). *PSFEx: Point Spread Function Extractor.* Astrophysics Source Code Library, record ascl:1301.001.

Bertin, E., & Arnouts, S. (1996). Sextractor: Software for source extraction. *Astron. Astrophys. Suppl. Ser.*, *117*(2), 393-404. Retrieved from https://doi.org/10.1051/aas:1996164 doi: 10.1051/aas:1996164

Bjorklund, R., Crandall, W. E., Moyer, B. J., & York, H. F. (1950, Jan). High energy photons from proton-nucleon collisions. *Phys. Rev.*, *77*, 213–218. Retrieved from https://link.aps.org/

doi/10.1103/PhysRev.77.213 doi: 10.1103/PhysRev.77.213

Bowyer, S., & Malina, R. (1991). The extreme ultraviolet explorer mission. *Advances in Space Research*, *11*(11), 205-215. Retrieved from https://www.sciencedirect.com/science/article/pii/027311779190077W doi: https://doi.org/10.1016/0273-1177(91)90077-W

Breus, V., Andronov, I. L., Dubovsky, P., Kim, Y., Yoon, J. N., & Petrk, K. (2025, 06). Spin-period variations in the intermediate polar rx j2133.7+5107. *Monthly Notices of the Royal Astronomical Society*, *541*(2), 1064-1068. Retrieved from https://doi.org/10.1093/mnras/staf921 doi: 10.1093/mnras/staf921

Brinkworth, C. S., Burleigh, M. R., Lawrie, K., Marsh, T. R., & Knigge, C. (2013). Measuring the rotational periods of isolated magnetic white dwarfs. *The Astrophysical Journal*, *773*(1), 47.

Buccheri, R., Bennett, K., Bignami, G. F., Bloemen, J. B. G. M., Boriakoff, V., Caraveo, P. A., ... Strong, A. W. (1983, December). Search for pulsed γ-ray emission from radio pulsars in the COS-B data. *AAP*, *128*, 245-251.

Buckley, D. A. (1997). Discless accretion in intermediate polars? *International Astronomical Union Colloquium*, *163*, 420423. doi: 10.1017/S0252921100042974

Buckley, D. A., Potter, S. B., Meintjes, P. J., Marsh, T. R., & Gänsicke, B. T. (2018). Polarimetric evidence of the first white dwarf pulsar: The binary system ar scorpii. *Galaxies*, *6*(1), 14.

Burleigh, M. R., Jordan, S., & Schweizer, W. (1998, dec). Phase-resolved far-ultraviolet hubble space telescope spectroscopy of the peculiar magnetic white dwarf re j0317−853. *The Astrophysical Journal*, *510*(1), L37. Retrieved from https://dx.doi.org/10.1086/311794 doi: 10.1086/311794

Cáceres, D. L., deCarvalho, S. M., Coelho, J. G., deLima, R. C. R., & Rueda, J. A. (2016, 11). Thermal x-ray emission from massive, fast rotating, highly magnetized white dwarfs. *Monthly Notices of the Royal Astronomical Society*, *465*(4), 4434-4440. Retrieved from https://doi.org/10.1093/mnras/stw3047 doi: 10.1093/mnras/stw3047

Caleb, M., Heywood, I., Rajwade, K., Malenta, M., Willem Stappers, B., Barr, E., ... others (2022). Discovery of a radio-emitting neutron star with an ultra-long spin period of 76 s. *Nature Astronomy*, *6*(7), 828–836.

Camenzind, M. (2007). *Compact objects in astrophysics: White dwarfs, neutron stars and black holes* (1st ed.). Berlin, Heidelberg: Springer-Verlag Berlin Heidelberg. Retrieved from https://doi.org/10.1007/978-3-540-49912-1 (eBook published 24 February 2007; Hardcover published 15 February 2007; Softcover published 23 August 2016) doi: 10.1007/978-3-540-49912-1

Campbell, C. G. (1985, 08). The maintenance of corotation in the strong polars. *Monthly Notices of the Royal Astronomical Society*, *215*(3), 509-516. Retrieved from https://doi.org/10.1093/mnras/215.3.509 doi: 10.1093/mnras/215.3.509

Carroll, B. W., & Ostlie, D. A. (2017). *An introduction to modern astrophysics*. Cambridge University Press.

CASA Team, Bean, B., Bhatnagar, S., Castro, S., Donovan Meyer, J., Emonts, B., ... Kern, J. (2022, November). CASA, the Common Astronomy Software Applications for Radio Astronomy. *PASP*, *134*(1041), 114501. doi: 10.1088/1538-3873/ac9642

Castro-Tirado, A. J., Soldn, J., Bernas, M., Pta, P., Rezek, T., Hudec, R., ... Gimnez, A. (1999). The burst observer and optical transient exploring system (bootes). *Astron. Astrophys. Suppl. Ser.*, *138*(3), 583-585. Retrieved from https://doi.org/10.1051/aas:1999362 doi: 10.1051/aas:1999362

Castro-Tirado, A. J. (2011, Jan.). Robotic astronomy and the bootes network of robotic telescopes. *Acta Polytechnica*, *51*(1). Retrieved from https://ojst2.is.cvut.cz/ojs/index.php/ap/article/view/1308 doi: 10.14311/1308

Chen, K., & Ruderman, M. (1993, January). Pulsar Death Lines and Death Valley. *ApJ*, *402*, 264. doi: 10.1086/172129

Cheng, K. S., Ho, C., & Ruderman, M. (1986, January). Energetic Radiation from Rapidly Spinning Pulsars. I. Outer Magnetosphere Gaps. *ApJ*, *300*, 500. doi: 10.1086/163829

Cropper, M. (1990). The polars. *Space Science Reviews*, *54*(3), 195–295.

Cumming, A., Marcy, G. W., & Butler, R. P. (1999, dec). The lick planet search: Detectability and mass thresholds. *The Astrophysical Journal*, *526*(2), 890. Retrieved from https://dx.doi.org/10.1086/308020 doi: 10.1086/308020

Damour, T., & Deruelle, N. (1986). General relativistic celestial mechanics of binary systems. ii. the post-newtonian timing formula. In *Annales de l'ihp physique théorique* (pp. 263–292).

de Jager, O. C., Raubenheimer, B. C., & Swanepoel, J. W. H. (1989, August). A powerful test for weak periodic signals with unknown light curve shape in sparse data. *AAP*, *221*, 180-190.

de Jager, O. C., & Bsching, I. (2010). The h-test probability distribution revisited: improved sensitivity. *A&A*, *517*, L9. Retrieved from https://doi.org/10.1051/0004-6361/201014362 doi: 10.1051/0004-6361/201014362

Debnath, L., & Debnath, L. (2002). The wavelet transform and its basic properties. *Wavelet Transforms and Their Applications*, 361–402.

Dessert, C., Long, A. J., & Safdi, B. R. (2019, Aug). X-ray signatures of axion conversion in magnetic white dwarf stars. *Phys. Rev. Lett.*, *123*, 061104. Retrieved from https://link.aps.org/doi/10.1103/PhysRevLett.123.061104 doi: 10.1103/PhysRevLett.123.061104

Dessert, C., Long, A. J., & Safdi, B. R. (2022, Feb). No evidence for axions from chandra observation of the magnetic white dwarf re j0317−853. *Phys. Rev. Lett.*, *128*, 071102. Retrieved from https://link.aps.org/doi/10.1103/PhysRevLett.128.071102 doi: 10.1103/PhysRevLett.128.071102

Deutsch, A. J. (1955, January). The electromagnetic field of an idealized star in rigid rotation in vacuo. *Annales d'Astrophysique*, *18*, 1.

Eastman, J., Siverd, R., & Gaudi, B. S. (2010, August). Achieving Better Than 1 Minute Accuracy in the Heliocentric and Barycentric Julian Dates. *PASP*, *122*(894), 935. doi: 10.1086/655938

Efron, B., & Tibshirani, R. J. (1994). *An introduction to the bootstrap*. Chapman and Hall/CRC.

Erber, T. (1966, Oct). High-energy electromagnetic conversion processes in intense magnetic fields. *Rev. Mod. Phys.*, *38*, 626–659. Retrieved from https://link.aps.org/doi/10.1103/RevModPhys.38.626 doi: 10.1103/RevModPhys.38.626

Ferrario, L., de Martino, D., & Gänsicke, B. T. (2015). Magnetic white dwarfs. *Space Science Reviews*, *191*, 111–169.

Ferrario, L., Vennes, S., Wickramasinghe, D. T., Bailey, J. A., & Christian, D. J. (1997, 12). EUVE J0317−855: a rapidly rotating, high-field magnetic white dwarf. *Monthly Notices of the Royal*

Astronomical Society, *292*(2), 205-217. Retrieved from https://doi.org/10.1093/mnras/292.2.205 doi: 10.1093/mnras/292.2.205

Ferrario, L., & Wickramasinghe, D. T. (2005, 01). Magnetic fields and rotation in white dwarfs and neutron stars. *Monthly Notices of the Royal Astronomical Society*, *356*(2), 615-620. Retrieved from https://doi.org/10.1111/j.1365-2966.2004.08474.x doi: 10.1111/j.1365-2966.2004.08474.x

Fisher, R. A. (1925). Theory of statistical estimation. In *Mathematical proceedings of the cambridge philosophical society* (Vol. 22, pp. 700–725).

Fontaine, G., Brassard, P., & Bergeron, P. (2001, apr). The potential of white dwarf cosmochronology1. *Publications of the Astronomical Society of the Pacific*, *113*(782), 409. Retrieved from https://dx.doi.org/10.1086/319535 doi: 10.1086/319535

Foster, G. (1996, January). Time Series Analysis by Projection. I. Statistical Properties of Fourier Analysis. *AJ*, *111*, 541. doi: 10.1086/117805

Foster, G. (1996). Wavelets for period analysis of unevenly sampled time series. *Astronomical Journal v. 112, p. 1709-1729*, *112*, 1709–1729.

Fukugita, M., Ichikawa, T., Gunn, J. E., Doi, M., Shimasaku, K., & Schneider, D. P. (1996, April). The Sloan Digital Sky Survey Photometric System. *AJ*, *111*, 1748. doi: 10.1086/117915

Gaia Collaboration, Brown, A. G. A., Vallenari, A., Prusti, T., de Bruijne, J. H. J., Babusiaux, C., ... Zwitter, T. (2021). Gaia early data release 3 - summary of the contents and survey properties. *A&A*, *649*, A1. Retrieved from https://doi.org/10.1051/0004-6361/202039657 doi: 10.1051/0004-6361/202039657

García-Berro, E., Lorén-Aguilar, P., Aznar-Siguán, G., Torres, S., Camacho, J., Althaus, L. G., ... Isern, J. (2012). Double degenerate mergers as progenitors of high-field magnetic white dwarfs. *The Astrophysical Journal*, *749*(1), 25.

Garca-Berro, E., Lorn-Aguilar, P., Aznar-Sigun, G., Torres, S., Camacho, J., Althaus, L. G., ... Isern, J. (2012, mar). Double degenerate mergers as progenitors of high-field magnetic white dwarfs. *The Astrophysical Journal*, *749*(1), 25. Retrieved from https://dx.doi.org/10.1088/0004-637X/749/1/25 doi: 10.1088/0004-637X/749/1/25

Gehrels, N., & Mszros, P. (2012). Gamma-ray bursts. *Science*, *337*(6097), 932-936. Retrieved from https://www.science.org/doi/abs/10.1126/science.1216793 doi: 10.1126/science.1216793

Ghisellini, G. (2013). *Radiative processes in high energy astrophysics* (Vol. 873). Springer.

Giacconi, R., & Tananbaum, H. (1980). The einstein observatory: New perspectives in astronomy. *Science*, *209*(4459), 865-876. Retrieved from https://www.science.org/doi/abs/10.1126/science.209.4459.865 doi: 10.1126/science.209.4459.865

Gold, T. (1969). Rotating neutron stars and the nature of pulsars. *Nature*, *221*(5175), 25–27.

Goldreich, P., & Julian, W. H. (1969, August). Pulsar Electrodynamics. *ApJ*, *157*, 869. doi: 10.1086/150119

Green, J. C., Froning, C. S., Osterman, S., Ebbets, D., Heap, S. H., Leitherer, C., ... Wilkinson, E. (2011, dec). The cosmic origins spectrograph. *The Astrophysical Journal*, *744*(1), 60. Retrieved from https://dx.doi.org/10.1088/0004-637X/744/1/60 doi: 10.1088/0004-637X/744/1/60

Harayama, A., Terada, Y., Ishida, M., Hayashi, T., Bamba, A., & Tashiro, M. S. (2013, 08). Search for Non-Thermal Emissions from an Isolated Magnetic White Dwarf, EUVE J0317 855, with Suzaku. *Publications of the Astronomical Society of Japan*, *65*(4), 73. Retrieved from https://doi.org/10.1093/pasj/65.4.73 doi: 10.1093/pasj/65.4.73

Harding, A., & Muslimov, A. (2005). Pulsar slot gaps and unidentified egret sources. *Astrophysics and Space Science*, *297*, 63–70.

Harding, A. K., & Muslimov, A. G. (2002, apr). Pulsar polar cap heating and surface thermal x-ray emission. ii. inverse compton radiation pair fronts. *The Astrophysical Journal*, *568*(2), 862. Retrieved from https://dx.doi.org/10.1086/338985 doi: 10.1086/338985

Harding, A. K., Stern, J. V., Dyks, J., & Frackowiak, M. (2008, jun). High-altitude emission from pulsar slot gaps: The crab pulsar. *The Astrophysical Journal*, *680*(2), 1378. Retrieved from https://dx.doi.org/10.1086/588037 doi: 10.1086/588037

Harding, A. K., Usov, V. V., & Muslimov, A. G. (2005, mar). High-energy emission from millisecond pulsars. *The Astrophysical Journal*, *622*(1), 531. Retrieved from https://dx.doi.org/

10.1086/427840 doi: 10.1086/427840

Hellier, C. (1996). The intermediate polars. In *International astronomical union colloquium* (Vol. 158, pp. 143–152).

Hellier, C. (2001). *Cataclysmic variable stars-how and why they vary*. Springer Science & Business Media.

Hertzsprung, E. (1905). Zur strahlung der sterne, teil 1. *Zeitschrift für wissenschaftliche Photographie, Photochemie und Photophysik*, *3*, 429–442.

Hessels, J. W. T., Ransom, S. M., Stairs, I. H., Freire, P. C. C., Kaspi, V. M., & Camilo, F. (2006). A radio pulsar spinning at 716 hz. *Science*, *311*(5769), 1901-1904. Retrieved from https://www.science.org/doi/abs/10.1126/science.1123430 doi: 10.1126/science.1123430

Hewett, P. C., Warren, S. J., Leggett, S. K., & Hodgkin, S. T. (2006, 04). The UKIRT Infrared Deep Sky Survey ZY JHK photometric system: passbands and synthetic colours. *Monthly Notices of the Royal Astronomical Society*, *367*(2), 454-468. Retrieved from https://doi.org/10.1111/j.1365-2966.2005.09969.x doi: 10.1111/j.1365-2966.2005.09969.x

Hewish, A., Bell, S., Pilkington, J., Scott, P., & Collins, R. (1968, February). Observation of a Rapidly Pulsating Radio Source. *Nature*, *217*(5130), 709-713. doi: 10.1038/217709a0

Hillas, A. M. (1984, January). The Origin of Ultra-High-Energy Cosmic Rays. *araa*, *22*, 425-444. doi: 10.1146/annurev.aa.22.090184.002233

Hirotani, K. (2006, dec). Particle accelerator in pulsar magnetospheres: Super-goldreich-julian current with ion emission from the neutron star surface. *The Astrophysical Journal*, *652*(2), 1475. Retrieved from https://dx.doi.org/10.1086/508317 doi: 10.1086/508317

Hobbs, G. B., Edwards, R. T., & Manchester, R. N. (2006, 05). tempo2, a new pulsar-timing package i. an overview. *Monthly Notices of the Royal Astronomical Society*, *369*(2), 655-672. Retrieved from https://doi.org/10.1111/j.1365-2966.2006.10302.x doi: 10.1111/j.1365-2966.2006.10302.x

Horne, J. H., & Baliunas, S. L. (1986, March). A Prescription for Period Analysis of Unevenly Sampled Time Series. *ApJ*, *302*, 757. doi: 10.1086/164037

Hu, Y.-D., Fernndez-Garca, E., Caballero-Garca, M. D., Prez-Garca, I., Carrasco-Garca, I. M.,

Castelln, A., ... Castro-Tirado, A. J. (2023). The burst observer and optical transient exploring system in the multi-messenger astronomy era. *Frontiers in Astronomy and Space Sciences*, *10*. Retrieved from https://www.frontiersin.org/journals/astronomy-and-space-sciences/articles/10.3389/fspas.2023.952887 doi: 10.3389/fspas.2023.952887

Hurley-Walker, N., Rea, N., McSweeney, S. J., Meyers, B. W., Lenc, E., Heywood, I., ... Williams, A. (2023, Jul 01). A long-period radio transient active for three decades. *Nature*, *619*(7970), 487-490. Retrieved from https://doi.org/10.1038/s41586-023-06202-5 doi: 10.1038/s41586-023-06202-5

Hurley-Walker, N., Zhang, X., Bahramian, A., McSweeney, S. J., O'Doherty, T. N., Hancock, P. J., ... Galvin, T. J. (2022, Jan 01). A radio transient with unusually slow periodic emission. *Nature*, *601*(7894), 526-530. Retrieved from https://doi.org/10.1038/s41586-021-04272-x doi: 10.1038/s41586-021-04272-x

Hyman, S. D., Lazio, T. J. W., Kassim, N. E., Ray, P. S., Markwardt, C. B., & Yusef-Zadeh, F. (2005). A powerful bursting radio source towards the galactic centre. *nature*, *434*(7029), 50–52.

Ikhsanov, N. R., & Biermann, P. L. (2006). High-energy emission of fast rotating white dwarfs. *A&A*, *445*(1), 305-312. Retrieved from https://doi.org/10.1051/0004-6361:20053179 doi: 10.1051/0004-6361:20053179

Irwin, J. A. (2021). *Astrophysics: decoding the cosmos*. John Wiley & Sons.

Isern, J., Garca-Berro, E., Klebi, B., & Lorn-Aguilar, P. (2017, feb). A common origin of magnetism from planets to white dwarfs. *The Astrophysical Journal Letters*, *836*(2), L28. Retrieved from https://dx.doi.org/10.3847/2041-8213/aa5eae doi: 10.3847/2041-8213/aa5eae

Jackson, J. D. (1975). *Classical electrodynamics*. New York, NY, USA: Wiley & Sons.

Jonas, J., & MeerKAT Team. (2016, January). The MeerKAT Radio Telescope. In *Meerkat science: On the pathway to the ska* (p. 1). doi: 10.22323/1.277.0001

Kaplan, Q. (2021). *The search for high-energy gamma-ray emission from the close binary system ar scorpii using fermi-lat data* (Master's thesis). University of the Free State.

Kashiyama, K., Ioka, K., & Kawanaka, N. (2011, Jan). White dwarf pulsars as possible cosmic ray electron-positron factories. *Phys. Rev. D*, *83*, 023002. Retrieved from https://link.aps.org/doi/10.1103/PhysRevD.83.023002 doi: 10.1103/PhysRevD.83.023002

Kepler, S. O., Winget, D. E., Nather, R. E., Bradley, P. A., Grauer, A. D., Fontaine, G., ... others (1991). A detection of the evolutionary time scale of the da white dwarf g117-b15a with the whole earth telescope. *The Astrophysical Journal. Chicago. Vol. 378, no. 2, pt. 2 (Sept. 1991), p. l45-l48*.

Kilic, M., Kosakowski, A., Moss, A. G., Bergeron, P., & Conly, A. A. (2021, dec). An isolated white dwarf with a 70 s spin period. *The Astrophysical Journal Letters*, *923*(1), L6. Retrieved from https://dx.doi.org/10.3847/2041-8213/ac3b60 doi: 10.3847/2041-8213/ac3b60

King, A., & Shaviv, G. (1984). X-ray emission from non-magnetic cataclysmic variables. *Nature*, *308*(5959), 519–521.

King, A. R., & Lasota, J.-P. (1991, September). Spin Evolution and Magnetic Fields in Cataclysmic Variables. *ApJ*, *378*, 674. doi: 10.1086/170467

Koyama, K., Tsunemi, H., Dotani, T., Bautz, M. W., Hayashida, K., Tsuru, T. G., ... Awaki, H. (2007, 01). X-Ray Imaging Spectrometer (XIS) on Board Suzaku. *Publications of the Astronomical Society of Japan*, *59*(sp1), S23-S33. Retrieved from https://doi.org/10.1093/pasj/59.sp1.S23 doi: 10.1093/pasj/59.sp1.S23

Kuiper, L., Hermsen, W., Krijger, J. M., Bennett, K., Schoenfelder, V., Carraminana, A., ... Bailes, M. (1998). *Comptel detection of pulsed emission from psr b1509-58 up to at least 10 mev.* Retrieved from https://arxiv.org/abs/astro-ph/9812405

Klebi, B., Jordan, S., Nelan, E., Bastian, U., & Altmann, M. (2010). Constraints on the origin of the massive, hot, and rapidly rotating magnetic white dwarf rej0317−853 from an hst parallax measurement⋆. *A&A*, *524*, A36. Retrieved from https://doi.org/10.1051/0004-6361/201015237 doi: 10.1051/0004-6361/201015237

Lattimer, J. M., & Prakash, M. (2004). The physics of neutron stars. *Science*, *304*(5670), 536-542. Retrieved from https://www.science.org/doi/abs/10.1126/science.1090720 doi: 10.1126/science.1090720

Lawrie, K. A., Burleigh, M. R., Barlow, B. N., O'Donoghue, D., Barstow, M. A., Marsh, T. R., ... Worters, H. (2013, January). Detecting the Orbital Motion of RE J0317−853 and LB 9802. In J. Krzesiński, G. Stachowski, P. Moskalik, & K. Bajan (Eds.), *18th european white dwarf workshop.* (Vol. 469, p. 385).

Lobato, R. V., Coelho, J. G., & Malheiro, M. (2015, 12). Radio pulsar death lines to sgrs/axps and white dwarfs pulsars. *AIP Conference Proceedings*, *1693*(1), 030003. Retrieved from https://doi.org/10.1063/1.4937186 doi: 10.1063/1.4937186

Lobato, R. V., Coelho, J. G., & Malheiro, M. (2017, jun). Ultra-high energy cosmic rays from white dwarf pulsars and the hillas criterion. *Journal of Physics: Conference Series*, *861*(1), 012005. Retrieved from https://dx.doi.org/10.1088/1742-6596/861/1/012005 doi: 10.1088/1742-6596/861/1/012005

Lomb, N. R. (1976). Least-squares frequency analysis of unequally spaced data. *Astrophysics and space science*, *39*, 447–462. doi: https://doi.org/10.1007/BF00648343

Longair, M. S. (2011). *High energy astrophysics.* Cambridge university press.

Lopes de Oliveira, R., Bruch, A., Rodrigues, C. V., Oliveira, A. S., & Mukai, K. (2020, jul). Ctcv j2056-3014: An x-ray-faint intermediate polar harboring an extremely fast-spinning white dwarf. *The Astrophysical Journal Letters*, *898*(2), L40. Retrieved from https://dx.doi.org/10.3847/2041-8213/aba618 doi: 10.3847/2041-8213/aba618

Lorimer, D. R., & Kramer, M. (2005). *Handbook of pulsar astronomy* (Vol. 4). Cambridge university press.

Lumb, D. H., Jansen, F. A., & Schartel, N. (2012). X-ray Multi-mirror Mission (XMM-Newton) observatory. *Optical Engineering*, *51*(1), 011009. Retrieved from https://doi.org/10.1117/1.OE.51.1.011009 doi: 10.1117/1.OE.51.1.011009

Lyutikov, M., Blandford, R. D., & Machabeli, G. (1999, 05). On the nature of pulsar radio emission. *Monthly Notices of the Royal Astronomical Society*, *305*(2), 338-352. Retrieved from https://doi.org/10.1046/j.1365-8711.1999.02443.x doi: 10.1046/j.1365-8711.1999.02443.x

Madzime, S. T. (2021). *The search for pulsed radio and gamma-ray emission from the cataclysmic variable system ae aquarii using meerkat and fermi-lat data* (Master's thesis). University of

the Free State.

Madzime, S. T., & Meintjes, P. (2023). A search for gamma-ray emission from a sample of highly magnetised white dwarfs using Fermi-LAT data. *PoS*, *HEASA2022*, 055. doi: 10.22323/1.426.0055

Malheiro, M., Rueda, J. A., & Ruffini, R. (2012, 06). SGRs and AXPs as Rotation-Powered Massive White Dwarfs. *Publications of the Astronomical Society of Japan*, *64*(3), 56. Retrieved from https://doi.org/10.1093/pasj/64.3.56 doi: 10.1093/pasj/64.3.56

Manchester, R. N., & Taylor, J. H. (1977). Pulsars.

Mardia, K. V. (1972). *Statistics of directional data*. London: Academic Press.

Marsh, T., Gänsicke, B., Hümmerich, S., Hambsch, F.-J., Bernhard, K., Lloyd, C., ... others (2016). A radio-pulsing white dwarf binary star. *Nature*, *537*(7620), 374–377.

Mattox, J. R., Bertsch, D. L., Chiang, J., Dingus, B. L., Digel, S. W., Esposito, J. A., ... Willis, T. D. (1996, April). The Likelihood Analysis of EGRET Data. *ApJ*, *461*, 396. doi: 10.1086/177068

Meintjes, P. J. (1993). *A study of tev gamma ray emission from the magnetic cataclysmic variable ae aquarii* (Doctoral dissertation). University of Potchefstroom.

Meintjes, P. J., Madzime, S. T., Kaplan, Q., & van Heerden, H. J. (2023). Spun-up rotation-powered magnetized white dwarfs in close binaries as possible gamma-ray sources: Signatures of pulsed modulation from ae aquarii and ar scorpii in fermi-lat data. *Galaxies*, *11*(1). Retrieved from https://www.mdpi.com/2075-4434/11/1/14 doi: 10.3390/galaxies11010014

Meintjes, P. J., & Venter, L. A. (2005, 06). The diamagnetic blob propeller in AE Aquarii and non-thermal radio to mid-infrared emission. *Monthly Notices of the Royal Astronomical Society*, *360*(2), 573-582. Retrieved from https://doi.org/10.1111/j.1365-2966.2005.09045.x doi: 10.1111/j.1365-2966.2005.09045.x

Melikidze, G. I., Gil, J. A., & Pataraya, A. D. (2000, dec). The spark-associated soliton model for pulsar radio emission. *The Astrophysical Journal*, *544*(2), 1081. Retrieved from https://dx.doi.org/10.1086/317220 doi: 10.1086/317220

Melrose, D. B. (2017, Jul 25). Coherent emission mechanisms in astrophysical plasmas. *Reviews*

of Modern Plasma Physics, *1*(1), 5. Retrieved from https://doi.org/10.1007/s41614-017-0007-0 doi: 10.1007/s41614-017-0007-0

Melrose, D. B., Rafat, M. Z., & Mastrano, A. (2020, 10). Pulsar radio emission mechanisms: a critique. *Monthly Notices of the Royal Astronomical Society*, *500*(4), 4530-4548. Retrieved from https://doi.org/10.1093/mnras/staa3324 doi: 10.1093/mnras/staa3324

Mereghetti, S. (2001, 12). The anomalous x-ray pulsars. *AIP Conference Proceedings*, *599*(1), 219-228. Retrieved from https://doi.org/10.1063/1.1434635 doi: 10.1063/1.1434635

Michel, F. C. (1991). *Theory of neutron star magnetospheres*. University of Chicago Press.

Minnie, L., Meintjes, P. J., & Maritz, J. (2024). X-ray and gamma-ray periodic analysis of the fast rotating, highly magnetic white dwarf EUVE J0317-85.5. *PoS*, *HEASA2023*, 011. doi: 10.22323/1.459.0011

Mitra, D., Gil, J., & Melikidze, G. I. (2009, apr). Unraveling the nature of coherent pulsar radio emission. *The Astrophysical Journal*, *696*(2), L141. Retrieved from https://dx.doi.org/10.1088/0004-637X/696/2/L141 doi: 10.1088/0004-637X/696/2/L141

Mitsuda, K., Bautz, M., Inoue, H., Kelley, R. L., Koyama, K., Kunieda, H., ... Yoshida, A. (2007, 01). The X-Ray Observatory Suzaku. *Publications of the Astronomical Society of Japan*, *59*(sp1), S1-S7. Retrieved from https://doi.org/10.1093/pasj/59.sp1.S1 doi: 10.1093/pasj/59.sp1.S1

Moffett, D. A., & Hankins, T. H. (1996, September). Multifrequency radio observations of the crab pulsar. *The Astrophysical Journal*, *468*, 779. Retrieved from http://dx.doi.org/10.1086/177734 doi: 10.1086/177734

Moos, H. W., Cash, W. C., Cowie, L. L., Davidsen, A. F., Dupree, A. K., Feldman, P. D., ... Zheng, W. (2000, jul). Overview of the far ultraviolet spectroscopic explorer mission. *The Astrophysical Journal*, *538*(1), L1. Retrieved from https://dx.doi.org/10.1086/312795 doi: 10.1086/312795

Morse, J. A. (1994, jun). A method for correcting aspect solution errors in rosat hri observations of compact sources. *Publications of the Astronomical Society of the Pacific*, *106*(700), 675. Retrieved from https://dx.doi.org/10.1086/133428 doi: 10.1086/133428

Muslimov, A. G., & Harding, A. K. (2003, may). Extended acceleration in slot gaps and pulsar high-energy emission. *The Astrophysical Journal*, *588*(1), 430. Retrieved from https://dx.doi.org/10.1086/368162 doi: 10.1086/368162

Neyman, J., & Pearson, E. S. (1967). On the use and interpretation of certain test criteria for purposes of statistical inference. part i. In *Joint statistical papers* (pp. 1–66). Berkeley: University of California Press. Retrieved 2024-12-25, from https://doi.org/10.1525/9780520339897-003 doi: doi:10.1525/9780520339897-003

Ng, C.-Y., Takata, J., Leung, G. C. K., Cheng, K. S., & Philippopoulos, P. (2014, may). High-energy emission of the first millisecond pulsar. *The Astrophysical Journal*, *787*(2), 167. Retrieved from https://dx.doi.org/10.1088/0004-637X/787/2/167 doi: 10.1088/0004-637X/787/2/167

Ochelkov, Y. P., & Usov, V. (1980). Curvature radiation of relativistic particles in the magnetosphere of pulsars: I: Theory. *Astrophysics and Space Science*, *69*, 439–460.

Offringa, A. R., McKinley, B., Hurley-Walker, N., Briggs, F. H., Wayth, R. B., Kaplan, D. L., ... Williams, C. L. (2014, 08). wsclean: an implementation of a fast, generic wide-field imager for radio astronomy. *Monthly Notices of the Royal Astronomical Society*, *444*(1), 606-619. Retrieved from https://doi.org/10.1093/mnras/stu1368 doi: 10.1093/mnras/stu1368

Olausen, S. A., & Kaspi, V. M. (2014, apr). The mcgill magnetar catalog⋆. *The Astrophysical Journal Supplement Series*, *212*(1), 6. Retrieved from https://dx.doi.org/10.1088/0067-0049/212/1/6 doi: 10.1088/0067-0049/212/1/6

Ostriker, J. P., & Gunn, J. E. (1969, September). On the Nature of Pulsars. I. Theory. *ApJ*, *157*, 1395. doi: 10.1086/150160

Parker, T. L. (2005). *Accretion characteristics in intermediate polars*. Open University (United Kingdom).

Patterson, J. (1994, mar). The dq herculis stars. *Publications of the Astronomical Society of the Pacific*, *106*(697), 209. Retrieved from https://dx.doi.org/10.1086/133375 doi: 10.1086/133375

Patterson, J., Branch, D., Chincarini, G., & Robinson, E. L. (1980, September). 33 second X-ray

pulsations in AE Aquarii. *ApJL*, *240*, L133-L136. doi: 10.1086/183339

Pelisoli, I., Marsh, T., Buckley, D. A., Heywood, I., Potter, S. B., Schwope, A., ... others (2023). A 5.3-min-period pulsing white dwarf in a binary detected from radio to x-rays. *Nature Astronomy*, *7*(8), 931–942. doi: https://doi.org/10.1038/s41550-023-01995-x

Pelisoli, I., Marsh, T. R., Dhillon, V. S., Breedt, E., Brown, A. J., Dyer, M. J., ... Wild, J. F. (2021, 11). Found: a rapidly spinning white dwarf in lamost j024048.51+195226.9. *Monthly Notices of the Royal Astronomical Society: Letters*, *509*(1), L31-L36. Retrieved from https://doi.org/10.1093/mnrasl/slab116 doi: 10.1093/mnrasl/slab116

Pelisoli, I., Sahu, S., Lyutikov, M., Barkov, M., Gnsicke, B. T., Brink, J., ... Ramrez, S. H. (2023, 11). Unveiling the white dwarf in J191213.72−441045.1 through ultraviolet observations. *Monthly Notices of the Royal Astronomical Society*, *527*(2), 3826-3836. Retrieved from https://doi.org/10.1093/mnras/stad3442 doi: 10.1093/mnras/stad3442

Possenti, A., Cerutti, R., Colpi, M., & Mereghetti, S. (2002). Re-examining the x-ray versus spin-down luminosity correlation of rotation powered pulsars. *A&A*, *387*(3), 993-1002. Retrieved from https://doi.org/10.1051/0004-6361:20020472 doi: 10.1051/0004-6361:20020472

Potter, S., Buckley, D., O'Donoghue, D., O'Conner, J., Fourie, P., Evans, G., ... Still, M. (2008). A new two channel high-speed photo-polarimeter (HIPPO) for the SAAO. In I. S. McLean & M. M. Casali (Eds.), *Ground-based and airborne instrumentation for astronomy ii* (Vol. 7014, p. 70145E). SPIE. Retrieved from https://doi.org/10.1117/12.789716 doi: 10.1117/12.789716

Predehl, P., Andritschke, R., Arefiev, V., Babyshkin, V., Batanov, O., Becker, W., ... Yaroshenko, V. (2021). The erosita x-ray telescope on srg. *A&A*, *647*, A1. Retrieved from https://doi.org/10.1051/0004-6361/202039313 doi: 10.1051/0004-6361/202039313

Ptri, J. (2019, 02). Pulsar gamma-ray emission in the radiation reaction regime. *Monthly Notices of the Royal Astronomical Society*, *484*(4), 5669-5691. Retrieved from https://doi.org/10.1093/mnras/stz360 doi: 10.1093/mnras/stz360

Rea, N., Hurley-Walker, N., Pardo-Araujo, C., Ronchi, M., Graber, V., Coti Zelati, F., ... DallOra, M. (2024, jan). Long-period radio pulsars: Population study in the neutron star and white

dwarf rotating dipole scenarios. *The Astrophysical Journal*, *961*(2), 214. Retrieved from https://doi.org/10.3847/1538-4357/ad165d doi: 10.3847/1538-4357/ad165d

Ricker, G. R., Winn, J. N., Vanderspek, R., Latham, D. W., Bakos, G. Á., Bean, J. L., ... Villasenor, J. (2014). Transiting Exoplanet Survey Satellite. *Journal of Astronomical Telescopes, Instruments, and Systems*, *1*(1), 014003. Retrieved from https://doi.org/10.1117/1.JATIS.1.1.014003 doi: 10.1117/1.JATIS.1.1.014003

Romani, R. W. (1996, October). Gamma-Ray Pulsars: Radiation Processes in the Outer Magnetosphere. *ApJ*, *470*, 469. doi: 10.1086/177878

Romani, R. W., & Yadigaroglu, I.-A. (1995, January). Gamma-ray pulsars: Emission zones and viewing geometries. *The Astrophysical Journal*, *438*, 314. Retrieved from http://dx.doi.org/10.1086/175076 doi: 10.1086/175076

Ruderman, M. A., & Sutherland, P. G. (1975, February). Theory of pulsars: polar gaps, sparks, and coherent microwave radiation. *ApJ*, *196*, 51-72. doi: 10.1086/153393

Russell, H. N. (1919). Some problems of sidereal astronomy. *Proceedings of the National Academy of Sciences*, *5*(10), 391–416.

Rybicki, G. B., & Lightman, A. P. (1986). *Radiative Processes in Astrophysics*.

Scargle, J. D. (1982, December). Studies in astronomical time series analysis. II. Statistical aspects of spectral analysis of unevenly spaced data. *ApJ*, *263*, 835-853. doi: 10.1086/160554

Schimeczek, C., & Wunner, G. (2014). Accurate 2d finite element calculations for hydrogen in magnetic fields of arbitrary strength. *Computer Physics Communications*, *185*(2), 614-621. Retrieved from https://www.sciencedirect.com/science/article/pii/S0010465513003275 doi: https://doi.org/10.1016/j.cpc.2013.09.023

Schmidt, G. D., Stockman, H. S., & Smith, P. S. (1992, October). Discovery of a Sub-Megagauss Magnetic White Dwarf through Spectropolarimetry. *ApJL*, *398*, L57. doi: 10.1086/186576

Schreiber, M. R., Belloni, D., Gänsicke, B. T., Parsons, S. G., & Zorotovic, M. (2021, April). The origin and evolution of magnetic white dwarfs in close binary stars. *Nature Astronomy*, *5*, 648-654. doi: 10.1038/s41550-021-01346-8

Schwope, A., Marsh, T. R., Standke, A., Pelisoli, I., Potter, S., Buckley, D., ... Dhillon, V.

(2023). X-ray properties of the white dwarf pulsar erassu j191213.9−441044. *A&A*, *674*, L9. Retrieved from https://doi.org/10.1051/0004-6361/202346589 doi: 10.1051/0004-6361/202346589

Seeds, M. A., & Backman, D. (2016). *Foundations of astronomy, enhanced.* Cengage Learning.

Segura, N. C., Pelisoli, I., Gnsicke, B. T., Coppejans, D. L., Steeghs, D., Aungwerojwit, A., ... Buckley, D. A. H. (2025). *A sibling of ar scorpii: Sdss j230641.47+244055.8 and the observational blueprint of white dwarf pulsars.* Retrieved from https://arxiv.org/abs/2506.20455

Shapiro, I. I. (1964, Dec). Fourth test of general relativity. *Phys. Rev. Lett.*, *13*, 789–791. Retrieved from https://link.aps.org/doi/10.1103/PhysRevLett.13.789 doi: 10.1103/PhysRevLett.13.789

Shapiro, S. L., & Teukolsky, S. A. (1983). *Black holes, white dwarfs and neutron stars. The physics of compact objects.* doi: 10.1002/9783527617661

Smith, R. C. (2006). Cataclysmic variables. *Contemporary Physics*, *47*(6), 363–386. Retrieved from https://doi.org/10.1080/00107510601181175 doi: 10.1080/00107510601181175

Stevens, J., Wark, R., Edwards, P., Breen, S., & Lee-Waddell, K. (2014). *Atca users guide* (Tech. Rep.). Technical report, CSIRO.

Stiller, R. A., Littlefield, C., Garnavich, P., Wood, C., Hambsch, F.-J., & Myers, G. (2018, sep). High-time-resolution photometry of ar scorpii: Confirmation of the white dwarfs spin-down. *The Astronomical Journal*, *156*(4), 150. Retrieved from https://doi.org/10.3847/1538-3881/aad5dd doi: 10.3847/1538-3881/aad5dd

Stockman, H. S., Schmidt, G. D., Berriman, G., Liebert, J., Moore, R. L., & Wickramasinghe, D. T. (1992, December). A Search for Circular Polarization in Cataclysmic Variables. *ApJ*, *401*, 628. doi: 10.1086/172091

Sturrock, P. A. (1971, March). A Model of Pulsars. *ApJ*, *164*, 529. doi: 10.1086/150865

Sunyaev, R., Arefiev, V., Babyshkin, V., Bogomolov, A., Borisov, K., Buntov, M., ... Voron, V. (2021). Srg x-ray orbital observatory - its telescopes and first scientific results. *A&A*, *656*, A132. Retrieved from https://doi.org/10.1051/0004-6361/202141179 doi: 10.1051/

0004-6361/202141179

Takahashi, T., Abe, K., Endo, M., Endo, Y., Ezoe, Y., Fukazawa, Y., ... Yonetoku, D. (2007, 01). Hard X-Ray Detector (HXD) on Board Suzaku. *Publications of the Astronomical Society of Japan*, *59*(sp1), S35-S51. Retrieved from https://doi.org/10.1093/pasj/59.sp1.S35 doi: 10.1093/pasj/59.sp1.S35

Tapia, S. (1977, March). Discovery of a magnetic compact star in the AM Herculis / 3U 1809+50 system. *ApJL*, *212*, L125-L129. doi: 10.1086/182390

Team, T. L. (2018). *The lynx mission concept study interim report.* Retrieved from https://arxiv.org/abs/1809.09642

Terada, Y., Hayashi, T., Ishida, M., Mukai, K., Dotani, T., Okada, S., ... Makishima, K. (2008, 04). Suzaku Discovery of Hard X-Ray Pulsations from a Rotating Magnetized White Dwarf, AEAquarii. *Publications of the Astronomical Society of Japan*, *60*(2), 387-397. Retrieved from https://doi.org/10.1093/pasj/60.2.387 doi: 10.1093/pasj/60.2.387

Thompson, D. J., Bailes, M., Bertsch, D. L., Cordes, J., D'Amico, N., Esposito, J. A., ... Ulmer, M. (1999, may). Gamma radiation from psr b105552. *The Astrophysical Journal*, *516*(1), 297. Retrieved from https://dx.doi.org/10.1086/307083 doi: 10.1086/307083

Trmper, J. (1982a). The rosat mission. *Advances in Space Research*, *2*(4), 241-249. Retrieved from https://www.sciencedirect.com/science/article/pii/0273117782900709 doi: https://doi.org/10.1016/0273-1177(82)90070-9

Trmper, J. (1982b). The rosat mission. *Advances in Space Research*, *2*(4), 241-249. Retrieved from https://www.sciencedirect.com/science/article/pii/0273117782900709 doi: https://doi.org/10.1016/0273-1177(82)90070-9

Usov, V., & Melrose, D. (1995). Pulsars with strong magnetic fields: Polar gaps, bound pair creation and nonthermal luminosities. *Australian Journal of Physics*, *48*(4), 571–612.

Usov, V. V. (1988, March). Generation of Gamma-Rays by a Rotating Magnetic White Dwarf. *Soviet Astronomy Letters*, *14*, 258.

van Heerden, H., Fernndez-Garca, E. J., Castro-Tirado, A. J., Martin-Carrillo, A., Castellon, A., del Pulgar, P., ... Hanlon, L. (2024). Status of Boyden observatory and equipment for optical

counterpart studies of high energy sources. *PoS*, *HEASA2023*, 015. doi: 10.22323/1.459.0015

Van Heerden, H. J. (2015). *A search for pulsed high-energy non-thermal emission from the nova-like variable system ae aquarii* (Doctoral dissertation). University of the Free State.

Van Horn, H. M. (2015). *Unlocking the secrets of white dwarf stars*. Springer.

Vennes, S., Schmidt, G. D., Ferrario, L., Christian, D. J., Wickramasinghe, D. T., & Kawka, A. (2003, aug). A multiwavelength study of the high-field magnetic white dwarf euve j0317−85.5 (=re j0317−853). *The Astrophysical Journal*, *593*(2), 1040. Retrieved from https://dx.doi.org/10.1086/376728 doi: 10.1086/376728

Vink, J. (2011, Dec 08). Supernova remnants: the x-ray perspective. *The Astronomy and Astrophysics Review*, *20*(1), 49. Retrieved from https://doi.org/10.1007/s00159-011-0049-1 doi: 10.1007/s00159-011-0049-1

Walker, M. F. (1954). Nova dq herculis (1934): an eclipsing binary with very short period. *Publications of the Astronomical Society of the Pacific, Vol. 66, No. 392, p. 230*, *66*, 230.

Warner, B. (1996). Torques and instabilities in intermediate polars. *Astrophysics and Space Science*, *241*, 263–294.

Warner, B. (2003). *Cataclysmic variable stars* (Vol. 28). Cambridge University Press.

Warner, B., & Wickramasinghe, D. T. (1991, 02). White-dwarf rotational equilibria in magnetic cataclysmic variable stars. *Monthly Notices of the Royal Astronomical Society*, *248*(3), 370-376. Retrieved from https://doi.org/10.1093/mnras/248.3.370 doi: 10.1093/mnras/248.3.370

Weatherall, J. C. (1994, June). Streaming Instability in Relativistically Hot Pulsar Magnetospheres. *ApJ*, *428*, 261. doi: 10.1086/174237

Weisskopf, M. C., Aldcroft, T. L., Bautz, M., Cameron, R. A., Dewey, D., Drake, J. J., ... Murray, S. S. (2003, Aug 01). An overview of the performance of the chandra x-ray observatory. *Experimental Astronomy*, *16*(1), 1-68. Retrieved from https://doi.org/10.1023/B:EXPA.0000038953.49421.54 doi: 10.1023/B:EXPA.0000038953.49421.54

Wickramasinghe, D. T., & Ferrario, L. (2000, jul). Magnetism in isolated and binary white dwarfs. *Publications of the Astronomical Society of the Pacific*, *112*(773), 873. Retrieved

from https://dx.doi.org/10.1086/316593 doi: 10.1086/316593

Wickramasinghe, D. T., Wu, K., & Ferrario, L. (1991, 04). Intermediate polars as low-field magnetic cataclysmic variables. *Monthly Notices of the Royal Astronomical Society*, *249*(3), 460-467. Retrieved from https://doi.org/10.1093/mnras/249.3.460 doi: 10.1093/mnras/249.3.460

Wilks, S. S. (1938). The large-sample distribution of the likelihood ratio for testing composite hypotheses. *The Annals of Mathematical Statistics*, *9*(1), 60–62. Retrieved 2024-12-25, from http://www.jstor.org/stable/2957648

Wolf, M. (1924). Bewegter stern in virgo: Bd-13 3834. *Astronomische Nachrichten, volume 222, p. 47*, *222*, 47.

Wood, M., Caputo, R., Charles, E., Mauro, M. D., Magill, J., & Perkins, J. (2017). *Fermipy: An open-source python package for analysis of fermi-lat data.* Retrieved from https://arxiv.org/abs/1707.09551

Wu, K. (2000). Accretion onto magnetic white dwarfs. *Space Science Reviews*, *93*(3), 611–649.

Wu, K., & Kiss, L. L. (2008). High and low states of the system am herculis. *A&A*, *481*(2), 433-439. Retrieved from https://doi.org/10.1051/0004-6361:20078556 doi: 10.1051/0004-6361:20078556

Wynn, G. A., King, A. R., & Horne, K. (1997, 04). A magnetic propeller in the cataclysmic variable AE Aquarii. *Monthly Notices of the Royal Astronomical Society*, *286*(2), 436-446. Retrieved from https://doi.org/10.1093/mnras/286.2.436 doi: 10.1093/mnras/286.2.436

Young, M., Manchester, R. N., & Johnston, S. (1999). A radio pulsar with an 8.5-second period that challenges emission models. *Nature*, *400*(6747), 848–849.

Zechmeister, M., & Kürster, M. (2009). The generalised lomb-scargle periodogram - a new formalism for the floating-mean and keplerian periodograms. *A&A*, *496*(2), 577-584. Retrieved from https://doi.org/10.1051/0004-6361:200811296 doi: 10.1051/0004-6361:200811296

Zhang, B., & Gil, J. (2005, sep). Gcrt j17453009 as a transient white dwarf pulsar. *The Astrophysical Journal*, *631*(2), L143. Retrieved from https://dx.doi.org/10.1086/497428 doi: 10.1086/497428

Appendix A

Periodic Analysis of ROSAT X-ray Light Curve Using Different Time Bins

A.1 X-ray Light Curve Binned at 30 seconds

The source and background regions were all kept as a circle with radius $17''$ centered on J0317's position.

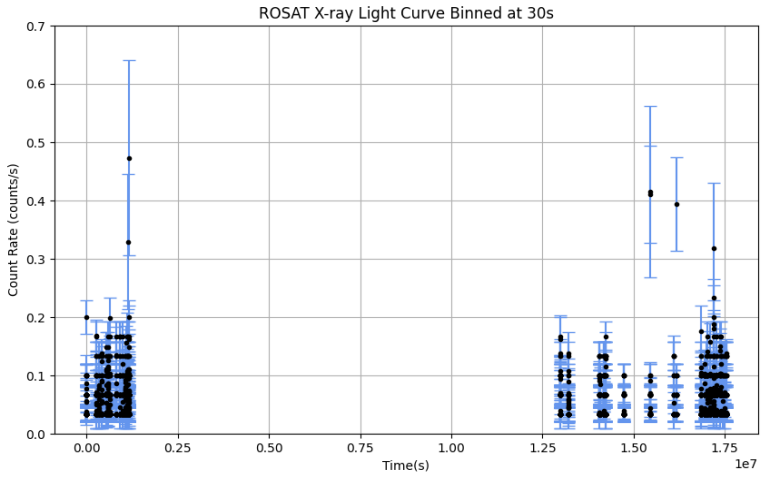

Figure A.1: 0.1-2.4 keV ROSAT light curve binned at 30 seconds.

The GLS periodogram of the 30 s binned light curve in Figure A.1 is shown below

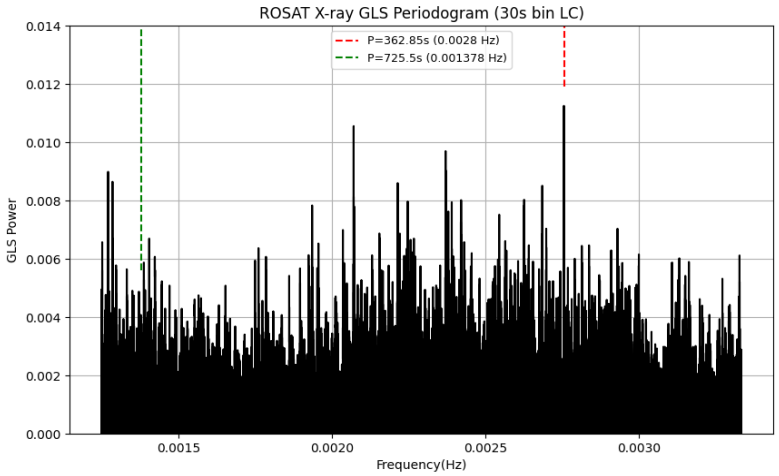

Figure A.2: GLS periodogram of the 30 s binned X-ray light curve in Figure A.1 showing a maximum peak at P∼362.85s

The FAP of the maximum peak is FAP=0.53 ($\sim 0.07\sigma$). The phase-folded X-ray light curve on both the rotation period P=725.5s and its first harmonic P∼362.85s respectively is shown below.

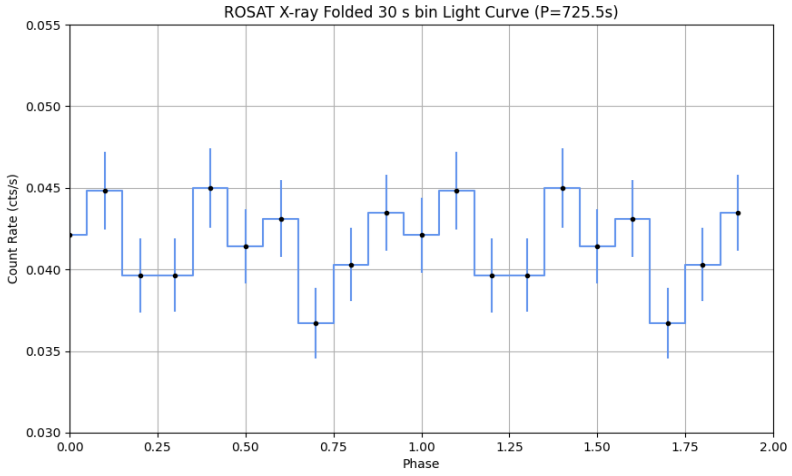

Figure A.3: ROSAT X-ray light curve binned at 30 s phase-folded on the spin period P=725.5s using ephemeris by Ferrario et al. (1997)

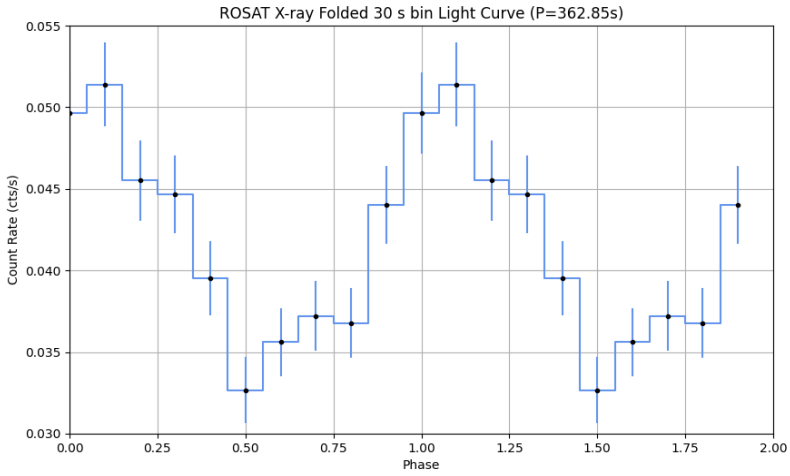

Figure A.4: ROSAT X-ray light curve binned at 30 s phase-folded on period P=362.85s using ephemeris by Ferrario et al. (1997)

A.2 X-ray Light Curve Binned at 50 seconds

The ROSAT X-ray light curve was then binned at 50 seconds still using the same $17''$ radius for the source and background region and is shown in Figure A.5 below and the corresponding GLS periodogram is shown in Figure A.6

The maximum peak is at a period P$\sim$362.86s and has FAP=0.076 ($\sim 1.43\sigma$) and the corresponding folded light curves on both the rotation period P=725.5s and its first harmonic $P\sim$362.86s respectively is shown in Figures below.

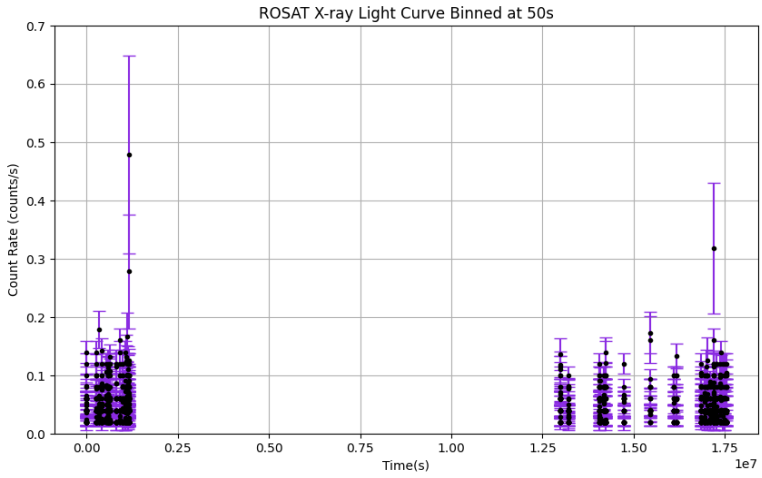

Figure A.5: 0.1-2.4 keV ROSAT X-ray light curve binned at 50 seconds.

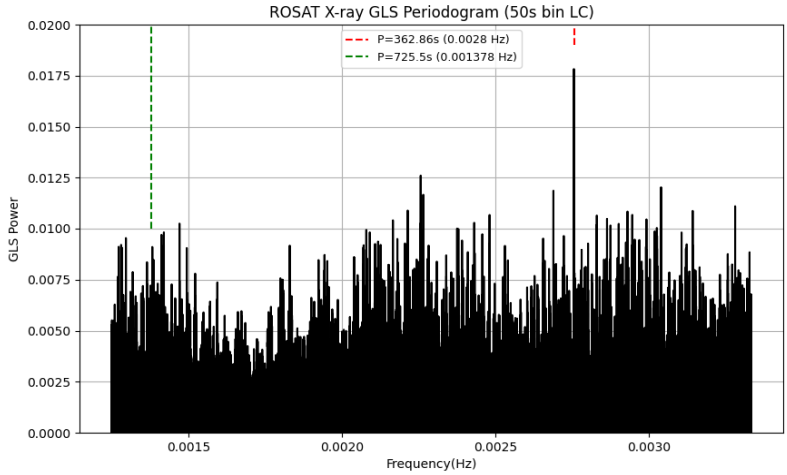

Figure A.6: GLS periodogram of the 50 s binned X-ray light curve in Figure A.5 showing a maximum peak at $P\sim$362.86s

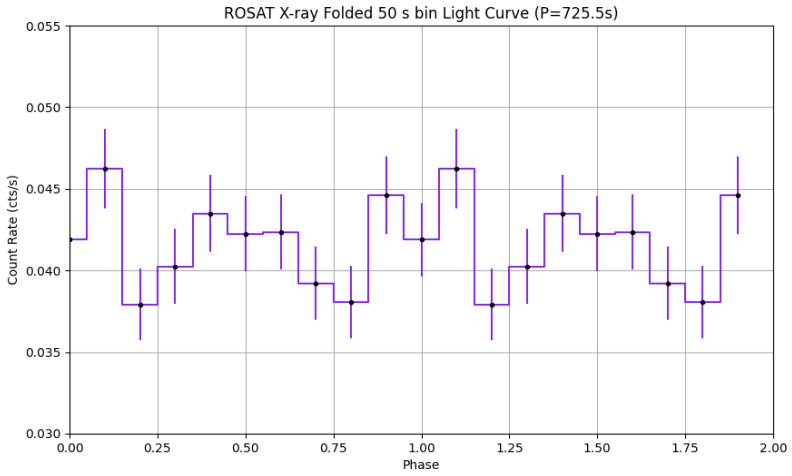

Figure A.7: ROSAT X-ray light curve binned at 50 s phase-folded on the spin period P=725.5s using ephemeris by Ferrario et al. (1997)

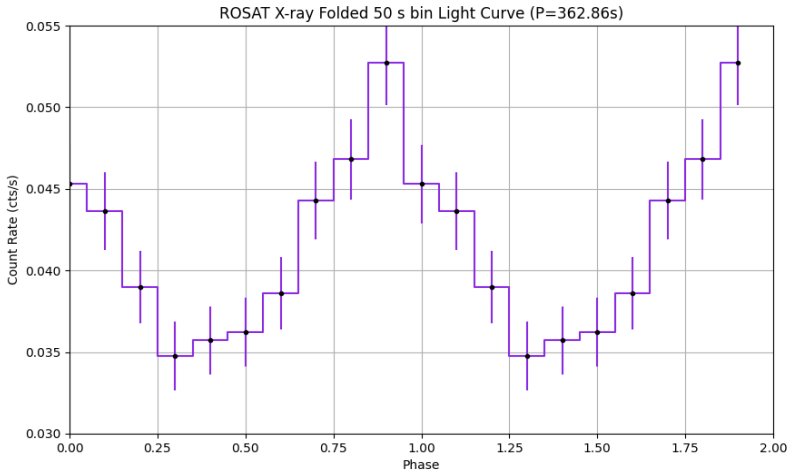

Figure A.8: ROSAT X-ray light curve binned at 50 s phase-folded on period P∼362.86s using ephemeris by Ferrario et al. (1997)

Appendix B

Periodogram Control Tests of J0317 in 0.5-10 GeV

Control tests of J0317 was done in the 0.5-10 GeV range at regions farther away from J0317's position. The Rayleigh test was performed on regions at a distance of 3°, 5°, 7° and 9° away from J0317's position shown in counts map below.

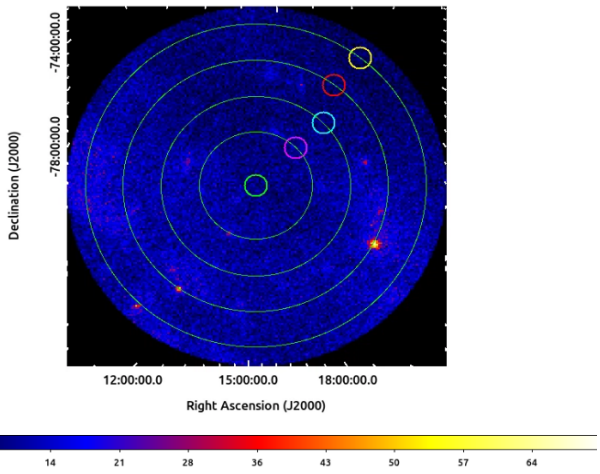

Figure B.1: 0.5-10 GeV 200×200 pixel counts map with 0.1° per pixel resolution of J0317 (0.6° radius green middle circle). Magenta, cyan, red and yellow 0.6° circles are on 3°, 5°, 7° and 9° radii circles respectively

B.1 Magenta Region

By using the same ephemeris, the Rayleigh periodogram in Figure B.2 below

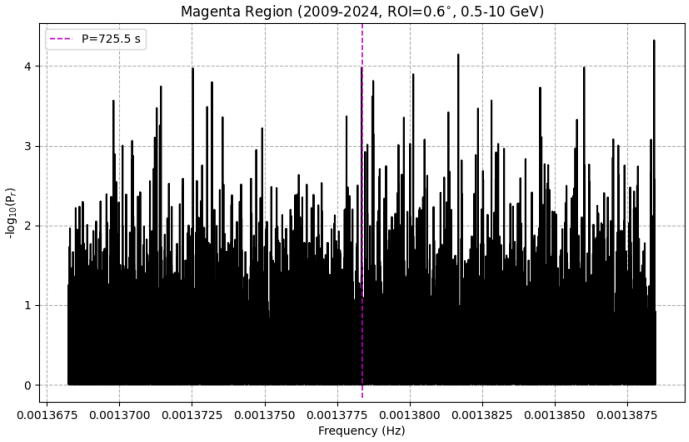

Figure B.2: Rayleigh periodogram of the magenta region showing no significant pulsations at the spin period of J0317.

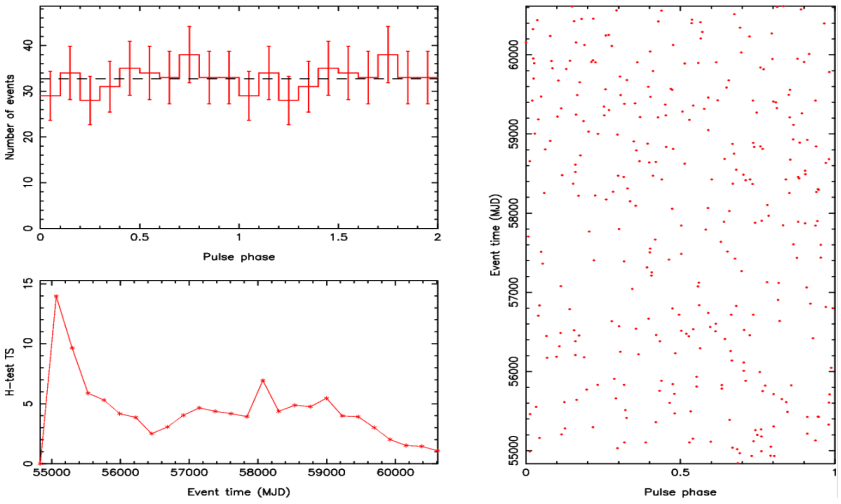

Figure B.3: H-test TS (bottom left), phase-folded γ-ray light curve (top left) and phaseogram of the magenta region using the same ephemeris by Ferrario et al. (1997).

From the Rayleigh periodogram, it is clear that there are no significant pulsations at the spin period of J0317 (P∼725.5). The H-test TS also confirms this by its very low value of TS∼1.

B.2 Cyan Region

The Rayleigh periodogram, folded light curve (using the same ephemeris) and H-test TS of the cyan region which is on a 5° in Figure B.1 also show no significant pulsations at J0317's spin period in Figures B.4 and B.5 below.

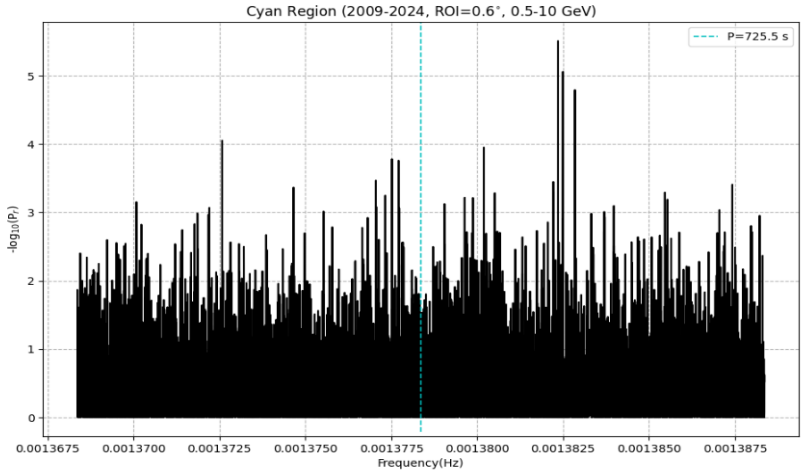

Figure B.4: Rayleigh periodogram of the cyan region showing no significant pulsations at the spin period of J0317.

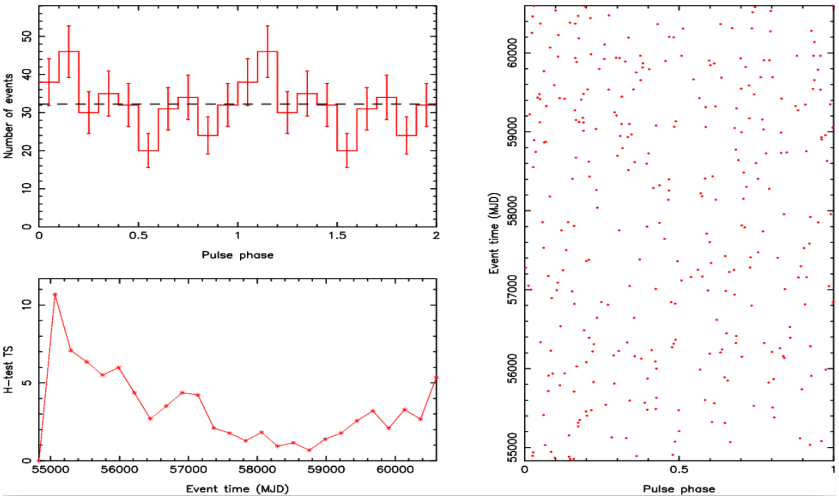

Figure B.5: H-test TS (bottom left), folded γ-ray light curve (top left) and phaseogram of the cyan region using the same ephemeris by Ferrario et al. (1997).

B.3 Red Region

The Rayleigh periodogram, folded light curve (using the same ephemeris) and H-test TS of the cyan region which is on a 7° circle centered on J0317's position in Figure B.1 also show no significant pulsations at J0317's spin period in Figures B.6 and B.7 below.

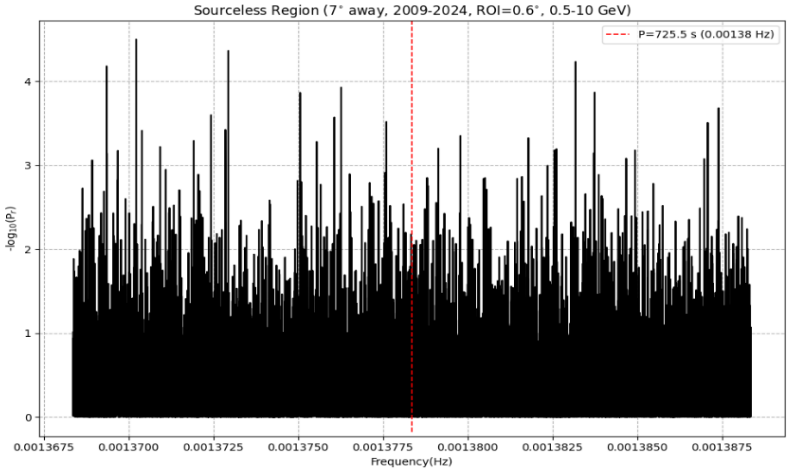

Figure B.6: Rayleigh periodogram of the red region showing no significant pulsations at the spin period of J0317.

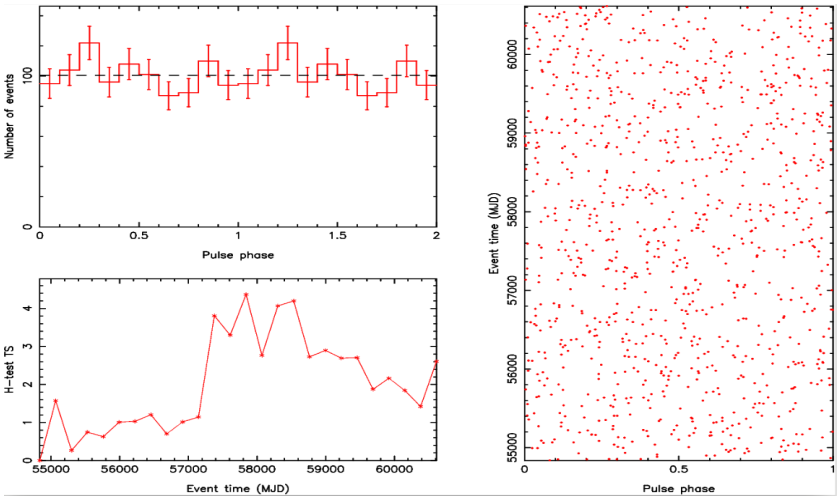

Figure B.7: H-test TS (bottom left), folded γ-ray light curve (top left) and phaseogram of the red region using the same ephemeris by Ferrario et al. (1997).

B.4 Yellow Region

The Rayleigh periodogram, folded light curve (using the same ephemeris) and H-test TS of the yellow region which is on a 9° in Figure B.1 also show no significant pulsations at J0317's spin period in Figures B.8 and B.7 below.

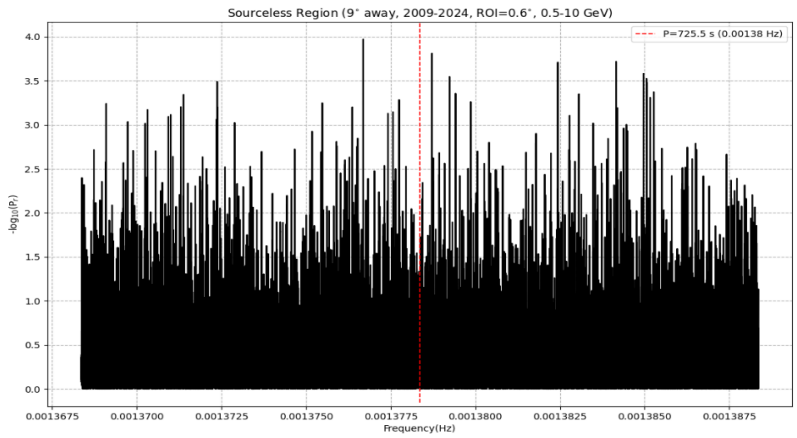

Figure B.8: Rayleigh periodogram of the yellow region showing no significant pulsations at the spin period of J0317.

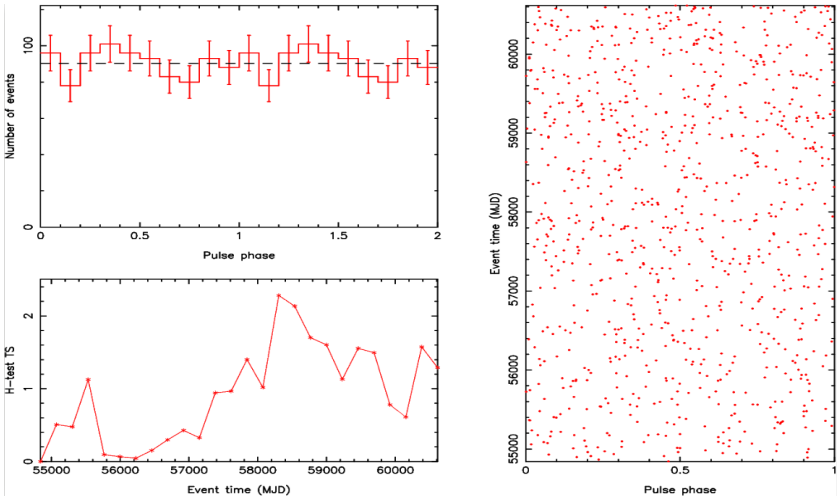

Figure B.9: H-test TS (bottom left), folded γ-ray light curve (top left) and phaseogram of the yellow region using the same ephemeris by Ferrario et al. (1997).

Based on these control tests, we can conclude that the pulsation from J0317's region is inherent to J0317 and not a result of the analysis techniques.

Appendix C

Periodogram Control Tests of TS gated data of J0317 in the 0.5-10 GeV band

We performed control tests on regions that lie on the circumferences of circles centred on J0317's coordinates with radii 3°, 5°, 7° and 9°. The TS gating analysis was performed on each of these ROI=0.6° regions and the Rayleigh test was executed on these regions. The regions are shown in Figure C.1 below.

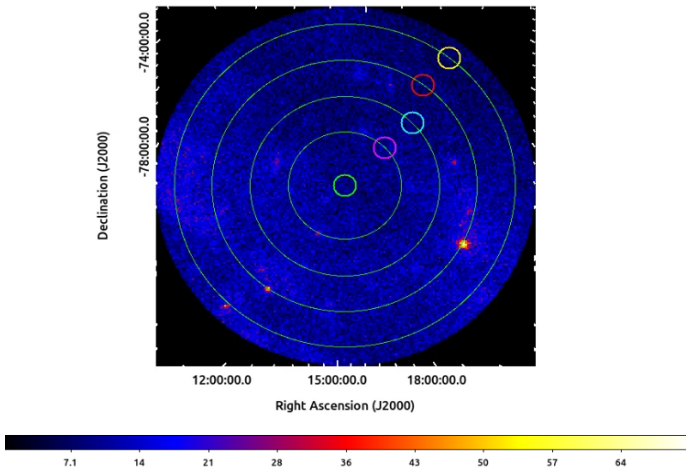

Figure C.1: 0.5-10 GeV 200×200 pixel counts map with 0.1° per pixel resolution of J0317 (0.6° radius green middle circle). Magenta, cyan, red and yellow 0.6° circles are on 3°, 5°, 7° and 9° radii circles respectively

C.1 TS Gated Magenta Region

The Rayleigh test was performed on the magenta region in Figure C.1 and the Rayleigh periodogram is shown in Figure below. A sample frequency of 2.00×10^{-11} Hz was used which is 1% of the Fourier resolution (2.00×10^{-9} Hz) with 1×10^{6} number of trials. This resulted in a period search range of ∼720-730 s. The Rayleigh periodogram of the TS gated magenta region is shown in Figure C.2 below together with zoomed in version in Figure C.3.

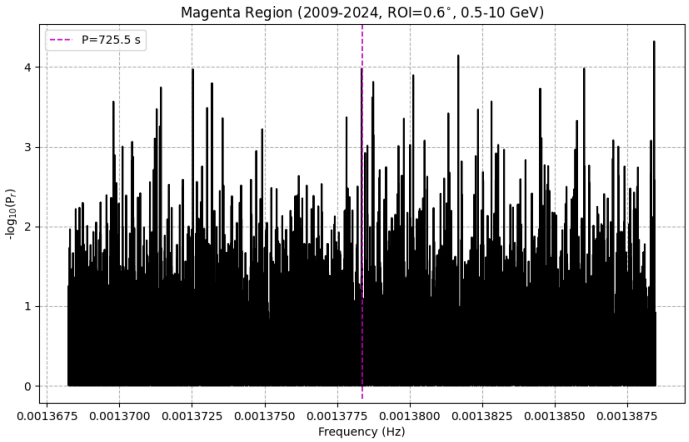

Figure C.2: Rayleigh periodogram of the TS gated magenta region showing no significant pulsations at the rotation period of J0317.

The Rayleigh periodogram of the TS gated magenta region shows no significant pulsation at the rotation period of J0317. The folded γ-ray light curve in Figure C.4 also shows no signatures of pulsed emission and the H-test TS also confirms this with a low TS∼3.

C.2 TS Gated Cyan Region

The same TS gated analysis was performed on the cyan region in Figure C.1 and the Rayleigh periodogram is shown in Figure C.5 below

The Rayleigh periodogram (Figure C.5) does show a peak near the spin period of J0317 and the folded light curve also shows some signatures of pulsed behavior but the H-test TS shows that

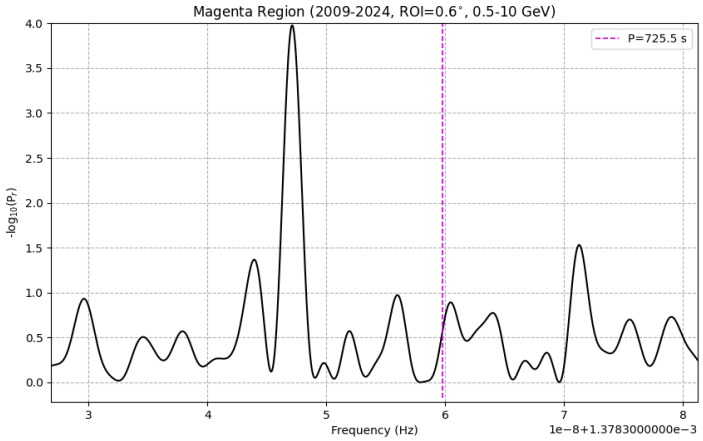

Figure C.3: Zoomed-in Rayleigh periodogram of the TS gated magenta region showing no significant pulsations at the spin period of J0317.

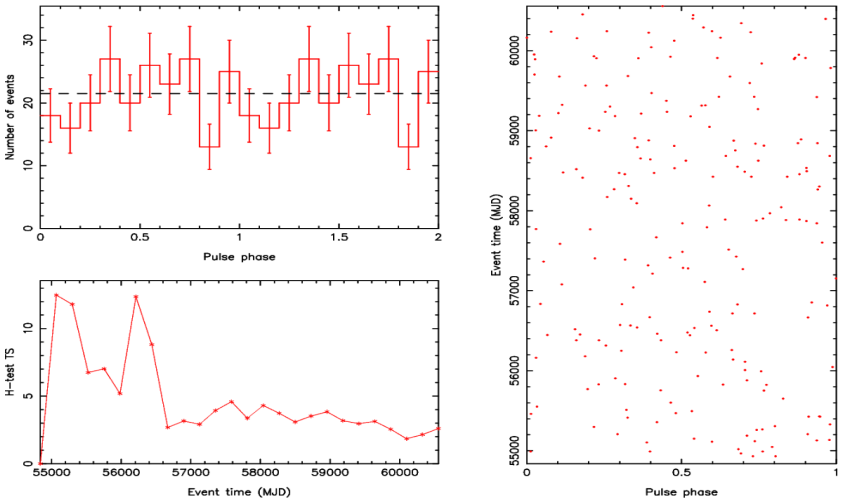

Figure C.4: H-test TS (bottom left), folded γ-ray light curve (top left) and phaseogram of the magenta region using the same ephemeris by Ferrario et al. (1997).

it is insignificant reaching a TS$\sim$7.

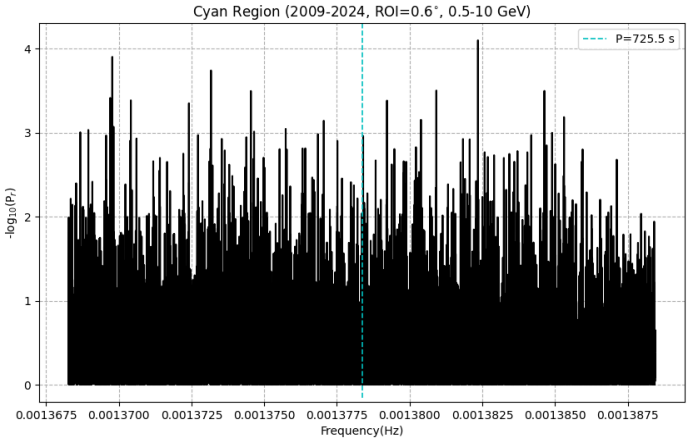

Figure C.5: Rayleigh periodogram of the TS gated cyan region showing no significant pulsations at the spin period of J0317.

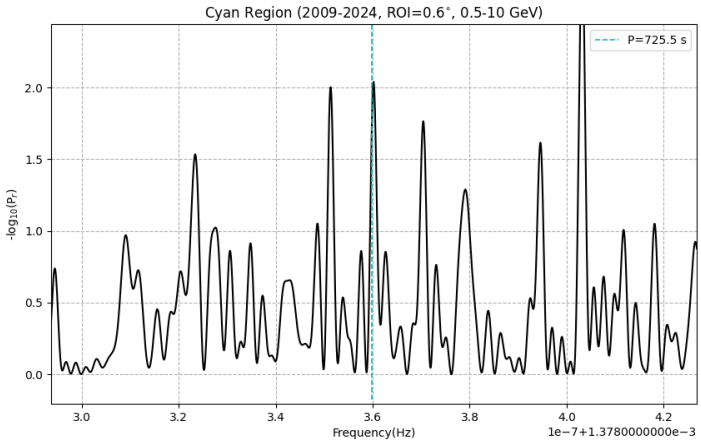

Figure C.6: Zoomed-in Rayleigh periodogram of the TS gated cyan region showing no significant pulsations at the spin period of J0317.

C.3 TS Gated Red Region

The same TS gated analysis was performed on the red region in Figure C.1 and the Rayleigh periodogram is shown in Figure C.8 below

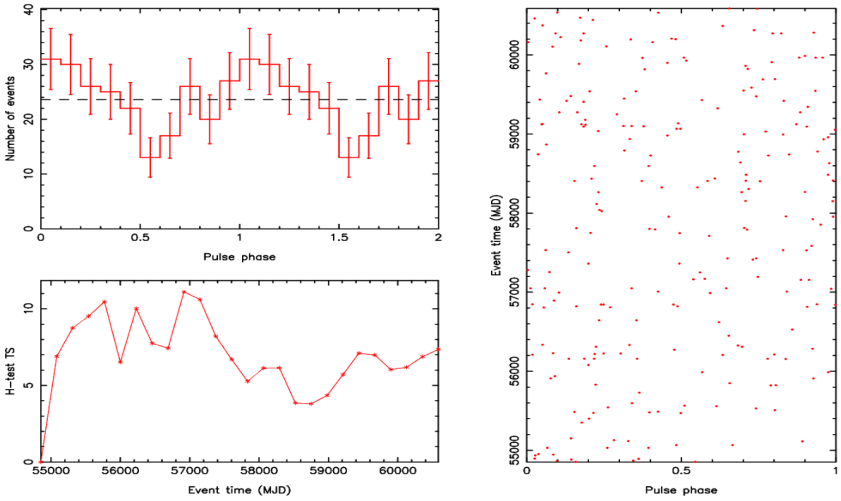

Figure C.7: H-test TS (bottom left), phase-folded γ-ray light curve (top left) and phaseogram of the cyan region using the same ephemeris by Ferrario et al. (1997).

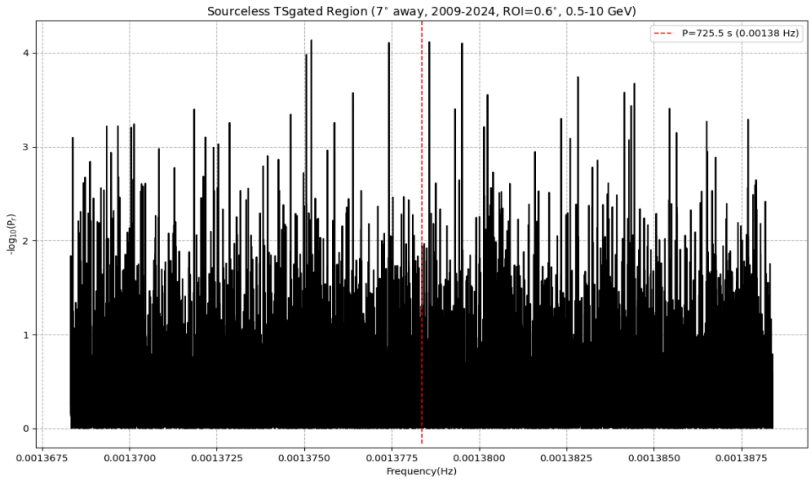

Figure C.8: Rayleigh periodogram of the TS gated red region showing no significant pulsations at the spin period of J0317.

C.4 TS Gated Yellow Region

The same TS gated analysis was performed on the yellow region in Figure C.1 and the Rayleigh periodogram is shown in Figure C.10 below

Both these TS gated regions revealed no significant pulsations at the spin period of J0317

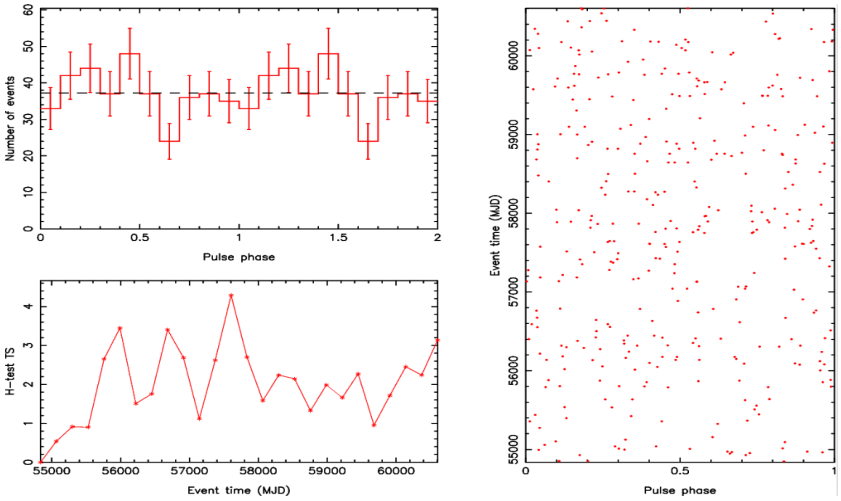

Figure C.9: H-test TS (bottom left), phase-folded γ-ray light curve (top left) and phaseogram of the red region using the same ephemeris by Ferrario et al. (1997).

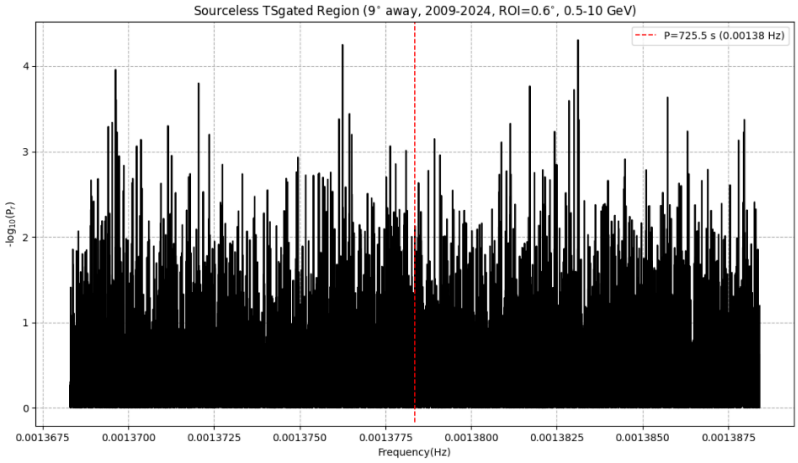

Figure C.10: Rayleigh periodogram of the TS gated yellow region showing no significant pulsations at the spin period of J0317.

suggesting that the pulsations from J0317 are **inherent to J0317 and not a feature introduced by the analysis techniques**.

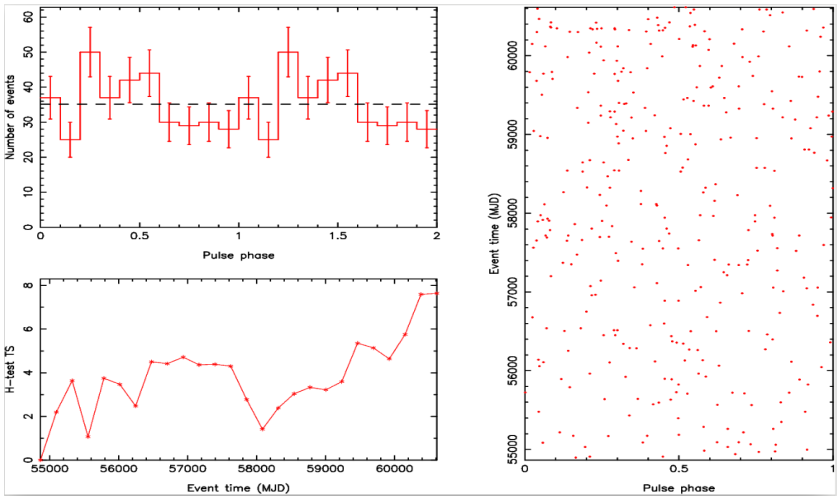

Figure C.11: H-test TS (bottom left), phase-folded γ-ray light curve (top left) and phaseogram of the yellow region using the same ephemeris by Ferrario et al. (1997).

Appendix D

Periodogram Control Tests of J1912 in the 0.5-10 GeV band

Control tests were done on sourceless ROI=0.6° regions on the circumferences of circles with radii 3°, 5°, 7° and 9° away from J1912. The regions are shown in Figure D.1 below.

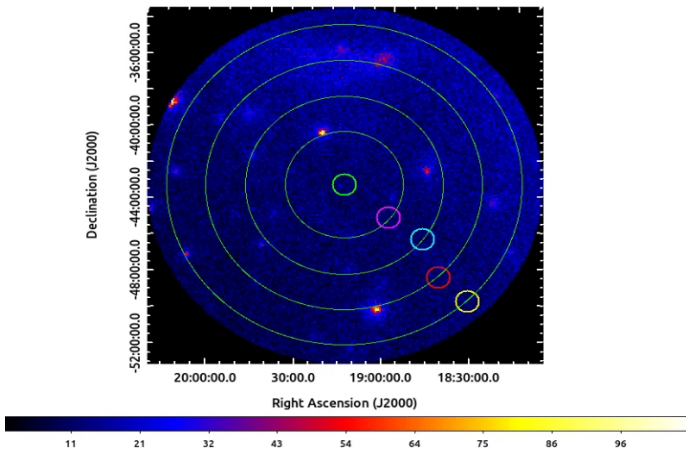

Figure D.1: 0.5-10 GeV 200×200 pixel counts map with 0.1° per pixel resolution of J1912 (0.6° radius green middle circle). Magenta, cyan, red and yellow 0.6° circles are on 3° and 5° radii circles respectively

D.1 Magenta Region

An unbinned analysis was conducted on the ROI=0.6° magenta region (RA=284.8450188°, DEC=-45.9738699°, J2000) keeping the standard *Fermi*-LAT data selection cuts the same. The steps of

the unbinned likelihood analysis are exactly the same as those performed in section 4.4.4. The Rayleigh test was then performed on this magenta region and the Rayleigh Periodogram is shown in Figure D.2 below.

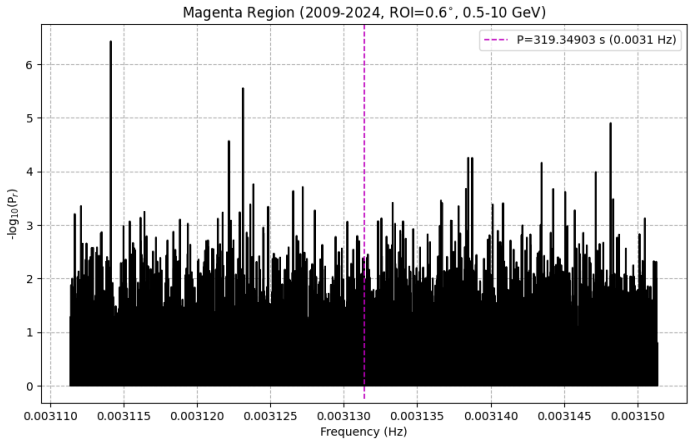

Figure D.2: Rayleigh periodogram of the magenta region showing no significant pulsations at the spin period of J1912.

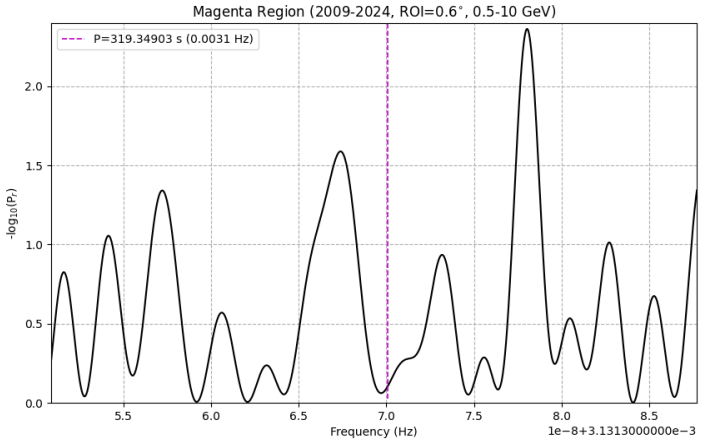

Figure D.3: Zoomed-in Rayleigh periodogram of the magenta region showing no significant pulsations at the spin period of J1912.

The γ-rays from this magenta region was then phase-folded on the rotation period of J1912 and

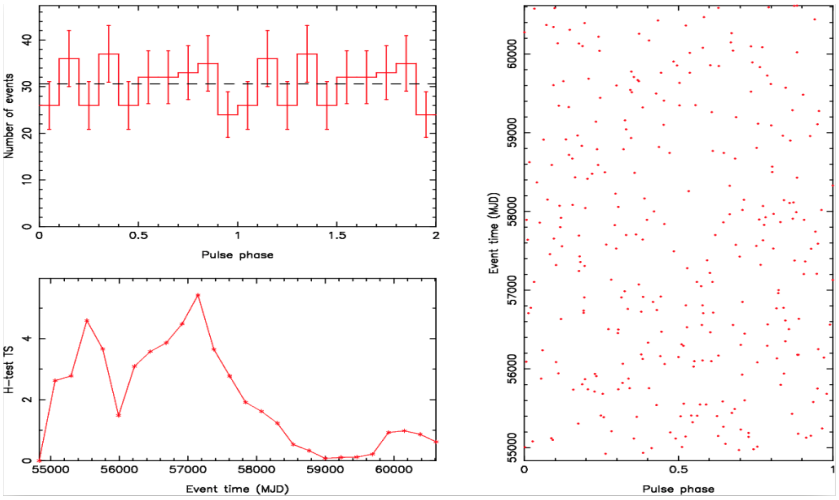

Figure D.4: H-test TS (bottom left), folded γ-ray light curve (top left) and phaseogram of the magenta region using the same ephemeris by Pelisoli, Marsh, et al. (2023).

using the same ephemeris provided by Pelisoli, Marsh, et al. (2023) and the folded γ-ray light curve is shown in Figure D.4

D.2 Cyan Region

The same unbinned analysis was conducted on the cyan region for which the coordinates are RA=282.2478500°, DEC=-47.0945178° (J2000) and the resulting Rayleigh periodogram of the cyan region is shown in Figure D.5.

The γ-rays from this cyan region was then phase-folded on the rotation period of J1912 and using the same ephemeris provided by Pelisoli, Marsh, et al. (2023) and the folded γ-ray light curve is shown in Figure D.7.

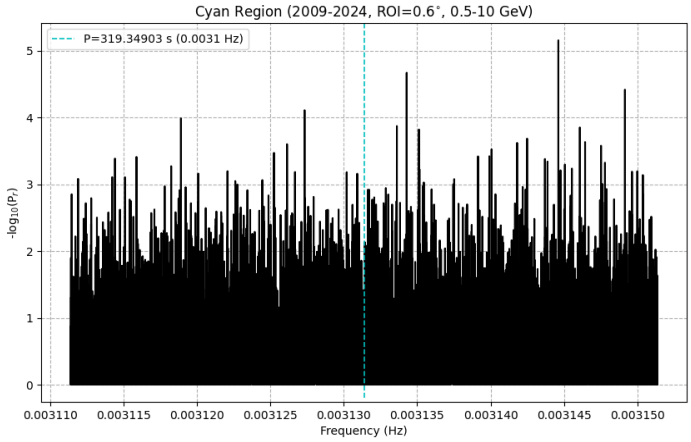

Figure D.5: Rayleigh periodogram of the cyan region showing no significant pulsations at the spin period of J1912.

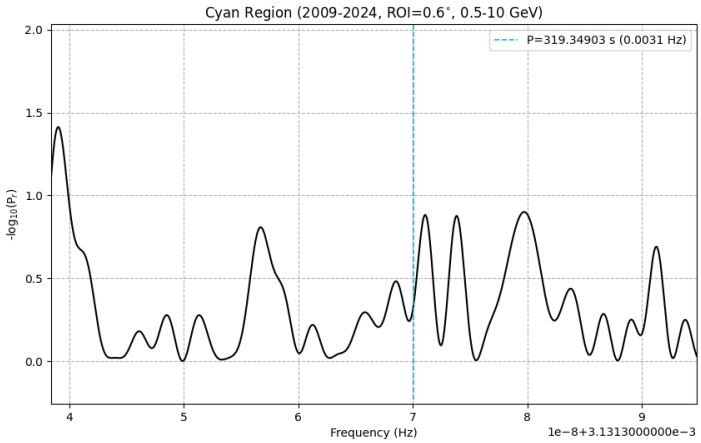

Figure D.6: Zoomed-in Rayleigh periodogram of the cyan region showing no significant pulsations at the spin period of J1912.

D.3 Red Region

The same unbinned analysis was conducted on the red region for which the coordinates are RA=280.8032709°, DEC=-49.1516967° (J2000) and the resulting Rayleigh periodogram of the cyan region is shown in Figure D.5.

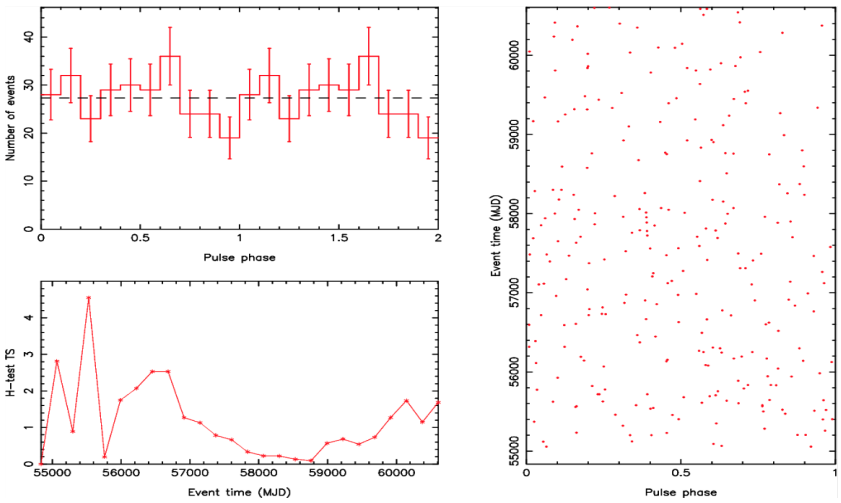

Figure D.7: H-test TS (bottom left), phase-folded γ-ray light curve (top left) and phaseogram of the cyan region using the same ephemeris by Pelisoli, Marsh, et al. (2023).

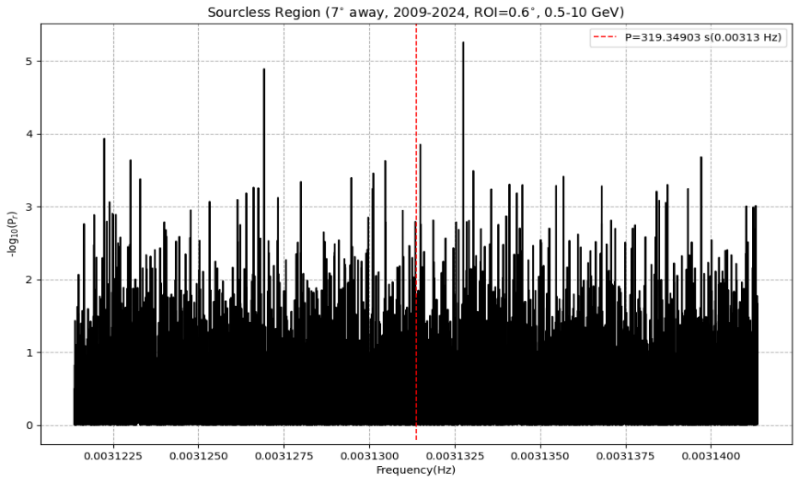

Figure D.8: Rayleigh periodogram of the red region showing no significant pulsations at the spin period of J1912.

D.4 Yellow Region

The same unbinned analysis was conducted on the yellow region for which the coordinates are RA=278.2991455°, DEC=-50.3474962° (J2000) and the resulting Rayleigh periodogram of the yellow region is shown in Figure D.10.

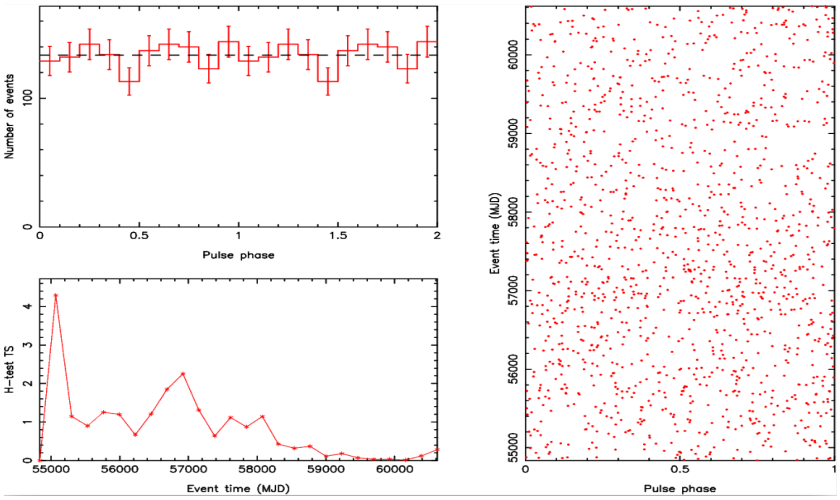

Figure D.9: H-test TS (bottom left), phase-folded γ-ray light curve (top left) and phaseogram of the red region using the same ephemeris by Pelisoli, Marsh, et al. (2023).

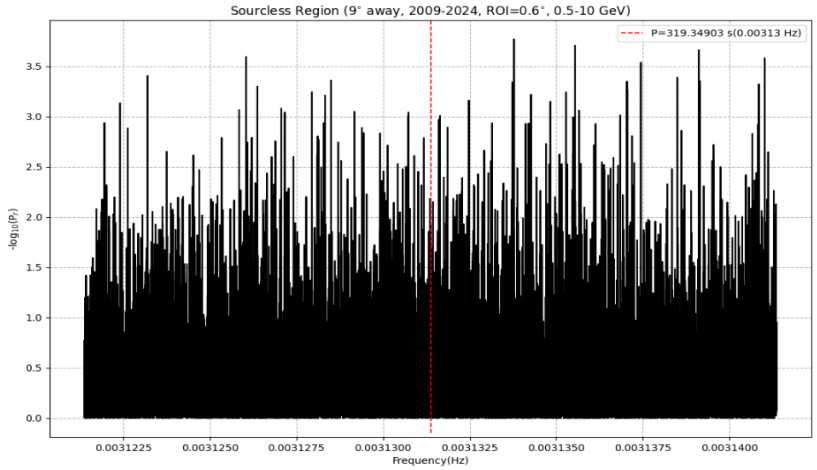

Figure D.10: Rayleigh periodogram of the yellow region showing no significant pulsations at the spin period of J1912.

Some of the phase-folded light curves do show signatures of pulsed emission but the H-test TS is low suggesting that this could just be statistical fluctuations. Therefore, these control tests on the sourceless regions reveal that the pulsations detected in the γ-rays from J1912 are **inherent to J1912 and not introduced by the analysis techniques.**

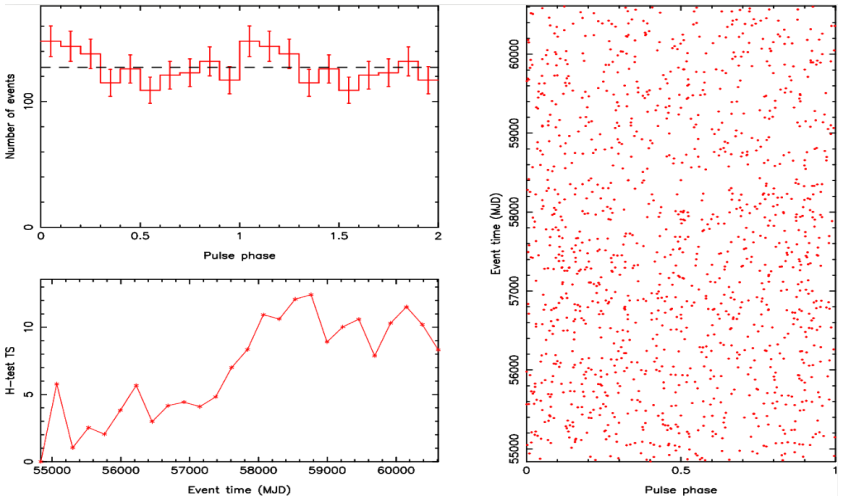

Figure D.11: H-test TS (bottom left), phase-folded γ-ray light curve (top left) and phaseogram of the yellow region using the same ephemeris by Pelisoli, Marsh, et al. (2023).

Appendix E

Periodogram Control Tests of the TS gated data of J1912 in the 0.5-10 GeV band

The same regions in Figure D.1 were subjected to the TS gating method (see section 4.4.6) while still keeping the same data selection cuts. The RA and DEC restriction was applied to respective regions.

E.1 TS Gated Magenta Region

After the application of the RA and DEC restriction to the high probability photon event file, the Rayleigh test was performed on the resulting event file and is shown in Figure E.1 together with a zoomed-in version of the Rayleigh periodogram in Figure E.2. The phase-folded γ-ray light curve on the rotation period given in Figure E.3.

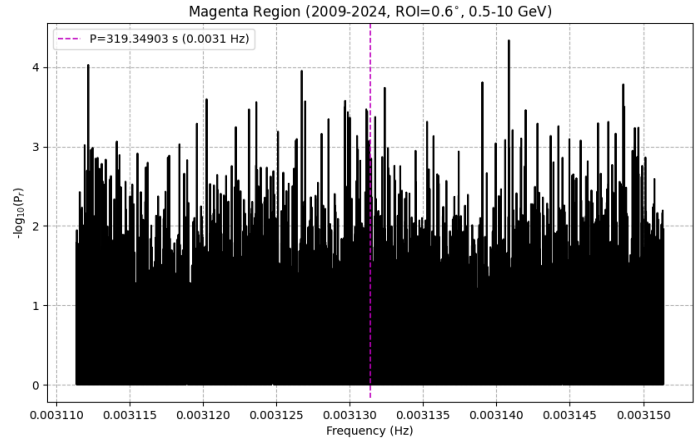

Figure E.1: Rayleigh periodogram of the TS gated magenta region showing no significant pulsations at the spin period of J1912.

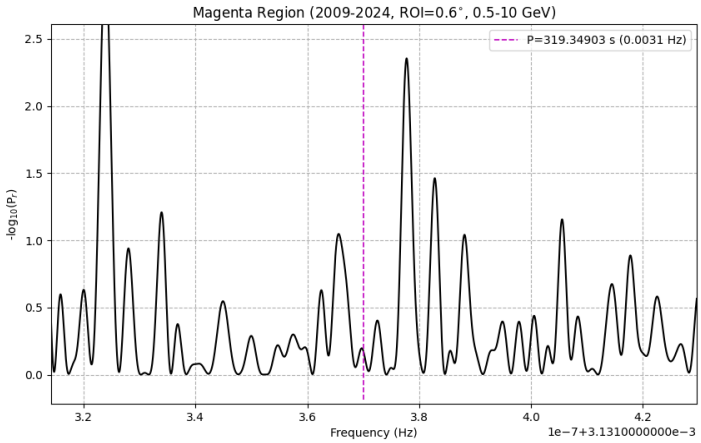

Figure E.2: Zoomed-in Rayleigh periodogram of the TS gated magenta region showing no significant pulsations at the spin period of J1912.

E.2 TS Gated Cyan Region

The phase-folded γ-ray light curve and the Rayleigh periodogram of the cyan region in Figure E.6 and Figure E.4 respectively.

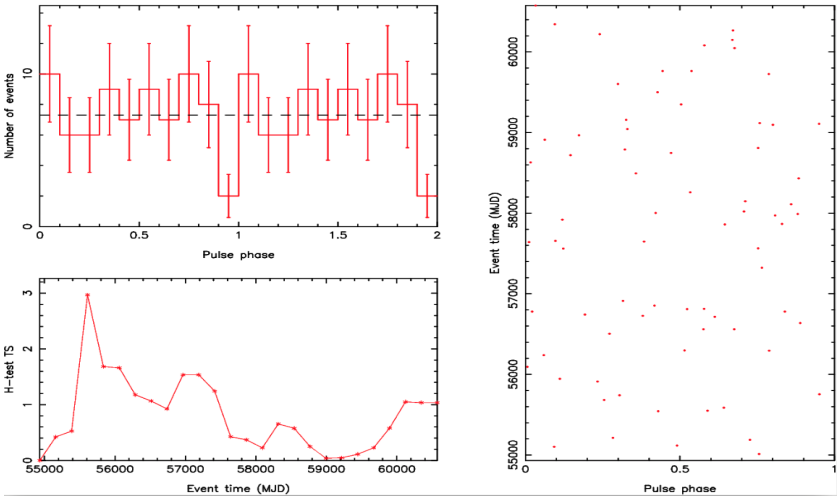

Figure E.3: H-test TS (bottom left), folded γ-ray light curve (top left) and phaseogram of the magenta region using the same ephemeris by Pelisoli, Marsh, et al. (2023).

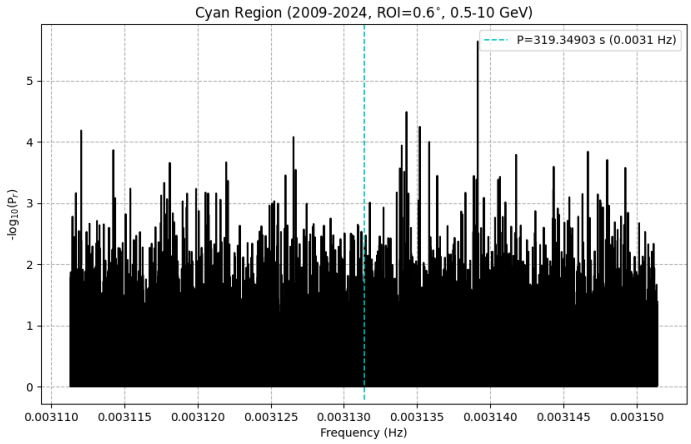

Figure E.4: Rayleigh periodogram of the TS gated cyan region showing no significant pulsations at the rotation period of J1912.

E.3 TS Gated Red Region

The phase-folded γ-ray light curve and the Rayleigh periodogram of the cyan region in Figure E.9 and Figure E.7 respectively.

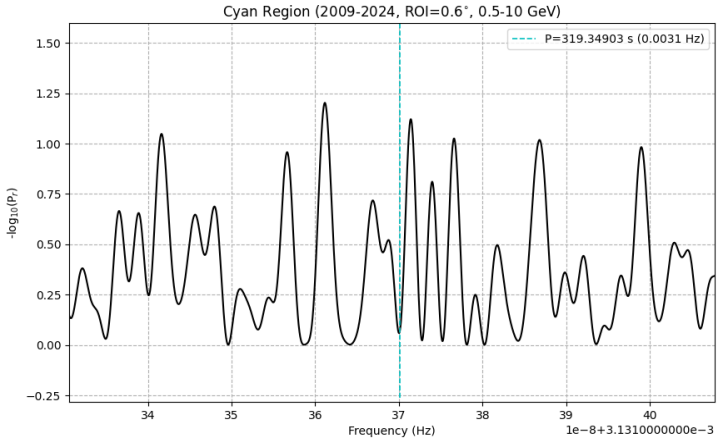

Figure E.5: Zoomed-in Rayleigh periodogram of the TS gated cyan region showing no significant pulsations at the spin period of J1912.

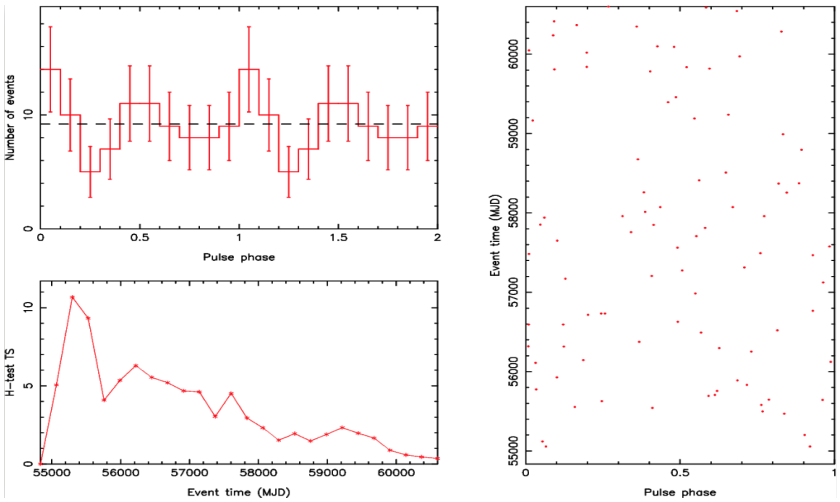

Figure E.6: H-test TS (bottom left), folded γ-ray light curve (top left) and phaseogram of the cyan region using the same ephemeris by Pelisoli, Marsh, et al. (2023).

E.4 TS Gated Yellow Region

The phase-folded γ-ray light curve and the Rayleigh periodogram of the yellow region in Figure E.12 and Figure E.10 respectively.

Since there are no significant pulsations (some of these regions do show "pulsed" behaviour

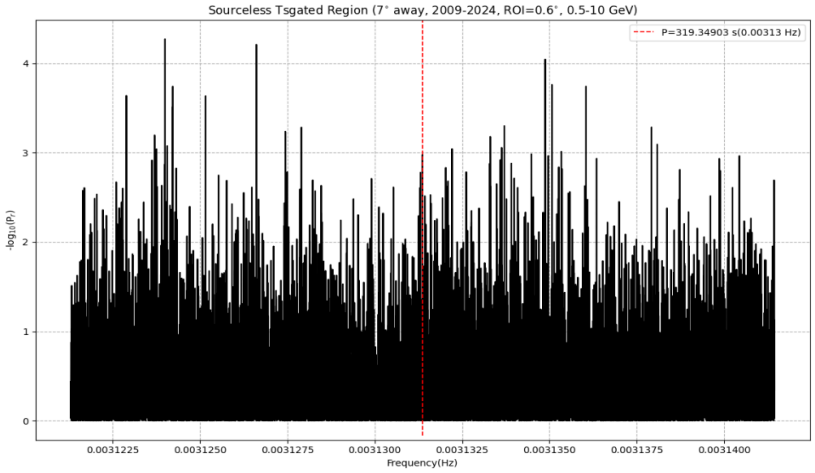

Figure E.7: Rayleigh periodogram of the TS gated red region showing no significant pulsations at the rotation period of J1912.

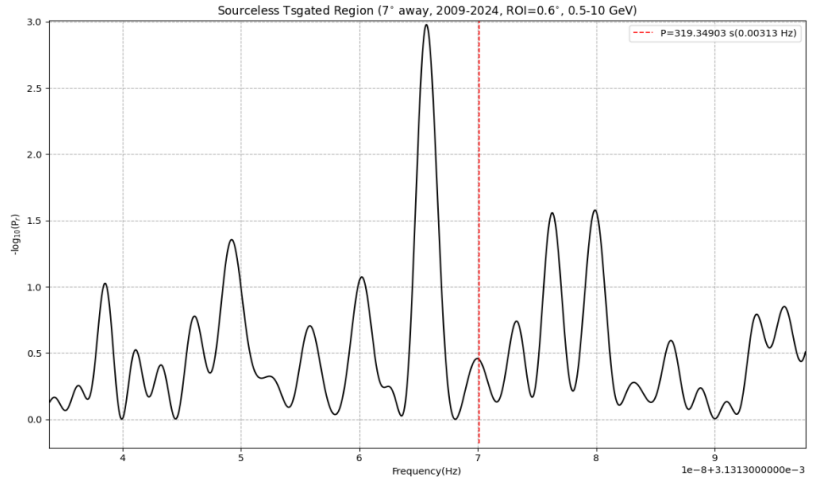

Figure E.8: Zoomed-in Rayleigh periodogram of the TS gated red region showing no significant pulsations at the spin period of J1912.

according to the phase-folded light curves but are not significant i.e. show a low H-test TS and the power at the spin period could just be coincidental or due to statistical fluctuations) above the background at the spin period of J1912 in either of these regions, we conclude that the γ-ray pulsations from J1912 using the **RA and DEC restriction are inherent to J1912.**

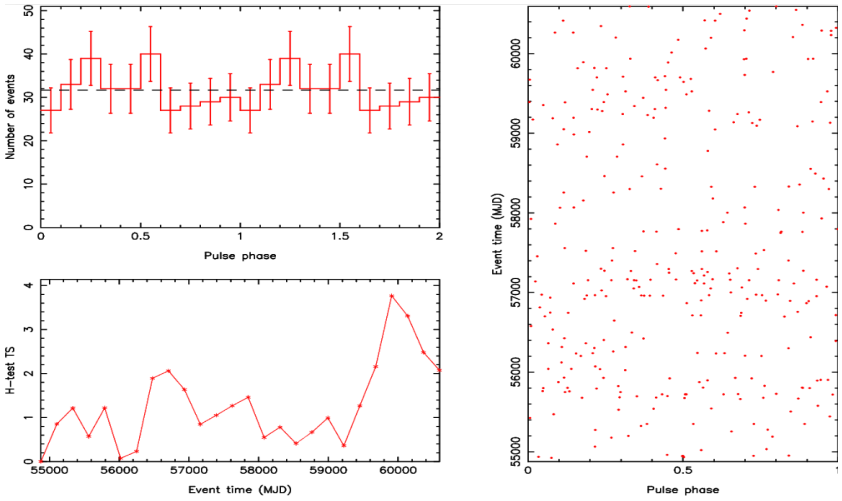

Figure E.9: H-test TS (bottom left), folded γ-ray light curve (top left) and phaseogram of the red region using the same ephemeris by Pelisoli, Marsh, et al. (2023).

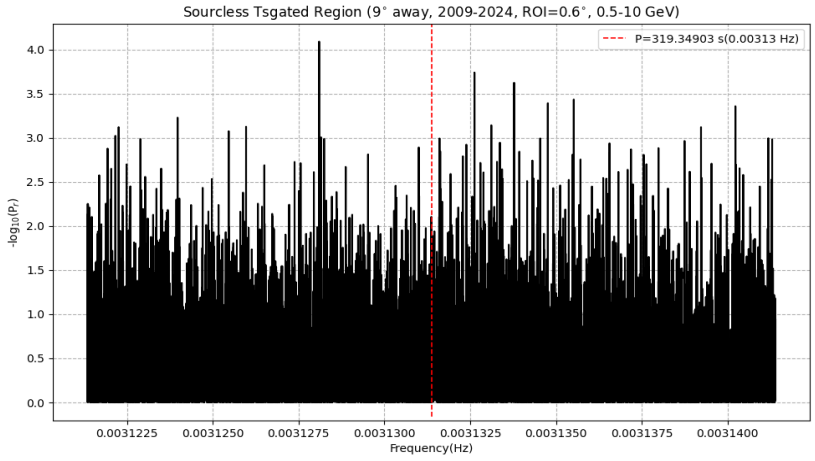

Figure E.10: Rayleigh periodogram of the TS gated yellow region showing no significant pulsations at the rotation period of J1912.

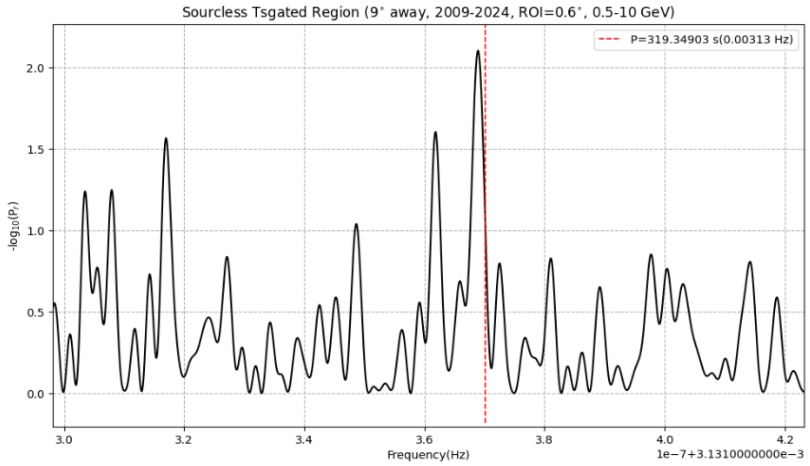

Figure E.11: Zoomed-in Rayleigh periodogram of the TS gated yellow region showing no significant pulsations at the spin period of J1912.

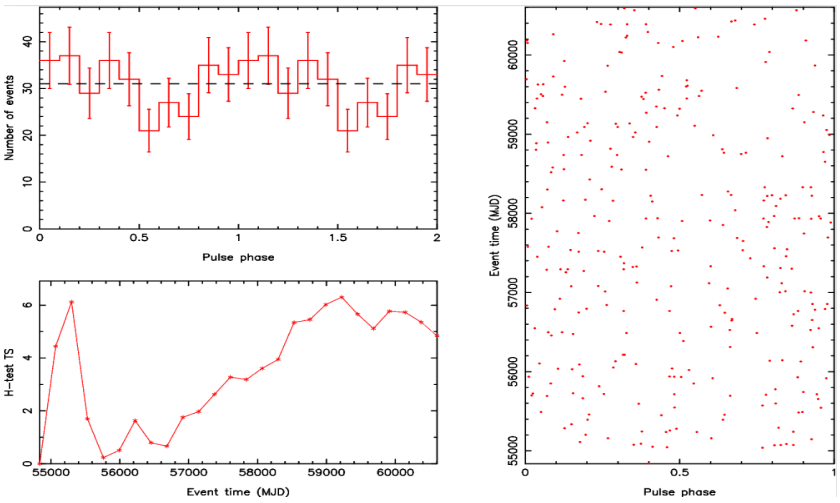

Figure E.12: H-test TS (bottom left), folded γ-ray light curve (top left) and phaseogram of the yellow region using the same ephemeris by Pelisoli, Marsh, et al. (2023).

Appendix F

Radiation Processes

This appendix provides a brief overview (based on Rybicki and Lightman (1986), Ghisellini (2013) and references therein) of the radiation processes that could explain the pulsed emission in both isolated (J0317) and binary (J1912) highly magnetic and fast rotating systems. Most of the radiation processes are briefly discussed here for **completeness** but the kind reader is referred to provided references for a complete and in-depth description of these processes.

F.1 Bremsstrahlung

F.1.1 Thermal Bremsstrahlung Emission

Emission from astrophysical sources can be categorized into two groups: non-thermal and thermal emission processes. In the thermal emission process, the population of particles producing the emission is best described by the Maxwell-Boltzmann velocity distribution (Irwin (2021))

$$n(v)dv = n\left(\frac{m}{2\pi kT}\right)^{3/2} exp\left(-\frac{mv^2}{2kT}\right) 4\pi v^2 dv \tag{F.1}$$

where $n(v)$ is the density of particles as a function of their velocity v, m is the particle's mass, k is Boltzmann's constant, T the temperature and n is the particle number density with velocity between the interval v and $v+dv$. From this distribution, it is evident that the emission is a function of T and hence the radiation emitted by the particles are directly related to their random motion

in the thermal gas. Non-thermal emission is emission that is independent of temperature T and results from charged particles accelerated by a magnetic or electric field. When a charged particle (electron) travels in the vicinity of an ion (another charged particle), this electron's path gets deflected due to the Coulomb field set up by the ion. This change in direction of the electron's path results in acceleration, and hence the electron emits radiation known as bremsstrahlung emission. A schematic is shown of the interaction is shown in Figure F.1 below.

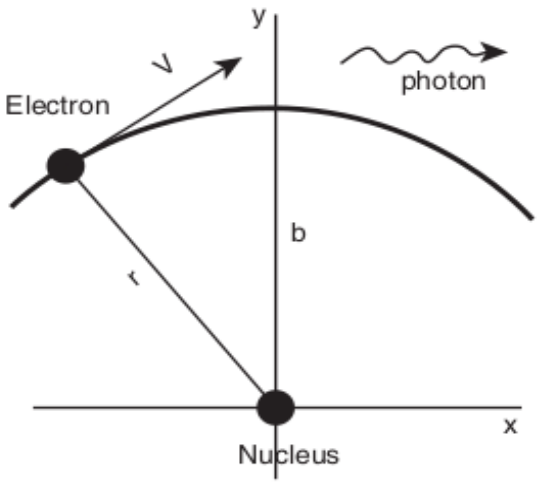

Figure F.1: Electron emitting thermal bremsstrahlung because it is deflected by a nucleus where the velocity vector of electron is V and b is the impact paramater (distance of closest approach). Adopted from Irwin (2021).

Bremsstrahlung emission is often called "free-free emission" because the electron in many cases does not recombine with the ion. The "collision" time of the electron and ion can be described as

$$\tau = \frac{b}{v} \tag{F.2}$$

where b is the "distance of closest approach" or impact parameter and v is the electron's velocity. And since only the direction of the electron's trajectory is changing we can assume constant acceleration (Ghisellini (2013))

$$a \approx \frac{e^2}{m_e b^2} \tag{F.3}$$

The emitted power by a moving charged particle is described by the Larmor formula

$$P = \frac{2e^2a^2}{3c^3} \tag{F.4}$$

which highly depends on the acceleration a of the charged particle. Substituting the acceleration equation F.3 in the Larmor formula yields

$$P = \frac{e^6}{m_e^2c^3b^4} \tag{F.5}$$

From the collision time in equation F.2, we get the characteristic frequency $\omega \approx 1/\tau = v/b$ and so the power radiated as a function of characteristic frequency is

$$P(\omega) \approx \frac{P}{\omega} = \frac{e^6}{m_e^2c^3vb^3} \tag{F.6}$$

and one can estimate the distance of closest approach i.e. the impact parameter b from the proton density (n_p) as $b \approx n_p^{-1/3}$. If one assumes that the emission from the electron is isotropic, then the emissivity is

$$j(\omega) \approx \frac{n_e n_p}{4\pi} \frac{e^6}{m_e^2c^3} \left[\frac{m_e}{kT}\right]^{1/2} \tag{F.7}$$

And if we integrate equation F.7 over frequency

$$\begin{aligned} j &= \int_0^{\omega_{max}} j(\omega)d\omega \\ &\approx \frac{n_e n_p}{4\pi} \frac{e^6}{m_e^2c^3} \left(\frac{m_e}{kT}\right)^{1/2} \frac{kT}{\hbar} \\ j &= \frac{n_e n_p e^6}{4\pi m_e^2c^3} \frac{(m_e kT)^{1/2}}{\hbar} \end{aligned} \tag{F.8}$$

where $\omega_{max} = kT/\hbar$. An exact expression for the emissivity can be obtained by noticing that

$\nu = \omega/2\pi$ which leads to

$$\begin{aligned} j(\nu) &= \frac{8}{3}\left(\frac{2\pi}{3}\right)^{1/2}\frac{n_e n_p e^6}{m_e^2 c^3}\left(\frac{m_e}{kT}\right)^{1/2} exp\left(-\frac{h\nu}{kT}\right)\bar{g}_{ff} \\ j &= \frac{4}{3\pi}\left(\frac{2\pi}{3}\right)^{1/2}\frac{n_e n_p e^6}{m_e^2 c^3}\frac{(m_e kT)^{1/2}}{\hbar}\bar{g}_{ff} \end{aligned} \tag{F.9}$$

where the exponential function was introduced because electrons can have energies greater than kT and belongs to the exponential part of the Maxwell-Boltzmann distribution (equation F.1) and $\bar{g}_{ff}$ is a correction factor known as the Gaunt factor and is a function of the energy of the electron and frequency of the emission. The Gaunt factor is given by (Rybicki and Lightman (1986))

$$g_{ff}(v,\omega) = \frac{\sqrt{3}}{\pi} ln\left(\frac{b_{max}}{b_{min}}\right) \tag{F.10}$$

where b_{max} and b_{min} are the maximum and minimum impact parameters respectively. By incorporating nuclei having various atomic number Z and number densities n, a generalized expression for the emissivity can be obtained (Ghisellini (2013))

$$\begin{aligned} j(\nu) &= 5.4 \times 10^{-39} Z^2 n_e n_i T^{-1/2} e^{-h\nu/kT}\bar{g} \\ j &= 1.13 \times 10^{-28} Z^2 n_e n_i T^{1/2}\bar{g} \end{aligned} \tag{F.11}$$

F.1.2 Thermal Bremsstrahlung Absorption

In order to gain insights into the overall spectrum from the thermal bremsstrahlung process, we must also consider the absorption coefficient of this process which tells us how efficiently the gas absorbs its own radiation without a background source present. The intensity of a black body is given by the Planck function (Carroll and Ostlie (2017))

$$B_\nu(T) = \frac{2h\nu^3}{c^2}\frac{1}{e^{h\nu/kT} - 1} \tag{F.12}$$

By using Kirchhoff's law for thermal emission

$$j_\nu = \alpha_\nu B_\nu(T) \tag{F.13}$$

the absorption coefficient $\alpha_\nu(\mathrm{cm}^{-1})$ can be obtained

$$\begin{aligned}
\alpha_\nu &= \frac{j_\nu}{B_\nu(T)} \\
&= \frac{4}{3}\left(\frac{2\pi}{3}\right)^{1/2} \frac{Z^2 n_e n_i e^6}{h m_e^2 c^2} \left(\frac{m_e c^2}{kT}\right)^{1/2} \frac{1 - e^{-h\nu/kT}}{\nu^3} \bar{g}_{ff} \\
\alpha_\nu &= 3.7 \times 10^8 \frac{Z^2 n_e n_i}{T^{1/2}} \frac{(1 - e^{-h\nu/kT})}{\nu^3} \bar{g}_{ff}
\end{aligned} \tag{F.14}$$

We can ignore the exponential term when $h\nu \gg kT$ which means that $\alpha_\nu \propto \nu^{-3}$. When $h\nu \ll kT$ (Rayleigh-Jeans regime) equation F.14 reduces to

$$\begin{aligned}
\alpha_\nu &= \frac{4e^6}{3m_e kc}\left(\frac{2\pi}{3m_e k}\right)^{1/2} T^{-3/2} Z^2 n_e n_i \nu^{-2} \bar{g}_{ff} \\
\alpha_\nu &= 0.018 T^{-3/2} Z^2 n_e n_i \nu^{-2} \bar{g}_{ff}
\end{aligned} \tag{F.15}$$

Using equation F.14, the optical depth τ_ν along the line of sight l can be approximated as

$$\begin{aligned}
\tau_\nu &= \int \alpha_\nu dl \\
&\approx (3.7 \times 10^8) T^{-1/2} Z^2 \nu^{-3} (1 - e^{-h\nu/kT}) \bar{g}_{ff} (n_e^2 l)
\end{aligned} \tag{F.16}$$

The intensity spectrum of bremsstrahlung of a source with radius R=10^{15}cm, particle density n_e=n_p= 10^{10} cm^{-3} plotted using different temperatures is shown in Figure F.2.

The final spectrum (without a background source present) is given by

$$I_\nu = B_\nu(T)(1 - e^{-\tau_\nu}) \tag{F.17}$$

for which we can differentiate between the optically thick ($\tau_\nu \gg 1$) and optically thin ($\tau_\nu \ll 1$) part

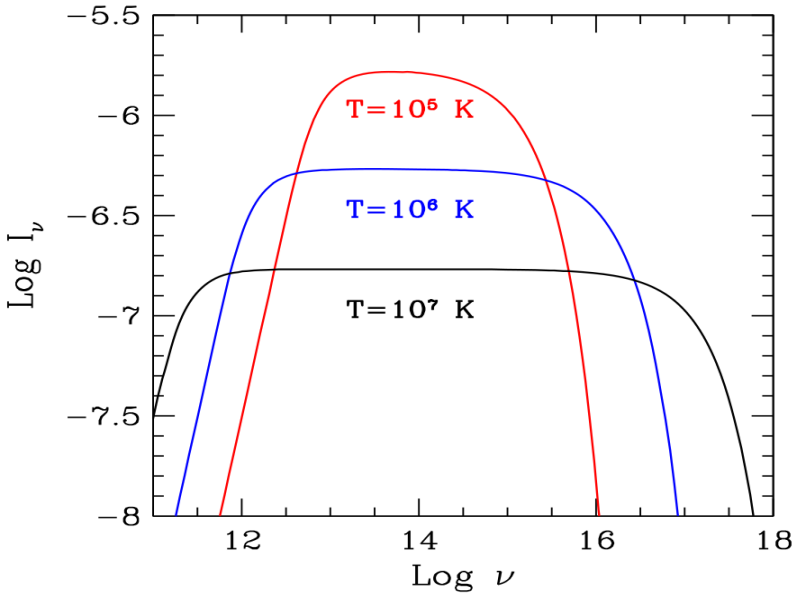

Figure F.2: Thermal bremsstrahlung intensity spectrum of R=10^{15}cm radius source and particle density n_e=n_p=10^{10}cm^{-3} with varying temperature. The Gaunt factor $\bar{g}_{ff}$ is set to a unity for simplicity. Figure adopted from Ghisellini (2013).

of the spectrum

$$\begin{aligned} I_\nu &= B_\nu(T) \quad (\tau_\nu \gg 1) \\ I_\nu &= j_\nu l \quad (\tau_\nu \ll 1) \end{aligned} \tag{F.18}$$

From Figure F.2, it is evident that at lower temperatures the optically thin part of the intensity is larger since $I_\nu \propto T^{-1/2}$ and at higher T the spectrum extends towards large frequencies. The self-absorbed part of the spectrum has a slope $\propto \nu^2$ and ends when the optical depth $\tau_\nu = \alpha_\nu R \sim 1$. Equation F.14 ensures that absorption occurs at lower frequencies since $\alpha_\nu \propto \nu^{-3}$ and by increasing the particle number density, the spectrum becomes self-absorbed at higher frequencies until it approaches the black-body spectrum as shown in Figure F.3.

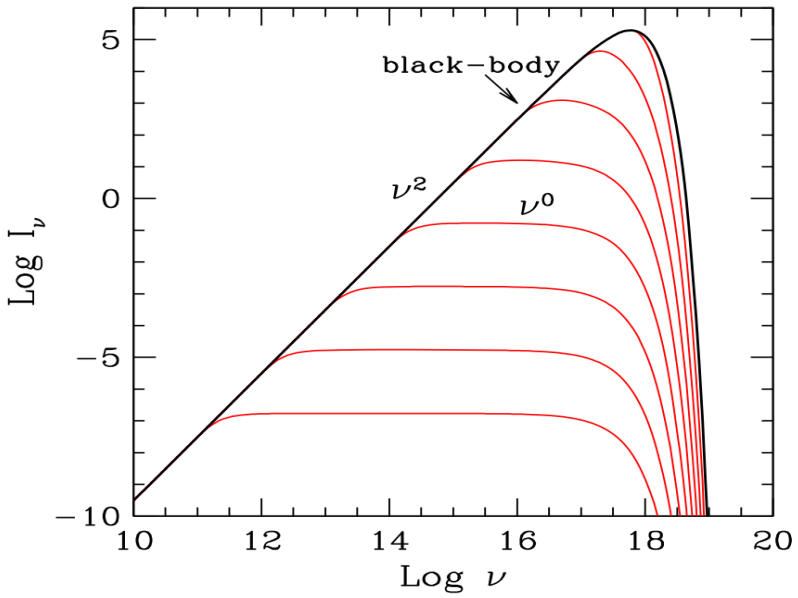

Figure F.3: Thermal bremsstrahlung intensity spectrum of R=10^{15}cm radius source and T=10^7K. The Gaunt factor $\bar{g}_{ff}$ is set to a unity for simplicity. The particle density n_e=n_p varies from 10^{10} cm^{-3}(bottom curve) to 10^{18}cm^{-3} (top curve). Figure adopted from Ghisellini (2013).

F.2 Cyclotron Radiation

Charged particles can also interact with magnetic field lines to produce radiation. When a non-relativistic (v≪c) electron spirals or gyrates about a magnetic field line it produces radiation at the gyration frequency and this emitted radiation is called cyclotron radiation. An electron with velocity $\vec{v}$ in magnetic field $\vec{B}$ will "feel" a so-called Lorentz force (without an electric field present) given by

$$\vec{F_e} = e\left(\frac{\vec{v}}{c} \times \vec{B}\right) \tag{F.19}$$

and the direction of this Lorentz force is $\perp$ to both $\vec{B}$ and $\vec{v}$ with magnitude

$$F_e = \frac{ev}{c} B sin\phi = \frac{ev}{c} B_\perp \tag{F.20}$$

where ϕ is the angle between $\vec{v}$ and $\vec{B}$ and $B_\perp = Bsin\phi$. The electron experiences the maximum Lorentz force when its velocity $\vec{v}$ is perpendicular the $\vec{B}$ field and will gyrate about the field line but if the electron is parallel to the $\vec{B}$ field line it will not experience a force and hence will not emit radiation. Since the Lorentz force causes the electron to gyrate we can equate it to the centripetal force

$$F_e = \frac{ev}{c} B_\perp = \frac{m_e v_\perp^2}{r_0} \tag{F.21}$$

where r_0 is the radius of gyration (gyroradius) which is given by

$$r_0 = \frac{m_e v_\perp c}{eB} = \frac{v_\perp T}{2\pi} = \frac{v_\perp}{2\pi\nu_0} \tag{F.22}$$

where $T = 1/\nu_0$ is the gyration period and using $v_\perp = 2\pi r_0/T$ we arrive at the cyclotron frequency (gyrofrequency)

$$\nu_0 = \frac{eB}{2\pi m_e c} \tag{F.23}$$

which is conveniently expressed as

$$\left[\frac{\nu_0}{MHz}\right] = 2.8 \left[\frac{B}{Gauss}\right] \tag{F.24}$$

Further inspection of equation F.24 reveals that the cyclotron frequency is entirely independent of the velocity and hence kinetic energy of the electron which means that particles with different velocities will emit radiation at the same frequency for the same $\vec{B}$-field strength.

F.3 Synchrotron Radiation

When relativistic ($v \sim c$) electrons spiral/gyrate in a magnetic field they emit synchrotron radiation. The emitted power by a moving charged particle is given by the Larmor formula (equation F.4). Since the emitted power is Lorentz invariant, we can specify the power in a reference frame moving with the electron as

$$P_e = P'_e = \frac{2e^2}{3c^3} a'^2 = \frac{2e^2}{3c^3}(a'^2_\perp + a'^2_\parallel) \tag{F.25}$$

Just because the power is invariant does NOT necessarily mean that the received and emitted power are the equivalent. The Lorentz transform of the perpendicular and parallel components are given by (Rybicki and Lightman (1986))

$$\begin{aligned} a'_{\perp} &= \gamma^2 a_{\perp} \\ a'_{\parallel} &= \gamma^3 a_{\parallel} \end{aligned} \tag{F.26}$$

where γ=$1/\sqrt{1-(v/c)^2}$ is known as the Lorentz factor. Substituting equations F.26 in equation F.25 results in the generalized Larmor formula

$$P_e = P'_e = \frac{2e^2}{3c^3}\gamma^4(\gamma^2 a_{\parallel}^2 + a_{\perp}^2) \tag{F.27}$$

Since the electrons have $v \sim c$, the $\gamma^2 a_{\parallel}^2$ term will not be important i.e. $a_{\parallel} = F_{\parallel}/\gamma m_o \rightarrow 0$ for $\gamma \rightarrow \infty$. Without an electric field, the relativistic Lorentz force is given by

$$\vec{F_L} = \frac{d(\gamma m \vec{v})}{dt} = \frac{e}{c}(\vec{v} \times \vec{B}) \tag{F.28}$$

with parallel component is $F_{L\parallel}$=0 since $a_{\parallel} = 0$ and the perpendicular component

$$\begin{aligned} F_{L\perp} &= \gamma m \frac{dv_{\perp}}{dt} = \frac{v_{\perp}}{c} eB \\ \therefore a_{\perp} &= \frac{Bevsin\theta}{\gamma mc} \end{aligned} \tag{F.29}$$

The Larmor radius r_L can now be obtained using $a_{\perp} = v_{\perp}^2/r_L$ which results in

$$r_L = \frac{v_{\perp}^2}{a_{\perp}} = \frac{\gamma mc^2 \beta sin\theta}{eB} \tag{F.30}$$

One can obtain the fundamental frequency of this gyration motion by noticing that it is the inverse of the time required for the electron to complete one orbit

$$\begin{aligned} \nu_B &= \frac{1}{T_{gyr}} \quad (T_{gyr} = \frac{2\pi r_L}{v_\perp}) \\ &= \frac{eB}{2\pi\gamma mc} \\ \therefore \nu_B &= \frac{\nu_L}{\gamma} \end{aligned} \tag{F.31}$$

where ν_L is the Larmor frequency. Substituting equation F.29 in equation F.25 one obtains a new form for the generalized Larmor formula

$$P_S = \frac{2e^4}{3m^2c^3} B^2\gamma^2\beta^2 sin^2\theta \tag{F.32}$$

By introducing $U_B = B^2/(8\pi)$ as the "magnetic energy density", the classical electron radius $r_0 = e^2/(m_e c^2)$ and the Thomson scattering cross-section $\sigma_T = (8\pi r_0^2)/3 = 6.65 \times 10^{-25} cm^2$ the emitted synchrotron power by an individual electron as a function of pitch angle is (Ghisellini (2013))

$$P_S(\theta) = 2\sigma_T c U_B \gamma^2\beta^2 sin^2\theta \tag{F.33}$$

which reduces to (when the pitch angles are distributed isotropically)

$$\langle P_S \rangle = \frac{4}{3}\sigma_T c U_B \gamma^2\beta^2 \tag{F.34}$$

F.3.1 Synchrotron Cooling Timescale

Using equation F.34 the synchrotron cooling timescale is (Ghisellini (2013))

$$\begin{aligned} t_{sync} &= \frac{E}{\langle P_S \rangle} = \frac{\gamma m_e c^2}{(4/3)\sigma_T c U_B \gamma^2\beta^2} \\ t_{sync} &\sim \frac{7.75 \times 10^8}{\gamma B^2} s \end{aligned} \tag{F.35}$$

which depends only on the electron Lorentz factors and the magnetic field strength.

F.3.2 Single Electron Spectrum

The radiation of a relativistic electron in a $\vec{B}$-field will be highly beamed in the direction of motion of the electron into a cone of angle $\theta = 1/\gamma$ shown in Figure F.4 below.

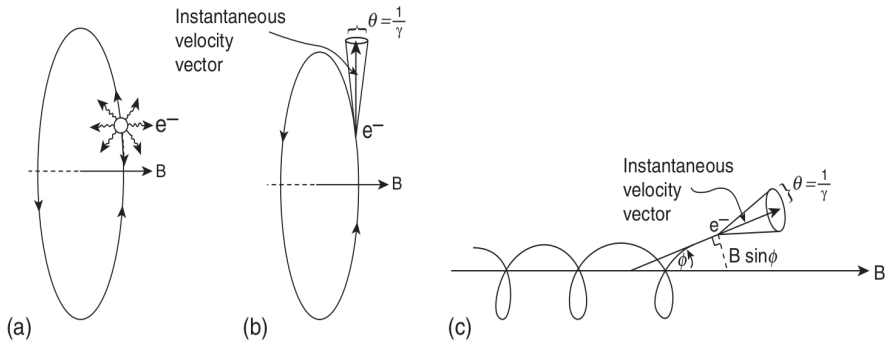

Figure F.4: **(a)** Cyclotron radiation emitted in all directions. **(b)** Synchrotron radiation highly beamed in the direction of motion into cone of angular radius $\theta = 1/\gamma$. **(c)** Helical motion of electron with beamed radiation into cone $\theta = 1/\gamma$. Figure adopted from Irwin (2021).

A stationary observer will see radiation from a relativistic electron from a small fraction of the orbit of the electron (AB) about the $\vec{B}$-field (see Figure F.5.)

When the electron approaches point A (Figure F.5) in its orbit, radiation will be beamed in a cone of angular radius $2/\gamma$ towards the observer. Upon approaching point B the last fraction of radiation will be beamed in the observer's direction and the electron will take $\Delta t_{ret} = (2\pi r_L/c)$ to reach point A again. An observer positioned at the center of the electron's orbit, the time it will take the electron to travel the distance AB is given by

$$\begin{aligned} \Delta t_e &= \frac{AB}{c} = \frac{2r_L}{\gamma c} = \frac{2}{\gamma c}\left(\frac{\gamma m_e c^2 \beta sin\theta}{eB}\right) = \frac{1}{\pi \nu_L} \\ \therefore \Delta t_e &= \frac{2}{2\pi\gamma\nu_B} \quad (\theta \to 90^\circ, v \to c) \end{aligned} \tag{F.36}$$

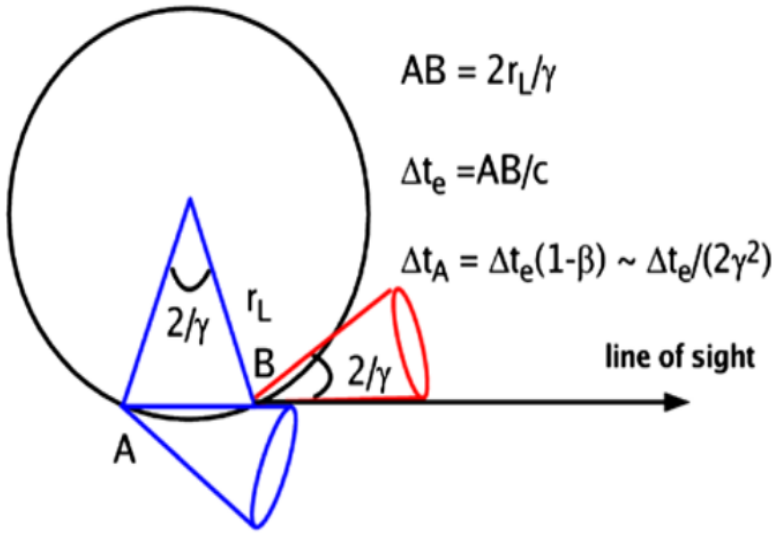

Figure F.5: Relativistic electron gyrating along a $\vec{B}$-field with pitch angle of 90° with trajectory a circle of radius r_L. As a result of the aberration of light, a stationary observer will see radiation when the beaming cone of total aperture angle $2/\gamma$ is directed toward them. Figure adopted from Ghisellini (2013).

The duration of the pulse from a stationary observer is given by

$$\begin{aligned} \Delta t_A &= \gamma(1-\beta cos\theta)(\Delta t_e/\gamma) \quad (\Delta t'_e = \Delta t_e/\gamma) \\ &= (1-\beta)\Delta t_e \quad (\theta \to 0^\circ) \\ \therefore \Delta t_A &= \frac{\Delta t_e}{2\gamma^2} \end{aligned} \tag{F.37}$$

The expression in equation F.37 signifies that the duration of the pulse according to the stationary observer will be shorter compared to the observer positioned at the center of the electron's orbit. The synchrotron frequency $\omega_s = 2\pi\nu_s$ is given by the inverse of equation F.37 which leads to

$$\nu_s = \frac{1}{2\pi\Delta t_A} = \gamma^3\nu_B = \gamma^2\nu_L = \gamma^2\left(\frac{eB}{2\pi m_e c}\right) \tag{F.38}$$

and it is at this frequency where the particle emits the majority of its power. The power as a

function of pitch angle, frequency and Lorentz factor of the relativistic electron is given by

$$P_s(\nu, \gamma, \theta) = \frac{\sqrt{3}e^3 B sin\theta}{m_e c^2} F(\nu/\nu_c) \tag{F.39}$$

where

$$F(\nu/\nu_c) = \frac{\nu}{\nu_c} \int_{\nu/\nu_c}^{\infty} K_{5/3}(y) dy \tag{F.40}$$

with $\nu_c = (3/2)\nu_s sin\theta$. These expressions describe the integrated power over the radiation pattern with $K_{5/3}$ being the modified Bessel function of order 5/3 and the function $F(\nu/\nu_c)$ is shown in Figure F.6 and peaks where $\nu \sim 0.29\nu_c$.

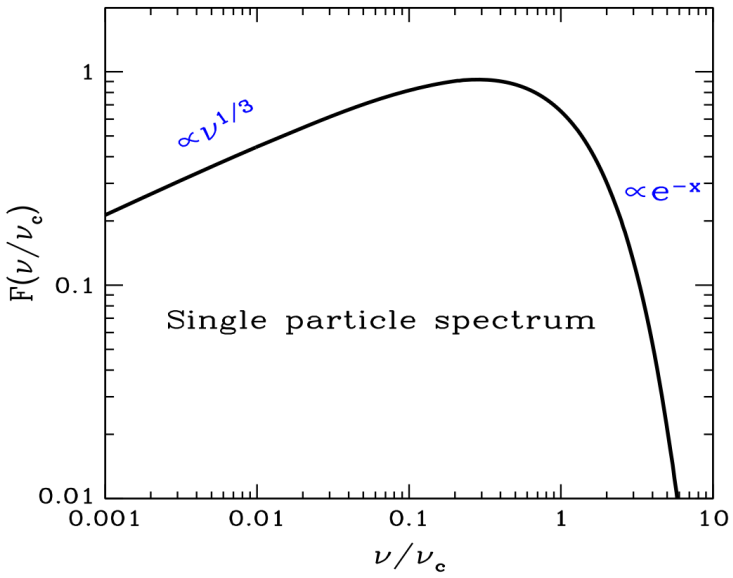

Figure F.6: Single electron synchrotron spectrum which peaks when $\nu \sim 0.29\nu_c$. Figure adopted from Ghisellini (2013).

From Figure F.6, at the low end of the frequency range the spectrum is well approximated by (low frequency approximation)

$$F(\nu/\nu_c) \rightarrow \frac{4\pi}{\sqrt{3}\Gamma(1/3)} \left(\frac{\nu}{2\nu_c}\right)^{1/3} \quad (\nu \ll \nu_c) \tag{F.41}$$

whereas at high frequencies (high frequency approximation)

$$F(\nu/\nu_c) \rightarrow \left(\frac{\pi}{2}\right)^{1/2} \left(\frac{\nu}{\nu_c}\right)^{1/2} e^{-\nu/\nu_c} \quad (\nu \gg \nu_c) \tag{F.42}$$

F.3.3 Emission from Many Electrons

Since synchrotron emission is a non-thermal process electron velocities do NOT follow a Maxwell-Boltzmann distribution (equation F.1). The particle energy distribution is well described by a power-law distribution given by

$$N(\gamma) = K\gamma^{-p} = N(E)\frac{dE}{d\gamma} \tag{F.43}$$

where $\gamma_{min} < \gamma < \gamma_{max}$. The emissivity of this power-law distribution is given by

$$\begin{aligned} j_\nu d\nu_s &\propto (1/4\pi)P_s(\theta)N(\gamma)d\gamma \\ j_\nu &\propto (1/4\pi)P_s(\theta)K\gamma^{-p}\frac{d\gamma}{d\nu_s} \end{aligned} \tag{F.44}$$

and if we use the fact that $P_s(\theta) \propto \gamma^2 B^2$ and $v_s \propto \gamma^2 B$, introduce $\gamma \propto \nu_s^{1/2} B^{-1/2}$ which means that $d\gamma/d\nu_s \propto \nu_s^{-1/2} B^{-1/2}$ and the emissivity becomes

$$j_\nu \propto \frac{1}{4\pi} K B^{(p+1)/2} \nu_s^{-(p-1)/2} \quad [ergcm^{-3}s^{-1}sr^{-1}Hz^{-1}] \tag{F.45}$$

This enables us to estimate the observed flux density from a synchrotron source by

$$\begin{aligned} F_\nu = \frac{L_\nu}{4\pi d^2} &= 4\pi j_s(\nu)\frac{V}{4\pi d_L^2} \\ &\propto K R_s \theta_s^2 B^{(p+1)/2} \nu^{-(p-1)/2} \\ \therefore F_\nu &\propto K R_s \theta_s^2 B^{1+\alpha} \nu_s^{-\alpha} \quad [ergcm^{-2}s^{-1}Hz^{-1}] \end{aligned} \tag{F.46}$$

where R_s is the radius of the source, θ_s its angular radius and the spectral index $\alpha = (p-1)/2$ where p is the particle distribution index.

F.3.4 Synchrotron Absorption

When photons are absorbed by relativistic electrons within a synchrotron-emitting cloud, the process is called synchrotron self-absorption. The self-absorbed part of a thermal source in local thermodynamic equilibrium (LTE) has a brightness that is well described by the Rayleigh-Jeans law

$$I_\nu = \frac{2kT_b\nu^2}{c^2} \tag{F.47}$$

where the radiation is in equilibrium with the thermal plasma and T_b is the brightness temperature. Since relativistic electrons emit synchrotron radiation, the thermal plasma is in equilibrium with the relativistic particle meaning that $kT_e \sim \gamma m_e c^2$. The electron Lorentz factor scale as $\gamma \sim \nu_s^{1/2} B^{-1}$ which allows us to express the electron temperature as $T_e \propto \gamma \propto \nu_s^{1/2} B^{-1/2}$. For a self-absorbed synchrotron source the brightness then scales as

$$\begin{aligned} I_\nu &\propto T_b \nu^2 \\ &\propto B^{-1/2}\nu_s^{5/2} \quad [ergcm^{-2}s^{-1}Hz^{-1}sr^{-1}] \end{aligned} \tag{F.48}$$

where we used $T_e = T_b$ for an optically thick source. Using equation F.48, the absorption coefficient is

$$\begin{aligned} \alpha_\nu &= \frac{j(\nu)}{I(\nu)} \propto \frac{KB^{(p+1)/2}\nu^{-(p-1)/2}}{\nu^{5/2}B^{-1/2}} \\ \therefore \alpha_\nu &= KB^{(p+1)/2}\nu^{-(p+4)/2} \end{aligned} \tag{F.49}$$

This allows one to determine the self-absorption frequency ν_t using $\tau_{\nu_t} = R\alpha_{\nu_t} = 1$ which means (Ghisellini (2013))

$$\nu_t \propto [RKB^{(p+2)/2}]^{2/(p+4)} \tag{F.50}$$

The spectrum of a partially self-absorbed source is shown in Figure F.7 where the spectrum peaks close to the self-absorption frequency ν_t.

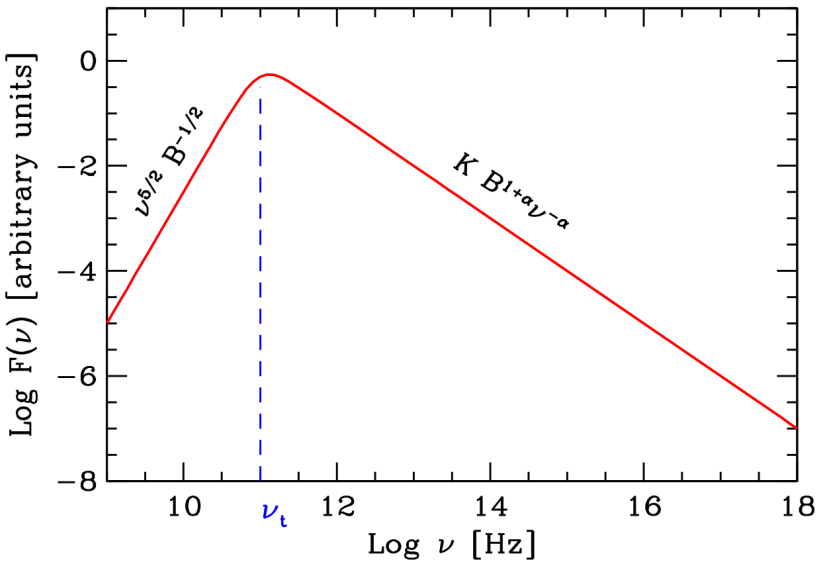

Figure F.7: A partially self-absorbed source spectrum peaking at the synchrotron self-absorption frequency ν_t. Figure adopted from Ghisellini (2013).

F.4 Curvature Radiation

Curvature radiation is analogous to synchrotron radiation but contrary to electrons spiraling/gyrating around the $\vec{B}$-field lines emitting radiation, the electrons move along the $\vec{B}$-fields emitting curvature radiation. Therefore, curvature radiation is primarily as a result of $\vec{B}$-field line curvature. Synchrotron radiation theory can be used to derive the formulae for curvature radiation. As was shown in section F.3.1, the synchrotron cooling time scales as $\tau_{sync} \propto \gamma^{-1}B^{-2}$(Ghisellini (2013)) resulting in particles rapidly losing the perpendicular velocity component with respect to the magnetic field. The particle then moves along the $\vec{B}$-field line and hence emits radiation with energy (Ruderman and Sutherland (1975), Lobato et al. (2017))

$$\epsilon_{curv} = \frac{3\hbar c}{2R_c}\gamma^3 \tag{F.51}$$

where $\hbar$ is the reduced Planck constant, $R_c \approx \sqrt{Rc/\Omega}$ is the curvature radius of the magnetic field lines and γ is the Lorentz factor of the particles. The spectrum for curvature radiation is given by

(Ochelkov and Usov (1980) and references therein)

$$p(\omega) = \frac{\sqrt{3}}{2\pi}\frac{e^2}{R_c}\gamma\frac{\omega}{\omega_c}\int_{\omega/\omega_c}^{\infty} K_{5/3}(x)dx \tag{F.52}$$

where $K_{5/3}$ describes the modified Bessel function of order 5/3 and the characteristic curvature photon frequency given by

$$\omega_c = \frac{3}{2}\frac{c}{R_c}\gamma^3 \tag{F.53}$$

The electron/positron energy loss due to curvature radiation is given by (Ruderman and Sutherland (1975))

$$P = \frac{2}{3}\frac{e^2 c}{R_c^2}\gamma^4 \tag{F.54}$$

From these equations, it is evident that the energy loss ($P \propto \gamma^4$) and characteristic curvature frequency ($\omega_c \propto \gamma^3$) strongly depends on the energy of the emitting particle. The function

$$F\left(\frac{\omega}{\omega_c}\right) = \frac{\omega}{\omega_c}\int_{\omega/\omega_c}^{\infty} K_{5/3}(x)dx \tag{F.55}$$

and hence the spectral curvature radiation power $p(\omega)$ decreases exponentially for $\omega \gg \omega_c$ and can be estimated as $p(\omega) \sim \omega^{1/3}$ for $\omega \ll \omega_c$ as shown in Figure F.8 below.

The curvature radiation emissivity is a function of observation frequency ω and on the location $\boldsymbol{r}$ given by (Ptri (2019))

$$j_{curv}(\boldsymbol{r},\omega) = \frac{\sqrt{3}}{2\pi}\alpha_{sf}\frac{\hbar c}{R_c(\boldsymbol{r})}\gamma F\left(\frac{\omega}{\omega_c(\boldsymbol{r})}\right) \tag{F.56}$$

where $\alpha_{sf} = e^2/4\pi\epsilon_o\hbar c$ is the "fine structure constant". This equation shows the spatial dependence of the curvature radiation emissivity. Since the charged particle travels along the magnetic field, most of the emission will be beamed in a cone of opening angle $\sim \gamma^{-1}$. Curvature radiation could possibly explain the pulsed γ-ray emission from most pulsars and has been recently proposed by Meintjes et al. (2023) and references therein to possibly explain the low-level pulsed γ-ray emission for both AR Scorpii and AE Aquarii. These authors provided a theoretical upper limit of $\leq$50

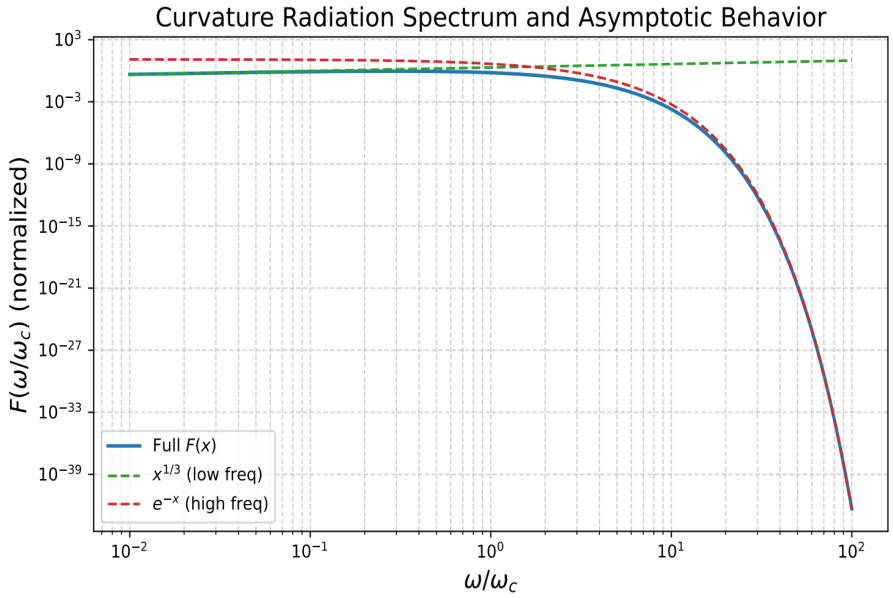

Figure F.8: Curvature radiation spectrum normalized to the characteristic frequency ω_c showing the exponential decrease for $\omega \gg \omega_c$ and $\omega^{1/3}$ as $\omega \ll \omega_c$.

GeV on the pulsed γ-ray emission from these fast spinning, highly magnetic white dwarfs using the curvature radiation mechanism to likely explain these pulsed γ-rays from these systems.

F.5 Compton Scattering

When an incoming photon interacts with a free electron and the photon's energy is comparable to or greater than the electron's rest mass energy i.e., $\epsilon_\gamma \geq m_e c^2$, some of the photon energy is transferred to the electron causing it to recoil resulting in the scattered photon to have less energy than the original photon. This scattering process is referred to as Compton scattering and is shown in Figure F.9 below.

This change in the photon energy (or wavelength) after the scattering can be calculated by using the conservation of momentum. The final and initial momentum of the electron and photon in four-momenta notation is given by

$$\vec{P_\gamma} + \vec{P_e} = \vec{P_\gamma'} + \vec{P_e'} \tag{F.57}$$

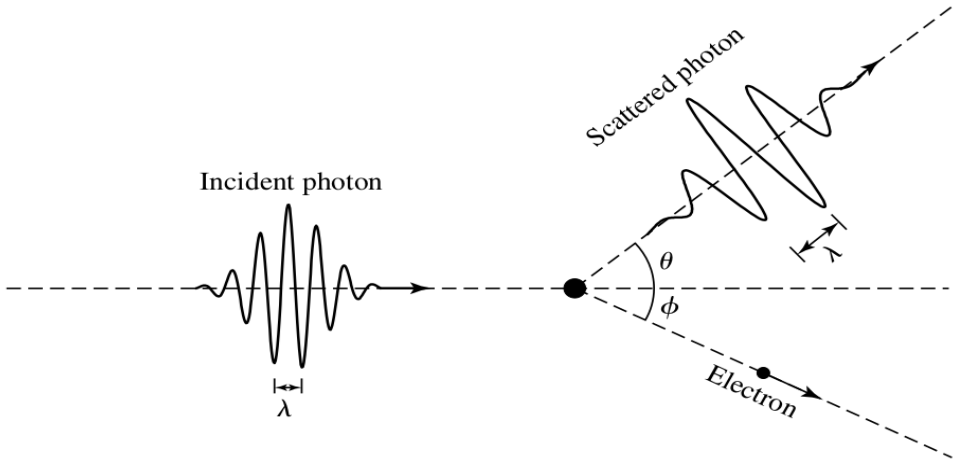

Figure F.9: The Compton effect in which the incident photon scatters off a free electron where θ and ϕ are the scattering angles of the scattered photon and electron respectively. Figure adopted from Carroll and Ostlie (2017).

where the vector notation of a photon is given by $\vec{P_\gamma} = (\epsilon/c, \vec{p})$ where $\vec{p}$ is the normal momentum of the photon. After squaring and rearranging terms in equation F.57, we get

$$\begin{aligned}\left[\frac{h\nu}{c}, \frac{h\nu}{c}\hat{k_1}\right] \cdot \left[\frac{mc^2}{c}, 0\right] &= \left[\frac{h\nu}{c}\frac{h\nu'}{c} - \frac{h\nu}{c}\frac{h\nu'}{c}\hat{k}^i_\mu \cdot \hat{k}^f_\mu\right] + \left[\frac{h\nu'}{c}, \frac{h\nu'}{c}\hat{k}^i_\mu\right] \cdot \left[\frac{mc^2}{c}, 0\right] \\ \frac{h\nu}{c}mc &= \frac{h\nu}{c}\frac{h\nu'}{c}(1 - cos\theta) + \frac{h\nu'}{c}mc \\ \frac{1}{\lambda} &= \frac{1}{\lambda}\frac{1}{\lambda'}\frac{h}{mc}(1 - cos\theta) + \frac{1}{\lambda'}\end{aligned} \tag{F.58}$$

where $\hat{k}$ is the photon wave number, $\hat{k}^i_\mu \cdot \hat{k}^f_\mu = cos\theta$ in which θ is the angle between the scattered and incident photon direction. This reduces to the well-known equation

$$\lambda' - \lambda = \Delta\lambda = \lambda_c(1 - cos\theta) \tag{F.59}$$

where $\lambda_c = h/m_e c$=2.426×10^{-10} cm gives the "Compton wavelength". When the wavelength of the incident photon is much greater than the "Compton wavelength" $\lambda \gg \lambda_c$ we can assume an elastic scattering where the scattered photon's energy remains the same after the scattering. This

interaction between a photon and electron is dependent on the cross-section which describes the probability that an incident photon will scatter off a free electron. There are two types of cross-sections: Thomson and Klein-Nishina cross-section.

F.5.1 Thomson Cross-Section

If we assume that the electron is at rest with a completely linearly polarized incident electromagnetic wave of frequency $\nu \ll m_e c^2/h$ (Ghisellini (2013)) where the oscillation velocity $v \ll c$ (to ignore the "Lorentz force" $F_L = (e/c)(\vec{v} \times \vec{B})$), the electron will start to oscillate as a result of the changing electric force $F_e = eE$ and the average of the squared acceleration in one cycle of the duration $T = 1/\nu$ is (Ghisellini (2013))

$$\langle a^2 \rangle = \frac{e^2 E_0^2}{2m_e^2} \tag{F.60}$$

for power emitted per unit solid angle (Larmor formula) is given by

$$\frac{dP}{d\omega} = \frac{e^4 E_0^2}{8\pi m_e^2 c^3} sin^2\theta \tag{F.61}$$

The incident wave flux is given by $S_i = cE_0^2/(8\pi)$ which allows us to determined the differential cross-section as

$$\frac{d\sigma}{d\Omega} = \frac{dP_e/d\Omega}{S_i} = \frac{e^4}{m_e^2 c^4} sin^2\theta = r_0^2 sin^2\theta \tag{F.62}$$

where $r_0 = e^2/(m_e c^2) \sim 2.8 \times 10^{-13}$ cm is the electron "classical radius" and if we integrate equation F.62 over the entire solid angle

$$\begin{aligned} \sigma_T &= \int \frac{d\sigma}{d\Omega} d\Omega \\ &= \int_0^{2\pi} \int_0^{\pi} r_0^2 sin^2\theta sin\theta d\theta d\phi \\ &= \frac{8\pi r_0^2}{3} \\ \therefore \sigma_T &= 6.65 \times 10^{-25} cm^2 \end{aligned} \tag{F.63}$$

which is called the Thomson cross-section.

F.5.2 Klein-Nishina Cross-Section

The Thomson cross-section gives a classical expression of the scattering probability between a photon and an electron. A general approach would be to include the quantum mechanical effects associated with the scattering. This is given by the Klein-Nishina formula

$$\frac{d\sigma_{KN}}{d\Omega} = \frac{3}{16\pi}\sigma_T \left(\frac{x_1}{x}\right)^2 \left[\frac{x}{x_1} + \frac{x_1}{x} - sin^2\theta\right] \tag{F.64}$$

where $x = \epsilon/m_o c^2$ and $x_1 = \epsilon_1/m_o c^2$ are respectively, the energies of the incident and scattered photon in the laboratory frame. In the non-relativistic regime ($x \ll 1$) we have (Rybicki and Lightman (1986))

$$\sigma_{KN} \approx \sigma_T \left(1 - 2x + \frac{26x^2}{5} + ...\right) \tag{F.65}$$

and in the extreme relativistic regime ($x \gg 1$)

$$\sigma_{KN} = \frac{3}{8}\frac{\sigma_T}{x}\left(ln2x + \frac{1}{2}\right) \tag{F.66}$$

A comparison between the Klein-Nishina and the Thomson cross-section is given in Figure F.10 below.

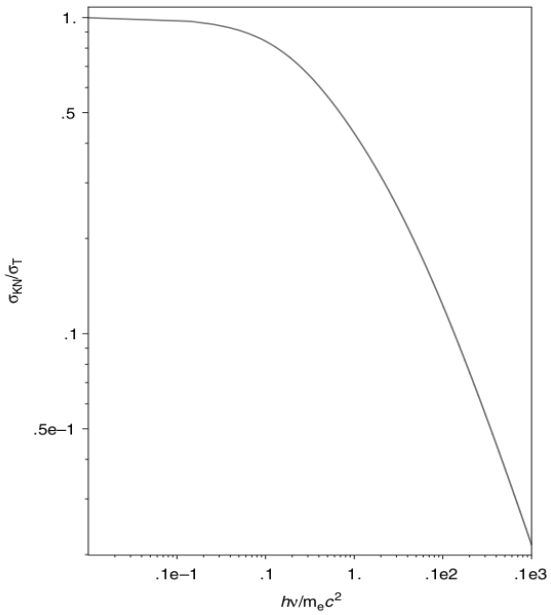

Figure F.10: Ratio of the Klein-Nishina and Thomson cross-section as a function of $x = h\nu/m_ec^2$. Figure adopted from Irwin (2021).

From Figure F.10, it is evident that as the photon energy increase ($x \gg 1$) the cross-section decreases which implies that ar higher energies Compton scattering becomes less efficient.

F.6 Inverse Compton Scattering

For a non-stationary electron with an energy exceeding the photon energy, some of the electron energy can be transferred to low energy photon. The photon gains energy and gets upscattered by the electron to higher energies. This process is called "Inverse Compton Scattering (ICS)". In the reference frame K' co-moving with the electron (Figure F.11), the energy of the incoming photon is given by

$$x' = x\gamma(1 - \beta cos\psi) \tag{F.67}$$

in which ψ is the angle between the photon direction and the electron's velocity.

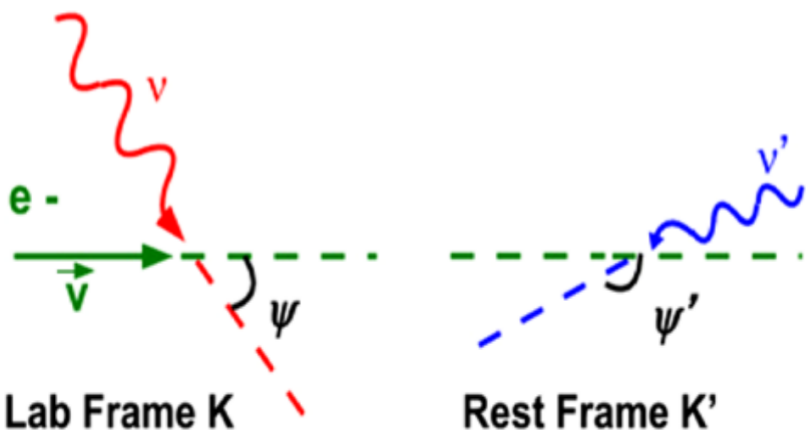

Figure F.11: An electron moving with velocity $\vec{v}$ in the laboratory frame K for which its velocity makes an angle ψ with the direction of incoming photon with frequency ν. In reference frame K' (electron is at rest) the photon with frequency ν' is coming from the front making an angle ψ' with the direction of the velocity. Figure adopted from Ghisellini (2013).

The transformation of angle in the electrons' rest frame is given by

$$cos\psi = \frac{\beta + cos\psi'}{1 + \beta cos\psi'} \tag{F.68}$$

and if we substitute equation F.68 in equation F.67

$$\begin{aligned} x' &= x\gamma \left[1 - \beta \left(\frac{\beta + cos\psi'}{1 + \beta cos\psi'}\right)\right] \\ \therefore x' &= \frac{x}{\gamma(1 + \beta cos\psi')} \end{aligned} \tag{F.69}$$

The scattered photon energy x'_1 will be the same as before the scattering in the Thomson regime where $x' \ll 1$. This suggests that $x'_1 = x'$ and if we go back to the reference frame K, an observer will see

$$x_1 = x'_1\gamma(1 + \beta cos\psi'_1) \tag{F.70}$$

together with the angle transformation

$$cos\psi_1' = \frac{cos\psi_1 - \beta}{1 - \beta cos\psi_1} \tag{F.71}$$

which after substitution reduces to

$$x_1 = x\left[\frac{1 - \beta cos\psi}{1 - \beta cos\psi_1}\right] \tag{F.72}$$

for which all parameters are now in the laboratory frame. This allows one to determine the maximum and minimum energies of the scattering. For a head-on collision $\psi = \pi$ and $\psi_1 = 0$ where the photon is scattered in the direction of the electron velocity and equation F.72 reduces to (Ghisellini (2013))

$$\begin{aligned} x_1 &= x\left(\frac{1+\beta}{1-\beta}\right) = x\gamma^2(1+\beta)^2 \\ \therefore x_1 &= 4\gamma^2 x \quad for \quad \gamma \gg 1 \end{aligned} \tag{F.73}$$

And for tail-on collisions in which the incident photon approaches from behind (Figure) where $\psi_1 = \pi$ and $\psi = 0$ (Ghisellini (2013))

$$\begin{aligned} x_1 &= x\left(\frac{1-\beta}{1+\beta}\right) = \frac{x}{\gamma^2(1+\beta)^2} \\ \therefore x_1 &= \frac{x}{4\gamma^2} \quad for \quad \gamma \gg 1 \end{aligned} \tag{F.74}$$

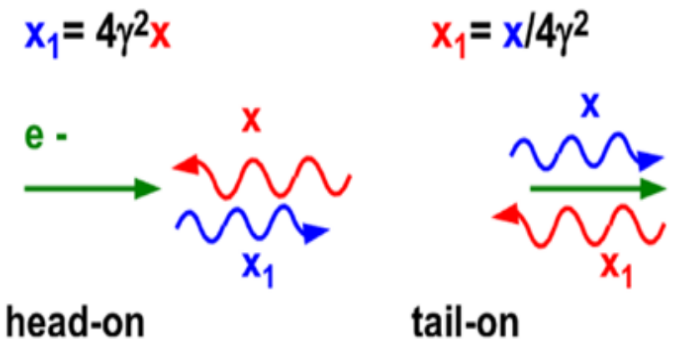

Figure F.12: Maximum (head-on) and minimum (tail-on) scattered energies. Figure adopted from Ghisellini (2013).

It is also possible to estimate the energy transferred to the photon if the photon is scattered into angle $\psi_1 \rightarrow 1/\gamma$ with respect to the laboratory observer which suggest that $cos\psi_1 \rightarrow \beta$ for which equation F.72 becomes

$$\begin{aligned} x_1 &= x\left[\frac{1-\beta cos\psi}{(1-\beta^2)}\right] \\ &= \gamma^2(1-\beta cos\psi)x \end{aligned} \tag{F.75}$$

which becomes $x_1 \approx \gamma^2 x$ if the photon approaches the electron from the side ($\psi \rightarrow \pi/2$) with respect to the laboratory observer.

F.6.1 ICS off an Isotropic Photon Distribution

It can be shown that a co-moving observer in reference frame K' moving through an isotropic photon field experiences an energy density

$$U' = \frac{4}{3}\Gamma^2 U_{iso} \tag{F.76}$$

If we assume that the co-moving observer in K' is moving at the same velocity as the relativistic electron while interacting with the isotropic photon field, one can determine the energy of the isotropically scattered photons. In the K' reference frame the energy is $U' = N\langle\epsilon'\rangle/V'$ and in the laboratory frame is $U = N\epsilon/V$. Equation F.76 then becomes

$$\frac{N'\langle\epsilon'\rangle}{V'} = \frac{4}{3}\Gamma^2\frac{N\langle\epsilon\rangle}{V} \tag{F.77}$$

If we let $V' = \Gamma V$ and consider the scattering to be elastic (Thomson regime, $\langle\epsilon'_1\rangle = \langle\epsilon'\rangle$) then

$$\frac{\langle\epsilon'_1\rangle}{\langle\epsilon\rangle} = \frac{4}{3}\Gamma^3 \tag{F.78}$$

In the laboratory frame, the scattered photon energy is $\langle\epsilon'_1\rangle = \Gamma(1-\beta\langle cos\psi\rangle)\langle\epsilon_1\rangle = \Gamma\langle\epsilon_1\rangle$ in which $\langle cos\psi\rangle = 0$. Equation F.78 then beautifully reduces to

$$\frac{\langle\epsilon_1\rangle}{\langle\epsilon\rangle} = \frac{4}{3}\Gamma^2 \tag{F.79}$$

F.6.2 The Total Loss Rate

The relativistic electron's total loss rate directly translates to the energy production rate of inverse Compton photons. If we consider all quantities in the laboratory reference frame then for a mono-directional photon distribution, the number of scatterings between photons and electrons per unit time interval is given by (Ghisellini (2013))

$$\frac{dN}{dt} = \int \sigma_T v_{rel} n(\epsilon) d\epsilon \tag{F.80}$$

where $v_{rel} = c - vcos\psi$ describes the relative velocity between incident photon and the electron. The production rate of inverse Compton photons can be determined by using

$$\frac{d\epsilon_\gamma}{dt} = \epsilon_1\frac{dN}{dt} \tag{F.81}$$

where

$$\epsilon_1 = \left[\frac{1-\beta cos\psi}{1-\beta cos\psi_1}\right]\epsilon \tag{F.82}$$

By substituting equations F.80 and F.82 into equation F.81, from the perspective of the observer in the K (laboratory) frame the photons interact with the electrons isotropically but are scattered into a cone with angle $\psi_1 \sim 1/\gamma$ ($cos\psi_1 \rightarrow \beta$) and then taking the spatial average results in

$$\langle\frac{d\epsilon_\gamma}{dt}\rangle = \left(1+\frac{\beta^2}{2}\right)c\sigma_T\gamma^2\int \epsilon n(\epsilon)d\epsilon \tag{F.83}$$

where $U_{ph} = \int \epsilon n(\epsilon)d\epsilon$ is the integrated background photon energy density. The power of the scattered radiation in the presence of an existing background photon field can be determined by

$$\begin{aligned} P_{IC}(\gamma) &= \langle\frac{d\epsilon_\gamma}{dt}\rangle - \sigma_T c U_{ph} \\ &= \left(1+\frac{\beta^2}{3}\right)\gamma^2 c\sigma_T U_{ph} - \sigma_T c U_{ph} \\ \therefore P_{IC}(\gamma) &= \frac{4}{3}\gamma^2\beta^2 c\sigma_T U_{ph} \end{aligned} \tag{F.84}$$

This bears a similar resemblance to equation F.34 for the synchrotron energy losses differing only by the energy densities. This implies that the origin of the emission will effectively be due to both Inverse Compton scattering and synchrotron processes if the region is filled with relativistic electrons, radiation and high magnetic fields.

F.6.3 Anisotropic Inverse Compton Scattering (ICS)

To investigate the ICS production rate in a anisotropic context we consider

$$\begin{aligned} \frac{d\epsilon_\gamma(cos\psi)}{dt} &= c\sigma_T\gamma^2(1-\beta cos\psi)^2\int \epsilon n(\epsilon)d\epsilon \\ &= \left[c\sigma_T\gamma^2\int \epsilon n(\epsilon)d\epsilon\right](1-\beta cos\psi)^2 \\ &= Constant(1-\beta\mu)^2 \quad where \quad \mu = cos\psi \\ \therefore P_\gamma(\mu) &= Constant(1-\beta\mu)^2 \end{aligned} \tag{F.85}$$

Using equation F.85, one can now investigate the integrated inverse Compton scattering rate over a range of angles

$$P_\gamma[\mu_1, \mu_2] = Constant \int_{\mu_1^{\mu_2}} (1 - \beta\mu)^2 d\mu \tag{F.86}$$

The inverse Compton scattered power of photons coming mainly from the front in which $\psi = [\pi, \pi/2] \rightarrow \mu = [-1, 0]$ and from the back where $\psi = [\pi/2, 0] \rightarrow \mu = [0, 1]$ (Figure F.13)

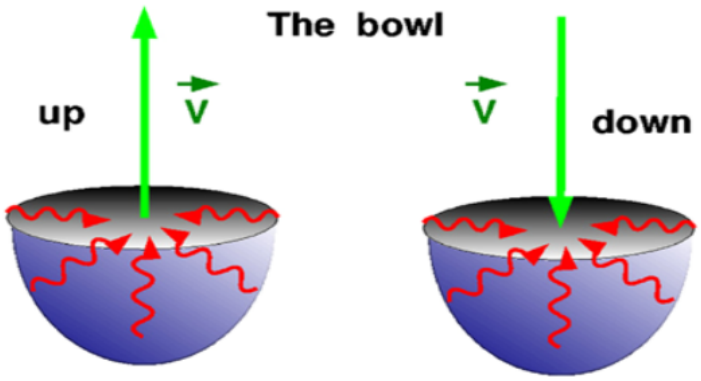

Figure F.13: Comparison between the ICS rate between photons coming from the front and back. Figure adopted from Ghisellini (2013).

$$\begin{aligned} \frac{P_\gamma(down)}{P_\gamma(up)} &= \frac{2\int_{-1}^{0}(1-\beta\mu)^2 d\mu}{2\int_{0}^{1}(1-\beta\mu)^2 d\mu} \\ &= \frac{1+\beta+\beta^2/3}{1-\beta+\beta^2/3} \\ &= 7 \quad for \quad \beta \rightarrow 1 \end{aligned} \tag{F.87}$$

which shows that the scattering rate of photons coming mainly from the front is 7 times more efficient than the scattering rate of photons coming mainly from behind. Repeating this process for the down

scattering rate between electrons and photons coming mainly from the $\psi = [\pi, 0] \rightarrow \mu = [-1, 1]$

$$\frac{P_\gamma(down)}{P_\gamma(side)} = \frac{2\int_{-1}^{0}(1-\beta\mu)^2 d\mu}{\int_{-1}^{1}(1-\beta\mu)^2 d\mu} = \frac{7}{4} \quad for \quad \beta \rightarrow 1 \tag{F.88}$$

F.6.4 Cooling Time Scale and Compactness

Using equation F.84, one can determine the inverse Compton cooling timescale

$$t_{IC} = \frac{\gamma m_e c^2}{P_{IC}(\gamma)} = \frac{\gamma m_e c^2}{(4/3)\beta^2\gamma^2 c\sigma_T U_{ph}} = \frac{3 m_e c^2}{4\sigma_T c\gamma U_{ph}} \quad for \quad \beta \rightarrow 1 \tag{F.89}$$

Utilizing equation F.89, one can determine the dimensionless compactness parameter l of a source which is basically the luminosity (L) divided by the radius (R)

$$\begin{aligned} t_{IC} &= \frac{3 m_e c^2}{4\sigma_T c\gamma U_{ph}} \\ &= \frac{3 m_e c^2}{4\sigma_T c\gamma (\frac{L}{4\pi R^2 c})} \\ &= \frac{3\pi m_e c^3 (R/c) R}{\sigma_T \gamma L} \\ \frac{t_{IC}}{(R/c)} &= \frac{3\pi m_e c^3 R}{\sigma_T \gamma L} \\ \therefore \frac{t_{IC}}{(R/c)} &= \frac{3\pi}{\gamma l} \end{aligned} \tag{F.90}$$

where

$$l = \frac{\sigma_T L}{m_e c^3 R} \propto \frac{L}{R} \tag{F.91}$$

If l is close to or larger than a unity, electrons with low energies will also cool by the ICS mechanism in less than the R/c.

F.6.5 Single Particle Spectrum

It is evident by now that the ICS mechanism increases the energy of a soft photon background by a factor γ^2 i.e. $\langle x_1 \rangle \sim \gamma^2 \langle x \rangle$ if the photons are approaching the electron from the front and if they

are coming from the back we have $\langle x_1 \rangle \sim 1/\gamma^2 \langle x \rangle$. The emission coefficient for a single electron spectrum is given by (Ghisellini (2013), see also Rybicki and Lightman (1986) for a complete derivation)

$$j_{IC}(x_1) = \frac{\sigma_T n I_0 (1+\beta)}{4\gamma^2 \beta^2 x_0} F_{IC}(x_1) \tag{F.92}$$

with the frequency dependent function F_{IC} (Ghisellini (2013))

$$\begin{aligned} F_{IC}(x_1) &= \frac{x_1}{x_0}\left[\frac{x_1}{x_0} - \frac{1}{(1+\beta)^2\gamma^2}\right]; \quad \frac{1}{(1+\beta)^2\gamma^2} < \frac{x_1}{x_0} < 1 \\ F_{IC}(x_1) &= \frac{x_1}{x_0}\left[1 - \frac{x_1}{x_0}\frac{1}{(1+\beta)^2\gamma^2}\right]; \quad 1 < \frac{x_1}{x_0} < (1+\beta)^2\gamma^2 \end{aligned} \tag{F.93}$$

where the first expression in equation F.93 describes the case when the scattered photon has less energy (downscattering, $F_{IC}(x_1) \propto x_1^2$) and the second expression describes upscattering where $F_{IC}(x_1) \propto x_1$. Figure F.14 below shows the behavior of $F_{IC}(x_1)$ for different γ values.

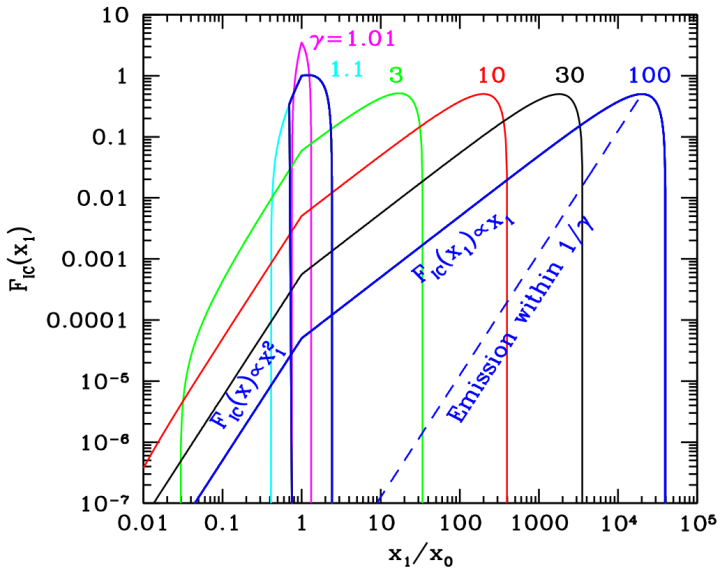

Figure F.14: ICS spectrum for electrons with different γ scattering a monochromatic isotropic photon field with dimensionless frequency x_0 where the dashed blue line displays to the emitted spectrum with a beaming cone $1/\gamma$ always containing 75% of the total power for any γ. Figure adopted from Ghisellini (2013).

From Figure F.14, the spectra of photons in a cone $1/\gamma$ always contain 75% of the total amount of power for any value of γ. Also evident is that a power law dependence arises when $\gamma \gg 1$.

F.6.6 Emission From Many Electrons

Similar to the synchrotron case, assume that the relativistic electrons have a power-law energy distribution (see equation F.43). If one assumes further an isotropic and monochromatic seed photon field with frequency ν_0 and keeping in mind the strong relation between ν_{IC} (scattered frequency) and the energy of the electron that produced it, we have (Ghisellini (2013))

$$\begin{aligned} \nu_{IC} &= \frac{4}{3}\gamma^2\nu_0 \\ \therefore \gamma &= \left(\frac{3\nu_{IC}}{4\nu_0}\right)^{1/2} \\ \therefore \left|\frac{d\gamma}{d\nu_{IC}}\right| &= \frac{\nu_{IC}^{-1/2}}{2}\left(\frac{3}{4\nu_0}\right)^{1/2} \end{aligned} \tag{F.94}$$

An electron with energy between $(\gamma, \gamma + d\gamma)$ produces radiation through IC scattering containing frequencies between $(\nu, \nu + d\nu)$ which allows us to express the emission coefficient as

$$\begin{aligned} j_\nu(\nu_{IC}) &= \frac{1}{4\pi}N(\gamma)P_{IC}\left|\frac{d\gamma}{d\nu_{IC}}\right| \\ \therefore j_\nu(\nu_{IC}) &= \frac{K}{4\pi}\frac{(4/3)^{(p-1)/2}}{2}\sigma_T c\beta^2\frac{U_{ph}}{\nu_0}\left(\frac{\nu_{IC}}{\nu_0}\right)^{-\alpha} \quad [ergcm^{-3}s^{-1}sr^{-1}Hz^{-1}] \end{aligned} \tag{F.95}$$

If the population of isotropic photons are non-monochromatic the emission coefficient becomes

$$j_\nu(\nu_{IC}) = \frac{K}{4\pi}\frac{(4/3)^{(p-1)/2}}{2}\sigma_T c\beta^2\left[\int \frac{U_\nu(\nu)}{\nu}\nu^\alpha d\nu\right]\nu_{IC}^{-\alpha} \tag{F.96}$$

where $U_{nu}(\nu)$ is the differential seed photon energy density spectrum. If we use the fact the $U_\nu(\nu) \propto \nu^{-\alpha}$

$$\begin{aligned} j_\nu(\nu_{IC}) &\propto \frac{(4/3)^{(p-1)/2}}{2}\sigma_T c\beta^2 \left[\int_{\nu_{min}}^{\nu_{max}} \frac{d\nu}{\nu}\right] \nu_{IC}^{-\alpha} \\ &\propto \frac{1}{4\pi}\frac{(4/3)^\alpha}{2}\frac{\tau_{IC}}{(R_*/c)}\nu_{IC}^{-\alpha} ln\left(\frac{\nu_{max}}{\nu_{min}}\right) \end{aligned} \tag{F.97}$$

where the selection of frequencies ν_{min} and ν_{max} can be investigated with the Figure below

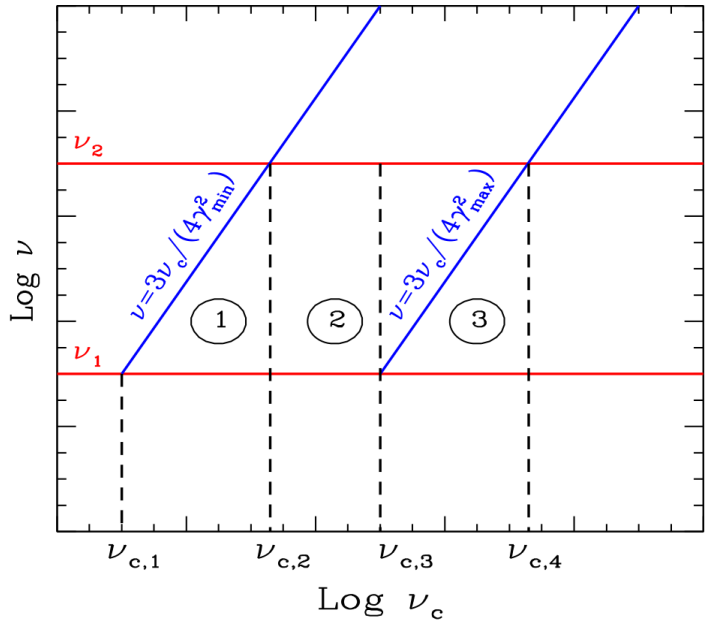

Figure F.15: $\nu - \nu_c$ plane where the blue diagonal lines limit the seed photon regions that can be utilized to obtain a frequency ν_c. Figure adopted from Ghisellini (2013).

From Figure F.15, it can be seen that seed photons with frequency ν_1 can be upscattered to frequencies

$$\nu_{IC,1} = \frac{4}{3}\gamma_{min}^2\nu_1 \quad \& \quad \nu_{IC,3} = \frac{4}{3}\gamma_{max}^2\nu_1 \tag{F.98}$$

while seed photons with frequency ν_2 can be upscattered to

$$\nu_{IC,2} = \frac{4}{3}\gamma_{min}^2\nu_2 \quad \& \quad \nu_{IC,4} = \frac{4}{3}\gamma_{max}^2\nu_2 \tag{F.99}$$

If $\gamma_{min} \ll \gamma_{max}$, a power-law spectrum can be observed if $\gamma_{max}^2 \nu_{min} \gg \gamma_{min}^2 \nu_{max}$ further implying that between $\nu_{IC,2} \rightarrow \nu_{IC,3}$ a power-law scattered spectrum will be observed.

F.6.7 Synchrotron Self-Compton (SSC) Scattering

We saw that if there are relativistic electrons present in a highly magnetized region then these relativistic electrons will produce synchrotron emission. The relativistic electrons in the same region can then "upscatter" these synchrotron photons to very high energies and this process is known as "synchrotron self-Compton (SSC)" scattering. In this process the relativistic electrons do work twice. The "seed" photons are being supplied by the synchrotron mechanism and one can get the emission coefficient for the ICS in this case as

$$\begin{aligned} j_\nu(\nu_{IC}) &= \frac{K}{4\pi}\frac{(4/3)^{(p-1)/2}}{2}\sigma_T c\beta^2 \left[\int \frac{U_{sync,\nu}(\nu)}{\nu}\nu^\alpha d\nu\right]\nu_{IC}^{-\alpha} \\ \therefore j_\nu(\nu_{IC}) &= \frac{1}{4\pi}\frac{(4/3)^\alpha}{2}\frac{\tau_{IC}}{(R_*/c)}\beta^2 \left[\int \frac{U_{sync,\nu}(\nu)}{\nu}\nu^\alpha d\nu\right]\nu_{IC}^{-\alpha} \end{aligned} \tag{F.100}$$

where the seed synchrotron photon density spectrum is given by

$$\begin{aligned} U_{sync,\nu}(\nu) &= \frac{L_{sync,\nu}(\nu)}{V} \times t_{esc} \\ &= 4\pi\left(\frac{L_{sync,\nu}(\nu)}{4\pi V}\right)\left(\frac{3R_*}{4c}\right) \\ &= 4\pi j_{sync,\nu}(\nu) \times \frac{3R_*}{4c} \end{aligned} \tag{F.101}$$

and if we substitute equation F.101 into F.100 we get

$$j_\nu(\nu_{IC}) = \frac{(4/3)^{\alpha-1}}{2}\tau_{IC}[j_{sync,\nu}(\nu_{IC})]ln\Lambda \tag{F.102}$$

where $j_\nu(\nu_{IC}) \propto KB^{1+\alpha}\nu_{IC}^{-\alpha}$ represents the synchrotron emission coefficient at the inverse Compton scattered frequency. It is clear that

$$\begin{aligned} j_\nu(\nu_{IC}) &\propto \tau_{IC} j_{sync,\nu}(\nu_{IC}) ln\Lambda \\ \frac{j_\nu(\nu_{IC})}{j_{sync,\nu}(\nu_{IC})} &\propto \tau_{IC} ln\Lambda \end{aligned} \tag{F.103}$$

which implies that the ratio of ICS and synchrotron flux is determined by the medium's optical depth (τ_{IC}) as shown in Figure F.16 below.

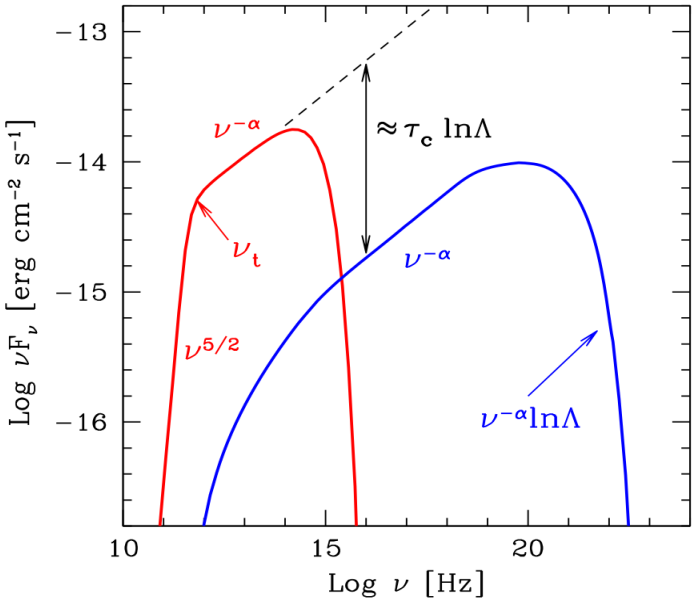

Figure F.16: Synchrotron Self-Compton spectrum showing the dependence on optical depth. Figure adopted from Ghisellini (2013).

We also see that

$$\begin{aligned} j_\nu(\nu_{IC}) &\propto \tau_{IC} j_{sync,\nu} \\ &\propto (K\sigma_T R_*)(KB^{1+\alpha}\nu_{IC}^{-\alpha} \\ &\propto K^2\sigma_T R_* B^{1+\alpha}\nu_{IC}^{-\alpha} \end{aligned} \tag{F.104}$$

where K^2 implies that the relativistic electrons do work twice.

F.7 Neutral Pion Decay

Very high energy γ-ray photons can also be emitted during nucleonic cascades that produces neutral (π^0) pions which quickly decays into γ-rays. The neutral pion was discovered by Bjorklund, Crandall, Moyer, and York (1950) where these authors measured an emission of ∼70 MeV photons while bombarding protons with nuclear targets. When relativistic protons collide they produce neutral and charged pions through the reaction

$$p + p \rightarrow \pi^-, \pi^+, \pi^0 \tag{F.105}$$

in which the charged pions having a short mean lifetime of 2.551×10^{-8}s decay into neutrinos and muons (Longair (2011))

$$\begin{aligned} \pi^+ &\rightarrow \mu^+ + \nu_\mu \\ \pi^- &\rightarrow \mu^- + \bar{\nu}_\mu \end{aligned} \tag{F.106}$$

The low energy muons with mean life time of 2.2001×10^{-6}s further decay into positrons, electrons and muon neutrinos (Longair (2011))

$$\begin{aligned} \mu^+ &\rightarrow e^+ + \nu_e + \bar{\nu}_\mu \\ \mu^- &\rightarrow e^- + \bar{\nu}_e + \nu_\mu \end{aligned} \tag{F.107}$$

The neutral pions decay very rapidly (mean life time of 1.78×10^{-16}s) into two γ-ray photons according to

$$\pi^0 \rightarrow \gamma + \gamma \tag{F.108}$$

Appendix G

Contributed Papers

PROCEEDINGS OF SCIENCE

X-ray and γ-ray periodic analysis of the fast rotating, highly magnetized white dwarf EUVE J0317-85.5

Lurgasho H. Minnie,[a,b,c,*] **Petrus J. Meintjes**[a,b] **and Jacques Maritz**[a,c]

[a] *University of the Free State,*
205 Nelson Mandela Dr, Park West, Bloemfontein, South Africa
[b] *Department of Physics*
[c] *Department of Engineering Sciences*

E-mail: MinnieLH@ufs.ac.za, MeintjPJ@ufs.ac.za, MaritzJM@ufs.ac.za

We report possible X-ray and γ-ray pulsations from the fast rotating, highly magnetic white dwarf EUVE J0317-85.5. Pulsed modulations were found at periods P=724.648±0.001s (-log(P_r)=5.60) at a significance of ~4.59σ and P=361.685±0.001s (-log(P_r)=5.19) at ~4.18σ in the *Fermi*-LAT γ-ray data set. These periods are close to, but significantly different from the spin period and half the spin period of the white dwarf, respectively. Although these γ-ray periods statistically exclude for instance, the optical periods (see Table 1), the folded γ-ray light curve and folded optical light curves are in agreement which could possibly suggest that the optical and γ-rays are related. Possible pulsed X-ray emission was found at a period of P=362.82±0.04s (FAP=3.28×10^{-5}) in the ROSAT X-ray data and at a period P~725.72s but at a low significance (FAP~0.60). The P~362.8s X-ray period is close to, but significantly different from the first harmonic of the spin period which was also observed in recent optical observations (see Table 1). These results may suggest that this white dwarf display pulsar-like properties with emission of radiation from its polar cap regions. The pulsed γ-ray emission is most likely produced by electrons moving along the magnetic field lines emitting curvature radiation, while the X-rays are possibly produced by pair-produced particles flowing back towards and heating the polar cap regions of the white dwarf.

High Energy Astrophysics of South Africa (HEASA)
5-9 September 2023
Mtunzini, KwaZulu-Natal, South Africa

*Speaker

PoS(HEASA2023)011

1. Introduction

EUVE J0317-85.5 (hereafter J0317) was identified by the ROSAT Wide Field Camera (WFC) [1] and Extreme Ultraviolet Explorer (EUVE, [2]) surveys. [1] identified this source as a highly magnetized white dwarf (WD) with a polar field strength of B=340 MG which showed optical variations at a period of P=725.4±0.9s. These authors used a dipole model that is offset along the dipole axis by 0.2 R_{WD} in the direction of the southern magnetic pole to estimate the magnetic field strength. They also proposed that this optical modulation could be due to the rotation of the WD. [1] found that J0317 is associated with another WD star, LB 9802, forming a resolved double DA (class of WD stars showing pressure-broadened hydrogen absorption lines in their spectra [3]) system but could not find any evidence of accretion occurring in this system, meaning that J0317 is an isolated WD. Utilizing the variation in the wavelength-averaged circular polarization in the extreme ultraviolet data from the EUVE Deep Survey, [4] determined a magnetic field strength of B=450 MG offset by 35% of the WD radius (viewed at an angle of 30°-60° to the dipole axis) and a spin period P=725.5±0.8s. [4] also determined pulsations at a period of P=362.9s which corresponds to half the spin period of the WD. [5] further refined this spin period using optical circular spectropolarimetry and found a period of P=725.727±0.001s. Given J0317's unusually high magnetic field and relatively fast spin period for an isolated WD, it is expected that this source behaves as a WD pulsar. A WD pulsar emits pulsed emission in a similar way as a neutron star (NS) pulsar, but the WD pulsar rotates at a much slower rate due to its large moment of inertia and its lower magnetic field (10^3-10^9 G, [6]). The pulsed emission from pulsars are mainly due to electrons getting accelerated by huge electric potentials, ΔV_{max}, usually above the polar caps and can be estimated by the following equation [7]

$$\Delta V_{max} = \frac{B_p \Omega^2 R^3}{2c^2} \tag{1}$$

Close to the polar cap regions, the electrons will rapidly radiate the perpendicular component of their acceleration due to the synchrotron mechanism in a timescale $\tau_s \sim 10^{-10}$s [8] leaving only the electron's parallel component of acceleration along the magnetic field lines to produce curvature photons with energy [9] [10] [11]

$$\epsilon_{CR} = \frac{3\hbar c \gamma_e^3}{2R_c} \tag{2}$$

where R_c is the radius of curvature given by

$$R_c \approx \sqrt{\frac{Rc}{\Omega}} \tag{3}$$

and γ_e is the Lorentz factor of the electrons given by

$$\gamma_e = \frac{e\Delta V}{m_e c^2} \tag{4}$$

A recent study [8] showed that curvature radiation in WD pulsar magnetospheres could produce γ-rays with energies $\epsilon_\gamma \leq$ 10 GeV. The curvature photons then interact with the magnetic fields of the compact object and produce $e^{\pm}$ pairs in the following process [12] [13]

$$\gamma \quad B \rightarrow e^- \quad e \tag{5}$$

The electrons from the process could then be further re-accelerated along the open magnetic field lines to produce γ-rays which could result in a pair cascade process. The positrons, on the other hand, could be accelerated back towards the surface of the WD which could result in the emission of X-rays ([14], [8] and references therein).

2. Data Processing and Analysis

2.1 ROSAT X-ray Data

X-ray data of J0317 was obtained from the online archive HEASARC . J0317 was observed with the ROSAT X-ray (0.1-2.4 keV) space telescope using the high resolution imager (HRI) [15]. Observations were made from 01/04/1996, 11:54:28.000 (UT) to 14/04/1996, 23:40:52.000 (UT). Additional observations were made from 29/08/1996, 17:49:13.00 (UT) to 21/10/1996, 11:27:42.00 (UT). The event files were barycentric corrected using the command ROSBARY that is part of HEAsoft data analysis software provided by NASA. X-ray events were extracted from a region of interest (ROI) of 17" centered around J0317 (RA=$03^h17^m16.1750^s$, DEC=-85°32'25.45", [16]). This ROI included LB 9802 because the ROSAT spacecraft could not resolve these two WDs. These events were then background subtracted using the same ROI in the same field where no source were detected to correctly model the background. Light curves binned at 100 seconds were then created using the events outlined above. These light curves were then used to search for possible periodic pulsations. The generalised Lomb-Scargle technique (GLS) [17] was used to search for periodic behaviour in the X-ray data as it is more sensitive than the standard Lomb-Scargle technique ([18], [19]) because it takes the measurement errors into account. The GLS periodogram is shown in Figure 1.

2.2 *Fermi*-LAT Data

Archived γ-ray data from the *Fermi*-LAT spacecraft [20] were retrieved from the *Fermi* Science Support Center (FSSC). The new Pass 8 LAT [21] γ-ray data was collected from the date range 01 January 2009, 00:00:00 to 02 December 2023, 00:00:00 between the energy range 0.5-10 GeV. The data was analysed with the *Fermi* Sciencetools (version v11r5p3) software provided by FSSC. A standard unbinned likelihood analysis was performed on the γ-ray events from a ROI of 0.6° centered around J0317 (RA=49.31602858°, DEC=-85.54043285°, J2000). Only SOURCE class events (evclass=128 and evtype=3) were selected and γ-ray photons from Earth's limb were excluded by choosing a zenith angle less than 90°. High quality data were obtained by using the expression "(DATA_QUAL>0)&&(LAT_CONFIG==1)" utilizing the GTMKTIME command. The background emission was modelled using the "gll_iem_v07.fits" file for the galactic diffuse emission and the "iso_P8R3_SOURCE_V3_v1.txt" file for extra-galactic diffuse emissions. Events were then further filtered by using the tool GTSRCPROB to only include photons originating from J0317 having a probability greater than 80%. These filtered event files were then used to search for pulsed γ-ray emission using the GTPSEARCH command. The Rayleigh periodograms are shown in Figures

https://heasarc.gsfc.nasa.gov/cgi-bin/W3Browse/w3browse.pl
https://heasarc.gsfc.nasa.gov/docs/software/heasoft/
https://fermi.gsfc.nasa.gov/ssc/
https://fermi.gsfc.nasa.gov/ssc/data/access/lat/BackgroundModels.html

2 and 4. The γ-ray events were then folded using ephemeris [4] and Tempo2 [22] timing analysis software with the *Fermi* plug-in [23]. The folded γ-ray light curves are shown in Figures 3 and 5.

3. Results and Discussions

3.1 X-ray Results

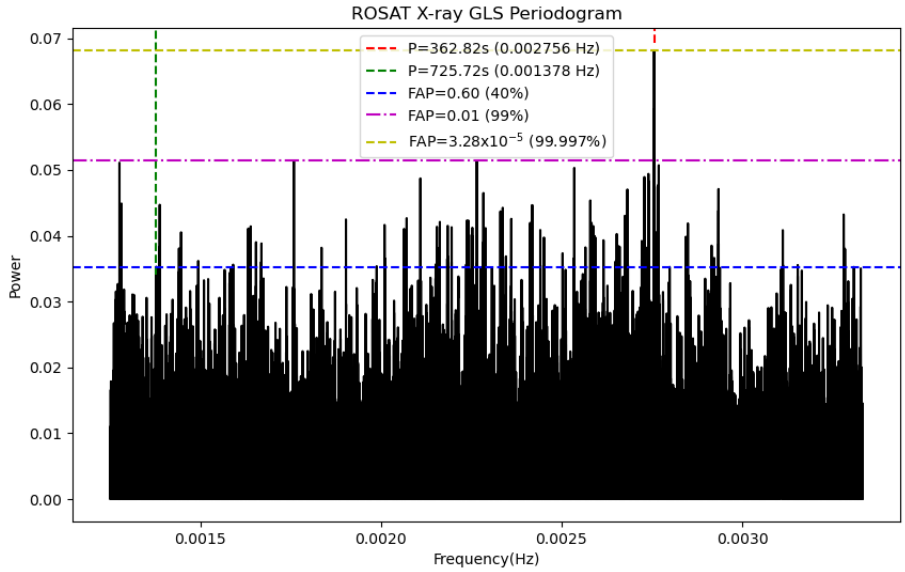

Figure 1: GLS Periodogram of X-ray data showing the spin period and half the spin period of J0317. Note this periodogram has been normalized according to [17]. The FAP=0.60 (40%, blue dotted horizontal line) corresponds to P~725.72s, FAP=0.01 (99%, magenta dash-dotted line) corresponds to the second highest peak in the periodogram P~568.58s and FAP=3.28×10^{-5} (99.997%, yellow dotted line) corresponds to P~362.82s.

The GLS periodogram is shown in Figure 1 and it shows possible X-ray pulsations at a period of P=362.82±0.04s. All uncertainty on periods were estimated using the bootstrap resampling method [24]. This period is in agreement with half the spin period of WD of P~362.9s found by [4] using the extreme ultraviolet data. The false-alarm probability (FAP) of this peak is FAP=3.28×10^{-5}. The FAP is the probability that a signal with no periodic component would lead to a peak in the periodogram of that height [25]. The FAP can be calculated by using

$$FAP(P_n) = 1 - [1 - prob(P > P_n)]^M \quad (6)$$

where M is the number of independent frequencies (can be estimated as the number of peaks in the periodogram) and P_n is the power threshold (see [17] for details). The spin period of P~725.72s in the X-rays of the WD was found (shown by green dotted line in Figure 1) but it was not significant (FAP~0.60). This could possibly suggest that there might be pulsed soft X-ray emission emanating from J0317 but additional soft X-ray observations are required to confirm this result. [4] suggested that the additional periodicity at half the spin period of the WD in their EUV data could be due

to surface abundance inhomogeneities at both the magnetic poles. The possible detection of soft X-ray pulsations at a similar period could suggest that the EUV and X-ray photons are produced at the same region on the WD. The X-rays could also be emitted by pair-produced particles flowing back towards the polar caps (PCs) or regions close to the PCs of the WD [14].

3.2 *Fermi*-LAT γ-ray Results

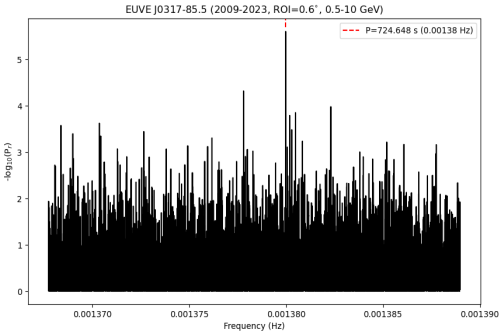

Figure 2: Rayleigh Periodogram showing pulsations at spin period of WD with -log(P_r)=5.60 (FAP=2.51×10^{-6}=99.9997%) at ~4.59σ.

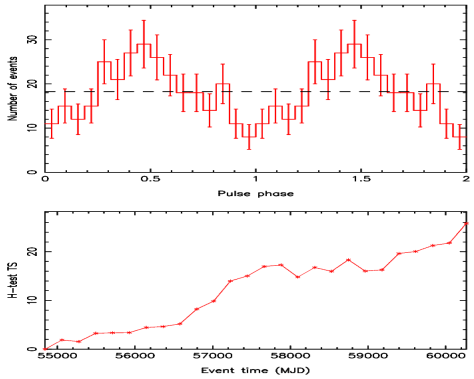

Figure 3: Folded γ-ray (0.5-10 GeV) light curve with spin period P=724.648s using ephemeris by [4]. The H-test Test Statistic is shown in the bottom panel.

The Rayleigh periodogram of the γ-ray data is shown in Figure 2 with a prominent peak at a period P=724.648±0.001s with a -log(P_r)=5.60 at a significance of ~4.59σ. This means that there is a $\approx 10^{-5.60}$ probability that this peak could be associated with noise. The significance was roughly estimated by selecting regions on either side of the Rayleigh periodogram excluding the highest peak and then calculating the average -log(P_r) of these regions. This average -log(P_r) was then subtracted from the -log(P_r) of the highest peak and the result was squared to give the variance. The standard deviation was calculated by taking the square root of the variance and this standard deviation represents the significance of the possible spin period . The periodogram was produced using the ephemeris by [4] and using a sampling frequency ν=2.12×$10^{-11} Hz$ with a number of trial frequencies set to 10^6. This sampling frequency corresponds to 0.01 times the Fourier resolution (ν=2.12×$10^{-9} Hz$). The Fourier resolution is the frequency spacing of a fast Fourier transform (FFT, [26]) and is given by $\Delta f = 1/T$, where T is the length of the observation. The γ-ray light curve is shown in Figure 3 folded on the spin period of the WD using the same ephemeris, shows that there is possible evidence of pulsed γ-ray emission at the spin period of this WD. This emission could possibly be from electrons moving along the strong magnetic field lines above the PCs of the WD emitting curvature photons. Upon first glance, the folded light curve seems to be single-peaked at a phase of about 0.45 but further inspection reveals that there is a second, albeit faint, peak emerging at a phase of about 0.85. The H-test [27] test statistic (TS) is shown in the bottom panel of Figure 3 and shows cumulative power at this spin period with time.

Given the weak second peak in the folded γ-ray light curve (see Figure 3), a search for γ-ray pulsations at half the spin period of the WD was done using the same ephemeris, sampling frequency

The exact procedure was followed to calculate the significance for the possible first harmonic.

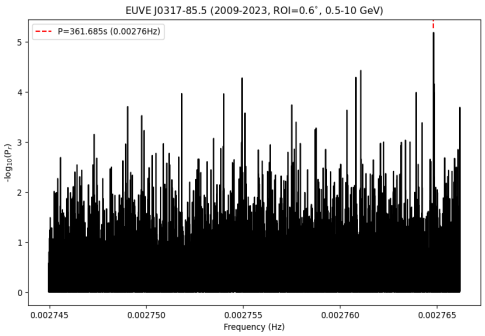

Figure 4: Rayleigh Periodogram showing pulsations at half the spin period of WD with -log(P$_r$)=5.19 (FAP=6.46×10^{-6}=99.9994%) at ~4.18σ.

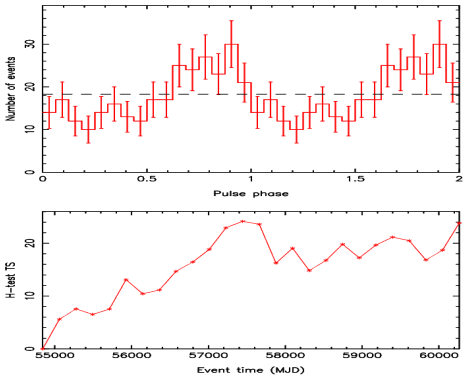

Figure 5: Folded γ-ray (0.5-10 GeV) light curve with half the spin period P=361.685s using ephemeris by [4]. The H-test Test Statistic is shown in the bottom panel.

and number of trials. Pulsations were found at a period of P=361.685±0.001s with -log(P$_r$)=5.19 at a significance of ~4.18σ shown in Figure 4. The single-peaked folded γ-ray light curve is shown in Figure 5. The corresponding H-test TS at this period is also shown at the bottom panel of Figure 5. For reasons that are still under investigation, both the spin period and its first harmonic in the γ-rays are lower than the ultraviolet [4] and recent optical periods (see Table 1). It is interesting that we found possible γ-ray pulsations close to but significantly different from the spin period and its first harmonic because this could possibly suggest that we are receiving γ-ray emission from both poles of the WD.

4. Conclusion

In this paper, we analyzed archival soft X-ray (0.1-2.4keV) data of EUVE J0317-85.5 from the ROSAT space telescope and found possible evidence of pulsed X-ray emission at a period of P=362.82±0.04s (FAP=3.28×10^{-5}=99.997%) which corresponds to half the spin period of the white dwarf (P≈725s). Possible pulsations were also found at a spin period of P~725.72s but it was not significant (FAP~0.60=40%) above the background noise. This could suggest that X-ray emission emanates from the white dwarf poles or that there might be surface abundance inhomogeneities on the white dwarf as suggested by [4]. The pulsed X-ray emission could also be due to the heating of the polar caps by the backward flow of pair-produced charged particles but additional high resolution soft X-ray observations are required to strengthen this claim. We also analyzed *Fermi*-LAT data in the energy range 0.5-10 GeV from 2009 to 2023 and found possible γ-ray pulsations at a period P=724.648±0.001s (-log(P$_r$)=5.60, FAP=2.51×10^{-6}=99.9997%, ~4.59σ) and a period P=361.685±0.001s (-log(P$_r$)=5.19, FAP=6.46×10^{-6}=99.9994%, ~4.18σ) which was close to but significantly different from the spin period and its first harmonic of the white dwarf. See Table 1 for a summary of pulsed periods. The possible detection of pulsed γ-ray emission at both these periods could suggest that the white dwarf is orientated nearly orthogonal to our line of sight. We suggest that the γ-ray pulsations from EUVE J0317-85.5 could be due to curvature radiation given

Wavebands	P_{spin}**(s)**	$P_{spin/2}$**(s)**	**FAP**(P_{spin})	**FAP**($P_{spin/2}$)
X-rays (0.1-2.4 keV)	725.72±0.20	362.82±0.04	0.60	3.28×10^{-5}
γ-rays (0.5-10 GeV)	724.648±0.001	361.685±0.001	2.51×10^{-6}	6.46×10^{-6}
Optical	725.76±0.14	362.46±0.10	0.0	1.41×10^{-8}

Table 1: Summary of spin periods and first harmonics for different wavebands. Recent ~9 hour optical (no filters were used) observations with Bootes-6 robotic telescope are also included for comparison. Errors on pulsed periods were estimated using the bootstrap resampling method [24].

the high magnetic field and relatively fast rotation period of this isolated white dwarf. These results suggest that EUVE J0317-85.5 does appear to behave as a pulsar but future radio observation are required to classify this source as a white dwarf pulsar.

5. Acknowledgments

The authors would like to dearly thank the organizers for the invitation to the HEASA 2023 conference and a reviewer for their instructive comments. We would also like to thank the High Performance Computing cluster at the University of the Free State as most of the data reduction and analysis was performed using the cluster.

References

[1] M.A. Barstow, S. Jordan, D. O'Donoghue, M.R. Burleigh, R. Napiwotzki and M.K. Harrop-Allin, *RE J0317 – 853: the hottest known highly magnetic DA white dwarf*, *Monthly Notices of the Royal Astronomical Society* **277** (1995) 971.

[2] S. Bowyer and R. Malina, *The extreme ultraviolet explorer mission*, *Advances in Space Research* **11** (1991) 205.

[3] B.W. Carroll and D.A. Ostlie, *An introduction to modern astrophysics*, Cambridge University Press (2017).

[4] L. Ferrario, S. Vennes, D.T. Wickramasinghe, J.A. Bailey and D.J. Christian, *EUVE J0317 — 855: a rapidly rotating, high-field magnetic white dwarf*, *Monthly Notices of the Royal Astronomical Society* **292** (1997) 205.

[5] S. Vennes, G.D. Schmidt, L. Ferrario, D.J. Christian, D.T. Wickramasinghe and A. Kawka, *A multiwavelength study of the high-field magnetic white dwarf euve j0317–85.5 (=re j0317–853)*, *The Astrophysical Journal* **593** (2003) 1040.

[6] L. Ferrario, D. de Martino and B.T. Gänsicke, *Magnetic white dwarfs*, *Space Science Reviews* **191** (2015) 111.

[7] P. Goldreich and W.H. Julian, *Pulsar Electrodynamics*, **157** (1969) 869.

[8] P.J. Meintjes, S.T. Madzime, Q. Kaplan and H.J. van Heerden, *Spun-up rotation-powered magnetized white dwarfs in close binaries as possible gamma-ray sources: Signatures of pulsed modulation from ae aquarii and ar scorpii in fermi-lat data*, *Galaxies* **11** (2023) .

[9] M.A. Ruderman and P.G. Sutherland, *Theory of pulsars: polar gaps, sparks, and coherent microwave radiation.*, **196** (1975) 51.

[10] F.C. Michel, *Theory of pulsar magnetospheres*, *Rev. Mod. Phys.* **54** (1982) 1.

[11] Y.P. Ochelkov and V.V. Usov, *Curvature radiation of relativistic particles in the magnetosphere of pulsars*, *Astrophysics and Space Science* **69** (1980) 439.

[12] T. ERBER, *High-energy electromagnetic conversion processes in intense magnetic fields*, *Rev. Mod. Phys.* **38** (1966) 626.

[13] P.A. Sturrock, *A Model of Pulsars*, **164** (1971) 529.

[14] D.L. Cáceres, S.M. de Carvalho, J.G. Coelho, R.C.R. de Lima and J.A. Rueda, *Thermal X-ray emission from massive, fast rotating, highly magnetized white dwarfs*, *Monthly Notices of the Royal Astronomical Society* **465** (2016) 4434.

[15] J. Trümper, *The rosat mission*, *Advances in Space Research* **2** (1982) 241.

[16] Külebi, B., Jordan, S., Nelan, E., Bastian, U. and Altmann, M., *Constraints on the origin of the massive, hot, and rapidly rotating magnetic white dwarf rej 0317-853 from an hst parallax measurement*, *AA* **524** (2010) A36.

[17] Zechmeister, M. and Kürster, M., *The generalised lomb-scargle periodogram - a new formalism for the floating-mean and keplerian periodograms*, *AA* **496** (2009) 577.

[18] N.R. Lomb, *Least-squares frequency analysis of unequally spaced data*, *Astrophysics and space science* **39** (1976) 447.

[19] J.D. Scargle, *Studies in astronomical time series analysis. I - Modeling random processes in the time domain*, **45** (1981) 1.

[20] M. Ackermann, M. Ajello, A. Albert, A. Allafort, W.B. Atwood, M. Axelsson et al., *The fermi large area telescope on orbit: Event classification, instrument response functions, and calibration*, *The Astrophysical Journal Supplement Series* **203** (2012) 4.

[21] W. Atwood, A. Albert, L. Baldini, M. Tinivella, J. Bregeon, M. Pesce-Rollins et al., *Pass 8: Toward the Full Realization of the Fermi-LAT Scientific Potential*, *arXiv e-prints* (2013) arXiv:1303.3514 [1303.3514].

[22] G.B. Hobbs, R.T. Edwards and R.N. Manchester, *tempo2, a new pulsar-timing package – I. An overview*, *Monthly Notices of the Royal Astronomical Society* **369** (2006) 655.

[23] P.S. Ray, M. Kerr, D. Parent, A.A. Abdo, L. Guillemot, S.M. Ransom et al., *Precise -ray timing and radio observations of 17 fermi -ray pulsars*, *The Astrophysical Journal Supplement Series* **194** (2011) 17.

[24] B. Efron and R.J. Tibshirani, *An introduction to the bootstrap*, Chapman and Hall/CRC (1994).

[25] J.T. VanderPlas, *Understanding the lomb–scargle periodogram*, *The Astrophysical Journal Supplement Series* **236** (2018) 16.

[26] E.O. Brigham, *The fast Fourier transform and its applications*, Prentice-Hall, Inc. (1988).

[27] O.C. de Jager, B.C. Raubenheimer and J.W.H. Swanepoel, *A powerful test for weak periodic signals with unknown light curve shape in sparse data.*, **221** (1989) 180.

PROCEEDINGS OF SCIENCE

Fermi-LAT Observations of fast rotating, magnetic white dwarfs J191213.72-441045.1 and EUVE J0317-85.5

Lurgasho H. Minnie,[a,b,c,*] **Pieter J. Meintjes**[a,b] **and Jacques Maritz**[a,c]

[a] *University of the Free State,*
205 Nelson Mandela Dr, Park West, Bloemfontein, South Africa
[b] *Department of Physics*
[c] *Department of Engineering Sciences*

E-mail: MinnieLH@ufs.ac.za, MeintjPJ@ufs.ac.za, MaritzJM@ufs.ac.za

We report the possible detection of pulsed γ-ray emission from one confirmed white dwarf pulsar J191213.72-441045.1 and a candidate white dwarf pulsar EUVE J0317-85.5 using ~15 years of data from the *Fermi*-LAT observatory. Pulsed γ-ray emission in the 0.5-10 GeV energy range from J191213.72-441045.1 were detected at a period of P=319.99±0.35s with a -log(Pr)=6.76 which corresponds to a significance of ~4.37σ using the H-test Test Statistic. This H-test Test Statistic avoids the application of statistical penalties to the periodogram. The phase-folded γ-ray light curve on this period is remarkably in phase with the recent optical observations of J191213.72-441045.1 suggesting that the pulsed γ-rays and optical photons might be emanating from the same region in J191213.72-441045.1. Pulsed γ-ray emission in the 0.5-10 GeV energy range were also found from the isolated, highly magnetic white dwarf EUVE J0317-85.5 at the period of P=724.65±0.54s with a -log(Pr)=5.02 which corresponds to significance of ~3.72σ using the H-test Test Statistic. The phase-folded γ-ray light curve on this period is also in phase with recent optical observations of EUVE J0317-85.5 using the BOOTES-6 robotic telescope. We propose that the pulsed γ-ray emission in the 0.5-10 GeV energy range from both of these fast spinning, magnetic white dwarfs is likely produced by the curvature radiation mechanism based on recent studies suggesting that fast spinning, magnetic white dwarfs to be possible low-level γ-ray emitters.

High Energy Astrophysics of South Africa (HEASA)
16-20 September 2025
Muldersdrift, Johannesburg

*Speaker

ISSN 1824-8039. Published by SISSA Medialab.

PoS(HEASA2025)062

1. Introduction

1.1 J191213.72-441045.1 (J1912)

J1912 is a white dwarf binary system that was discovered by [1] and [2] to emit pulsed emission from radio up to X-rays at a period of ~5.3 minutes. J1912 is in a tight binary orbit with orbital period of ~4.03 hours with a secondary companion of spectral type M4.5±0.5 [1]. The white dwarf in J1912 has a mass of M=1.2±0.2 $M_{\odot}$ and the secondary a mass of M=0.25±0.05 $M_{\odot}$. This M-dwarf fills ~90% of its Roche lobe and [1] detected a flare in the X-ray and optical light curves for which they proposed to be an accretion-induced flare as a result of early onset mass transfer from the M-dwarf to the white dwarf. [3] further refined the white dwarf mass to M=0.59±0.02 $M_{\odot}$ with radius R=0.0131±0.004 $R_{\odot}$ and determined an orbital inclination of i=59±6° and also estimated an upper limit of the white dwarf magnetic field of ≤50 MG. A white dwarf spin period of P=319.34903(8)s and a relatively high magnetic field strength of ≤50 MG, J1912 might indeed possess the required properties to accelerate charged particles like electrons to high energies resulting in pulsar-like γ-ray emission through processes like perhaps curvature radiation [4] although we do not exclude other mechanisms like perhaps inverse Compton scattering of the seed photons from the M-dwarf.

1.2 EUVE J0317-85.5 (J0317)

J0317 was discovered by [5] to emit optical pulsations at a period of P=725.4±0.9s and these authors estimated a magnetic field strength of B~340 MG. [5] found that J0317 was accompanied by a non-magnetic white dwarf LB 9802 but they could not detect any accretion occurring in this system mainly because LB 9802 was 7.2″ away from J0317 which corresponds to a projected separation of ~200 AU ([6]) making J0317 effectively an isolated white dwarf. [7] did ultraviolet observations of J0317 and found pulsations at a period of P=725.5±0.8s and the first harmonic P=362.9s. These authors refined the magnetic field strength to B=450 MG using spectropolarimetric studies. Given this high magnetic field and relatively fast spin period, J0317 could indeed be a white dwarf pulsar candidate.

2. Data Processing and Analysis

2.1 *Fermi*-LAT Observations of J1912

The new Pass 8 [8] γ-ray data from the *Fermi*-LAT spacecraft [9] were retrieved from the *Fermi* Science Support Center (FSSC[1]) from 01 January 2009, 00:00:00 to 05 November 2024, 00:00:00 in the energy range 0.5-10 GeV. The standard unbinned likelihood analysis was carried out on γ-ray events in a region of interest (ROI) of 1° centered around J1912 (right ascension (RA)=288.057166°, declination (DEC)=-44.17919007°, J2000). SOURCE class events (evclass=128 and evtype=3) were selected and γ-ray photons originating from Earth's limb were excluded by choosing the zenith angle to be less than 90°. The command `gtmktime` was used with expression "(DATA_QUAL>0)&&(LAT_CONFIG==1)" to only include the good time intervals (GTIs, times where *Fermi*-LAT collected good quality data) and the background emission was modelled using "iso_P8R3_SOURCE_V3_v1.txt" for extra-galactic diffuse emission and the

[1] https://fermi.gsfc.nasa.gov/ssc/

"gll_iem_v07.fits[2]" file for galactic diffuse emission. The ROI was further reduced to 0.6° to exclude spurious background emission and the command `gtsrcprob` was used to only include γ-ray photons having a probability of >80% originating from J1912. These γ-ray photons have recorded RA and DEC coordinates and we further restrict the DEC of these γ-ray photons to -45°≤DEC≤-44° followed by a RA restriction of 288°≤RA≤289°. The final γ-ray event file was then used to run a periodic analysis using the Rayleigh test [10] that is part of the `gtpsearch` tool which performs on-the-fly barycentric corrections. Using the `Tempo2` [11] tool with the *Fermi*-plugin [12] γ-ray events were then phase-folded (see Rayleigh periodogram in Figure 1) on this predominant period using the spin ephemeris BJD(TDB) = 2459772.142522(24) + 0.0036961693(10)E provided by [1]. To create a spectral energy distribution (SED) of J1912, we used the TS gating method (see [13]). This method involves dividing the whole ∼15 years of data into 5-day sections, running the likelihood analysis on those sections and then only considering sections having TS>0. The SED (see Figure 2) across the whole 0.1-500 GeV energy range with a ROI=10° was used to account for *Fermi*-LAT's broad point-spread function at lower energies ([9], [14]) was created using the TS gated event files together with *FermiPy* [15].

2.2 *Fermi*-LAT Observations of J0317

Some of the same *Fermi*-LAT data selection criteria described in section 2.1 were also followed for J0317 i.e., 01 January 2009, 00:00:00 to 05 November 2024, 00:00:00, energy range 0.5-10 GeV, size of the ROI=1° centered on J0317's coordinates (RA=49.31602858°, DEC=-85.54043285°, J2000). A standard unbinned likelihood analysis was then performed considering these criteria. The ROI was also reduced to 0.6° and `gtsrcprob` was used to only include γ-ray photons that have probability >80% originating from J0317[3]. A periodic analysis was performed on this event file using the Rayleigh Test and the events were phase-folded (see Figure 3) on this predominant period and an SED of J0317 is shown in Figure 4.

3. Results and Discussion

3.1 J1912

From Figure 1, there is a predominant pulsation close to the spin period of the white dwarf in J1912 at P=319.99±0.34s where the error on the period was calculated using the bootstrap resampling method [18]. This period is about ∼5.74σ with a false-alarm probability (FAP) of ∼1.74×10^{-7}(99.99998%) compared to the background periodogram noise. A more robust approach is using the *H-test test statistic* ([17] and references therein) in Figure 1 to estimate the probability of uniformity which scales as Prob(>H)≈$e^{-0.4H}$ ([17]) where H is the maximum *H-test test statistic* and Figure 1 reveals a maximum TS∼30 corresponding to a probability of uniformity of ∼6.14×10^{-6} or ∼4.37σ in the Gaussian distribution. We quote ∼4.37σ as the more robust significance because it avoids the application of statistical penalties to the periodogram. The phase-folded light curve on this predominant period is phase-aligned with the optical phase-folded light curves using the same spin ephemeris.

[2] https://fermi.gsfc.nasa.gov/ssc/data/access/lat/BackgroundModels.html

[3] An RA and DEC restriction on J0317 resulted in an insufficient amount of γ-ray photon for a reliable periodic analysis.

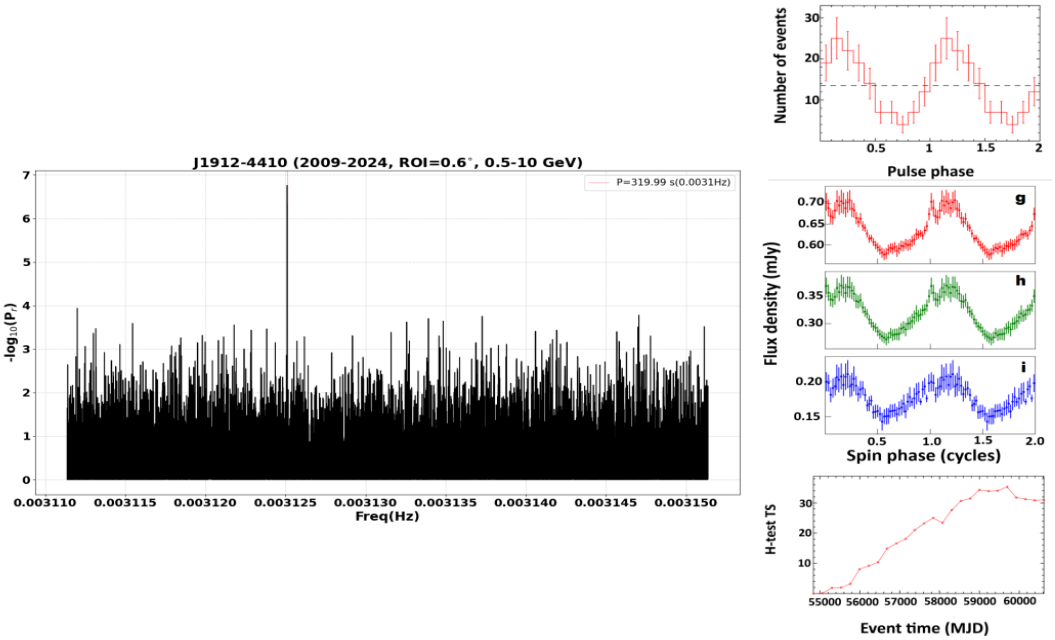

Figure 1: Rayleigh periodogram (left) showing pulsations at P=319.99±0.35s at -log(P_r)= 6.76 with ~4.37σ. Right showing the phase-folded γ-ray (0.5-10 GeV) light curve (top right) on predominant period using spin ephemeris by [1]. Optical observations from [1] are also shown in **g, h** and **i** (i_s, g_s and u_s ULTRACAM [16] filters respectively). The *H-test test statistic* [17] is shown in the bottom panel.

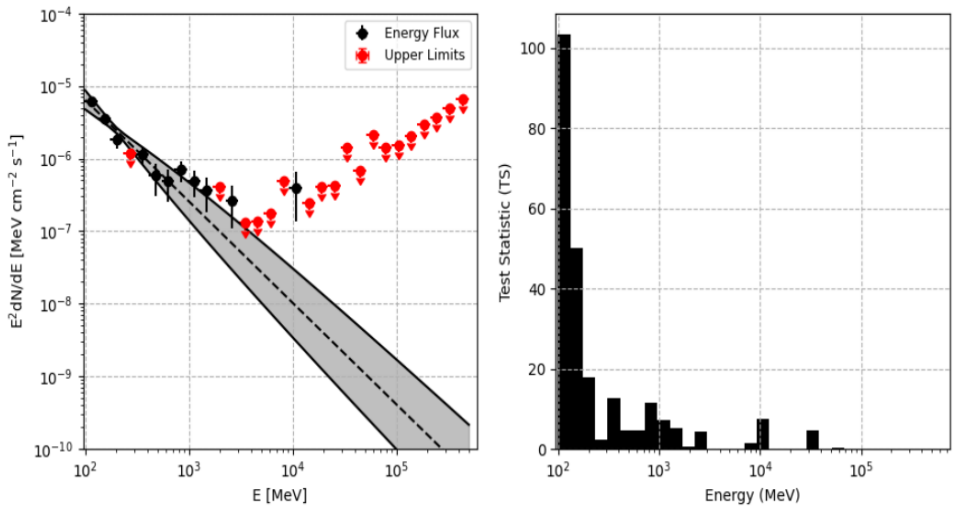

Figure 2: SED of J1912 in the energy 0.1-500 GeV range. Histogram shows the TS distribution with energy.

This might suggest that the optical and γ-ray photons originate from the same regions on the white dwarf in J1912. We propose that this pulsed γ-ray photons in the 0.5-10 GeV range could be due to the curvature radiation mechanism ([4] and references therein) since a recent study by [19] suggested that these highly magnetic and fast rotating white dwarfs might indeed emit low-level pulsed γ-ray emission at energies <50 GeV. The SED and TS histogram is shown in Figure 2 indicates that the γ-ray emission from J1912 is well-described by a power law with index Γ=3.34±0.18 at energies below ~10 GeV.

3.2 J0317

The predominant period in Figure 3 is at P=724.65±0.54s with ~4.01σ with FAP=9.55×10^{-6} (99.99905%) compared to the periodogram noise. The *H-test TS* reaches a maximum value of TS~23 which corresponds a probability of uniformity of ~1.0×10^{-4} or a ~3.72σ using the Gaussian distribution. Phase-folding the γ-ray photons on this period with the spin ephemeris T$_0$= HJD 2450237.72019 provided by [7] reveals that it is double-peaked per rotation with a second faint peak at spin phase ~1. This could possibly be the first harmonic of the spin period of J0317. This γ-ray phase-folded light curve is phase-aligned with recent optical phase-folded light curves using the BOOTES-6 ([20], [21]) robotic telescope at the Boyden Observatory. This might also suggest that the pulsed γ-ray photons and optical photons originate from the same region in the isolated white dwarf.

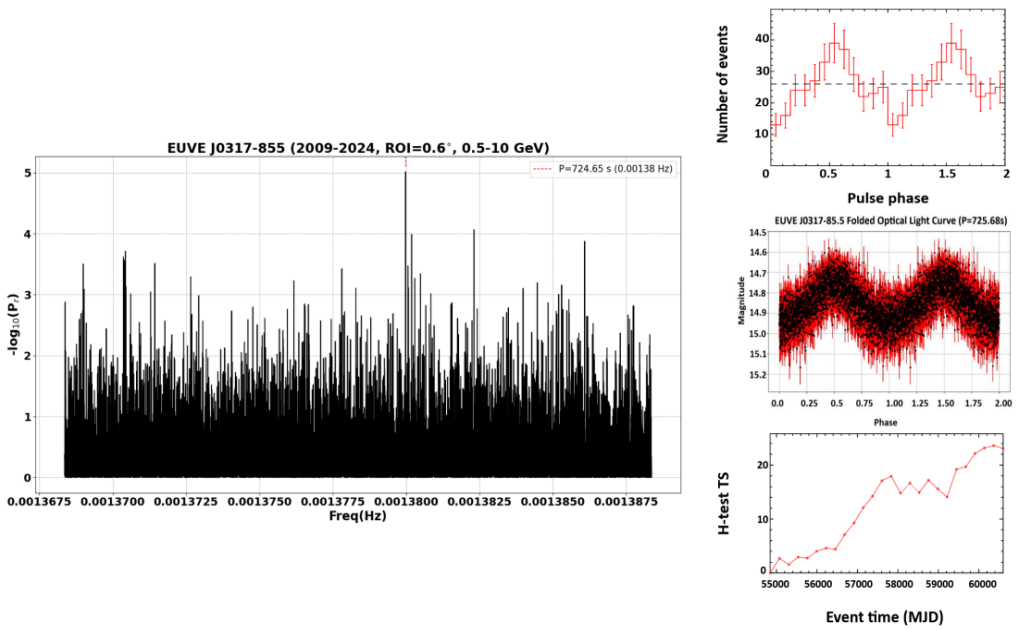

Figure 3: Rayleigh periodogram (left) showing pulsations at P=724.64±0.54s at -log(P$_r$)= 5.02 with ~3.72σ. Right showing the phase-folded γ-ray (0.5-10 GeV) light curve (top) on predominant period using ephemeris by [7]. BOOTES-6 optical observations is also shown in the middle panel. The *H-test test statistic* [17] is shown in the bottom panel.

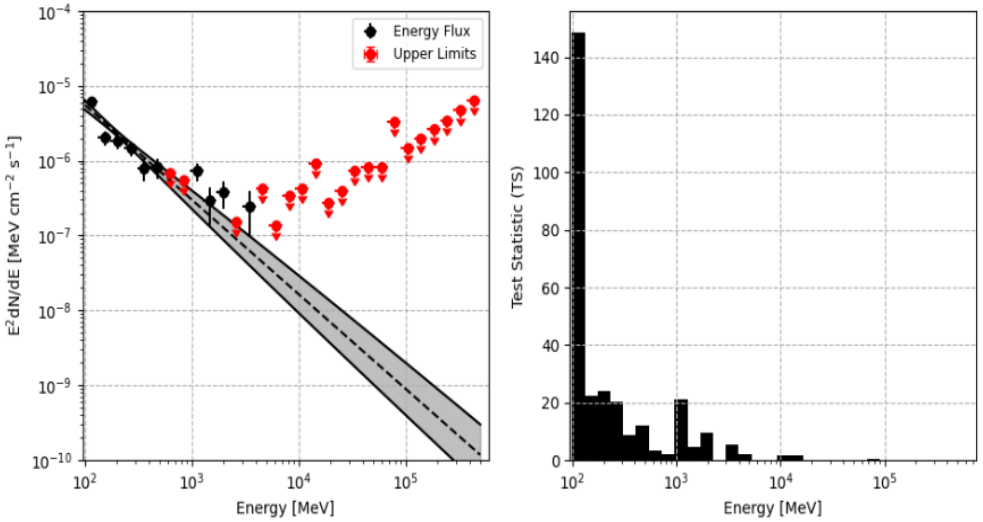

Figure 4: SED of J0317 in the energy 0.1-500 GeV range. Histogram shows the TS distribution with energy

Figure 4 shows the SED that is also well described by a power-law model with spectral index Γ=3.26±0.20 with most of the γ-ray emission at energies below ~10 GeV. For both J1912 and J0317, an order of magnitude within parameter estimates reveal that both sources could possibly accelerate electrons to higher energies with electric potentials ranging from $\Delta V_{max} \approx 10^{12}$-$7\times10^{12}$ V (see [19] and references therein). The scale height above the polar caps where these electrons could be accelerated is $h_{max} \approx 10^8$ cm with maximum Lorentz factors of $\gamma_{max} \leq 10^8$ with a radius of curvature $R_c \approx 10^{10}$ cm. Given that the energy of curvature photons scale as $\epsilon_c \propto \gamma^3 R_c^{-1}$ reveals an upper limit of $\epsilon_c \leq 10$ GeV for both sources and this is seen in the SED for both sources showing similar power-law behaviour where the γ-ray emission is located below $\leq$10 GeV.

4. Conclusions

We detect possible pulsed γ-ray emission from both the white dwarf binary system J1912 and the isolated white dwarf J0317 in the energy range 0.5-10 GeV. In J1912, we detect a period of P=319.99±0.34s at a ~4.37σ using the *H-test test statistic*. The phase-folded γ-ray light curve is phase-aligned with the optical observations from [1] using the same spin ephemeris. Using the TS gating method and *FermiPy* ([15]), we produced an SED which revealed that most of the emission is emitted below an energy range <10 GeV with a power-law model with a spectral index of Γ=3.34±0.18. For J0317, we detect a period of P=724.64±0.54s at ~3.72σ. The phase-folded γ-ray light curve is also phase-aligned with the phase-folded optical light curve from the BOOTES-6 robotic telescope using the same spin ephemeris. This might also suggest that the pulsed optical photons and γ-ray photons originate from the same regions from J0317. The SED of J0317 is well-described by a power-law model with a spectral index of Γ=3.26±0.20 in energies below <10 GeV. We propose the curvature radiation mechanism for the possible pulsed emission close to the spin periods of both J1912 and J0317 since a recent study by [19] did suggest the at these fast

rotating and high magnetised white dwarfs might emit pulsed low-level γ-ray emission at energies below <50 GeV.

5. Acknowledgments

We would like to thank the organisers of HEASA 2025 for the invitation to the conference. We also thank the University of the Free State's High Performance Centre (HPC) for the computational resources, Interdisciplinary Centre for Digital Futures (ICDF) and the Grid Related Research Group (GRRG) for financial assistance.

References

[1] I. Pelisoli, T. Marsh, D. A. Buckley, I. Heywood, S. B. Potter, A. Schwope et al., *Nat. Astron.* **7** (2023) 931.

[2] Schwope, A., Marsh, T. R., Standke, A., Pelisoli, I., Potter, S., Buckley, D. et al., *A&A* **674** (2023) L9.

[3] I. Pelisoli, S. Sahu, M. Lyutikov, M. Barkov, B. T. Gänsicke, J. Brink et al., *MNRAS* **527** (2023) 3826.

[4] V. V. Usov, *Soviet Astronomy Letters* **14** (1988) 258.

[5] M. A. Barstow, S. Jordan, D. O'Donoghue, M. R. Burleigh, R. Napiwotzki and M. K. Harrop-Allin, *MNRAS* **277** (1995) 971.

[6] S. Vennes, G. D. Schmidt, L. Ferrario, D. J. Christian, D. T. Wickramasinghe and A. Kawka, *ApJ* **593** (2003) 1040.

[7] L. Ferrario, S. Vennes, D. T. Wickramasinghe, J. A. Bailey and D. J. Christian, *MNRAS* **292** (1997) 205.

[8] W. Atwood, A. Albert, L. Baldini, M. Tinivella, J. Bregeon, M. Pesce-Rollins et al., *arXiv e-prints* (2013) arXiv:1303.3514 [1303.3514].

[9] M. Ackermann, M. Ajello, A. Albert, A. Allafort, W. B. Atwood, M. Axelsson et al., *ApJ Suppl. Ser.* **203** (2012) 4.

[10] K. V. Mardia, *Statistics of directional data*, Probability and mathematical statistics. Academic Press, London, 1972, https://doi.org/10.1111/j.2517-6161.1975.tb01550.x.

[11] G. B. Hobbs, R. T. Edwards and R. N. Manchester, *MNRAS* **369** (2006) 655.

[12] P. S. Ray, M. Kerr, D. Parent, A. A. Abdo, L. Guillemot, S. M. Ransom et al., *ApJ Suppl. Ser.* **194** (2011) 17.

[13] S. T. Madzime and P. Meintjes, *PoS* **HEASA2022** (2023) 055.

[14] W. B. Atwood, A. A. Abdo, M. Ackermann, W. Althouse, B. Anderson, M. Axelsson et al., *ApJ* **697** (2009) 1071.

[15] M. Wood, R. Caputo, E. Charles, M. Di Mauro, J. Magill, J. S. Perkins et al. in *35th International Cosmic Ray Conference (ICRC2017)*, vol. 301 of *International Cosmic Ray Conference*, p. 824, July, 2017, 1707.09551, DOI.

[16] V. S. Dhillon, T. R. Marsh, M. J. Stevenson, D. C. Atkinson, P. Kerry, P. T. Peacocke et al., *MNRAS* **378** (2007) 825.

[17] de Jager, O. C. and Büsching, I., *A&A* **517** (2010) L9.

[18] B. Efron and R. J. Tibshirani, *An Introduction to the Bootstrap*. Chapman and Hall/CRC, 1 ed., 1994, 10.1201/9780429246593.

[19] P. J. Meintjes, S. T. Madzime, Q. Kaplan and H. J. van Heerden, *Galaxies* **11** (2023) .

[20] H. van Heerden, E. J. Fernández-García, A. J. Castro-Tirado, A. Martin-Carrillo, A. Castellon, P. del Pulgar et al., *PoS* **HEASA2023** (2024) 015.

[21] A. J. Castro-Tirado, *Acta Polytech.* **51** (2011) .